Dynamical Production of Hadrons and Photons in Hydrodynamics + Transport Approaches for Relativistic Heavy-Ion Collisions

Dissertation

zur Erlangung des Doktorgrades
doctor philosophiae naturalis
der Naturwissenschaften

Vorgelegt beim Fachbereich Physik (13)
der Johann Wolfgang Goethe-Universität
in Frankfurt am Main

von
Anna Karen Schäfer
aus Usingen

Frankfurt am Main, 2021
(D 30)

vom Fachbereich 13 (Physik) der
Johann Wolfgang Goethe-Universität als Dissertation angenommen.

Dekan: Prof. Dr. Harald Appelshäuser

Gutachter: Prof. Dr. Hannah Elfner, Prof. Dr. Horst Stöcker

Datum der Disputation:

Contents

List of Figures

List of Tables

Zusammenfassung

Diese Dissertation basiert auf folgenden Publikationen:

- Anna Schäfer, Juan M. Torres-Rincon, Jonas Rothermel, Niklas Ehlert, Charles Gale, and Hannah Elfner. "Benchmarking a nonequilibrium approach to photon emission in relativistic heavy-ion collisions". In: Phys. Rev. D 99.11 (2019), p. 114021 [1]
- Anna Schäfer, Juan M. Torres-Rincon, Charles Gale, and Hannah Elfner. "A Non-Equilibrium Approach to Photon Emission from the Late Stages of Relativistic Heavy-Ion Collisions". In: Nucl. Phys. A 1005 (2021), p. 121772 [2]
- Oscar Garcia-Montero, Jan Staudenmaier, Anna Schäfer, Juan M. Torres-Rincon, and Hannah Elfner. "The role of proton-antiproton regeneration in the late stages of heavy-ion collisions". arXiv: 2107.08812. Submitted to Phys. Rev. C (2021) [3]
- Anna Schäfer, Iurii Karpenko, and Hannah Elfner. "Conservation laws in a novel hybrid approach". arXiv: 2109.08578. Submitted to Proceedings of Science (CPOD 2021) [4]
- Anna Schäfer, Oscar Garcia-Montero, Jean-François Paquet, Hannah Elfner, and Charles Gale. "Out-of-Equilibrium Photon Production in the Late Stages of Relativistic Heavy-Ion Collisions". arXiv: 2111.13603. Submitted to Phys. Rev. C (2021) [5]
- Anna Schäfer, Iurii Karpenko, Xiang-Yu Wu, Jan Hammelmann, and Hannah Elfner. "Particle production in a hybrid approach for a beam energy scan of Au+Au/Pb+Pb collisions between $\sqrt{s_{NN}}$ = 4.3 GeV and $\sqrt{s_{NN}}$ = 200.0 GeV". arXiv: 2112.08724. Submitted to Eur. Phys. J. A (2021) [6]

Gegenstand dieser Arbeit ist die theoretische Beschreibung relativistischer Schwerionenkollisionen im Hinblick auf Hadronen- und Photonenproduktion. Schwerionenkollisionen stellen eine experimentelle Möglichkeit dar, die kleinsten Bausteine unserer Materie zu erforschen und den Zustand unseres Universums wenige Mikrosekunden nach dem Urknall zu reproduzieren. Dazu werden zwei "schwere Ionen", in der Regel Atomkerne, auf Geschwindigkeiten nahe der Lichtgeschwindigkeit beschleunigt und zur Kollision gebracht. Die dabei freigesetzte Energie hat die Produktion einer Vielzahl neuer Teilchen zur Folge, die miteinander interagieren während der Feuerball expandiert und sich abkühlt. Die Endprodukte können schießlich im Detektor nachgewiesen werden, was Rückschlüsse auf das zuvor erzeugte Medium zulässt. Zu den Forschungseinrichtungen bei denen Schwerionenkollisionen experimentell durchgeführt werden zählen beispielsweise das *Conseil Européen pour la Recherche Nucléaire* (CERN), das *Brookhaven National Lab* (BNL), die *Gesellschaft für Schwerionenforschung* (GSI) oder das *Joint Institute for Nuclear Research* (JINR). Dort ermöglichen unterschiedlich konstruierte Beschleunigeranlagen Schwerionenkollisionen bei unterschiedlichen Energien und Baryonendichten, wodurch verschiedene Bereiche des QCD-Phasendiagramms zugänglich sind. Das QCD-Phasendiagramm gibt den Zustand stark wechselwirkender Materie (QCD-Materie) in Abhängigkeit der Temperatur und der Netto-Baryonendichte an. Bei geringen Temperaturen und Dichten, wie im Grundzustand, liegt QCD-Materie in Form gebundener Zuständen, sogenannter Hadronen vor. Bei hohen Temperaturen und/oder Dichten brechen diese gebundenen Zustände allerdings auseinander und deren Bestandteile, Quarks und

Gluonen, können frei existieren. Dieser Zustand wird als Quark-Gluon-Plasma (QGP) bezeichnet. Bei geringen Dichten erfolgt der Übergang vom Quark-Gluon-Plasma zum Hadronengas durch einen Crossover, während bei höheren Dichten ein Phasenübergang erster Ordnung erwartet wird. Dies impliziert die Existenz eines kritischen Endpunktes, dessen Lokalisation Gegenstand vieler aktueller Forschungsprojekte ist. Dazu zählen unter anderem der *Beam Energy Scan II* (BES II) am BNL, das NA61/SHINE Experiment am CERN, sowie in Zukunft die *Facility for Antiproton and Ion Research* (FAIR) an der GSI und die *Nuclotron-based Ion Collider fAcility* (NICA) am JINR. Bei diesen Programmen werden Schwerionenkollisionen bei niedrigeren und mittleren Energien durchgeführt, um den Bereich des QCD-Phasendiagramms zu erkunden, bei dem niedrigere Temperaturen und hohe Baryonendichten, bzw. mittlere Temperaturen und mittlere Baryonendichten vorliegen. Um den Bereich des QCD-Phasendiagramms bei niedrigeren Dichten und hohen Temperaturen zu untersuchen, bedarf es Schwerionenkollisionen bei hohen Energien, wie sie zum Beispiel mit dem *Large Hadron Collider* (LHC) am CERN und dem *Relativistic Heavy-Ion Collider* (RHIC) am BNL durchgeführt werden.
Die experimentelle Durchführung relativistischer Schwerionenkollisionen allein ist allerdings nicht ausreichend, um ein vollständiges Bild der zugrundeliegenden Mechanismen, Prozesse und Eigenschaften zu erhalten. Vielmehr ist es notwendig, die experimentell ermittelten Ergebnisse mit denen theoretischer Modellrechnungen und Simulationen zu vergleichen. Dies ermöglicht zum einen die Verifikation und Validierung bereits bestehender Erkenntnisse, im Fall von Übereinstimmung der experimentellen und theoretischen Ergebnisse, und gibt zum anderen Hinweise auf ein unzureichendes theoretisches Verständnis, im Fall von Nichtübereinstimmung. Zur theoretischen Beschreibung relativistischer Schwerionenkollisionen bedarf es unterschiedlicher Modelle, um die Dynamiken in den verschiedenen Energiebereichen, nicht zuletzt aufgrund unterschiedlicher relevanter Freiheitsgrade, korrekt darstellen zu können. So hat es sich bewährt, Schwerionenkollisionen bei niedrigen Energien im Rahmen von Transportmodellen mit hadronischen Freiheitsgraden zu beschreiben. Beispiele hierfür sind SMASH, UrQMD, PHSD, GiBUU oder JAM. Diese stellen eine effektive Lösung der Boltzmann-Gleichung dar, indem das Kollisionsintegral durch Formationen und Zerfälle hadronischer Resonanzen modelliert wird. Transportmodelle haben den Vorteil, dass die gesamte Raum-Zeit-Impuls-Information aller Teilchen zu jedem Zeitpunkt verfügbar ist. Interaktionsketten können daher vollständig vom Endzustand in den Anfangszustand zurückverfolgt werden, wohingegen im Experiment lediglich der Endzustand zugänglich ist. Bei höheren Kollisionsenergien verlieren hadronische Transportmodelle allerdings ihre Anwendbarkeit, da die relevanten Freiheitsgrade nicht mehr Hadronen, sondern Partonen sind. Einige hadronische Transportmodelle sind daher an ein String-Modell gekoppelt, womit sich auch partonische Interaktionen modellieren lassen, sodass der Anwendungsbereich hin zu höheren Energien erweitert wird. Bei sehr hohen Kollisionsenergien sind jedoch auch erweiterte Transportmodelle nicht in der Lage, die Dynamik korrekt darzustellen. Stattdessen werden Schwerionenkollisionen in diesem Energiebereich in der Regel mit Hybridmodellen beschrieben, bei denen relativistische Hydrodynamik an hadronischen Transport gekoppelt wird. Der heiße und dichte Feuerball wird dabei meist mit viskoser Hydrodynamik in 3+1D beschrieben. Die Evolution des Mediums wird so lange fortgeführt, bis die Dichte zu gering für eine Gleichgewichtsannahme ist. Ist dies der Fall, werden die Fluid Elemente in Hadronen transformiert, sodass sie in einem Transportmodell weiter propagiert werden können. Darin werden die verbleibenden Interaktionen ausgeführt, bis sämtliche Hadronen schließlich chemisch und kinetisch ausfrieren. Zusammenfassend ist zu betonen, dass solche Hybridmodelle insbesondere geeignet sind, um die Dynamik von Schwerionenkollisionen

bei hohen Energien zu beschreiben, während Transportmodelle bei niedrigen Energien verwendet werden. Die theoretische Beschreibung von Schwerionenkollisionen bei mittleren Energien stellt allerdings nach wie vor eine Herausforderung dar. Hybridmodelle bestehend aus Hydrodynamik+Transport sind auch in diesem Energiebereich vielversprechende Kandidaten, jedoch ist hier die Realisierung des Anfangszustandes nichttrivial. Aufgrund der langsameren Dynamik ist die unmittelbare Deposition von Energiedichte, Baryonendichte und Ladungsdichte in der hydrodynamischen Phase eine fragwürdige Annahme. Ferner stellt die korrekte Modellierung der Baryonen-Dynamik, insbesondere des Baryon-Stoppings, in diesem Energiebereich oft eine Herausforderung für Hybridmodelle dar. Nichtsdestotrotz entspricht dieser Energiebereich gerade der Region des QCD-Phasendiagramms, in dem ein Phasenübergang erster Ordnung sowie der postulierte kritische Endpunkt zu erwarten sind. Der mittlere Energiebereich ist demnach für die Erforschung von QCD-Materie von besonderem Interesse. Es ist daher notwendig, adäquate theoretische Modelle zu entwickeln, die in der Lage sind, die Dynamik von Schwerionenkollisionen von geringen bis hin zu hohen Energien zu beschreiben, um deren Ergebnisse mit experimentellen Beobachtungen zu vergleichen. Die Entwicklung ebensolcher Modelle steht im Mittelpunkt dieser Dissertation.

Zunächst wird ein neues Hybridmodell eingeführt, das `SMASH-vHLLE-hybrid`, das zur theoretischen Beschreibung relativistischer Schwerionenkollisionen herangezogen werden kann. Der Anwendungsbereich liegt bei Kollisionsenergien zwischen $\sqrt{s_{NN}} = 4.3$ GeV und $\sqrt{s_{NN}} = 5.02$ TeV. Das hadronische Transportmodell `SMASH` ist darin an `vHLLE` gekoppelt, womit die viskose, hydrodynamische Evolution in 3+1D modelliert wird. Die Initialisierung von `vHLLE` erfolgt auf einer Hyperfläche konstanter Eigenzeit und basiert auf einer mit `SMASH` simulierten Kern-Kern Kollision. Diese Eigenzeit ergibt sich aus der Überlappzeit der beiden Kerne und ist somit abhängig von der Kollisionsenergie. Nach der hydrodynamischen Evolution erfolgt die Partiklisierung der Fluid Elemente auf einer Hyperfläche konstanter Energiedichte, $e_{crit} = 0.5$ GeV/fm^3, was technisch mit dem `SMASH-hadron-sampler` realisiert wird. Die weitere Propagation der damit generierten Hadronen erfolgt erneut mit `SMASH` bis das Medium eine so geringe Dichte aufweist, dass keine Interaktionen mehr stattfinden. Es ist dann chemisch und kinetisch ausgefroren. Zentraler Gegenstand dieser Arbeit ist die numerische Umsetzung des `SMASH-vHLLE-hybrid`s auf Basis der bereits existierenden Modelle `SMASH` und `vHLLE`, die jeweils modifiziert werden mussten, um die Schnittstellen realisieren zu können. Ferner ist für die Realisierung des Partiklisierungsprozesses die Zustandsgleichung des Hadronen-Resonanz-Gases notwendig, das sich aus den Freiheitsgerade von `SMASH` zusammensetzt. Die Determinierung dieser Zustandsgleichung als Funktion der Energiedichte, Baryonendichte und elektrischen Ladungsdichte wird daher ebenfalls diskutiert.
Bevor das `SMASH-vHLLE-hybrid` zur Beschreibung relativistischer Schwerionenkollisionen verwendet wird, erfolgt eine Validierung im Hinblick auf Quantenzahlerhaltung, sowie ein Vergleich zu anderen Hybridmodellen. Es wird demonstriert, dass die Gesamtenergie, Baryonenzahl und elektrische Ladung im Verlauf von Au+Au/Pb+Pb Kollisionen zwischen $\sqrt{s_{NN}} = 4.3$ GeV und $\sqrt{s_{NN}} = 200.0$ GeV mit einer Abweichung von maximal 7% im Mittel erhalten ist. Dies kann als minimale Validierung des Modells verstanden werden. Die Verletzung der Quantenzahlerhaltung ist mit begrenzten Gittergenauigkeiten in der Initialisierung der hydrodynamischen Evolution sowie mit kleinen Ungenauigkeiten der Zustandsgleichung des `SMASH` Hadronen-Resonanz-Gases im Bereich geringer Energiedichten zu erklären. Die Verletzung der Quantenzahlerhaltung ist bei geringen Kollisionsenergien ausgeprägter als bei hohen und beträgt daher in den meisten Fällen erheblich weniger als 7%. Zusätzlich werden Ergebnisse des `SMASH-vHLLE-hybrid`s zu Validierungszwecken mit denen

aus einem SMASH+CLVisc Hybrid und aus einem UrQMD+vHLLE Hybrid verglichen. Dabei wird eine perfekte Übereinstimmung mit den Ergebnissen des SMASH+CLVisc Hybrids gefunden, was insbesondere die hydrodynamische Evolution validiert. Im Vergleich zum UrQMD+vHLLE Hybrid ist eine gute, aber nicht perfekte Übereinstimmung der Ergebnisse zu erkennen. Diese ist bedingt durch Unterschiede in den hadronischen Transportmodellen UrQMD und SMASH. Nichtsdestotrotz stellt die gute Übereinstimmung mit anderen Hybridmodellen in Kombination mit der zuvor beschriebenen annähernden globalen Quantenzahlerhaltung eine erfolgreiche Validierung des SMASH-vHLLE-hybrids dar, sodass dieses in der Folge zur theoretischen Beschreibung relativistischer Schwerionenkollisionen herangezogen werden kann.
Im Rahmen dieser Arbeit werden die Rapiditätsspektren und transversalen Massenspektren von Pionen, Protonen und Kaonen in Au+Au/Pb+Pb Kollisionen zwischen $\sqrt{s_{NN}} = 4.3$ GeV und $\sqrt{s_{NN}} = 200.0$ GeV bestimmt und mit experimentellen Ergebnissen konfrontiert. Eine gute Übereinstimmung sowohl der Rapiditäts- als auch der transversalen Massenspektren ist zu beobachten. Insbesondere im Vergleich zu einer Beschreibung dieser Kollisionen allein im Rahmen eines hadronischen Transportmodells - ohne zwischenzeitliche hydrodynamische Phase - ist zu erkennen, dass eine signifikant bessere Übereinstimmung mit den experimentell gemessenen Spektren erreicht wird, wenn das SMASH-vHLLE-hybrid verwendet wird. Ferner ist das Hybridmodell in der Lage, die experimentell beobachteten Baryon-Dynamiken über einen großen Bereich von Kollisionsenergien qualitativ korrekt zu reproduzieren. Der Übergang von einem einzelnen Peak im Protonen Rapiditätsspektrum bei geringen Kollisionsenergien zu einer Doppelpeak-Struktur für höhere Energien ist klar zu identifizieren und das Baryonen-Stopping bei mittleren Rapiditäten deutlich erkennbar. Zusätzlich werden Anregungsfunktionen für die Multiplizität bei Midrapidität und den mittleren transversalen Impuls sowie für den elliptischen und triangulären Fluss betrachtet. Auch hier ist zu beobachten, dass sich die Übereinstimmung mit experimentellen Ergebnissen bei Heranziehung eines Hybridmodells im Vergleich zu einem reinen Transportmodell signifikant verbessert. Es zeigt sich, dass die experimentell gemessenen Impulsanisotropien v_2 und v_3 insbesondere bei niedrigen Energien durch das SMASH-vHLLE-hybrid unterschätzt werden. Dies ist mit einer zu kurzen Lebenszeit des hydrodynamischen Feuerballs zu erklären und bedarf einer besseren Initialisierung der hydrodynamischen Phase bei geringen Kollisionsenergien, beispielsweise durch Verwendung dynamischerer Anfangsbedingungen.
Darüberhinaus wird das SMASH-vHLLE-hybrid zur Simulation von Au+Au/Pb+Pb Kollisionen zwischen $\sqrt{s_{NN}} = 17.3$ GeV und $\sqrt{s_{NN}} = 5.02$ TeV verwendet, um die Auswirkungen von Proton-Antiproton Annihilationen und Regenerationen in der späten Rescattering Phase von Schwerionenkollisionen auf die finalen Proton und Antiproton Multiplizitäten zu beurteilen. Konkret wird die Proton-Antiproton Annihilation in 5 Pionen und die entsprechende Rückreaktion $p + \bar{p} \leftrightarrow 5\ \pi$ betrachtet, die in SMASH implementiert ist. Die Anzahl der Annihilationen und Rückreaktionen lässt sich daher für Kollisionen verschiedener Zentralitäten und Energien konkret bestimmen. Dabei zeigt sich, dass im Verlauf der Rescattering Phase 20-30% der gesamten (Anti)Protonen 4π-Multiplizität, die durch Annihilationen verloren geht, durch die Rückreaktion regeneriert wird. Bei Midrapidität beträgt dieser Anteil 50%. Der Regenerationsanteil ist in beiden Fällen unabhängig von der Energie oder Zentralität der Kollision. Es ist daher essentiell, die dynamische Annihilation und insbesondere die Regeneration von Baryon-Antibaryon Paaren in der späten Rescattering Phase nicht zu vernachlässigen, um eine möglichst adäquate, theoretische Beschreibung relativistischer Schwerionenkollisionen zu gewährleisten.
Das SMASH-vHLLE-hybrid eignet sich als neues Hybridmodell zur Beschreibung relativistischer

Schwerionenkollisionen über einen großen Bereich von Kollisionsenergien. Es ist in dieser Arbeit eingeführt und gründlich validiert worden. Ferner ist über den gesamten Energiebereich eine gute Übereinstimmung mit experimentell ermittelten Spektren demonstriert worden, insbesondere im Hinblick auf Baryon-Stopping-Dynamiken. Zum gegenwärtigen Zeitpunkt basiert das `SMASH-vHLLE-hybrid` auf einer Initialisierung der hydrodynamischen Phase bei konstanter Eigenzeit. Eine Erweiterung auf dynamischere Anfangsbedingungen stellt einen nächsten Schritt dar, um die Genauigkeit bei geringen Kollisionsenergien zu erhöhen. Darüber hinaus kann das `SMASH-vHLLE-hybrid` mit verschiedenen Zustandsgleichungen für die Evolution des hydrodynamischen Feuerballs - mit und ohne Phasenübergang erster Ordnung - verwendet werden, um die Auswirkungen auf Endzustandsobservablen systematisch zu untersuchen.

Ein weiteres Hybridmodell, das in dieser Dissertation Anwendung findet, ist ein `MUSIC+SMASH` Hybrid, womit die Produktion von Photonen in Schwerionenkollisionen bei RHIC/LHC Energien untersucht wird. Photonen sind wertvolle Sonden da sie, im Gegensatz zu Hadronen, im gesamten Verlauf der Kollision produziert werden und ohne weitere zwischenzeitliche Wechselwirkung mit dem Medium detektiert werden können. Dies ist bedingt durch die Tatsache, dass Photonen lediglich elektro-schwach, nicht aber stark wechselwirken können. Sie tragen daher Information direkt aus dem Feuerball in den Detektor, mit denen das Medium zeit-integriert charakterisiert werden kann. Die Produktion von Photonen in Schwerionenkollisionen bei RHIC/LHC Energien ist zum gegenwärtigen Zeitpunkt noch nicht vollständig verstanden. Bisher existiert kein theoretisches Modell, das in der Lage ist, die experimentell gemessenen Multiplizitäten und gleichzeitig den elliptischen Fluss direkter Photonen zu reproduzieren. Diese Beobachtung wird in der Literatur als *Direktes Photonen Puzzle* bezeichnet.
In dieser Arbeit wird der Einfluss von Nichtgleichgewichtsdynamiken in der späten Rescattering Phase bei Au+Au/Pb+Pb Kollisionen hoher Energien auf die Produktion von Photonen untersucht. Ein `MUSIC+SMASH Hybrid` eignet sich dafür in besonderem Maße, da die Photonen-Raten, die für die makroskopische, hydrodynamische Beschreibung mit `MUSIC` verwendet werden, auf denselben effektiven Feldtheorien basieren, wie die Wirkungsquerschnitte, die mikroskopisch im hadronischen Transportmodell `SMASH` implementiert werden. Dies ermöglicht zum einen eine konsistente Beschreibung von Photonenproduktion über die verschiedenen Stadien der Kollision hinweg und erlaubt zum anderen einen direkten Vergleich zwischen einer Modellierung der Rescattering Phase mit hadronischem Transport und einer Approximation derselben mittels Hydrodynamik. Letzteres entspricht zum jetzigen Zeitpunkt der typischen Herangehensweise, um die Produktion von Photonen in hochenergetischen Schwerionenkollisionen theoretisch zu beschreiben, Nichtgleichgewichtsdynamiken werden dabei jedoch vernachlässigt.
Bevor das `MUSIC+SMASH` Hybrid zur Beschreibung von Photonenproduktion herangezogen werden kann, ist es notwendig, die entsprechenden Wirkungsquerschnitte zu bestimmen und in `SMASH` zu implementieren. Die zugrundeliegenden Feldtheorien sowie die daraus resultierenden Wirkungsquerschnitte für die Produktion von Photonen in $2 \to 2$ Streuprozessen und Pion-Pion Bremsstrahlung sind in dieser Arbeit beschrieben. Die Wirkungsquerschnitte als auch deren Implementierung in `SMASH` werden ferner auf Basis thermischer Photonen-Raten im Gleichgewicht erfolgreich validiert. Mit dem `MUSIC+SMASH` Hybrid werden anschließend Au+Au Kollisionen bei $\sqrt{s_{\mathrm{NN}}} = 200.0$ GeV und Pb+Pb Kollisionen bei $\sqrt{s_{\mathrm{NN}}} = 2.76$ TeV modelliert und die entsprechenden Transversalimpulsspektren sowie der elliptische Fluss von Photonen extrahiert. Dabei wird unterschieden zwischen (i) einer Beschreibung der Kollision

im Rahmen des MUSIC+SMASH Hybrids, worin Nichtgleichgewichtsdynamiken die Rescattering Phase charakterisieren, und (ii) einer ausschließlich makroskopischen Beschreibung im Rahmen von MUSIC, sodass die Rescattering Phase hydrodynamisch approximiert wird. Betrachtet man zunächst lediglich die Rescattering Phase in Au+Au/Pb+Pb Kollisionen bei $\sqrt{s_{NN}} = 200.0$ GeV und $\sqrt{s_{NN}} = 2.76$ TeV ist zu erkennen, dass die Transversalimpulsspektren im Nichtgleichgewichtsfall einen geringfügig steileren Verlauf aufweisen als bei einer Approximation mittels Hydrodynamik. Ferner sind die Impulsanisotropien im Nichtgleichgewichtsfall erheblich stärker ausgeprägt, der elliptische Fluss ist um bis zu 70% höher als im Gleichgewichtsfall. Kombiniert man diese Photonen aus der Rescattering Phase nun mit denjenigen, die aus der hydrodynamischen Phase oberhalb der Transitionstemperatur $T = 150$ MeV stammen, ergeben sich lediglich marginale Unterschiede in den p_T Spektren. Dies liegt nicht zuletzt an der großen Menge an Photonen aus dieser heißeren Phase, die das Gesamtspektrum insbesondere bei höheren p_T dominieren. Dementsprechend ist für höhere p_T auch kein signifikanter Unterschied im kombinierten elliptischen Fluss zu erkennen. Für $p_T \lesssim 1.4$ GeV ergibt sich im Nichtgleichgewichtsfall jedoch ein erheblich erhöhter elliptischer Fluss. Bei RHIC Energien ist dieser um bis zu 30% und bei LHC Energien um bis zu 20% höher als im Gleichgewichtsfall.
Gerade im Bereich geringer p_T ist es daher essentiell, Nichtgleichgewichtsdynamiken in der Rescattering Phase für die Beschreibung von Photonenproduktion nicht zu vernachlässigen. Es sei allerdings erwähnt, dass die hier durchgeführte Studie qualitativer Natur ist und einem vereinfachten Zugang entspricht, bei dem Event-für-Event Fluktuationen als auch Viskositäten vernachlässigt wurden. Eine Wiederholung derselben Studie unter Einbeziehung von Event-für-Event Fluktuationen und Viskositäten stellt nun den nächsten Schritt dar, um die Eigenschaften von Photonen aus Schwerionenkollisionen tiefer zu verstehen und daraus Rückschlüsse auf das stark wechselwirkende Medium ziehen zu können. Ferner sind in SMASH bisher nur die dominierenden Produktionskanäle für Photonen implementiert. Es ist daher notwendig, das hier beschriebene Framework mit zusätzlichen Produktionskanälen zu erweitern, um eine genauere Beschreibung der Photonenproduktion in relativistischen Schwerionenkollisionen ermöglichen zu können.

Zusammenfassend sind in dieser Arbeit zwei Hybridmodelle zur theoretischen Beschreibung relativistischer Schwerionenkollisionen herangezogen worden. Das neu entwickelte SMASH-vHLLE-hybrid ist für Au+Au/Pb+Pb Kollisionen zwischen $\sqrt{s_{NN}} = 4.3$ GeV und $\sqrt{s_{NN}} = 5.02$ TeV angewendet worden, um die Produktion von Hadronen zu untersuchen. Dabei ist eine gute Übereinstimmung mit experimentellen Ergebnissen über einen großen Energiebereich gefunden worden. Es stellt die Basis für eine Vielzahl neuer Studien dar, um die Eigenschaften stark wechselwirkender Materie zu erforschen. Ferner ist die Notwendigkeit der Rückreaktion von Proton-Antiproton Annihilationen in der späten Rescattering Phase verdeutlicht worden. 20-30% der gesamten (Anti)Protonen Multiplizität wird durch die Rückreaktion regeneriert.
Die Beschreibung von Photonenproduktion in Schwerionenkollisionen bei RHIC/LHC Energien ist ferner im Rahmen eines MUSIC+SMASH Hybrids erfolgt. Dabei ist die Notwendigkeit für Nichtgleichgewichtsdynamiken in der späten Rescattering Phase demonstriert worden. Insbesondere der elliptischen Fluss von Photonen ist bei geringen transversalen Impulsen um bis zu 30% höher, wenn die Rescattering Phase mit mikroskopischem Transport außerhalb des Gleichgewichtes, anstelle von Hydrodynamik im Gleichgewicht beschrieben wird.

1 Introduction

The smallest constituents of matter can be studied by means of relativistic heavy-ion collisions. Atomic nuclei are accelerated to velocities close to the speed of light, collide, and release a tremendous amount of energy. Consequently, a variety of new particles are produced, which can then be collected in the detector. Their analysis gives access to a wide range of observables which encapsulate the properties of the smallest constituents of matter. Adequate theoretical models to compare to are crucial for a proper understanding of the experimentally obtained results. In this thesis, an attempt is made to provide a detailed theoretical description of heavy-ion collisions and their observables at intermediate and high collision energies by employing so-called hybrid approaches.

1.1. The Standard Model of Particle Physics

There are four fundamental forces in physics: The strong interaction, the weak interaction, the electromagnetic interaction, and gravitation; in descending order of their strengths. They are characterized by different strengths and ranges and act on particles with different properties. While gravitation acts on massive objects, the electromagnetic, the weak, and the strong interactions act on objects carrying electric, weak, and colour charge, respectively.
In the standard model of particle physics, all elementary particles are classified according to their properties and related to the strong, the weak, and the electromagnetic interaction. As depicted in Figure 1.1, the elementary particles can be classified into different groups: quarks, leptons, gauge bosons, and the Higgs boson, forming a group of its own. While quarks carry colour charge and are thus subject to the strong interaction, leptons are weakly-interacting particles. In addition, all quarks, as well as the e, μ and τ lepton, carry electric charge and hence also respond to the electromagnetic interaction. The interactions themselves are mediated through the exchange of so-called gauge bosons. These are spin-1 particles that transmit the fundamental forces among the fundamental particles. As such gluons (g) mediate the strong interaction, the photon (γ) the electromagnetic interaction, and the W and Z bosons the weak interaction. Finally, the Higgs field, of which the Higgs boson is a quantum excitation in a particle state, is required for the W and Z boson to be massive. In what follows, particular emphasis is laid on the strong and the electromagnetic interaction, for these two being of central interest in the scope of this thesis.

1.1.1. The Strong Interaction

The strong interaction is the strongest, yet the shortest-ranged interaction of the four fundamental forces. Its range can be computed to $\approx 10^{-15}$ m $= 1$ fm, which approximately corresponds to the radius of a proton or a neutron. The strong interaction is responsible for the confinement of quarks into hadrons, as well as their clustering into nuclei.
Theoretically, the properties of the strong interaction are described by quantum chromodynamics (QCD), which is a non-abelian SU(3) gauge theory. Therein, the interactions of quarks

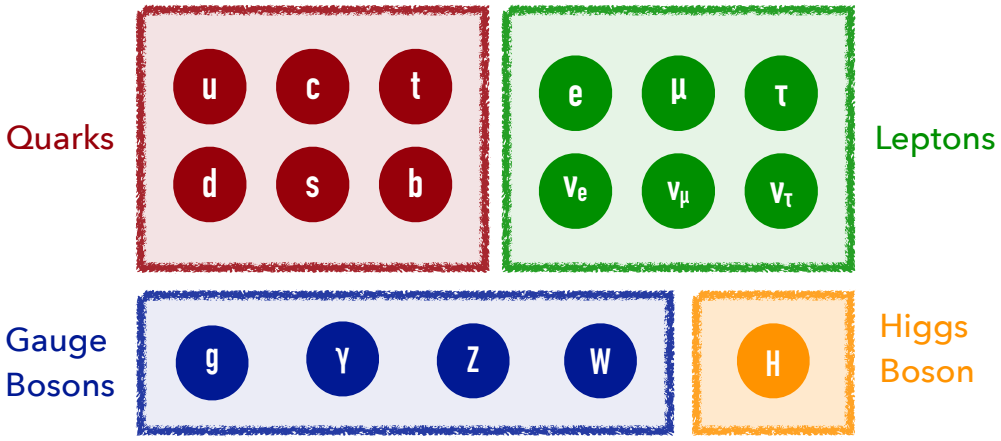

Figure 1.1.: The standard model of particle physics.

and gluons occur through the exchange of colour charge and the corresponding Lagrangian reads [7, 8]:

$$\mathcal{L}_{\mathrm{QCD}} = \bar{\psi}\left(i\,\gamma^{\mu}\left(\partial_{\mu} - i\,g\,T^{a}\,A^{a}_{\mu}\right) - m\right)\psi \;-\; \frac{1}{4}\,G^{a}_{\mu\nu}\,G^{\mu\nu\;a}, \tag{1.1}$$

Here, ψ denotes the quark wave function, γ^{μ} the Dirac matrices, and A_{μ} the gluon field. T^{a} are the generators of SU(3) and $G^{a}_{\mu\nu} = \partial_{\mu}A^{a}_{\nu} - \partial_{\nu}A^{a}_{\mu} + g\,f^{abc}A^{b}_{\mu}\,A^{c}_{\nu}$ is the gluon field strength tensor with f_{abc} being the structure constants. Since gluons, the gauge bosons of QCD, carry colour charge, they can couple to themselves, thus enabling self-interaction. This is accounted for in the last term of the gluon field strength tensor. Another characteristic property of QCD is the energy dependence of the coupling constant, usually referred to as *asymptotic freedom* [9, 10]. As depicted in Figure 1.2, the coupling constant α_s is large at low momentum transfers Q and decreases with rising momentum transfers. Under normal conditions, where the coupling constant is large, quarks and gluons can thus not be observed as free particles. They are rather confined into hadrons, the bound states of QCD. It is particularly this property that complicates the investigation and understanding of quarks and gluons. They are not directly accessible but require a hot and dense medium to be released from confinement. This medium is created in heavy-ion collisions, in which a deconfined plasma of quarks and gluons is produced once the collision energy is sufficiently high. A profound description of heavy-ion collisions is provided in Sec. 1.2.

Chiral Symmetry

Another important property of QCD is chiral symmetry, more concretely its explicit and spontaneous breaking. Chirality accounts for the behaviour of a fermion spinor under chiral transformations, figuratively sometimes referred to as "left- or right-handedness" of a fermion. The fermion wave function Ψ, describing the quarks in the QCD Lagrangian (c.f. Eq. (1.1)), is field-theoretically represented by a spinor. This spinor can be decomposed into a left-handed

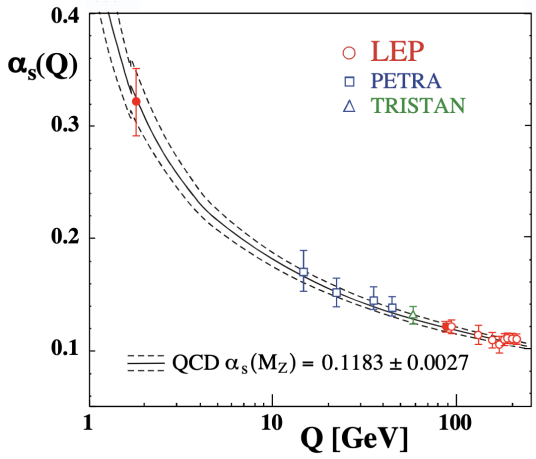

Figure 1.2.: *Running coupling* of the QCD coupling constant, taken from [11].

and a right-handed component such that

$$\psi = \psi_L + \psi_R \tag{1.2}$$

$$\text{where} \quad \psi_L = P_L\ \psi = \frac{1}{2}(1-\gamma^5)\ \psi \quad \text{and} \quad \psi_R = P_R\ \psi = \frac{1}{2}(1+\gamma^5)\ \psi. \tag{1.3}$$

P_L and P_R denote the left- and right-handed projection operators, respectively, and γ^5 is, in the Dirac basis of gamma matrices, defined as $\gamma^5 = i\ \gamma^0\gamma^1\gamma^2\gamma^3$. As described above, QCD is an SU(3) gauge theory. Hence, its chiral symmetry representation is $SU(3)_R \times SU(3)_L$. The left- and right-handed spinors Ψ_L and Ψ_R respond differently on chiral transformations within the $SU(3)_R \times SU(3)_L$ representation [12]. The corresponding transformation law reads

$$\psi \to e^{-i\ \theta^a T^a\ \gamma^5}\ \psi \qquad\qquad a \in \{1, ..., 8\}, \tag{1.4}$$

with T^a being the generators of SU(3) and θ^a the rotation angles in the chiral space of left- and right-handed spinors. The generators can be expressed in terms of the Gell-Mann matrices λ^a as $T^a = \frac{\lambda^a}{2}$ [13]. The Gell-Mann matrices are briefly described in App. E.
The QCD Lagrangian is chirally symmetric in the chiral limit of massless quarks. Since quarks are not massless however, chiral symmetry is explicitly broken. On the other hand, the quark masses are significantly smaller than those of hadrons, the bound states of QCD. Chiral symmetry can thus be considered an approximate symmetry of QCD [14].
In addition, the QCD Lagrangian is invariant under chiral transformations while its ground state $\langle\bar{\psi}\psi\rangle$ is not [12]. This originates from a mixing of left- and right-handed spinor components when employing a chiral transformation on the ground state:

$$\bar{\psi}\psi \ = \ (\bar{\psi}_L + \bar{\psi}_R)\ (\psi_L + \psi_R) \ = \ \psi_R\bar{\psi}_L + \psi_L\bar{\psi}_R \tag{1.5}$$

Because of this property, the invariance of the QCD Lagrangian but not of its ground state, chiral symmetry is spontaneously broken [15]. Nonetheless, the symmetry is expected to be restored at extreme temperatures and densities.

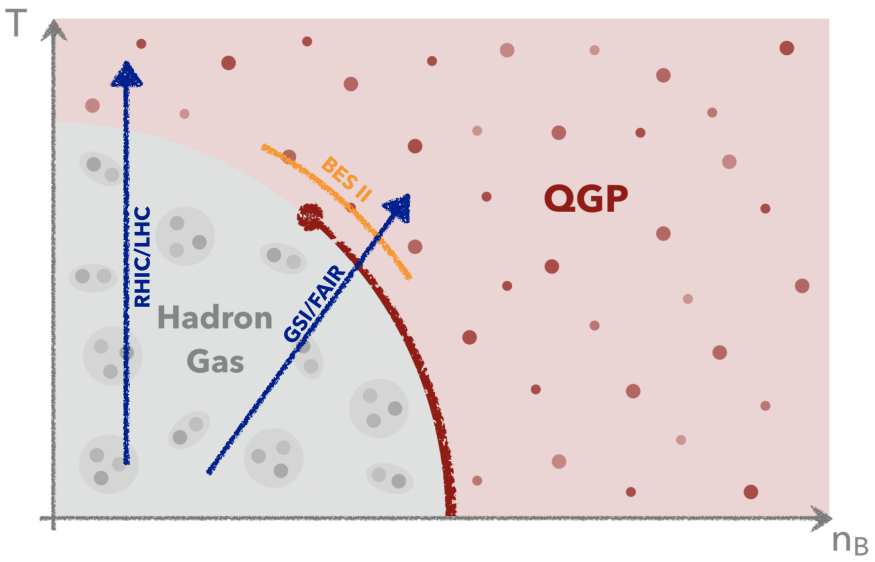

Figure 1.3.: Phase diagram of QCD.

1.1.2. The Electromagnetic Interaction

Unlike the strong interaction, the electromagnetic interaction has an infinite range, but its strength decreases with rising distances. It acts on particles that carry electric charge and is mediated by the exchange of massless photons. In contrast to gluons, photons are electrically neutral and can thus not interact with themselves. The quantum field theory that describes the electromagnetic interaction is quantum electrodynamics (QED), an abelian U(1) gauge theory [16, 17]. The corresponding Lagrangian is

$$\mathcal{L}_{\mathrm{QED}} = \bar{\psi}\left(i\,\gamma^{\mu}\left(\partial_{\mu} - ie\,A_{\mu}\right) - m\right)\psi \;-\; \frac{1}{4}\,F_{\mu\nu}\,F^{\mu\nu}, \tag{1.6}$$

where ψ denotes the fermion wave function, γ^{μ} the Dirac matrices, A_{μ} the photon gauge field and $F_{\mu\nu} = \partial_{\mu}A_{\nu} - \partial_{\nu}A_{\mu}$ the electromagnetic field strength tensor. Unlike in QCD, the energy dependence of the QED coupling constant is negligible such that it can be approximated to $\alpha = \frac{1}{137}$ [18], even in heavy-ion collisions where a highly-energetic medium is created.

1.2. Heavy-Ion Collisions

The properties of the fundamental building blocks of matter can be studied in the context of relativistic heavy-ion collisions. There are a number of experimental facilities where heavy-ion collisions are performed under different conditions. Among these are, for example, the *Conseil Européen pour la Recherche Nucléaire* (CERN), the *Brookhaven National Lab* (BNL), the *Gesellschaft für Schwerionenforschung* (GSI) and the *Joint Institute for Nuclear Research* (JINR). These provide heavy-ion beams with different beam energies, thus giving access to different regions of the QCD phase diagram.

The QCD phase diagram is qualitatively depicted in Figure 1.3. It provides a mapping of the temperature T and net baryon density n_B of a strongly interacting medium to its QCD state. Under normal conditions, that is low temperatures and baryon densities, strongly interacting matter forms a gas of hadrons, confining quarks and gluons (lower-left corner in

Figure 1.3). With increasing temperatures and/or baryon densities the coupling becomes weaker, hadrons break apart, and a plasma of free quarks and gluons is produced (upper-right region in Figure 1.3). This plasma is denoted as quark-gluon plasma (QGP) and becomes accessible due to asymptotic freedom. Strongly interacting matter has to undergo a phase transition to reach a QGP state from a hadron gas state and vice versa. It is known from Lattice QCD calculations that along the temperature axis, where the baryon density is low, this transition takes the shape of a smooth cross over at temperature $T_c \approx 150$ MeV [19, 20]. Along the horizontal axis, a first order phase transition is expected [21] (red band in Figure 1.3). This further implies the existence of a critical end point somewhere between the first order phase transition region and the cross over region [22]. Its location is however unclear, and the quest for it is subject of numerous recent research projects [23]. Among these is, for example, the *Beam Energy Scan II* (BES II) program [24] at the *Relativistic Heavy-Ion Collider* (RHIC) at BNL, the NA61/SHINE experiment [25, 26] at the CERN *Super Proton Synchrotron* (SPS) as well as future experiments at the *Facility for Antiproton and Ion Research* (FAIR) [27] at GSI and the *Nuclotron-based Ion Collider fAcility* (NICA) [28] at JINR. Note, that these experiments aim at the understanding of the QCD phase diagram in the intermediate energy regime, close to the postulated critical end point, as depicted in Figure 1.3. In addition, low-energy heavy-ion collisions, as analyzed for example within the *High Acceptance Di-Electron Spectrometer* (HADES) experiment [29] at GSI, the NA49 program [26] at CERN SPS, or the future CBM experiment at GSI [27], give access to QCD matter at even higher baryon densities. They aim at identifying the relevant degrees of freedom characterizing QCD matter at these densities and at determining whether or not the spontaneously broken chiral symmetry is restored (c.f. Sec. 1.1.1). Furthermore, such low-energy collisions can contribute to understanding neutron stars and their mergers since the equations of state characterizing the collision medium and the core of neutron stars are expected to be similar [30]. To explore the QCD phase diagram at vanishing baryon densities, on the other hand, highly energetic collisions are essential. The highest collision energies are currently achieved with the RHIC at BNL and the LHC at CERN. At BNL, Au+Au collisions are performed up to $\sqrt{s_{NN}} = 200$ GeV and analyzed, for example, by the *Pioneering High Energy Nuclear Interaction eXperiment* (PHENIX) [31] or the *Solenoid Tracker At RHIC* (STAR) [32]. At LHC, Pb+Pb collisions reaching up to $\sqrt{s_{NN}} = 5.02$ TeV are, amongst others, analyzed by *A Large Ion Collider Experiment* (ALICE) [33], *A Toroidal LHC ApparatuS* (ATLAS) [34], or *Compact Muon Solenoid* (CMS) [35]. Heavy-ion collisions at these energies provide access to the properties of quarks and gluons, the mechanism of (re-)confinement as well as chiral symmetry restoration. In addition, the state of our universe microseconds after the Big Bang is reproduced in heavy-ion collisions at RHIC/LHC energies. The evolution of the universe can thus be studied in the laboratory through high-energy heavy-ion collisions. The trajectory of such heavy-ion collisions in the QCD phase diagram is qualitatively depicted in Figure 1.3, with the leftmost arrow in parallel to the temperature axis. This also corresponds to the trajectory of our universe succeeding the Big Bang.

1.2.1. Theoretical Modelling

It is necessary to relate the experimentally obtained results to theoretical models to properly interpret the measured quantities and gain a profound understanding of the underlying dynamics. However, it is challenging, if not impossible, to describe collisions in all regions of the QCD phase diagram with one single theoretical model. The reasons are diverse and include, for example, differences in the underlying degrees of freedom, the existence of a

cross-over, a first order, or no phase transition in the trajectory, or significant differences in the magnitudes of chemical potentials. Depending on the collision energy, theoretical predictions are thus provided by different kinds of models, tailored to reproduce the underlying properties as accurately as possible.

As such, the standard approach to describe heavy-ion collisions at low energies is the application of so-called transport approaches with hadronic degrees of freedom. Transport approaches provide a microscopic description of the particles in the system and rely on resonance dynamics and nuclear potentials to evolve the hadronic medium. They can be classified into two types of models: *Boltzmann-Uehling-Uhlenbeck* (BUU) approaches, or *quantum molecular dynamics* (QMD) approaches [36]. The former rely on applying the test particle method to provide an effective solution of the relativistic Boltzmann equation

$$p_\mu \, \partial^\mu \, f + m \, \partial_{p_\mu} \, (F^\mu \, f) \; = \; C(f). \tag{1.7}$$

The left-hand side describes the time evolution of the one-particle distribution function f for particles with mass m and 4-momentum p_μ that are subject to an external force F^μ. The right-hand side corresponds to the collision integral $C(f)$, which is modeled through formations and decays of hadronic resonances. Among others, prominent examples for BUU codes are SMASH [37], GiBUU [38], HSD [39] or pBUU [40, 41]. In QMD approaches, on the other hand, each particle is represented by a Gaussian wave packet whose time evolution is determined from a many-body Hamiltonian encapsulating kinetic properties as well as nucleon potentials. This is, for example, realized in the QMD approaches JAM [42], IQMD [43], AMD [44], RQMD [45], or UrQMD [46]. Note, that the major difference between BUU and QMD approaches lies in their treatment of potentials, directly influencing particle correlations. While potentials in QMD approaches are calculated from the individual particles' momenta and distances, BUU approaches rely on local densities. As such, correlations between particles are conserved in QMD approaches, while this information is lost in BUU approaches. In cascade mode, where potentials are deactivated, both approaches are expected to yield identical results. Recent studies showed however that even in cascade mode there are differences among several QMD and BUU codes. These differences are found to be relatively small and are expected to originate from differences in the underlying numerical implementation and the in-medium resonance treatments [47].
The major advantage of applying transport approaches lies in the fact that the whole space-time evolution of every single particle is known throughout the medium's evolution. Trajectories, as well as decay chains, can thus be traced back entirely and related to final state observables. This property has triggered the development of transport approaches whose applicability can also be extended to intermediate collision energies. In most cases, this is achieved by exciting the hadrons to strings, consisting of quark-antiquark pairs, whose vertices can interact on the basis of partonic cross sections. As an example, the transport approaches UrQMD, SMASH, HSD, JAM, or GiBUU comprise such an extension to intermediate collision energies. To further push the applicability of transport approaches to even higher energies, multi-phase transport approaches, such as PHSD [48] and AMPT [49], have also been developed. The medium is described with a transport approach relying on hadronic degrees of freedom at low energies and partonic degrees of freedom at high energies. The collection of transport approaches is completed by purely partonic transport approaches aiming at the description of heavy-ion collisions at RHIC/LHC energies. This is, for example, realized in the BAMPS [50] or ZPC [51] transport codes.

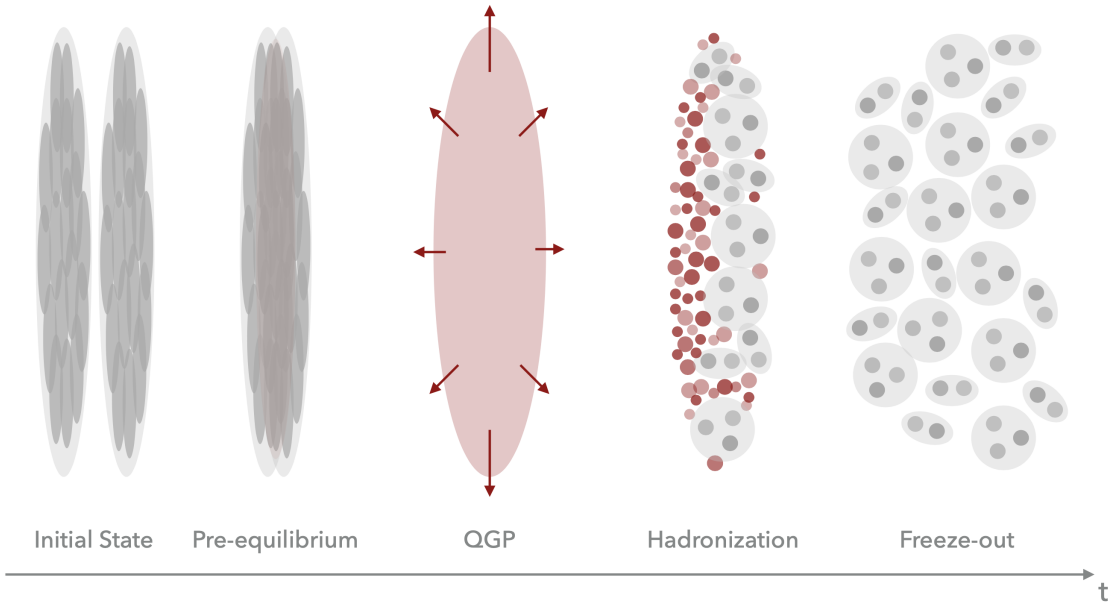

Figure 1.4.: Schematic evolution (from left to right) of a heavy-ion collision involving an intermediate quark-gluon plasma stage.

The theoretical modelling of heavy-ion collisions is not restricted to transport theory. The standard description for high-energy heavy-ion collisions is provided by so-called hybrid approaches which are successful at reproducing a range of experimental observables [52–54]. Therein, the different stages of the collision, characterized by vastly different properties, are accounted for with different kinds of models. These different properties are sketched in Fig. 1.4, where the evolution of a heavy-ion collision at high collision energies is displayed. In the beginning, the Lorentz-contracted nuclei, consisting of hadrons as degrees of freedom, provide the initial state. After the collision, a pre-equilibrium state is formed, which is dominated by hard partonic interactions. Subsequently, the medium thermalizes and an expanding quark-gluon plasma is created, characterized by quark and gluon degrees of freedom. As the medium expands, cools and gets more dilute, these partons reconfine into hadrons that freeze out chemically and kinetically in the final rescattering stage. Hybrid approaches for high-energy heavy-ion collisions aim at capturing these different properties to provide an accurate theoretical description. In practice, viscous hydrodynamics is usually applied to describe the hot, dense fireball and coupled to a non-equilibrium afterburner to model the late, dilute stages. Examples for such hybrid approaches with distinct initial conditions, relying on different realizations of the hydrodynamical stage and employing different hadronic afterburners include [53, 55–64].

There are different types of models to initialize the hydrodynamical evolution. Averaged initial conditions can, for example, be extracted from the Glauber Model [65, 66], Glauber-inspired event-by-event initial conditions based on eikonal entropy deposition are provided in the $T_R ENTo$ ansatz [67], initial conditions from the colour-glass condensate are obtained in the *IP Glasma* approach [68, 69], and microscopic initial conditions with event-by-event fluctuations incorporated by construction can be extracted directly from hadronic transport approaches [63]. Once initialized, the hot and dense medium is evolved according to viscous

hydrodynamics, satisfying the hydrodynamic equations

$$\partial_\mu T^{\mu\nu} = 0 \qquad \text{and} \tag{1.8}$$

$$\partial_\mu \, J_i{}^{\mu} = 0 \qquad i = B, S, Q, \tag{1.9}$$

which represent the conservation of the 1^{st} and 2^{nd} moments of Eq. (1.7), the Boltzmann equation [70]. More concretely, Eq. (1.8) encapsulates the conservation of energy and momentum through conservation of $T^{\mu\nu}$, the energy-momentum tensor, and Eq. (1.9) implies current conservation of $J_i{}^{\mu}$, the 4-current of quantum number i. In the context of heavy-ion collisions, these conserved quantum numbers are baryon number (B), strangeness (S) and electric charge (Q). Another necessary ingredient to perform the hydrodynamical evolution is the *equation of state* (EoS). It provides a fundamental relation between the energy density e and the baryon, strangeness and charge densities n_B, n_S, n_Q to the associated thermodynamic quantities temperature T, pressure P and baryon, strange and charge chemical potentials μ_B, μ_S, μ_Q. It is through the equation of state, how the properties of the medium influence the evolution of the system. Unfortunately, the full QCD equation of state is not yet understood in its entirety; it remains subject of topical research programs. As a consequence, various equations of state to characterize QCD matter have been developed, focusing on different regions of the QCD phase diagram, considering different degrees of freedom, incorporating different features, and relying on different methods. For vanishing chemical potentials, the QCD equation of state can be extracted directly from lattice QCD calculations. Prominent examples in (2+1)-flavour QCD are provided by the *HotQCD* [19] and *Wuppertal-Budapest* [20] collaborations, both results characterized by a crossover transition from quark to hadron degrees of freedom. Finite chemical potentials limit the applicability of first-principle lattice QCD calculations, though, owing to the fermion sign problem [71]. Nonetheless, there have been different attempts to extend lattice QCD approaches beyond vanishing chemical potentials. These include for instance Taylor expansion [72–74], reweighting techniques [75, 76], or simulations at imaginary chemical potentials [77, 78]. The therewith obtained results are however only reliable for as long as the chemical potentials are small, else they are dominated by uncontrolled systematic uncertainties [79]. For larger baryon densities, it is possible to extract the equation of state, for example, from a chiral model relying on chiral symmetry restoration [80], from the PNJL model beyond the mean field approximation [81], from a quasiparticle approach [82], from the 3D Ising model universality class [83], or from the VDF model [84]. Note, that these equations of state contain a first order phase transition as well as a critical end point and are matched to a hadron resonance gas at lower temperatures and baryon densities. The equation of state of the hadron resonance gas can, if approximating the hadrons as point particles, be determined directly from solutions of the coupled thermodynamic equations, as for example realized in Sec. 2.1.8. Along more sophisticated approaches are e.g. the excluded volume technique [85–88] to consider finite eigenvolumes of the hadrons, the Hagedorn mass spectrum to account for the resonance spectrum above 2 GeV in mass [89–91] or a combination of both [92]. The hadronic equation of state encapsulates the properties of QCD matter at low temperatures and baryon densities, i.e. the lower-left corner in Fig. 1.3. Moving to higher baryon densities and vanishing temperatures the QCD equation of state corresponds to that of compact starts, such as neutron stars. Popular approaches to extract the neutron star equation of state are, for example, based on holographic QCD [93], or chiral perturbation theory in combination with perturbative QCD [94]. Finally, a combined framework providing a QCD equation of state that fulfills constraints from lattice QCD, as well as from nuclear matter and neutron stars is provided in [95].

Once the desired equation of state is incorporated into the hydrodynamics model, the medium created in high-energy heavy-ion collisions can be evolved according to Eqs. (1.8) and (1.9). The solutions of these equations are determined relying on different types of algorithms. Among these are, for example, the HLLE (Harten-Lax-van Leer-Einfeldt) algorithm [96–98] as employed in [99, 100], the SHASTA (SHarp and Smooth Transport Algorithm) algorithm [101–104] as employed in [105, 106], or the KT (Kurganov-Tadmor) algorithm [107] as employed in [108]. These algorithms provide different possibilities to solve the Riemann problem [70] associated with the hydrodynamic equations (1.8) and (1.9). Note, that hydrodynamics is only applicable if the mean free path of the particles is much smaller than the system size. The evolution is thus performed until the medium gets too dilute, which is usually determined from the energy density or temperature falling below a predefined critical value[1]. The resulting final state of the hydrodynamical stage, a collection of fluid elements, needs then be re-transformed into particles for the subsequent afterburner evolution. Particlization of the fluid elements is achieved by evaluating the Cooper-Frye formula [109] for each particle species:

$$\frac{dN}{d\vec{p}} = \frac{d}{(2\pi)^3} \int_\Sigma \left[f_0(x,\vec{p}) + \delta f_{\text{shear}}(x,\vec{p}) + \delta f_{\text{bulk}}(x,\vec{p}) \right] \frac{p^\mu \, d\Sigma_\mu}{E_{\vec{p}}} \tag{1.10}$$

Here, $dN/d\vec{p}$ is the momentum distribution of the particle species, d is the degeneracy factor, p^μ and $E_{\vec{p}}$ the particle's 4-momentum and energy, Σ the freezeout hypersurface, and $d\Sigma_\mu$ its normal vector. f_0 is the vacuum one-particle distribution function and δf_{shear}, and δf_{bulk} the viscous and bulk corrections to f_0, respectively. There are different possibilities to realize the particlization process, relying on different algorithms and assumptions. In most cases, the so-called *oversampling technique* is employed where quantum numbers are conserved on average when sampling multiple events from the same freezeout hypersurface. This is, for example, realized in [110] relying on a mode sampling algorithm, in [59, 60] utilizing adaptive rejection sampling, in [111] with a Monte Carlo method, or in [112] with the SPREW or SER algorithms. These rely on a grand-canonical ensemble for the thermal distribution functions. Recently, a new method was introduced, assuming a micro-canonical ensemble and employing a Metropolis algorithm [113] to allow for event-by-event quantum number conservation, which is in particular important to study fluctuations.
The particles sampled from the Cooper-Frye formula are finally propagated in the non-equilibrium afterburner stage, where the remaining hadronic interactions are performed. Hadronic transport approaches, such as, e.g. SMASH, UrQMD or JAM, are usually applied to model this late, dilute stage. The resulting final state particle spectra can then be compared to experimental measurements obtained in the facilities listed above. Among these hadronic observables are, for example, rapidity, transverse mass or transverse momentum spectra, as well as excitation functions for multiplicities, mean transverse momentum or harmonic flow coefficients. An overview of the observables presented throughout this thesis is provided in App. A.

In the above, the standard descriptions of heavy-ion collisions at low and high collision energies, respectively transport approaches and hydrodynamics+transport approaches, have been introduced. However, the heavy-ion community still lacks a theoretical standard description of heavy-ion collisions at intermediate collision energies, which are expected to provide access to the designated region of interest in the quest for the postulated first order phase transition and critical end point of the QCD phase diagram. It is thus of fundamental impor-

[1] Common critical values are $\epsilon_{\text{crit}} = 0.5$ GeV/fm^3 or $T_{\text{crit}} = 0.15$ GeV [5, 6], which are also employed in the scope of this work.

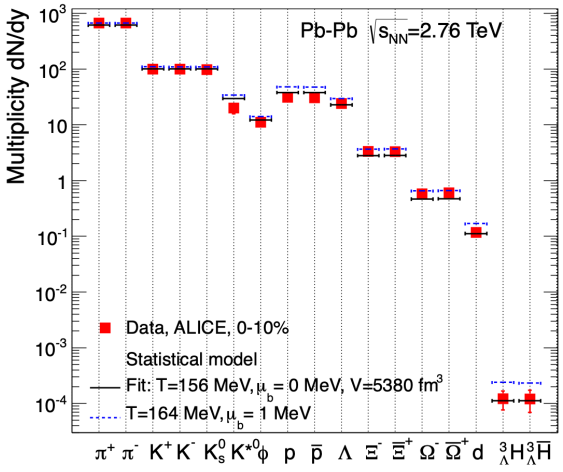

Figure 1.5.: Hadron abundances as measured by the ALICE collaboration in central Pb+Pb collisions at $\sqrt{s_{NN}}$ = 2.76 TeV (markers) in comparison to thermal model predictions (lines). Figure taken from [118].

tance to develop state-of-the-art approaches to theoretically model the evolution of heavy-ion collisions at intermediate collision energies. Promising candidates to this end are again hydrodynamics+transport hybrid approaches. Therein, it is challenging to properly model the initialization of hydrodynamics, since the assumption of an instantaneous deposition of energy, baryon number and electric charge is questionable in the intermediate collision energy regime. Furthermore, it is unclear whether a single highly-dense fireball is created or rather different smaller blobs of dense matter are formed, evolve, vanish, and are potentially re-formed throughout the evolution. First attempts to tackle the former problem were recently made in [114], where the hydrodynamical evolution is initialized dynamically, relying on source terms of the hydrodynamic fields, thus avoiding an instantaneous initialization. Regarding the latter, recent attempts alternatively rely on the extension of a hadronic transport approach by a so-denoted *forced canonical thermalization* [115]. Therein, the medium's evolution is modelled utilizing hadronic transport, unless the rest frame energy densities locally exceed a pre-defined critical value. In these high-density regions, rapid thermalization is assumed, and particles are produced thermally according to the grand-canonical ensemble.
In addition to the two aforementioned approaches, another candidate to model heavy-ion collisions at intermediate collision energies is introduced in this work: The `SMASH-vHLLE-hybrid`. The `SMASH-vHLLE-hybrid` is a novel hybrid approaches relying on the hadronic transport approach `SMASH` for the initial and final stage and on the hydrodynamical model `vHLLE` for the intermediate fireball evolution. It is in great detail introduced in Sec. 2.2.

1.2.2. The Proton Anomaly

Thermal models are successfully applied to describe the hadron abundances measured in heavy-ion collisions at a range of collision energies [116]. The thermal multiplicities of the hadrons are estimated within the statistical hadronization model, relying only on the temperature, baryon chemical potential and effective volume of the fireball [116, 117]. The agreement between the thermal estimate and the experimentally measured multiplicities can be seen in Fig. 1.5 for a number of hadron species. The red markers denote the experimentally measured multiplicities in central Pb+Pb collisions at $\sqrt{s_{NN}}$ = 2.76 TeV and the black lines the ther-

mal model estimate. A good agreement is obtained for nearly all hadron species presented therein, with the exception of protons and anti-protons. These are noticeably overestimated within the thermal model [117–119], which is referred to as the *proton anomaly*. A potential resolution for this mismatch was proposed in [120], it relies on the inclusion of π-nucleon interactions. An alternative explanation is provided by baryon-antibaryon annihilations in the late hadronic rescattering stage [121–123]. Thermal models rely on the assumption that the medium chemically freezes out in an equilibrated state, late-stage non-equilibrium interactions are therefore neglected. It is known from hydrodynamics+transport approaches though that a significant amount of inelastic interactions occur in this late, non-equilibrium stage; indicating a chemical freezout at later times. Furthermore, such late-stage interactions are known to be important for final state particle spectra [122, 124]. In view of protons and anti-protons, an improved agreement with experimental measurements is achieved once annihilations of baryons and anti-baryons in the late stages are accounted for [121, 122, 124–126]. What is not accounted for in these models is the regeneration of protons and anti-protons via the back reaction of the annihilation processes. This reaction is usually challenging to model in microscopic transport approaches since protons and anti-protons dominantly annihilate into multiple pions. The back-reaction thus requires either multi-particle interactions or a chain of binary interactions. Both are to some extend implemented in the hadronic transport `SMASH`. Its application within hydrodynamics+transport approaches thus allows to assess the impact of such regeneration processes. This is realized within the `SMASH-vHLLE-hybrid` for a range of collision energies and centralities. It is in greater details described in Sec. 2.5.

1.2.3. Electromagnetic Probes and the Direct Photon Flow Puzzle

In addition to hadronic observables, which were briefly introduced in the above, electromagnetic probes provide another set of observables to study the properties of the medium created in heavy-ion collisions. Electromagnetic probes can be divided into three subgroups: correlated lepton-antilepton pairs, usually referred to as *dileptons*, *photons*, and *neutrinos*. They are characterized by a common property which is the inability to interact via the strong interaction, as they interact exclusively via the electroweak interaction. It is particularly this feature that makes them valuable probes in heavy-ion collisions. While hadronic observables suffer from numerous re-scatterings between their production and detection, photons, dileptons, and neutrinos traverse the strongly interacting medium nearly unaffected. Their mean free path is significantly larger than the system size, such that they carry unperturbed information from the medium to the detector. Furthermore, photons, dileptons, and neutrinos can provide a time-integrated picture of the entire evolution, for all three being produced in all stages of the collision.
There are two types of photons produced in heavy-ion collisions, *direct photons* and *decay photons*. The former account for the majority of produced photons and stem from decays of hadronic resonances; the latter are directly produced in partonic or hadronic interactions. Direct photons can be further split into contributions from *prompt photons* that are produced in the first initial binary collisions, *pre-equilibrium photons* which are emitted from the medium before thermalization, *thermal photons* which are produced from a partonic or hadronic thermal medium, and *photons from jet-medium interactions* which, as the name suggests, originate from interactions of jets (highly-energetic partons traversing the medium, creating a shower of particles) with the medium. Subject of this work are however only thermal photons produced in the hadronic stage of the collisions, e.g. photons from $\pi + \pi$ bremsstrahlung processes as well as from $2 \rightarrow 2$ scatterings involving pions and ρ mesons.

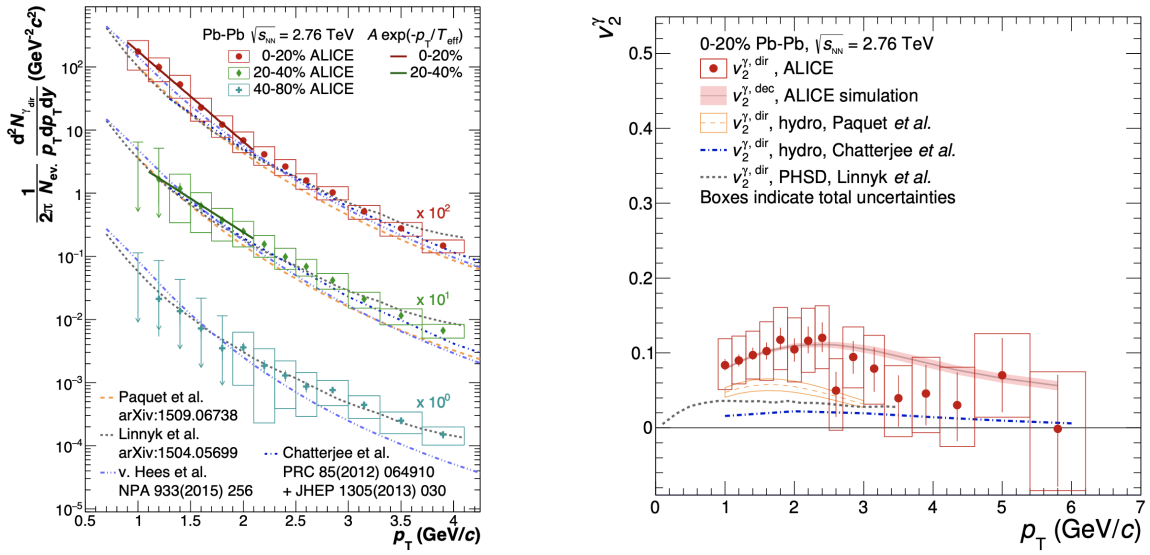

Figure 1.6.: Direct photon p_T spectra (left, taken from [132]) and direct photon v_2 (right, taken from [133]) as measured by the ALICE collaboration in Pb+Pb collisions at $\sqrt{s_{NN}}$ = 2.76 TeV in comparison to different model predictions. For the p_T spectra, three different centrality classes are presented, while for v_2 only the 0-20% most central collisios are displayed.

The Direct Photon Flow Puzzle

Measurements of direct photons in Au+Au collisions at $\sqrt{s_{NN}}$ = 200 GeV [127–129] as well as in Pb+Pb collisions at $\sqrt{s_{NN}}$ = 2.76 TeV [130, 131] have revealed significant differences to theoretical predictions. While, as described above, hadronic observables at these collision energies are well described by hydrodynamics+transport approaches, photon data remain a challenge. This becomes evident in Fig. 1.6, where the direct photon p_T spectra (left) and v_2 (right), as measured by the ALICE collaboration in Pb+Pb collisions at $\sqrt{s_{NN}}$ = 2.76 TeV [132, 133], are displayed and compared to different theoretical predictions [134–138]. While there is a decent agreement between the experimentally measured p_T-differential photon yield and theoretical models, the direct photon elliptic flow v_2 is significantly underestimated. The measured direct photon v_2 is much larger than theoretically expected and comparable to that of pions. This property and also any model's inability to simultaneously describe the measured photon yield and elliptic flow [134, 136, 139–141] have been denoted the *direct photon puzzle* [142].

Recent attempts to improve the theoretical understanding of photon production in heavy-ion collisions have majorly focused on early-stage pre-equilibrium photons through, i.e. HBT correlations [143], solutions of the Boltzmann equation in the Fokker-Planck limit [144], rapid thermalization scenarios [145], as well as on improved emission rates [146–148], cross sections [149], and more dynamical models [150–152]. In the presented work, special emphasis is laid on thermal photons produced in the late hadronic stage of the evolution. More concretely, the impact of a non-equilibrium treatment in the hadronic afterburner stage is assessed by comparing photon emission in a hydrodynamics+transport approach to a purely hydrodynamical evolution. To guarantee an equivalent comparison, both models rely on an identical effective field-theoretical description to determine the rates and cross sections serving as input for the hydrodynamical and transport evolution, respectively. See Sec. 3.3 for further details.

1.3. Structure of this Thesis

Two major topics are covered in this thesis:

1. The development of the `SMASH-vHLLE-hybrid` and its application to study bulk observables as well as (anti-)proton annihilation and regeneration in heavy-ion collisions across a wide range of collision energies.

2. The implementation of photon production in `SMASH` and its application within a `MUSIC+SMASH` hybrid to assess the impact of non-equilibrium dynamics in the afterburner stage in view of photon production.

Hence, this thesis consists of two major chapters. In Chapter 2, the `SMASH-vHLLE-hybrid` is introduced and applied to describe heavy-ion collisions across a wide range of collision energies. First, however, the properties and features of the hadronic transport approach `SMASH` are described in Sec. 2.1, for the `SMASH-vHLLE-hybrid` relies heavily on it. Particular focus is put on the equation of state of the `SMASH` hadron resonance gas and its determination in Sec. 2.1.8. It is required within the `SMASH-vHLLE-hybrid` for the particlization process. In continuation, the `SMASH-vHLLE-hybrid` is introduced in Sec. 2.2 including all relevant submodules as well as the realization of the corresponding interfaces. It is validated thoroughly in Sec. 2.3 regarding consistency at the interfaces as well as global quantum number conservation. Once validated, the `SMASH-vHLLE-hybrid` is employed in an event-by-event setup to study particle production in Au+Au/Pb+Pb collisions ranging from $\sqrt{s_{NN}} = 4.3$ GeV to $\sqrt{s_{NN}} = 200.0$ GeV in Sec. 2.4. Hadronic rapidity and transverse mass spectra as well as excitation functions for the mid-rapidity yield and the mean transverse momentum are confronted with experimental data. Furthermore, excitation functions for elliptic and triangular flow are studied for different centrality classes. In continuation, the `SMASH-vHLLE-hybrid` is employed with averaged initial conditions to assess the role of proton and anti-proton annihilation and regeneration in heavy-ion collisions between $\sqrt{s_{NN}} = 17.3$ GeV and $\sqrt{s_{NN}} = 5.02$ TeV. This study is conducted in Sec. 2.5 and concludes the second chapter of this thesis.

The focus of Chapter 3 lies on the production of photons in a hadronic medium. The derivation of cross sections for mesonic photon production in binary scatterings, as well as pion bremsstrahlung is described in Sec. 3.1. Their implementation in the hadronic transport approach `SMASH` is subsequently explained in Sec. 3.2. These cross sections, as well as their implementation, are further validated in Sec. 3.2.1, and an extension to ρ mesons with a finite width is made in Sec. 3.2.2. In Sec. 3.3 `SMASH` is employed within a hybrid approach consisting of `MUSIC` and `SMASH` to assess the impact of non-equilibrium dynamics in the hadronic rescattering stage in view of photon production at RHIC/LHC energies. The approach is introduced in Sec. 3.3.1 and is briefly validated in Sec. 3.2.1. It relies on the same field-theoretical framework for hadronic photon production for the macroscopic description with `MUSIC` as well as for the microcscopic description with `SMASH`. In Sec. 3.3.4, photon transverse momentum spectra and elliptic flow are compared between a non-equilibrium description (via hadron transport) and a local-equilibrium description (via hydrodynamics) in the afterburner stage to assess the importance of non-equilibrium dynamics.

This thesis is concluded with Chapter 4, where the presented models and results are briefly summarized. Finally, an outlook is provided where the different possibilities to further extend the presented approaches and studies are discussed.

2

Hadron Production with the SMASH-vHLLE-hybrid

Hybrid approaches successfully describe heavy-ion collisions at high collision energies, while hadronic transport constitutes the standard approach at low collision energies. For heavy-ion collisions at intermediate energies on the other hand, which are believed to provide access to the region of the QCD phase diagram, where the location of the first order phase transition and critical end point are expected, there is no such standard description yet. Hybrid approaches whose range of applicability is extended towards lower collision energies are a promising candidate, though. Previous works to this end include, for example, [55, 57, 59, 63]. These have however either not been applied below $\sqrt{s_{NN}} = 7.7$ GeV or have issues properly reproducing the baryon stopping dynamics at lower collision energies. Yet, an accurate description of these baryon dynamics is crucial for a proper modelling of the evolution at intermediate beam energies as well as for studies concerning fluctuations of conserved charges. Recent progress has been made in [114, 153, 154], where frameworks towards a more dynamical initialization of the hydrodynamic stage are introduced. These are in particular important at lower collision energies where the initial state is longer-lived.

This chapter introduces the `SMASH-vHLLE-hybrid` as a newly-developed hybrid model suitable to describe heavy-ion collisions ranging from $\sqrt{s_{NN}} = 4.3$ GeV to $\sqrt{s_{NN}} = 5.02$ TeV. It is publicly available on Github[1]. Since the development of the `SMASH-vHLLE-hybrid` constitutes a major component of this PhD work, it is explained in great detail in the following. First, however, the hadronic transport approach `SMASH` is introduced, as the `SMASH-vHLLE-hybrid` relies heavily on it. Next, the `SMASH-vHLLE-hybrid` is described with particular emphasis on the different submodules as well as the realization of the interfaces. It is validated thoroughly regarding consistency at the interfaces and conservation of quantum numbers.
Subsequently, the `SMASH-vHLLE-hybrid` is applied to study particle production in heavy-ion collisions covering a wide range of collision energies. A good agreement with experimental data for pion, proton and kaon rapidity and transverse mass spectra as well as excitation functions for the mid-rapidity yield and the mean transverse momentum is obtained. In particular, the experimentally observed baryon stopping dynamics at intermediate collision energies are well reproduced.
Furthermore, the `SMASH-vHLLE-hybrid` is employed to investigate the annihilation and regeneration of $p\bar{p}$ pairs in the hadronic rescattering stage of heavy-ion collisions. It is found that independently of the energy or centrality of the collision, between 20% and 50% (depending on the rapidity range) of the (anti-)proton yield lost to annihilations is re-generated in the hadronic rescattering stage, which underlines the importance of the back reaction for the final particle yield.
The results presented in this chapter are published in [3, 4, 6].

[1] `https://github.com/smash-transport/smash-vhlle-hybrid`

2.1. SMASH

SMASH (**S**imulating **M**any **A**ccelerated **S**trongly-Interacting **H**adrons) [37, 155, 156] is a hadronic transport approach capable of describing the dynamics of heavy-ion collisions at low and intermediate collision energies. It constitutes an effective solution of the relativistic Boltzmann equation (c.f. Eq. (1.7)) by modelling the collision integral through decays, formations and elastic scatterings of hadronic resonances. Each hadron is represented as a point particle and propagated on straight lines (if potentials are deactivated). It can undergo interactions of different kinds in which its properties are modified and trajectories altered. Transport approaches bear the advantage that the full space-time information of every single particle is available throughout the entire evolution. This implies that, as opposed to experimentally performed heavy-ion collisions in which only the final state is detectable, the properties of the medium can be extracted at any time during the evolution. Interaction chains can be traced back entirely from the final to the initial state, which allows to relate the properties of the medium at intermediate times to final state observables.
The SMASH code is open-source and publicly available on Github [155]. Version control is employed to ensure reproducibility and transparency of the obtained results. Documentation of the source code is available under [157] and a user guide under [158]. SMASH is further regularly validated in different setups ranging from elementary density, detailed balance or cross section checks to full heavy-ion collisions where hadron and dilepton production is confronted with experimental data. The corresponding analysis framework, the `SMASH-analysis` is also publicly available [159] and the resulting validations are assembled in [160].
SMASH was introduced in [37] and has been applied to study a wealth of observables and phenomena since. These range from equilibrium studies to extract hadronic transport coefficients [161–165] via an expanding gas of hadrons within a Friedmann–Robertson–Walker metric, confronting it with an analytical solution of the Boltzmann equation [166], to actual heavy-ion collisions. The latter includes studies of bulk observables [3, 37, 167, 168], flow [169], strangeness production [170, 171], baryon stopping [172], deuteron production [173–175], and dilepton production [176]. Results obtained with SMASH have been confronted with those of other transport models in [47, 177–179]. Furthermore, SMASH was applied to explore forced thermalization scenarios [115], dense nuclear matter [84], and the importance of the neutron skin effect [180]. Within the JETSCAPE framework, transport coefficients as well as the nuclear matter equation of state have also been studied [56, 181].

2.1.1. Test Particle Method and Potentials

SMASH can be classified as a BUU code (c.f. Sec. 1.2.1) for it relies on the test particle method to obtain an effective solution of the Boltzmann equation (c.f. Eq. 1.7) and to realize mean-field potentials. For this, each actual particle is represented by N_{test} test particles and the interaction cross sections σ scaled down accordingly:

$$N \to N\, N_{\text{test}} \qquad \sigma \to \sigma \,/\, N_{\text{test}} \tag{2.1}$$

With this increased number of particles, it is possible to locally determine smooth densities required to compute the potentials and equations of motion. In the limit of $N_{\text{test}} \to \infty$ an exact solution of the Boltzmann equation (c.f. Eq. (1.7)) is restored. Currently, there are four types of potentials implemented: The *Skyrme potential* [37] as an effective nucleon potential to describe the attractive forces amongst the nucleons at low densities, the *symmetry potential* [37] is applied to account for asymmetric nuclei regarding their constituent numbers

of protons and neutrons, the *VDF potential* [84] is a covariant nucleon potential for dense nuclear matter, and the *Coulomb potential* [182] accounts for the electromagnetic interaction among the nucleons. It shall be noted, though, that potentials are deactivated for the scope of this work, and SMASH is applied in *cascade mode + frozen Fermi motion*, that is without potentials and *Pauli blocking* (accounting for quantum statistics). The feature of *frozen Fermi motion* allows to consider Fermi momenta for collisions, but not for the propagation [37]. Since the collision energies considered in the presented work are relatively high, and the impact of potentials and Pauli blocking decreases with rising collision energy, this approximation is justified.

2.1.2. Degrees of Freedom

The SMASH degrees of freedom include all hadrons listed by the PDG [183] up to a mass of $m \approx 2.35$ GeV. Among these are, for example, the light mesons such as $\pi, \rho, \eta, \omega, \phi$, or K, higher mesonic resonances, the $N, \Delta, \Lambda, \Sigma, \Xi, \Omega$ baryons as well as multiple higher excitations of these. Resonances with a width smaller than $\Gamma = 10^{-5}$ GeV are considered stable, else they are represented by vacuum Breit-Wigner spectral functions:

$$\mathcal{A}(m) = \frac{2\,N}{\pi} \frac{m^2\,\Gamma(m)}{(m^2 - M_0^2)^2 + m^2\,\Gamma(m)^2}\,, \tag{2.2}$$

where N is the normalization factor that ensures $\int_0^\infty \mathcal{A}(m)\,dm = 1$, M_0 the resonance's pole mass, m its off-shell mass and $\Gamma(m)$ its width. Note that, although vacuum spectral functions are being used, the widths are mass-dependent following the Manley-Saleski Ansatz [184].

2.1.3. Collision Criteria

There are two conceptually different collision criteria in SMASH: A *geometric* collision criterion and a *stochastic* collision criterion. While the former is based on a geometrical interpretation of the interaction cross section [46, 185], the latter relies on a collision probability (which is proportional to the interaction cross section) to perform the interactions.
In the case of the geometric collision criterion, two particles can interact if their transverse distance at the time of closest approach d_{trans} is smaller than the interaction distance d_{int}:

$$d_{trans} < d_{int} = \sqrt{\frac{\sigma_{tot}}{\pi}}, \tag{2.3}$$

with $\sigma_{tot} = \sum \sigma_{partial}$ being the total interaction cross section, i.e. the sum of all partical cross sections, each corresponding to a different final state [37, 46]. The caveat with this geometrical interpretation of the cross section is that it is not covariant, though, as the time ordering is not unique, and hence a frame dependence of the results is introduced [186]. To circumvent this problem, SMASH was recently extended by a covariant collision criterion [187, 188]. This is achieved by expressing the spatial distance of two particles in covariant form and from this defining a unique time and position for the collision [187]. Since SMASH-2.0 this covariant collision criterion is the default used in SMASH and, unless stated differently (as in Sec. 2.5), applied throughout this work.
Geometrical collision criteria of any kind are limited to binary interactions, since it is challenging to formulate a geometric collision criterion for multiple particles [189]. As opposed

to geometrical collision criteria, stochastic collision criteria do not rely on the definition of a distance, but on probabilities, thus giving access to multi-particle interactions. A stochastic collision criterion was recently introduced in SMASH to treat binary as well as $3 \leftrightarrow 1$, $3 \leftrightarrow 2$ and $5 \leftrightarrow 2$ processes [3, 175]. In the case of binary interactions, the collision probability in a cell with volume $\Delta^3 x$ and within a time interval Δt is defined as

$$P_{2\to m} = \frac{\Delta t}{\Delta^3 x}\, v_{\mathrm{rel}}\, \sigma_{2\to m}, \tag{2.4}$$

where v_{rel} is the relative velocity of the two particles and $\sigma_{2\to m}$ the interaction cross section of the two incoming particles to form the final state m [175]. This probability is then applied to randomly determine whether or not two particles interact. It is straightforward to extend Eq. (2.4) to probabilities of arbitrary $n \to m$ processes once the corresponding cross sections are known [3, 175, 189]. In Sec. 2.5 SMASH is applied with the stochastic collision criterion to directly model the $p\bar{p}$ annihilation process to five pions as well as the corresponding back reaction: $p\bar{p} \leftrightarrow 5\ \pi$. The collision probability for the $5\ \pi \to p\bar{p}$ regeneration reaction, $P_{5\to 2}$, is defined as [189]:

$$P_{5\to 2} = \frac{g_1' g_2'}{g_1 g_2 g_3 g_4 g_5}\, \frac{S_{12345}}{S_{12}'}\, \frac{1}{32\ E_1 E_2 E_3 E_4 E_5}\, \frac{\Delta t}{(\Delta^3 x)^4}\, \frac{\lambda(s, m_1'^2, m_2'^2)}{\Phi_5}\, \frac{1}{4\ \pi\ s}\, \sigma_{2\to 5}. \tag{2.5}$$

Here, primed quantities correspond to final state particles, unprimed quantities to initial state particles. g_i and S_i denote the spin degeneracy and symmetry factors, respectively, E_i are the energies of the incoming particles, $\Delta^3 x$ is the cell volume, and Δt the time interval. $\lambda(a, b, c) = (a - b - c)^2 - 4\ bc$ is the Källén function and Φ_5 denotes the integrated 5-body phase space. Mandelstam s is the squared center-of-mass momentum, and $\sigma_{2\to 5}$ the interaction cross section for which it is assumed that the underlying matrix element depends only on Mandelstam s, but is independent of the final state particle momenta.
For further details about the derivation of Eqs. (2.4) and (2.5), the implementation of the stochastic collision criterion in SMASH, as well as the collision probabilities for $3 \leftrightarrow 2$ and $3 \leftrightarrow 1$ reactions, the interested reader may consult [3, 175, 189].

2.1.4. Collision Term

A fundamental ingredient of any transport model is the underlying set of interaction cross sections and decay properties that make up the collision term of the Boltzmann equation. There are different possibilities for the particles in SMASH to interact. These include binary elastic and inelastic scatterings, resonance formations and decays, multi-particle interactions, as well as string excitations and fragmentations. The shape of these cross sections as a function of collision energy $\sqrt{s_{NN}}$ is displayed exemplarily for a $p+\pi^-$ scattering in Fig. 2.1, employing the geometric collision criterion. At low collision energies, the cross sections are dominated by resonance dynamics while for rising collision energies soft and hard string processes are the leading contributions.

Elastic and Inelastic Binary Scatterings

The cross sections for a number of elastic scattering processes are experimentally well constrained, SMASH thus relies on parametrizations of these (i.e. for NN, $N\bar{N}$, NK, πN, dπ, $\bar{\mathrm{d}}\pi$, dN, and $\bar{\mathrm{d}}\bar{\mathrm{N}}$) [46, 170, 190, 191] to model elastic collisions. If no experimental data is

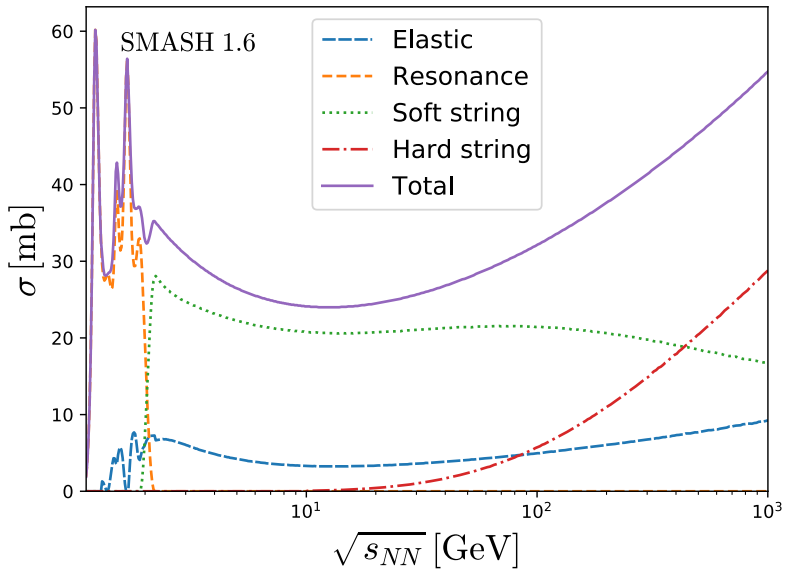

Figure 2.1.: Cross sections for a $p+\pi^-$ interaction sorted by interaction type as obtained with `SMASH-1.6` employing the geometric collision criterion. Figure taken from [172].

available for a pair of hadrons, the additive quark model (AQM) [46] is employed to assign an elastic cross section to the scattering process.

Inelastic binary collisions in `SMASH` can be classified into the following subgroups of interactions [189, 192, 193]:

(i) Single resonance excitation, e.g. $NN \to NR$ with nucleon resonances $R = \Delta, N^*, \Delta^*$, or $KN \to K\Delta$

(ii) Double resonance excitation, e.g. $NN \to RR$ with nucleon resonances $R = \Delta, N^*, \Delta^*$

(iii) Resonance absorption, e.g. $NR \to NN$ and $RR \to NN$ with nucleon resonances $R = \Delta, N^*, \Delta^*$, or $K\Delta \to KN$

(iv) Strangeness exchange, e.g. $\bar{K}N \to \pi\Upsilon$ with hyperons $\Upsilon = \Lambda, \Sigma, \Xi$

(v) Inelastic charge exchange, e.g. $KN \to KN$, or $KN \leftrightarrow K\Delta$, with N and K accounting for the full isospin multiplets

(vi) Resonant $N\bar{N}$ annihilation, e.g $N\bar{N} \to h_1\rho$

The cross sections for single and double resonance excitation (subgroup (i) and (ii)) as a function of squared collision energy s are defined as [37]

$$\sigma_{ab\to cd}(s) = \frac{(2J_c+1)\,(2J_d+1)}{s\,|\vec{p}_i|} \times \sum_I \left(C^I_{ab} C^I_{cd}\right)^2 \frac{|\mathcal{M}|^2(s,I)}{16\,\pi} \times \mathcal{I} \tag{2.6}$$

with a, b and c, d being the initial and final state particles, respectively. $\vec{p}_i$ is the center-of-mass momentum of the initial state, J_i denotes the spin of particle i and $C^I_{ab,cd}$ are the

Clebsch-Gordan coefficients. These account for the coupling of the initial and final state to the total isospin. $|\mathcal{M}|^2$ is the squared matrix element that encapsulates the underlying interaction's properties. In the case of $NN \to N\Delta$ scatterings, it follows directly from the Dmitriev one-boson-exchange (OBE) model [194], else a parametrization depending on the isospin and masses of the final state particles is employed. This is in detail described in [37, 46, 189, 193]. Finally, $\mathcal{I}$ serves as a placeholder for the integration over the final state, accounting for the resonance spectral function(s). In the case of single resonance excitations, where d is a stable particle, this integral reads

$$\mathcal{I} = \int_{m_c^{min}}^{\sqrt{s}-m_d} \mathcal{A}_c(m)\ |\vec{p}_f|(\sqrt{s}, m, m_d)\ dm \tag{2.7}$$

with m_c^{min} being the lowest possible mass of resonance c, typically defined by the sum of the decay product masses in the lightest accessible decay channel. $\vec{p}_f$ is the center-of-mass momentum of the final state and $\mathcal{A}_c(m)$ is the resonance spectral function of resonance c, depending on the resonance mass m. For double resonance excitations, $\mathcal{I}$ is defined as

$$\mathcal{I} = \int_{m_c^{min}}^{\sqrt{s}-m_d^{min}} \int_{m_d^{min}}^{\sqrt{s}-m_c^{min}} \mathcal{A}_c(m_c)\ \mathcal{A}_d(m_d)\ |\vec{p}_f|(\sqrt{s}, m_c, m_d)\ dm_c\ dm_d. \tag{2.8}$$

Eq. (2.8) represents an extension of Eq. (2.7) by virtue of an additional integration over the spectral function $\mathcal{A}_d(m_d)$ of resonance d.

The inverse process of the single and double resonance excitations is the resonance absorption process (subgroup (iii)). The corresponding absorption cross sections follow directly from the production cross section by employing the principle of detailed balance [37]. For both single and double resonance absorption, this cross section reads

$$\sigma_{cd\to ab}(s) = (2J_a + 1)\ (2J_b + 1)\ \frac{\mathcal{S}_{cd}}{\mathcal{S}_{ab}}\ \left|\frac{\vec{p}_f}{\vec{p}_i}\right|\ \frac{1}{s}\ \times \sum_I \left(C^I_{ab} C^I_{cd}\right)^2 \frac{|\mathcal{M}|^2(s, I)}{16\ \pi} \tag{2.9}$$

where c and d could either be two resonances or one resonance and one stable particle. $\mathcal{S}_{ab}$ and $\mathcal{S}_{cd}$ are the symmetry factors of the initial and final state, accounting for whether or not both particles form part of the same isospin multiplet.

The cross sections for the strangeness exchange processes (subgroup (iv)) rely on an energy-dependent parametrization [195] of the kind

$$\sigma_{K\bar{N}\leftrightarrow\pi\Upsilon} = \frac{A}{(\sqrt{s} - B)^2} \tag{2.10}$$

with A and B being free parameters, whose values are listed in [170]. Note, that these processes are usually realized via an intermediate hyperon resonance, such that $\bar{K}N \leftrightarrow \Upsilon^* \leftrightarrow \pi\Upsilon$ [189].

For the charge exchange processes (subgroup (v)), `SMASH` follows the framework introduced in `GiBUU`, where the charge exchange cross sections are obtained from directly parametrizing

the experimentally measured cross sections for inelastic $KN \leftrightarrow KN$ or $KN \leftrightarrow K\Delta$ scatterings [38, 196].

Finally, $N\bar{N}$ annihilation (subgroup (vi)) via resonances is implemented as a chain of binary interactions to model the 5-pion final state: $N\bar{N} \leftrightarrow h_1\rho \leftrightarrow \rho\pi\pi\pi \leftrightarrow \pi\pi\pi\pi\pi$. The alternative, direct treatment via multi-particle interactions, is described below. The cross section employed to model the annihilation process is the remainder when subtracting the elastic contribution from the parametrized total $N\bar{N}$ cross section [3].

Resonance Formations and Decays

The inelastic cross sections for resonance formations are directly related to the decay width of the inverse process, the resonance decay, and can be determined via

$$\sigma_{ab\to R}(s) = \frac{2\,J_R+1}{(2\,J_a+1)\,(2\,J_b+1)}\,\mathcal{S}_{ab}\,\frac{2\,\pi^2}{\vec{p}_i^{\,2}}\,\Gamma_{ab\to R}(s)\,\mathcal{A}_R(\sqrt{s})\;, \tag{2.11}$$

where $J_{R,a,b}$ is the spin of particle $R, a,$ or b, $\mathcal{S}_{ab}$ is the symmetry factor accounting for (non-)identical particles in the initial state, $\vec{p}_i^{\,2}$ is the center-of-mass momentum in the initial state, $\Gamma_{ab\to R}(s)$ the partial decay width of the process, and $\mathcal{A}_R(\sqrt{s})$ the resonance spectral function [37]. Note though, that in the case of unstable initial state particles, the decay width $\Gamma_{ab\to R}(s)$ requires modification according to the Manley-Saleski treatment as described in [37, 184].

The decay probability of any resonance in its rest frame within a time interval Δt is related to the resonance's total decay width Γ_{tot} via

$$P_{decay} = \frac{\Delta t}{\tau} = \Delta t\;\Gamma_{tot} \tag{2.12}$$

where τ is the resonance life time in its rest frame. Note, that the total decay width is defined as the sum of partial decay widths of all possible decay channels:

$$\Gamma_{tot} = \sum \Gamma_{partial} \tag{2.13}$$

Resonances in `SMASH` decay statistically according to Eq. (2.12).

Multi-Particle Interactions

Multi-particle interactions denote a new type of interaction recently introduced in `SMASH` [3, 175, 189] to account for scatterings involving more than two particles in the initial state. Owing to the limitations of the geometric collision criterion discussed in Sec. 2.1.3, multi-particle interactions require application of the stochastic collision criterion. As of `SMASH-2.1`, multi-particle interactions extend the list of hadronic interactions by the following processes:

- $3 \leftrightarrow 1$ interactions: $3\pi \leftrightarrow \omega$, $3\pi \leftrightarrow \phi$, and $\eta\pi\pi \leftrightarrow \eta'$
- $3 \leftrightarrow 2$ interactions: $np\pi \leftrightarrow d\pi$ and $npN \leftrightarrow dN$
- $5 \leftrightarrow 2$ interactions: $5\pi \leftrightarrow N\bar{N}$

The corresponding cross sections for $3 \leftrightarrow 1$ resonance formations are derived from the inverse process, the resonance decay, in analogy to the $2 \leftrightarrow 1$ case presented in Eq. (2.11). The deuteron cross sections for the $3 \leftrightarrow 2$ processes are obtained from parametrizations of the experimentally measured deuteron-hadron cross sections as described in [173]. The cross sections for the $5 \leftrightarrow 2$ process are, as in the resonance case, the remainder when subtracting the elastic contribution from the parametrized total $N\bar{N}$ cross section.

String Excitations and Fragmentations

The last set of interactions that are implemented in `SMASH` are string excitations and fragmentations [172]. Generally, string processes provide a possibility to extend the applicability of hadronic transport approaches beyond the energy range where resonance interactions dominate the dynamics. `SMASH` relies on `PYTHIA` to realize string dynamics, which is an event generator for collisions of elementary particles, nucleons and nuclei [197, 198].
There are two string frameworks in `SMASH`: soft and hard strings. As the name suggests, the former account for lower-energy interactions and the latter for interactions at higher collision energies. As such, hard string processes are accessible above $\sqrt{s} = 10$ GeV only, soft string processes already from $\sqrt{s} = 1.9$ GeV upwards. This property can also be observed in Fig. 2.1. However, the transition region from resonances to strings is not uniquely defined, but is different for each underlying interaction type. For $N\pi$ collisions the transition range applied in `SMASH` is $\sqrt{s} \in [1.9, 2.2]$ GeV, for NN collisions it is $\sqrt{s} \in [3.5, 4.5]$ GeV, else it is determined from the masses of the initial states particles m_a and m_b via: $\sqrt{s} \in [m_a + m_b + 0.9, m_a + m_b + 1.9]$ GeV.
The cross section for string processes is defined as the remainder of the total cross section when subtracting the elastic contribution:

$$\sigma_{\text{string}} = \sigma_{\text{tot}} - \sigma_{\text{el}} \tag{2.14}$$

The total string cross section σ_{string} contains contributions from the partial cross sections σ_{SD} accounting for single-diffractive processes, σ_{DD} for double-diffractive processes, and σ_{ND} for non-diffractive processes. These refer to scatterings, in which one of the incoming hadrons is excited to a string (SD), both incoming hadrons are excited to a string (DD), and both hadrons are excited to a string, but only after having exchanged a valence quark (ND). The cross sections for the single-diffractive and double-diffractive processes stem directly from `PYTHIA`. The cross sections for non-diffractive processes are the remainder of the total string cross section when subtracting the contributions from diffractive processes:

$$\sigma_{\text{ND}} = \sigma_{\text{string}} - \sigma_{\text{SD}} - \sigma_{\text{DD}} \tag{2.15}$$

The strings are excited and subsequently fragment into final-state hadrons again. Both the excitation as well as the fragmentation of non-diffractive processes are realized with `PYTHIA`, of which version `8.303` is employed in `SMASH-2.1`. For all other processes, the string excitation and fragmentation is realized directly in `SMASH` [172].

Angular Distributions

The angular distributions of the final state particles created in resonance decays in SMASH are isotropic. More concretely, the outgoing particles are sampled isotropically in the rest frame of the interaction and subsequently boosted back to the computational frame.
The angular distributions of elastic collisions, string processes, as well as the specific binary scatterings $NN \to NN$, $NN \to N\Delta$, $NN \to NN^*$, and $NN \to N\Delta^*$ are anisotropic (as of SMASH-2.1). For the two former binary scattering processes, SMASH relies on a parametrization of the angular distributions provided in [199]. For the two latter, the angular distributions are parameterized according to $d\sigma/dt \propto t^{-a}$ [37], and the parameter a is extracted from a fit to experimental data measured by the HADES collaboration [200]. For lack of alternatives, the angular distributions for all elastic scatterings also rely on the parametrization provided in [199] for NN scatterings.
In the case of final state particles produced in string processes, the angular distributions are assigned in the fragmentation process and thus originate from PYTHIA [197].
It shall further be noted, that the cross sections for photon production in SMASH are also anisotropic. Photons, for not being hadrons, are not among the usual degrees of freedom of SMASH though. Instead, they experience a perturbative treatment which is in great detail described in Sec. 3.2.

2.1.5. Collision Finding and Propagation

Unless potentials are activated in SMASH, particles are propagated on straight lines until experiencing an interaction.
The collision findig is realized as follow: In each time step, all interactions the incoming particles could potentially undergo are found with the desired collision criterion, as described in Sec. 2.1.3. Note, that for this first step in the collision finding, the total interaction cross section of the incoming particles is consulted, independently of the final state. Once all potential actions are collected, they are sorted by interaction time and the particles are propagated from action to action. Upon performing these actions, the specific interaction process the incoming particles undergo has yet to be determined. This is achieved by collecting all accessible processes and randomly choosing one, utilizing the partial cross sections (or branching ratios in case of resonance decays) as a weight. Once the interaction process is defined, the action is performed, and the final state particles are generated. The list of actions is updated accordingly, and all particles are propagated to the next action, which implies that the identical particles can in principle interact multiple times within the same time step. This procedure is repeated until all actions are performed and the end time of the simulation is reached.

2.1.6. Box, Sphere, Collider, and List Modus

There are four different modi in which SMASH can be employed. These include a collider simulation, a box simulation, a sphere simulation and an afterburner application via the list modus. The sphere modus provides an opportunity to study the properties of an expanding medium that is initialized as a sphere. However, since it is not employed within this thesis, it is not explained further. The interested reader may consult [37, 166] for additional information. The remaining modi are briefly introduced in the following.

Infinite Matter

Infinite matter simulations can be carried out in SMASH utilizing the box modus. Technically, this box is implemented with periodic boundary conditions, thus mimicking infinite matter. It can be initialized either from specific particle multiplicities or thermally from a Poisson distribution around the expectation value of the grand-canonical ensemble at given temperature T and chemical potential μ. The momenta are sampled from a Maxwell-Boltzmann distribution that is also subject to Poissonian fluctuations.
Infinite matter simulations are useful for studying the properties of a thermally and chemically equilibrated medium. In this work, they are applied in Sec. 3.2 to validate the implementation of photon production in SMASH by comparing the resulting equilibrium photon rates to their semi-analytical counterparts.

Nucleus-Nucleus Collisions

The collider modus of SMASH gives access to simulating the dynamics of relativistic heavy-ion collisions. For this, the protons and neutrons that form the colliding nuclei are initialized from a Woods-Saxon distribution according to

$$\frac{dN}{d^3r} = \frac{\rho_0}{\exp\left(\frac{r-r_0}{d}\right)+1}, \tag{2.16}$$

where d is the diffusiveness and ρ_0 and r_0 the saturation density and radius in the limit of $d \to 0$, where the nucleus is a hard sphere.
The default values applied are [37, 201]:

$$\rho_0 = 0.168 \text{ fm}^{-3} \tag{2.17}$$

$$r_0 = \begin{cases} r_{\text{proton}}\, A^{1/3} & \text{if } A \leq 16 \\ (1.12\, A^{1/3} - 0.86\, A^{-1/3}) \text{ fm} & \text{if } A > 16 \end{cases} \tag{2.18}$$

$$d = \begin{cases} 0.545 \text{ fm} & \text{if } A \leq 16 \\ 0.54 \text{ fm} & \text{if } A > 16 \end{cases}, \tag{2.19}$$

with the proton radius $r_{\text{proton}} = 1.2$ fm and the total number of nucleons in the nucleus A. Exceptions are made for a range of nuclei though, the experimentally most commonly used ones. These exceptions are [37]:

Furthermore, the deformation of nuclei is implemented as an additional feature in SMASH. It can be used to account for nuclear geometries other than a spherical shape. This is achieved by expressing the radius in spherical coordinates and expanding it in spherical harmonics. The expansion coefficients then determine the shape of the sampled nucleus and the geometrical structure of its deformation. Further details about this procedure are provided in [37, 180]. Deformed nuclei are however not subject of this work.

Once the colliding nuclei are initialized geometrically, they are distributed in space-time. The z-axis is defined to be the collision axis, and their initial positions are chosen such that the

	$^{238}_{92}$U	$^{208}_{82}$Pb	$^{197}_{79}$Au	$^{63}_{29}$Cu	$^{96}_{40}$Zr	$^{96}_{44}$Ru
ρ_0 [fm^{-3}]	0.166	0.161	0.1695	0.1686	0.1673	0.1604
r_0 [fm]	6.86	6.67	6.38	4.30641	5.02	5.085
d [fm]	0.556	0.54	0.535	0.5977	0.46	0.46

Table 2.1.: Specific Woods-Saxon parameters applied in SMASH for U, Pb, Au, Cu, Zr, and Ru nuclei.

spheres with radii $r_{0,i} + d_i$ touch at time $t = 0$ and at $z = 0$ in central collisions. If non-central collisions are simulated, the impact parameter b, characterizing the offset at which the nuclei collide, needs further be taken into account. In this case, the nuclei are shifted along the x-axis about $b/2$ each. After initialization, the nuclei collide with the provided collision energy, and the hadronic interactions are performed as detailed above.

Hadronic Afterburner

The list modus provides an opportunity to initialize SMASH from an external particle list such that the implied hadronic interactions can subsequently be performed. This modus is particularly useful to describe the late, hadronic rescattering stage in hydrodynamics+transport models that are employed to describe heavy-ion collisions at high collision energies (c.f. Sec. 1.2.1). For this, SMASH expects an external list in a predefined format that contains the full momentum-space information and relevant properties of each particle. If this particle list is not characterized by a constant time t, the particles are back-propagated according to their momenta. They successively show up in the evolution once their formation time is completed. The particles are then propagated and the remaining hadronic interactions performed until the medium is too dilute.

2.1.7. Electromagnetic Probes

The emission of electromagnetic probes in terms of photons and dileptons is further implemented as an option in SMASH. Since neither photons nor dileptons are hadrons, they are not subject to the strong interaction. Yet, they can be produced in hadronic scattering processes or resonance decays via the electromagnetic interaction. It can safely be assumed that they escape the strongly-interacting fireball nearly unaffected, owing to the weakness of the electromagnetic interaction. Their mean free path is much larger than the size of the system. This justifies the perturbative treatment employed in SMASH to model dilepton and photon emission. Photon production is explained in detail in Sec. 3.2, hence only the production of dileptons is briefly introduced in the following. The interested reader is referred to [176, 189] for a broader introduction.

Dielectrons can be produced in SMASH in direct or Dalitz decays of hadronic resonances. As of SMASH-2.1, decays to μ or τ lepton pairs are not yet implemented. The production mechanism of dileptons [176] relies on the *Time Integration Method*, also referred to as *Shining Method* [202, 203]. This implies the continuous emission (shining) of dileptons during the propagation

of a resonance and assigning a specific weight to each produced dilepton:

$$w_{sh} = \frac{\Delta t}{\gamma}\, \Gamma_{e^+e^-}, \tag{2.20}$$

where w_{sh} is the shining weight, $\frac{\Delta t}{\gamma}$ is the time the resonance is propagated in the rest frame and $\Gamma_{e^+e^-}$ is the branching ratio of the dilepton decay channel. Eq. (2.20) defines the shining weight for a direct dilepton decay; it is straightforward to extend it to Dalitz decays, as described in [189]. The shining weight accounts for the reduced probability of the resonance to decay into a dilepton final state instead of a hadronic final state. Note, that the inclusion of dilepton decay channels for hadronic resonances further introduces additional contributions to the resonance spectral functions below the hadronic thresholds.

The perturbative treatment in SMASH implies that the final state particles of the dilepton and photon processes are not further propagated in the evolution. They are rather directly printed to a separate output and the hadronic interaction performed normally as if no electromagnetic process had occurred.

2.1.8. Hadron Resonance Gas Equation of State

It is possible to derive the equation of state of the SMASH hadron resonance gas from the SMASH list of degrees of freedom. This equation of state is in particular necessary to apply SMASH as an afterburner in hydrodynamics+transport hybrid approaches. A consistent equation of state is of fundamental importance to guarantee consistency at the interface when switching from a macroscopic description via hydrodynamics to a microscopic description via transport. The importance of a matching equation of state for the particlization process in the SMASH-vHLLE-hybrid is demonstrated in Sec. 2.3.
The equation of state (EoS) generally provides a mapping of the thermodynamic quantities energy density e, net baryon density n_B, net charge density n_Q and net strangeness density n_S to the temperature T, the pressure p, the baryon chemical potential μ_B, the charge chemical potential μ_Q, and the strange chemical potential μ_S. In the context of heavy-ion collisions, the net strangeness density can be approximated as $n_S = 0$ fm^{-3}. The explicit dependence of the thermodynamic quantities T, p, μ_B, μ_Q, and μ_S on the net strangeness density is thus neglected within this work, assuming a vanishing net strangeness density. Hence, the SMASH equation of state presented herein and later applied in the SMASH-vHLLE-hybrid provides the mapping:

$$(e, n_B, n_Q) \;\rightarrow\; (T, p, \mu_B, \mu_Q, \mu_S) \tag{2.21}$$

This mapping follows from the properties of the underlying gas of hadrons, consisting of the SMASH degrees of freedom, and can be determined by solving the set of coupled equations

$$\begin{aligned} e &= e\ (T, \mu_B, \mu_Q, \mu_S) \\ n_B &= n_B\ (T, \mu_B, \mu_Q, \mu_S) \\ n_Q &= n_Q\ (T, \mu_B, \mu_Q, \mu_S) \\ n_S &= n_S\ (T, \mu_B, \mu_Q, \mu_S), \end{aligned} \tag{2.22}$$

to determine T, μ_B, μ_Q, and μ_S and extract p with Eq. (2.27) presented below. Note, that

T, μ_B, μ_Q, and μ_S in turn depend on e, n_B, n_Q, and n_S. In accordance with SMASH, an ideal Boltzmann hadron gas is assumed in the grand-canonical ensemble for which the baryon, charge, and strangeness densities are defined as [115]

$$n_B = \frac{T^3}{2\,\pi^2\,(\hbar c)^3} \sum_i^N g_i\; B_i\; \exp\left(\frac{\mu_i}{T}\right) \left(\frac{m_i}{T}\right)^2 K_2\left(\frac{m_i}{T}\right) \tag{2.23}$$

$$n_Q = \frac{T^3}{2\,\pi^2\,(\hbar c)^3} \sum_i^N g_i\; Q_i\; \exp\left(\frac{\mu_i}{T}\right) \left(\frac{m_i}{T}\right)^2 K_2\left(\frac{m_i}{T}\right) \tag{2.24}$$

$$n_S = \frac{T^3}{2\,\pi^2\,(\hbar c)^3} \sum_i^N g_i\; S_i\; \exp\left(\frac{\mu_i}{T}\right) \left(\frac{m_i}{T}\right)^2 K_2\left(\frac{m_i}{T}\right), \tag{2.25}$$

with $\mu_i = \mu_B B_i + \mu_Q Q_i + \mu_S S_i$ being the chemical potential, g_i the spin degeneracy factor and m_i the mass of the i-th particle. B_i, Q_i, and S_i are the quantum numbers baryon number, electric charge and strangeness, respectively. T is the temperature and K_2 are the modified Bessel functions of the second kind [204]. The sum accounts for all hadronic degrees of freedom in SMASH except for the σ meson as its inclusion imposes problems in the particlization process. The energy density and pressure are further required to find the SMASH equation of state. For an ideal Boltzmann gas, these are defined as

$$e = \frac{T^4}{2\,\pi^2\,(\hbar c)^3} \sum_i^N g_i \left(\frac{m_i}{T}\right)^2 \left(3\; K_2\left(\frac{m_i}{T}\right) + \frac{m_i}{T}\; K_1\left(\frac{m_i}{T}\right)\right) \qquad \text{and} \tag{2.26}$$

$$p = T \sum_i^N n_i = T \sum_i^N \frac{T^3}{2\,\pi^2\,(\hbar c)^3}\; g_i\; \exp\left(\frac{\mu_i}{T}\right) \left(\frac{m_i}{T}\right)^2 K_2\left(\frac{m_i}{T}\right). \tag{2.27}$$

The solutions of the coupled equations (2.22) are then determined numerically for an ideal Boltzmann gas with SMASH degrees of freedom within the grand-canonical ensemble. This is achieved with a root solver algorithm relying on the `GNU Scientific Library` [2] [205]. Unfortunately, this solver is highly sensitive to the choice of the initial approximation. It is likely to fail in converging if the initial approximation is not close enough to the actual solution. This is in particular problematic for decreasing energy densities, where the hadron resonance gas is loosely populated, as well as close to the kinematic thresholds. The kinematic thresholds arise from the composition of the hadron gas, i.e. its lightest baryon and electrically charged particle. These are the (anti-)proton with $m_{p,\bar{p}} = 0.938$ GeV and the pion with $m_\pi = 0.138$ GeV, respectively. The kinematically accessible region is thus restricted to $e \geq m_p\,|n_B|$ and $e \geq m_\pi\,|n_Q|$. The issues of the root solver algorithm to converge at low energy densities and close to the kinematic thresholds become apparent in the left panel of Fig. 2.2. The resulting temperature T is presented as a function of the baryon density n_B and the charge density n_Q at fixed energy density $e = 0.3$ GeV/fm^3 as directly obtained with the root solver. Here, the convergence issue is exemplarily presented for the temperature T, but the p, μ_B, μ_Q, and μ_S profiles suffer from the same problems. In the left panel of Fig. 2.2 it becomes apparent that far from the kinematic thresholds, the solutions are perfectly smooth, while for increasing baryon densities, the solutions become unstable and the resulting temperature profile unphysically spiky[3]. This spiky structure is particularly

[2] Concretely, the `gsl_root_fsolver` is employed.

[3] Note, that if the solver fails to find an appropriate solution, it falls back to $T = p = \mu_B = \mu_Q = \mu_S = 0$.

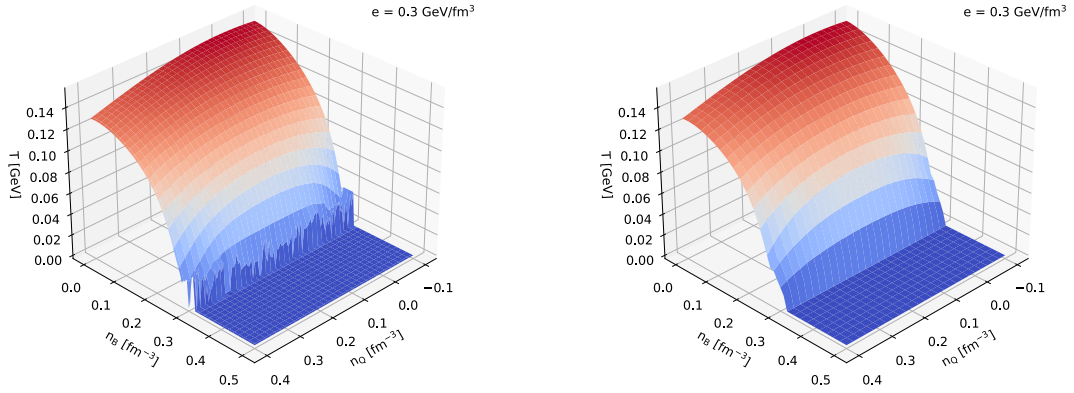

Figure 2.2.: Temperature profile of the SMASH hadron resonance gas as a function of the baryon density n_B and the charge density n_Q at fixed energy density $e = 0.3$ GeV/fm^3. On the left, results obtained directly with a solver algorithm for Eqs. (2.22) without further modifications is presented, on the right the improved version where the spiky structure at the thresholds is smoothened.

problematic when it comes to employing the SMASH hadron resonance gas equation of state for the particlization process in hybrid models at intermediate collision energies, where a relatively large fraction of cells is characterized by combinations of (e, n_B, n_Q) close to the kinematic thresholds. These implications are discussed in greater detail when validating the SMASH-vHLLE-hybrid in Sec. 2.3. Yet, it is essential to find an accurate equation of state of the SMASH hadron resonance, valid also at low energy densities and close to the kinematic thresholds, in order for it to be applied within hybrid models relying on SMASH for the hadronic afterburner evolution. This is achieved by (i) solving Eqs. (2.22) for different grid spacings in (e, n_B, n_Q) and varying initial approximations, (ii) spline inter- and extrapolations of the reliable solutions for Eqs. (2.22) in 2D-slices at fixed e, n_B, and n_Q, and (iii) subsequently averaging the therewith obtained thermodynamic quantities at each grid point. Where necessary, manual fine-tuning finalizes to process of finding an equation of state mapping from (e, n_B, n_Q) to $(T, p, \mu_B, \mu_Q, \mu_S)$ for the SMASH hadron resonance gas that is as accurate and smooth as possible. This equation of state is perfectly reliable at high energy densities but is by no means perfect at low energy densities or close to the kinematic thresholds. Nevertheless, it provides a good approximation in those regions where the root solver algorithm fails to converge. The improved temperature profile as a function of the baryon density n_B and the charge density n_Q at fixed energy density $e = 0.3$ GeV/fm^3 is presented in the right panel of Fig. 2.2. One sees that, in comparison to the left panel, the spiky structure is smoothed out, and the temperature profile is available across the entire kinematically accessible region. The full, improved equation of state for the thermodynamic quantities T, p, μ_B, μ_Q, and μ_S, in the range $e \in [0.01, 1.0]$ GeV/fm^3, $n_B \in [0.0, 0.5]$ fm^{-3}, and $n_Q \in [-0.1, 0.4]$ fm^{-3}, and accounting for all hadronic degrees of freedom of the SMASH hadron resonance gas, is available in tabularized format under [206]. Different attempts were made to find a parametrization of the equation of state for it to be applied without the need for interpolations in hydrodynamics+transport models. Unfortunately, these attempts remained unsuccessful. Nonetheless, they are briefly documented in App. B.

For validation purposes, the resulting SMASH equation of state at vanishing net baryon, net

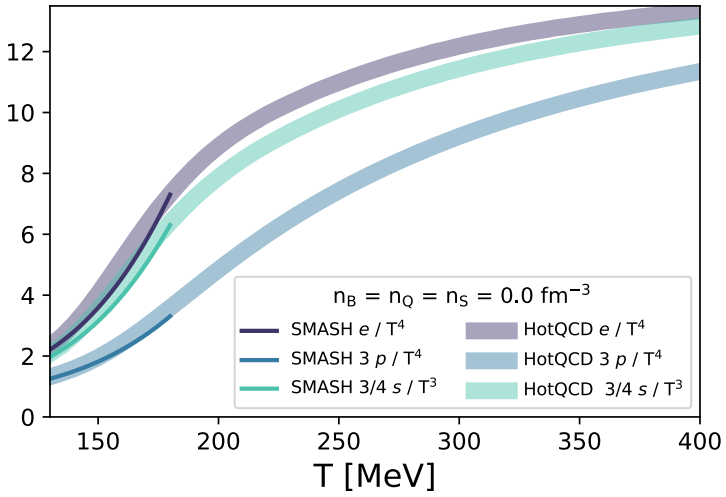

Figure 2.3.: Equation of state of the SMASH hadron resonance gas in terms of the energy density e, pressure p, and entropy density s (lines) in comparison to results obtained within 2+1-flavour lattice QCD [19] (bands) for vanishing net baryon, net charge and net strangeness densities.

electric charge and net strangeness densities is compared to lattice QCD results obtained in 2+1-flavour QCD [19] by the HotQCD collaboration in Fig. 2.3. Lines denote the SMASH hadron resonance gas, bands the lattice QCD equation of state. The energy density e, pressure p and entropy density s, normalized to different orders of the temperature T, are in decent agreement with lattice QCD results at low temperatures, where both approaches are expected to yield approximately similar results. This is considered a validation of the SMASH hadron resonance gas equation of state determined with the procedure detailed above.

2.2. The SMASH-vHLLE Hybrid

The SMASH-vHLLE-hybrid is a novel modular hybrid approach consisting of SMASH, vHLLE, and the SMASH-hadron-sampler. The central element of the presented PhD work is the development and thorough validation of the SMASH-vHLLE-hybrid, based on the already existing SMASH and vHLLE codes. Although existent beforehand, these codes required extensions and modifications of different kinds to realize the respective interfaces. This includes the extension of SMASH by a new output containing initial conditions for hydrodynamical simulations, the extension of vHLLE to allow initialization from an external SMASH particle list, the determination of the SMASH hadron resonance gas equation of state (c.f. Sec. 2.1.8) to be embedded in vHLLE, as well as the extension of vHLLE to employ the SMASH equation of state when creating the transition hypersurface for the particlization process. Particlization is realized with the SMASH-hadron-sampler that also needed to be developed. It is based on a particle sampler originally created to couple vHLLE to UrQMD [59, 207]. From this, the sampling algorithm is adopted; otherwise it is modified such that it is directly coupled to SMASH. This simplifies the sampling of particles according to the SMASH hadron resonance gas and enables the creation of a properly formatted output suitable to initialize the hadronic afterburner evolution. Finally, the different components of the SMASH-vHLLE-hybrid are wrapped by CMake [208] to automatically handle the execution of the different submodules and to consistently propagate input/output files as well as parameters needed in multiple stages (e.g. viscosities for the hydrodynamical evolution and the sampling process). Furthermore, the SMASH-vHLLE-hybrid is coupled to the SMASH-analysis to directly provide fully analyzed and averaged particle spectra. The SMASH-vHLLE-hybrid is publicly available on Github [209].
In what follows, the different components of the SMASH-vHLLE-hybrid, and the realization of the interfaces, are described in great detail.

2.2.1. Initial Conditions

The initial conditions in the SMASH-vHLLE-hybrid are provided by the SMASH hadronic transport approach. For this, the nucleus-nucleus collision is initialized normally at a certain collision energy, as described in Sec. 2.1.6. The full evolution of the collision is however not completed, the particles are rather propagated and interact until reaching a hypersurface of constant proper time τ_0. They are removed from the evolution once this iso-τ hypersurface is crossed and printed to a separate output file that is later used to initialize the macroscopic evolution in vHLLE. The proper time until which the particles are propagated is determined from nuclear overlap as the passing time of the two nuclei [59, 63]:

$$\tau_0 = \frac{R_p + R_t}{\sqrt{\left(\frac{\sqrt{s_{NN}}}{2\ m_N}\right)^2 - 1}}, \tag{2.28}$$

where R_p and R_t are the radii of the projectile and target nucleus, respectively. $\sqrt{s_{NN}}$ is the collision energy of the nucleus-nucleus collision and $m_N = 0.938$ GeV is the nucleon mass. Note though, that this passing time is lower bound by $\tau_0 = 0.5$ fm, for collective dynamics to evolve even in high-energy collisions where the nuclei are significantly Lorentz-contracted. Once a particle reaches the hypersurface at $\tau = \tau_0$, it is removed from the evolution, the remaining particles are still evolved and undergo interactions until eventually also reaching this hypersurface. One might argue that the removal of particles modifies the underlying dy-

namics since local densities are altered. It was verified though that the final state observables remain unaffected, no matter if the particles remain in the medium or are removed from it. Once all particles have crossed the hypersurface, the iso-τ particle list serves as initial conditions for the subsequent hydrodynamical evolution in `vHLLE`.

Technical Implementation

Technical details about the implementation of such initial conditions for hydrodynamics in `SMASH` are briefly summarized in the following. This implementation is two-fold: It consists of extending `SMASH` first by a new type of interaction, the so-denoted `HypersurfacecrossingAction`, and second by a new type of output, the `ICOutput`, containing the particles and their properties when crossing the iso-τ hypersurface. The `HypersurfacecrossingAction` can be understood as an additional interaction possibility the particles have in each timestep. Unlike the collision finding of scatterings and decays (c.f. Sec. 2.1.5), the collision finding of a `HypersurfacecrossingAction` does not rely on a cross section or branching ratio. It is rather evaluated in each time step, respectively between two interactions, whether or not a particle crosses the hypersurface of constant proper time τ_0 during its propagation. `SMASH` relies on cartesian coordinates, where the proper time of a particle is defined as

$$\tau = \sqrt{t^2 - z^2} \tag{2.29}$$

with t and z being its time and z-position. Eq. (2.29) implies that, to also capture particles with large z, the evolution has to be performed until large times t. The user thus needs to ensure the runtime of the `SMASH` simulation is long enough for all particles to cross the hypersurface. A corresponding warning is implemented if the runtime is too short. It can further happen that the radicand in Eq. (2.29) is negative (cases with $|t| < |z|$) [4]. This is ignored, and the particles remain in the evolution until eventually fulfilling Eq. (2.29) with $|t| > |z|$. To find a `HypersurfacecrossingAction`, the proper time of each particle is evaluated at the beginning and end of each time step:

$$\tau_{\mathrm{start}} = \sqrt{t_{\mathrm{start}}^2 - z_{\mathrm{start}}^2} \qquad \text{and} \qquad \tau_{\mathrm{end}} = \sqrt{t_{\mathrm{end}}^2 - z_{\mathrm{end}}^2} \tag{2.30}$$

If the particle crosses the τ_0-hypersurface within the timestep $[t_{\mathrm{start}},\ t_{\mathrm{end}}]$, the following condition must be fulfilled:

$$\tau_{\mathrm{start}} \ < \ \tau_0 \ \leq \ \tau_{\mathrm{end}} \tag{2.31}$$

If this condition is met, the interaction position, i.e. the position at which the hypersurface is crossed, needs further be determined. This is achieved by drawing a straight line between $(t_{\mathrm{start}}, z_{\mathrm{start}})$ and $(t_{\mathrm{end}}, z_{\mathrm{end}})$ and finding the crossing position (t^*, z^*) on this trajectory such

[4] Owing to Poissonian fluctuations, this may happen if a constituent nucleon is sampled at a position further away from the centre of the nucleus than the nucleus' radius+diffusiveness. If this nucleon is additionally located along the beam axis, it is characterized by a finite z position at time $t = 0$ fm which then implies an imaginary proper time τ.

that Eq. (2.29) is fulfilled. The corresponding time of crossing, t^* is then provided by

$$t^* = \frac{m\, n}{1-m^2} + \frac{\sqrt{(1-m^2)\,\tau_0^2 + n^2}}{1-m^2} \tag{2.32}$$

where m is the slope and n the intercept of the straight line connecting the starting and end point. Note, that there are in principle two solutions for the point of interception, the second corresponding to a negative sign before the second fraction. Only the solution presented in Eq. (2.32) does however fulfill $t^* \in [t_{start}, t_{end}]$. The corresponding z-coordinate of the crossing position is then provided by

$$z^* = m\, t^* + n. \tag{2.33}$$

Once the interaction point of the `HypersurfacecrossingAction` is found, the particles are propagated on straight lines from t_{start} to t^* without further, intermediate interactions and are finally removed from the evolution.

The removal of a particle from the `SMASH` evolution goes in hand with writing its properties to the initial conditions output. This output is either provided in the `SMASH` standard formats `OSCAR, binary, ROOT`, or `HepMC` (c.f. [158]), or in the newly-implemented `ICOutput` format. The `ICOutput` is specifically constructed such that it can directly serve as input for the `vHLLE` hydrodynamics code. It is provided as a `.dat` file consisting of multiple lines and columns. Each line corresponds to a particle, and the different columns contain different particle properties necessary for the initialization of `vHLLE`. The column structure is as follows:

$$\tau\ [\mathtt{fm}] \quad x\ [\mathtt{fm}] \quad y\ [\mathtt{fm}] \quad \eta \quad m_T\ [\mathtt{GeV}] \quad p_x\ [\mathtt{GeV}] \quad p_y\ [\mathtt{GeV}] \quad y_{rap} \quad \mathtt{PDG} \quad Q\ [e]$$

with units provided in square brackets if the quantity is not unitless. Here, (τ, x, y, η) is the 4-position of the particle in Milne coordinates, where the space-time rapidity η is defined as $\eta = 0.5\ \log(\frac{t+z}{t-z})$. m_T is the transverse mass, p_x and p_y are the momentum components in x and y-direction, and y_{rap} is the momentum-space rapidity defined as $y_{rap} = 0.5\ \log(\frac{E+p_z}{E-p_z})$. `PDG` denotes the particle's unique PDG code [18] and `Q` its electric charge.
These properties are sufficient to define a density profile of the underlying event and with this initialize the hydrodynamical evolution in `vHLLE`.

Both new features, the `HypersurfacecrossingAction` and the `ICOutput` are available in `SMASH` since version `SMASH-2.0` [156].

2.2.2. Hydrodynamical Evolution

The evolution of the hot and dense fireball in terms of fluid dynamics is performed with `vHLLE`. That is a 3+1D viscous hydrodynamics approach, solving the Riemann problem associated with the hydrodynamic equations (c.f. Eq. (1.8) and (1.9)) within the second-order Israel-Stewart framework [210, 211]. It relies on Milne coordinates, where the space-time four-vector is defined as $x^\mu = (\tau, x, y, \eta)$. The proper time τ is defined as in Eq. (2.29), x and y are identical to the cartesian x and y coordinates, and the space-time rapidity η is related to cartesian

coordinates via $\eta = 0.5\ \log(\frac{t+z}{t-z})$. `vHLLE` was introduced in [99] and employed within a hybrid approach consisting of `UrQMD` and `vHLLE` in [59]. Results of the latter are compared to those obtained with the `SMASH-vHLLE-hybrid` in Sec. 2.3. The approach is publicly available on Github [212] and briefly introduced in the following, which is based on [99] and [59].

Initialization from an External Particle List

In the context of the `SMASH-vHLLE-hybrid`, the hydrodynamical evolution with `vHLLE` is initialized from the particle list provided by `SMASH` on the iso-τ hypersurface. The `SMASH-vHLLE-hybrid` relies on event-by-event hydrodynamics. The hydrodynamical evolution is thus initialized multiple times from single `SMASH` events, which allows for fluctuating initial conditions. These are however not in full local equilibrium as the individual particles create peaks in the local densities that can later produce shock waves in the hydrodynamical evolution. Isotropization of the initial state needs thus be enforced upon initialization, at proper time $\tau = \tau_0$. This is realized by distributing the quantum numbers of each particle according to a Gaussian density profile to the hydrodynamical cells with indices $\{i, j, k\}$ according to

$$\Delta P^{\alpha}_{ijk} = P^{\alpha}\ C\ \exp\left(-\frac{\Delta x_i^2 + \Delta y_j^2}{R_\perp^2}\ -\ \frac{\Delta\eta_k^2}{R_\eta^2}\ \gamma_\eta^2\ \tau_0^2\right) \tag{2.34}$$

$$\Delta N^{0}_{ijk} = N^{0}\ C\ \exp\left(-\frac{\Delta x_i^2 + \Delta y_j^2}{R_\perp^2}\ -\ \frac{\Delta\eta_k^2}{R_\eta^2}\ \gamma_\eta^2\ \tau_0^2\right) \tag{2.35}$$

In the above, P^{α} denotes the particle's 4-momentum and N^0 the particle's quantum number, which is a placeholder for the baryon, electric charge and strangeness quantum number. Δx_i, Δy_j, and $\Delta\eta_k$ are the differences between the particle's position the centre of the cell with index $\{i, j, k\}$. τ_0 is the initial proper time and $\gamma_\eta = \cosh(y_p - \eta)$ is the Lorentz factor in the comoving frame at space-time rapidity η, where y_p denotes the momentum-space rapidity. $R_\perp$ and R_η are the transversal and longitudinal smearing factors which control how widely the properties of each particle are smeared. These smearing factors are by no means fixed; they need rather be adjusted individually for each sampled collision system at a specific energy. Further information about this is provided in Sec. 2.4. Finally, C is the normalization constant, ensuring

$$\sum_{ijk} \exp\left(-\frac{\Delta x_i^2 + \Delta y_j^2}{R_\perp^2}\ -\ \frac{\Delta\eta_k^2}{R_\eta^2}\ \gamma_\eta^2\ \tau_0^2\right) = 1, \tag{2.36}$$

and thus allowing for quantum number conservation at the interface. Here, the sum accounts for all cells on the grid. The resulting contributions of energy, momentum, baryon number, electric charge and strangeness in terms of ΔP^{α}_{ijk} and ΔN^{0}_{ijk} are transformed into Milne coordinates and added to each cell. For further information about this initialization procedure, the interested reader is referred to the original publication [99].

Evolution of the Viscous Fluid

Once initialized, the medium is evolved according to viscous hydrodynamics by solving the hydrodynamic equations

$$\partial_\mu T^{\mu\nu} = 0 \qquad \text{and} \tag{2.37}$$

$$\partial_\mu \, J_i{}^\mu = 0 \qquad i = B, S, Q, \tag{2.38}$$

which were already introduced in Sec. 1, but are repeated here for completeness. The energy-momentum tensor $T^{\mu\nu}$, whose conservation is encapsulated in Eq. (2.37), can be decomposed into

$$T^{\mu\nu} = e \; u^\mu u^\nu - \Delta^{\mu\nu}(p + \Pi) + \pi^{\mu\nu}. \tag{2.39}$$

Here, e denotes the energy density in the fluid rest frame and p the equilibrium pressure. Π and $\pi^{\mu\nu}$ are the bulk pressure and the shear-stress tensor accounting for bulk viscous and shear viscous effects, respectively. u^μ is the flow velocity in the Landau frame and $\Delta^{\mu\nu} = g^{\mu\nu} - u^\mu \, u^\nu$ the projection operator orthogonal to u^μ. The charge currents whose conservation is contained by Eq. (2.38) can further be decomposed into

$$J_i{}^\mu = n_i \; u^\mu + V_i^\mu \tag{2.40}$$

with n_i being the densities of the conserved charges, that is the baryon number, electric charge or strangeness, and V_i^μ the corresponding charge diffusion currents. The set of equations provided by Eq. (2.37) and Eq. (2.38) is closed with the equation of state through which the properties of the described medium enter. In this work, the equation of state characterizing the hot and dense medium is taken from [80].
The solutions of the hydrodynamic equations are obtained in the second-order Israel-Stewart framework [213] in the 14-momentum approximation, where shear-bulk coupling terms are accounted for [210, 211]. The algorithm employed to solve the hydrodynamic equations is a Godunov-type relativistic Harten-Lax-van Leer-Einfeldt (HLLE) approximate Riemann solver [96–99]. It provides an effective solution of the hydrodynamic equations in each time step and hence allows for propagation of the medium. The evolution is performed until all cells have dropped below a predefined energy density, at which the transition from a macroscopic description via hydrodynamics to a microscopic description via hadronic transport takes place. In the context of the presented work, $e_{crit} = 0.5$ GeV/fm^3 is employed, which is a criterion also used in other hybrid models [59, 114, 214].

Freezeout Hypersurface

The final state of the hydrodynamic stage is represented by the freezeout hypersurface. It contains all cells of the hydrodynamical evolution along with their thermodynamic properties at the point when their energy density drops below the critical energy density e_{crit}. This hypersurface serves as input for the subsequent sampling process where hadrons are produced from the collection of hypersurface elements. The hypersurface is found dynamically during the evolution with the `CORNELIUS` subroutine [110]. `CORNELIUS` provides not only the location of the freezeout hypersurface, but also the normal vectors characterizing the hypersurface

elements. These are required to calculate the effective volume of each hypersurface element, which is needed for the particlization process (c.f. Sec. 2.2.3). For further details about CORNELIUS, including the technical realization, the interested reader is referred to [110].

For reference, the format and structure of the freezeout hypersurface is presented in the following. It is a table in .dat format, in which every line corresponds to one hypersurface element. There are 27 columns containing their properties. These are:

$$\tau \quad x \quad y \quad \eta \quad d\sigma_\mu \quad u^\mu \quad T \quad \mu_B \quad \mu_Q \quad \mu_S \quad \pi^{\mu\nu} \quad \Pi$$

Here, τ, x, y, and η are the space-time coordinates of the hypersurface elements, $d\sigma_\mu$ are their normal vectors, and u^μ the flow velocities characterizing them. T is the element's temperature and μ_B, μ_Q, μ_S its baryon, electric charge and strangeness chemical potentials, respectively. $\pi^{\mu\nu}$ is the shear-stress tensor and Π the bulk pressure. Note, that $d\sigma_\mu$ and u^μ each contain four components while $\pi^{\mu\nu}$ contains ten independent components. All of these are printed to the freezeout hypersurface.
Another important property regarding the creation of the freezeout hypersurface is the fact that for the determination of the thermodynamic quantities T, μ_B, μ_Q, and μ_S, the equation of state of the SMASH hadron resonance gas is employed instead of the equation of state based on which the medium is evolved[5]. This is of fundamental importance in order to ensure quantum number conservation in the sampling process. This hadronic equation of state is determined from the SMASH hadron resonance gas as described in Sec. 2.1.8 and implemented in tabularized format in vHLLE. Linear interpolations between the grid points are employed where necessary. The implications for quantum number conservation in the sampling process, originating from an inaccurate equation of state upon creation of the freezeout hypersurface, are demonstrated in Sec. 2.3.

2.2.3. Particlization

Particlization of the fluid elements on the freezeout hypersurface is achieved with the SMASH-hadron-sampler. It is based on a sampling routing originally developed within [59] to couple vHLLE to UrQMD for a vHLLE+UrQMD hybrid approach. In the presented work, the original sampler is modified such that SMASH is employed as a third party library. This bears the advantage that particles can be sampled according to the SMASH hadron resonance gas more easily while at the same time providing an output format that matches the requirements for the SMASH list modus (c.f. Sec. 2.1.6) for the afterburner evolution. The SMASH-hadron-sampler is also available publicly on Github [215].

Sampling Procedure

Particlization with the SMASH-hadron-sampler is realized within the grand-canonical ensemble such that each fluid element can be sampled individually. Technically, this is realized as follows. First, the total thermal multiplicities, accounting for all degrees of freedom of the SMASH hadron resonance gas[6], passing through each hypersurface element i are calculated by

[5] It is ensured that the equation of state employed for the hydrodynamical evolution matches a hadron resonance gas towards lower energy densities.

[6] Note, that we exclude the leptons $e^\pm, \mu^\pm, \tau^\pm$, the photon γ and the σ meson from the SMASH particle list for the sampling process. These are not among the usual hadronic degrees of freedom of SMMASH, but form

means of

$$N_i^{tot} = V_i \sum_{k=1}^{N_{dof}} \frac{(2J_k+1)\ m_k^2\ T_i}{2\ \pi^2} \sum_{i=1}^{11} \frac{s_k^{i+1}}{i}\ K_2\left(\frac{i\ m_k}{T_i}\right)\ \exp\left(\frac{i\ \mu_k}{T_i}\right), \tag{2.41}$$

where the first sum with index k accounts for all `SMASH` degrees of freedom such that J_k is the spin and m_k the mass of the k-th degree of freedom. s_k accounts for its quantum state where $s_k = 1$ in the case of Bose statistics and $s_k = -1$ for Fermi statistics. μ_k is the chemical potential of the k-th degree of freedom determined from

$$\mu_k = B_k\ \mu_{B,i}\ +\ Q_k\ \mu_{Q,i}\ +\ S_k\ \mu_{S,i}, \tag{2.42}$$

where B_k, Q_k, and S_k are its baryon number, electric charge and strangeness, respectively. $\mu_{B,i}$, $\mu_{Q,i}$, and $\mu_{S,i}$ are the baryon, electric charge and strangeness chemical potentials of the i-th hypersurface element. In Eq. (2.41), T_i further denotes its temperature and V_i its effective volume. The latter can be determined from the normal vector of the hypersurface element, $d\sigma_\mu$, and the flow velocity u^μ via

$$V_i\ =\ d\sigma_{\mu,i}\ u_i^\mu. \tag{2.43}$$

The actual number of particles to sample for the i-th hypersurface element, $N_{part,\ i}$, is then determined from a Poisson distribution with mean N_i^{tot}. If $N_{part,\ i} > 0$ for a given hypersurface element, hadrons are sampled according to their relative abundances, where resonances are sampled at their pole masses. Momentum is assigned relying on the Cooper-Frye formula [109] provided in Eq. (1.10) and the particles' positions are determined from the centre of the hypersurface element. An additional smearing in the η direction is employed to prevent sampling all particles of one hypersurface element at exactly the same position. The above-described procedure, starting from the random determination of $N_{part,\ i} > 0$ is repeated for each event that is to be sampled for the hadronic rescattering stage. The particles sampled for the individual events are further printed to an output file in `OSCAR2013` format, which is the required input format for the `SMASH` list modus.

2.2.4. Hadronic Rescattering Stage

Finally, the remaining hadronic interactions of the previously sampled particles are performed by `SMASH` utilizing the list modus as described in Sec. 2.1.6. As the medium gets more and more dilute, it eventually freezes out, first chemically, implying that the particle species do not change anymore, and finally kinetically, when there is no more momentum transfer between the particles.

2.3. Validation of the SMASH-vHLLE-hybrid

Before the above-described `SMASH-vHLLE-hybrid` is employed to simulate relativistic heavy-ion collisions at a range of collision energies, it is systematically validated in terms of

part of the particle list to allow for additional features. They are also excluded for the determination of the `SMASH` equation of state in Sec. 2.1.8.

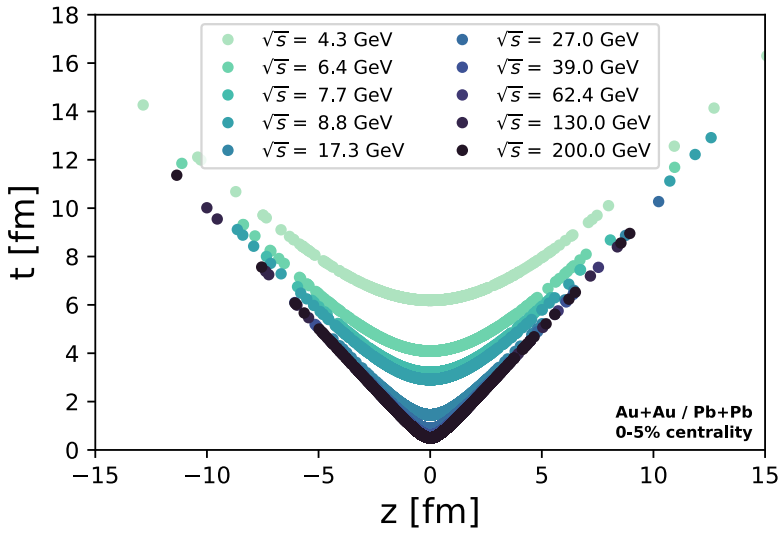

Figure 2.4.: z and t coordinates of the particles on the iso-τ hypersurface, which serves as initial conditions for the hydrodynamical evolution, as extracted from SMASH for central Au+Au/Pb+Pb collisions at different collision energies. Lighter colours correspond to lower collision energies, darker colours to higher ones.

consistency at the interfaces and quantum number conservation. In addition, results obtained with the SMASH-vHLLE-hybrid are confronted with those from other hybrid approaches consisting of (i) SMASH and CLVisc and (ii) vHLLE and UrQMD.

Owing to the modular nature of hybrid approaches, interfaces are created when switching from a microscopic description to a macroscopic one and vice versa. The first is located at the transition from SMASH to vHLLE, where the enforcement of local equilibrium at the initialization of hydrodynamics (c.f. Sec. 2.2.2) leads to discontinuities. The second results from the somewhat sharp transition from vHLLE to SMASH, where the strongly coupled fluid evolution is superseded by a hadronic transport evolution with vacuum properties. It shall be noted, that these inconsistencies represent a conceptual problem of all hybrid approaches employed for heavy-ion collisions. Yet, overcoming them is beyond the scope of this work. Nonetheless, minimal consistency within the SMASH-vHLLE-hybrid is provided by on-average quantum number conservation at the interfaces.
The results presented in this section are published in [4] and in [6].

2.3.1. Consistency at the Interfaces

SMASH → vHLLE

The fluctuating 3D initial states for the event-by-event hydrodynamical evolution are obtained from SMASH as described in Sec. 2.2.1. The transition from microscopic transport to macroscopic fluid dynamics is realized on a hypersurface of constant proper time. In the following it is verified that all particles extracted from the transport evolution are indeed located on such an iso-τ hypersurface, in which case the emission coordinates follow a

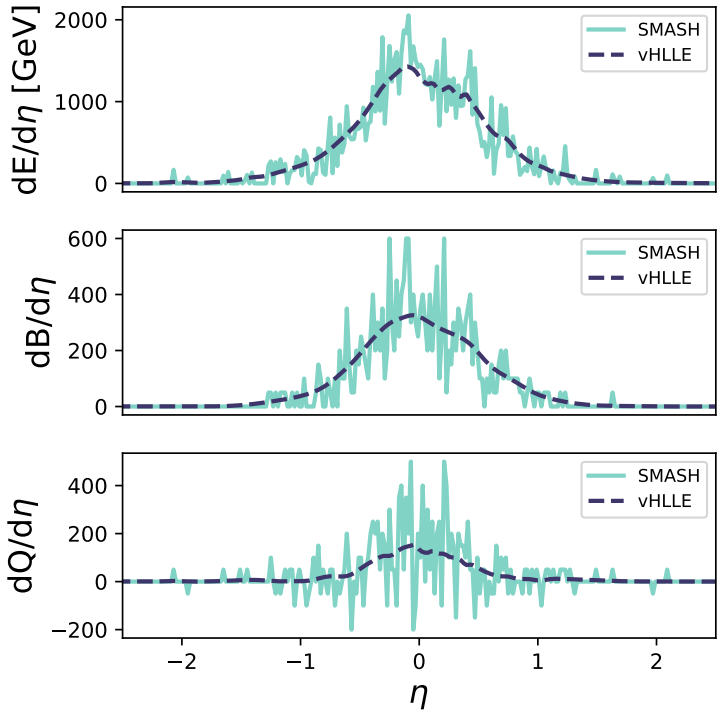

Figure 2.5.: Conserved quantities E, B and Q as a function of space-time rapidity η at the initial SMASH $\rightarrow$ vHLLE interface for one single event of a Pb+Pb collision at $\sqrt{s_{NN}} = 8.8$ GeV. The SMASH state (solid lines) is compared to the smeared state used to initialize the hydrodynamical evolution in vHLLE (dashed line). Ideal hydrodynamics is applied and spectators are excluded.

rectangular hyperbola[7] in the z-t plane. This is seen in Fig. 2.4, where the coordinates of the particles on the iso-τ hypersurface of one single SMASH event are plotted in the Cartesian z-t plane. These emission coordinates are those obtained in central Au+Au/Pb+Pb collisions ranging from $\sqrt{s_{NN}} = 4.3$ GeV to $\sqrt{s_{NN}} = 200.0$ GeV. Lighter colours denote lower, darker colours higher collision energies. Every single marker corresponds to one hadron being located on the iso-τ hypersurface. It is found that all particles corresponding to a given collision energy are indeed located on a hyperbola. Furthermore, the collisions at lower collision energies result in hyperbola characterized by larger radii of curvature and are also located further from the centre at $t = z = 0$. This is expected since collisions at lower energies result in larger values for τ_0, for which the radius of curvature is larger, and vice versa. The results presented in Fig. 2.4 thus serve as a successfully passed sanity check for the initial SMASH particle list.

The initial conditions for the hydrodynamical evolution are obtained by smearing the particles on this hypersurface as described in Sec. 2.2.2. The effect of this smearing is demonstrated in Fig. 2.5, where the $dE/d\eta$ (upper), $dB/d\eta$ (center), and $dQ/d\eta$ (lower)

[7] As described above, the transformation laws from Cartesian to Milne coordinates are provided by $\tau = \sqrt{t^2 - z^2}$ and $\eta = 0.5 \log(\frac{t+z}{t-z})$. In this case, the re-transformation is achieved with $t = \tau \cosh(\eta)$ and $z = \tau \sinh(\eta)$. With these it is straightforward to show that the hyperbolic equation for a rectangular hyperbola, $\frac{z^2 - t^2}{a^2} = 1$ is satisfied if the radius of convergence at the vertices a equals the proper time τ.

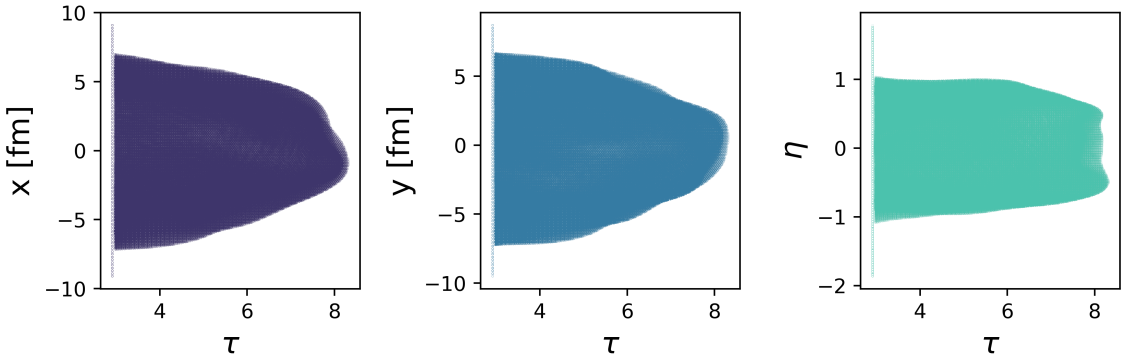

Figure 2.6.: Coordinates of the elements on the freezeout hypersurface of the hydrodynamical evolution with `vHLLE` obtained from a single hydrodynamical event in central Pb+Pb collisions at $\sqrt{s_{NN}} = 8.8$ GeV. Every marker denotes the location of one hypersurface element.

distribution is presented as a function of space-time rapidity η. Solid lines correspond to the non-smoothed initial state from the transport evolution, dashed lines to its smeared counterpart, indicating the initial condition for the hydrodynamical evolution. Note, that the results presented in Fig. 2.5 rely on one of many single `SMASH` events obtained in a Pb+Pb collision at $\sqrt{s_{NN}} = 8.8$ GeV in the event-by-event setup. Regarding the $dE/d\eta$, $dB/d\eta$, and $dQ/d\eta$ distributions in Fig. 2.5, it is observed that the spiky structure characterizing the single underlying `SMASH` event is smoothed successfully, without significant loss of quantum numbers. This validates the handling of the `SMASH` $\rightarrow$ `vHLLE` interface. It is further possible to get an idea about the magnitude of the event-by-event fluctuations present in the initial state when consulting Fig. 2.5.

vHLLE $\rightarrow$ SMASH

To validate the second interface, the properties of the freezeout hypersurface created by the `CORNELIUS` subroutine are analyzed in the following.

First, the coordinates in terms of (τ, x, y, η) of all elements on the freezeout hypersurface are collected in Fig. 2.6. In the left panel, the location of these elements in the τ-x plane is presented, in the centre panel their location in the τ-y plane, and in the right panel their location in the τ-η plane. Every circle marks the coordinates of one hypersurface element. One sees that the distribution of these marker is smooth because there are no visible holes. In addition, one observes that as proper time evolves, the volume of the medium with $e > e_{crit}$ shrinks in x, y, and η direction. This is expected from the expansion of the medium resulting in a decrease of the energy density. Furthermore, the fluctuating nature of the underlying `SMASH` event becomes apparent in all three dimensions. Based on the observed reduction of the medium's volume as well as the hole-less distribution of the freezeout hypersurface cells, one can deduce that, in combination with the fact that the `CORNELIUS` subroutine has already been tested thoroughly in [110] and was already successfully applied in other hybrid models, the freezeout hypersurface is constructed properly, also within the `SMASH-vHLLE-hybrid`.

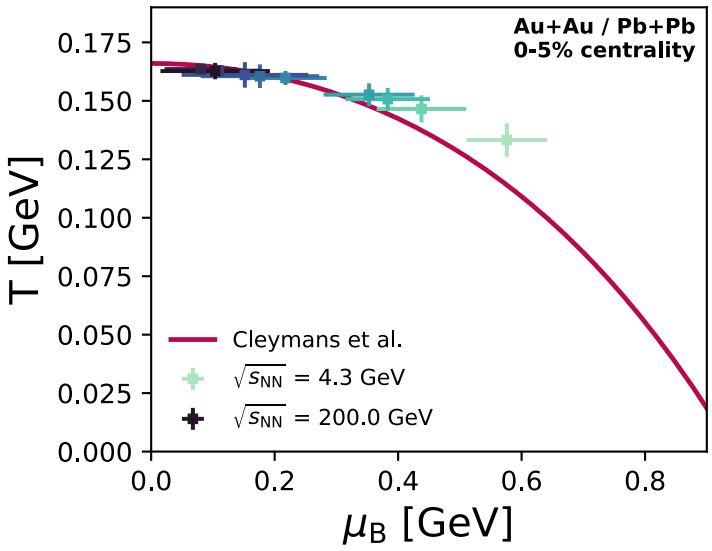

Figure 2.7.: Mean freezeout coordinates of the patches on the vHLLE freezeout hypersurface for central Au+Au/Pb+Pb collisions at $\sqrt{s_{NN}}$ = 4.3 GeV (light blue), 6.4 GeV, 7.7 GeV, 8.8 GeV, 17.3 GeV, 27.0 GeV, 39.0 GeV, 62.4 GeV, 130.0 GeV, and 200.0 GeV (dark blue). The error bars correspond to the widths of the T and μ_B distributions, the solid line to a parametrization of experimentally obtained freezeout properties, taken from [216].

Second, the vHLLE $\rightarrow$ SMASH interface is investigated by analyzing the properties of the freeze-out hypersurface elements in the T-μ_B plane. For this, the expectation values of the temperature T and the baryon chemical potential μ_B are determined from the collection of elements that make up the full freezeout hypersurface at different collision energies. Their locations in the T-μ_B plane are depicted in Fig. 2.7, where the differently coloured markers correspond to the results obtained with the SMASH-vHLLE-hybrid in central Au+Au/Pb+Pb collisions at the different energies. Lower energies are represented by lighter colours, higher energies by darker colours. The positions of the markers correspond to the mean of the T and μ_B distributions, while the vertical and horizontal bars denote their corresponding width. The mean and standard deviation are obtained by weighting each hypersurface element with its energy density via

$$\langle A \rangle = \sum_{n=0}^{N} A_n \, \frac{e_n}{\sum_{n=0}^{N} e_n} \tag{2.44}$$

$$\sigma_A = \sum_{n=0}^{N} (A_n - \langle A \rangle)^2 \, \frac{e_n}{\sum_{n=0}^{N} e_n}, \tag{2.45}$$

where A is a placeholder for the quantity of interest, that is T or μ_B, N is the total number of hypersurface elements, and e_n is the energy density of the n-th hypersurface element. The solid line in Fig. 2.7 corresponds to a parametrization of the chemical freezeout line. It is deduced from experimentally measured hadron abundances within the statistical hadroniza-

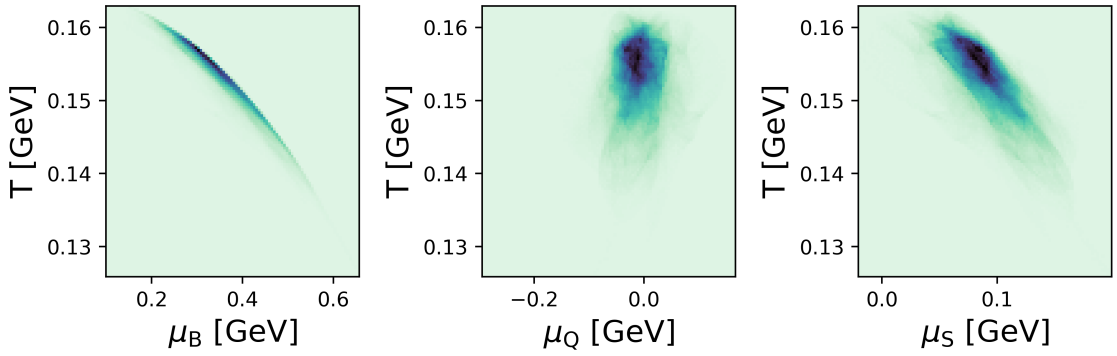

Figure 2.8.: Distribution of the hypersurface elements in the T-μ_B (left), T-μ_Q (center), and T-μ_S (right) planes in a central Pb+Pb collision at $\sqrt{s_{NN}} = 8.8$ GeV. In the darker regions, more hypersurface elements are located, in the lighter regions less.

tion model [216, 217]. It is observed that, as expected, collisions at higher energies result in a freezeout hypersurface characterized by higher temperatures and lower baryon-chemical potentials, while in the case of lower collision energies, relatively lower temperatures and higher baryon-chemical potentials are found. Furthermore, the observed energy dependence is qualitatively in accordance with the shape of the parametrization from [216, 217]. The fact that the transition from hydrodynamics to hadronic transport happens above the chemical freezeout line is expected since in the particlization process a wide range of hadrons are produced that have not yet frozen out chemically. The freezeout happens dynamically in the rescattering stage once the inelastic collisions of all hadron species have ceased. Nonetheless, the good qualitative agreement with the parametrized chemical freezeout line is considered another validation of the `SMASH-vHLLE-hybrid`.

It shall be noted, that the spread of the freezeout elements in the T-μ_B, T-μ_Q, and T-μ_S planes is significant already in single hydrodynamics events. This becomes apparent in Fig. 2.8, where the properties of the freezeout elements of a single hydrodynamical event are collected in a μ_B-T (left), μ_Q-T (center), and μ_S-T (right) diagram in terms of a two-dimensional histogram. Darker colours represent regions with more hypersurface elements, lighter colours regions with less. The presented distributions are obtained with the `SMASH-vHLLE-hybrid` in a central Pb+Pb collision at $\sqrt{s_{NN}} = 8.8$ GeV. The large spread of the freezeout elements in T, μ_B, μ_Q, and μ_S already observed in a single hydrodynamic event at a single collision energy allows deducing that a large fraction of the phase diagrams can be covered already with a limited range of beam energies. Similar observations were already made in [218].

Furthermore, it is possible to analyze the freezeout properties presented in Fig. 2.7 with respect to the centrality of the collision. This can be found in Fig. 2.9 where the markers again denote the mean and the bars the respective variance. More central collisions are represented by darker coloured markers, more peripheral collisions by lighter ones. The same collision energies as in Fig. 2.7 are presented, where the properties of lower-energy collisions are found on the lower right and those of higher-energy collisions at the upper left. The darkmost markers, corresponding to a centrality of 0-5%, are those displayed in Fig. 2.7. It is observed that the general dependence on the collision centrality, in the range from 0-5% to 40-50% most central collisions, is moderate. Especially for high-energy collisions, the freezeout

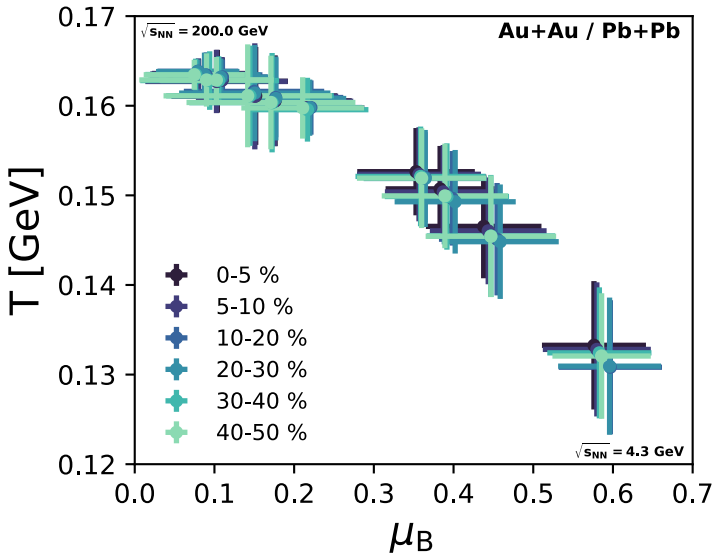

Figure 2.9.: Centrality dependence of the properties of the hydrodynamical freezeout hypersurface. More central collisions are represented by darker colours, more peripheral collisions by lighter colours. Lower collision energies can be found in the lower right corner, higher collision energies in the upper left corner.

properties are nearly unaffected by centrality variation. Towards lower collision energies, a stronger, yet small, centrality dependence is observed.

2.3.2. Global Conservation Laws

The conservation of quantum numbers throughout the different stages of a hybrid approach constitute the minimal requirement for it to be capable of describing the dynamics of heavy-ion collisions. Hence, the global and on-average conservation of quantum numbers, in terms of energy, net baryon number, and net electric charge, is evaluated in the following. This is achieved by monitoring the evolution of these quantum numbers throughout the different modules of the `SMASH-vHLLE-hybrid`. Particular emphasis is put on the necessity of the hadronic equation of state employed to create the freezeout hypersurface at the end of hydrodynamical evolution to match the hadron resonance gas according to which particles are created in the particlization process. Conservation laws cannot be fulfilled if the equation of state does not match the properties of the underlying gas of hadrons.

In Sec. 2.1.8, the `SMASH` hadron resonance gas equation of state was introduced and its deduction from the `SMASH` degrees of freedom described. The coupled Eqs. (2.22) are solved under the assumption of an ideal Boltzmann gas within the grand-canonical ensemble by means of a root solver algorithm. As described in Sec. 2.1.8, the resulting equation of state is inaccurate at low energy densities and close to the kinematic thresholds, where the algorithm has issues in converging. To circumvent this problem, an improved version of the `SMASH` equation of state was determined by varying the initial approximations, falling back to interpolations between those points where the solver succeeded, and manual fine-tuning where necessary. For details, please consult Sec. 2.1.8. In the following, two versions of the equation of state are employed

within the SMASH-vHLLE-hybrid to realize the creation of the freezeout hypersurface of vHLLE in order to assess the implications for quantum number conservation. The first equation of state relies solely on the root solver results for Eqs. (2.22), without further modification, and is thus denoted the *unmodified equation of state*. The second version of the equation of state contains all approximation and improvements, and is the one published in [206]. It is denoted the *improved equation of state*.

In Figure 2.10, the evolution of the conserved quantities energy E (upper row), baryon number B (centre row), and electric charge Q (lower row) throughout the different stages of the SMASH-vHLLE-hybrid are presented for heavy-ion collisions ranging from $\sqrt{s_{NN}} = 4.3$ GeV to $\sqrt{s_{NN}} = 200.0$ GeV. In the left column, results obtained with the *unmodified equation of state* are displayed, in the right column those obtained with the *improved equation of state*. These figures are to be understood as follows: The evolution of the conserved quantity from the initial to the final stage of the SMASH-vHLLE-hybrid is presented from left to right. The value displayed for E, B, or Q is normalized to its respective initial value to identify deviations more easily.
Quantum number conservation is enforced in SMASH; consequently there are no violations up to the SMASH $\rightarrow$ vHLLE interface.
Violations of conservation laws are observed in the vHLLE stage of the SMASH-vHLLE-hybrid, though. These are understood to stem from (i) the transition to Milne coordinates and (ii) finite grid effects upon creation of the freezeout hypersurface. Regarding the former, it shall be noted, that in its original form, that is in Cartesian coordinates, the Godunov-type algorithm employed in vHLLE preserves the total quantum numbers by construction. In Milne coordinates however, the hydrodynamic equations contain non-vanishing source terms. These are integrated numerically with finite accuracy, such that the total energy, baryon number and electric charge of the system varies a little. Typically these values increase by a few per cent within the hydrodynamical evolution [219]. The latter explanation for conservation law violations in the hydrodynamical stage is related to the handling of the hadron resonance gas equation of state in vHLLE. For lack of an appropriate parametrization (c.f. Sec.2.1.8), the SMASH hadron resonance gas equation of state is implemented in tabularized format with fixed grid points in the direction of the energy density e, baryon density n_B and charge density n_Q. Hence, multidimensional interpolations between these grid points are required to obtain the resulting thermodynamical properties. As the number of grid points in the underlying table is finite, this procedure naturally introduces small inaccuracies. At higher energy densities, the thermodynamic quantities depend relatively little on e, n_B, and n_Q such that the introduced inaccuracies are small. On the other hand, at lower energy densities, the thermodynamic quantities show a stronger dependence on e, n_B, and n_Q. Therefore, the approximation by means of interpolations is not as accurate as for higher energy densities and the resulting inaccuracies larger. Typically, the total energy, baryon number and electric charge decrease by a few per cent when constructing the freezeout hypersurface. The fact that the interpolations are differently accurate for different values of the energy density further implies that the conservation law violations caused by finite grid effects when constructing the freezeout hypersurface are larger for heavy-ion collisions at lower collision energies. At lower collision energies a larger fraction of the full medium is characterized by smaller energy densities such that the relative contribution of inaccurate evaluations of the equation of state is larger. This effect can be observed in Fig. 2.10, where the loss of total energy, baryon number and electric charge in the vHLLE stage is largest for collisions with the lowest collision energy, that is $\sqrt{s_{NN}} = 4.3$ GeV. In addition, the

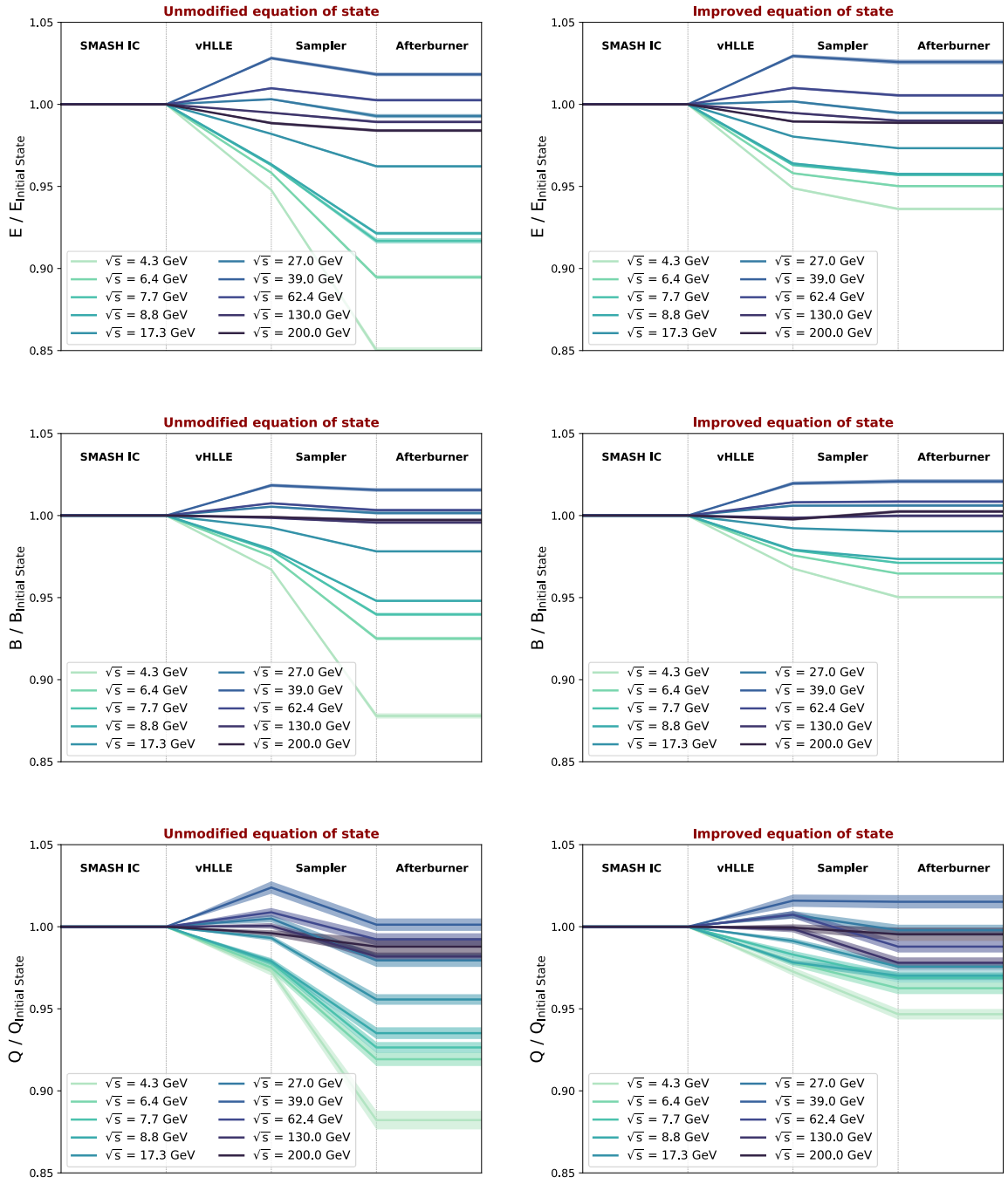

Figure 2.10.: Conservation of total energy (upper panel), baryon number (centre panel) and electric charge (lower panel) throughout all stages of the `SMASH-vHLLE-hybrid`. The leftmost ends corresponds to the initial state, the rightmost ends to the final state. The left column of plots originates from a setup with the *unmodified equation of state*, while for the right column of plots the *improved equation of state* of the `SMASH` hadron resonance gas was used. See Sec. 2.1.8 for further details about these equations of state. Note, that for this study ideal hydrodynamics is employed.

SMASH equation of state is only valid above $e = 0.01$ GeV/fm^3. At the initialization of the hydrodynamical evolution a small fraction of cells, typically located at the borders of the fireball, is characterized by an energy density $e \leq 0.01$ GeV/fm^3, which is below the range of applicability of the SMASH hadron resonance gas equation of state (c.f. Sec. 2.1.8). Lacking possibilities to assign thermodynamic quantities $(T, p, \mu_B, \mu_Q, \mu_S)$ to these cells, we have decided to neglect their contribution for the sake of not introducing additional uncertainties. Naturally, this treatment results in loss of E, B, and Q, which becomes more severe the lower the collision energy, as relatively more cells are characterized by small energy densities. It is however verified, that at most 1.57% of the total energy, 0.74% of the total baryon number, and 0.29% of the total electric charge are lost in Au+Au collisions at $\sqrt{s_{NN}} = 4.3$ GeV, which is where the fraction of cells with $e \leq 0.01$ GeV/fm^3 is the largest. It shall further be noted, that both effects, the increase of quantum numbers due to numerical inaccuracies when integrating the source terms in Milne coordinates on the one side and the decrease due to finite grid effects when evaluating the equation of state on the other side, are present at all collision energies and partially counteract each other. In summary, the total energy, baryon number and electric charge are violated by no more than 5.5%, 3.5%, and 2.5% in the vHLLE stage, respectively.
In the next stage, the sampling process, the effect of a mismatch in the hadronic equation of state applied to construct the freezeout hypersurface in vHLLE becomes apparent. While for the *unmodified equation of state* (left column in Fig. 2.10), severe violations of global energy, baryon number and charge conservation are observed, those quantum numbers are approximately conserved when relying on the *improved equation of state* (right column in Fig. 2.10). It is further found that the violation of conservation laws in the setup with the *unmodified equation of state* get more severe the lower the collision energy. This is related to the fact that the *unmodified equation of state* is especially troublesome at low energy densities. The lower the collision energy, the larger the fraction of cells falling into the problematic region, such that their relative contribution to the total quantum numbers E, B and Q is higher. Comparing the energy, baryon number and charge violations observed in the sampling stage of the vHLLE hybrid between the left column (*unmodified equation of state*) and the right column (*improved equation of state*) in Fig. 2.10 it can be stated that with the *unmodified equation of state* the total energy is undersampled by $\approx 10\%$ and the total baryon number and electric charge by ≈ 9 %, while with the *improved equation of state* the energy and baryon number are sampled with a precision of 2% or more, the electric charge with a precision of 3% or more. The reader is reminded that although the *improved equation of state* is much more accurate in characterizing the SMASH hadron resonance gas than the *unmodified equation of state*, it still constitutes an approximation at lower energy densities (c.f. Sec. 2.1.8). This explains the violation of quantum number conservation observed in the sampling process of the SMASH-vHLLE-hybrid, which are of the order of those detected in the hydrodynamical stage, even when relying on the *improved equation of state*. The results in Fig. 2.10 demonstrate that a well matching hadronic equation of state at the particlization interface is of fundamental importance to fulfill conservation laws in a hydrodynamics+transport approach.
Finally, perfect quantum number conservation is observed for the hadronic rescattering stage, i.e. afterburner stage, which is again related to the fact that this property is enforced in SMASH.

In summary, for the entire evolution of the system within the SMASH-vHLLE-hybrid, violations of quantum number conservation by at most 7% are found for collisions between $\sqrt{s_{NN}} = 4.3$ GeV and $\sqrt{s_{NN}} = 200.0$ GeV, which is considered an overall good validation of

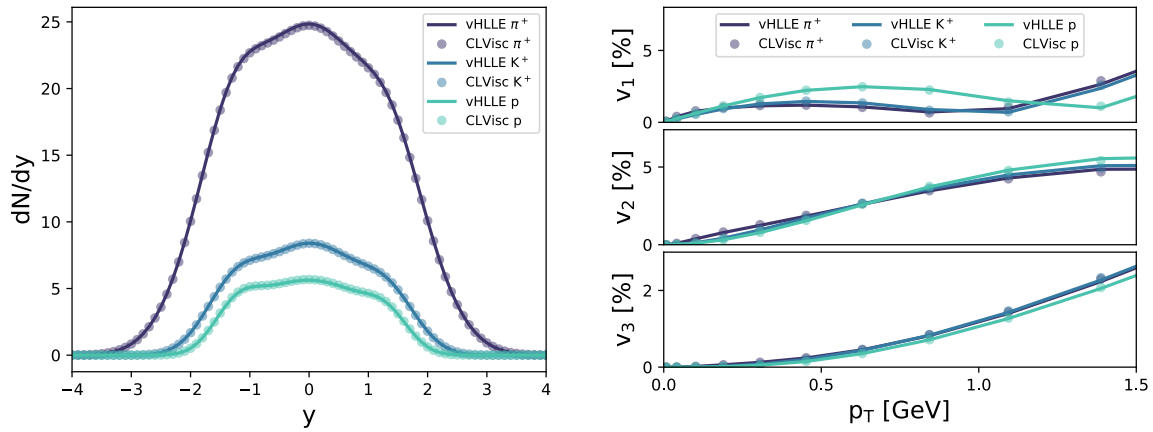

Figure 2.11.: Comparison of the dN/dy spectrum (left) and anisotropic flow coefficients (right) of pions, protons and kaons as obtained from directly evaluating the Cooper-Frye formula on the `vHLLE` and the `CLVisc` freezeout hypersurfaces. An identical `SMASH` initial state is used, as well as identical smearing parameters and equations of state.

the presented approach. It shall be noted, though, that the herein presented results correspond to global and on-average conservation of the quantities E, B, and Q, which constitutes the minimal requirement. Alternative approaches allowing for event by event conservation of quantum numbers include, for example, [220, 221].

2.3.3. Comparison to a SMASH+CLVisc Hybrid Approach

Another validation of the `SMASH-vHLLE-hybrid` with respect to the hydrodynamical evolution and the creation of the freezeout hypersurface is performed by comparing the outcome of the `SMASH-vHLLE-hybrid` to results obtained with a hybrid approach coupling the initial conditions from `SMASH` to a hydrodynamical evolution by means of `CLVisc` [106, 222]. Just as `vHLLE`, `CLVisc` is a 3+1D viscous hydrodynamics model aiming at the description of relativistic heavy-ion collisions. For consistency, both evolutions rely on the identical initial state from a single `SMASH` event in a Pb+Pb collision at $\sqrt{s_{NN}} = 8.8$ GeV. For an adequate comparison, contributions in the corona region[8] are neglected, since they are treated differently in `vHLLE` and `CLVisc`. For the Gaussian smearing, $R_\eta = 1.0$ and $R_\perp = 1.4$ are applied and for simplification, ideal hydrodynamics with $\eta/s = 0$ is used. The evolution relies on a chiral model equation of state [80]. We refrain from switching to the `SMASH` equation of state for the creation of the freezeout hypersurface since for this qualitative study, the Cooper-Frye formula is evaluated directly on the freezout hypersurface, making the switching of the equation of state superfluous as neither particlization, nor the afterburner evolution are performed.
The results obtained in both approaches are presented in Fig.2.11, where the rapidity spectra of pions, kaons and protons can be found on the left and their anisotropic flow coefficients v_1, v_2, and v_3 on the right. Results obtained with `SMASH+vHLLE` are denoted with solid lines, those obtained with `CLVisc+vHLLE` with filled circles. A perfect agreement is observed for the longitudinal multiplicity distribution as well as the anisotropic flow coefficients for all

[8] The corona region denotes the collection of cells whose energy density is below the critical energy density already at the initialization of the hydrodynamical evolution. These cells are directly written to the freezeout hypersurface and are not further propagated in the hydrodynamical evolution.

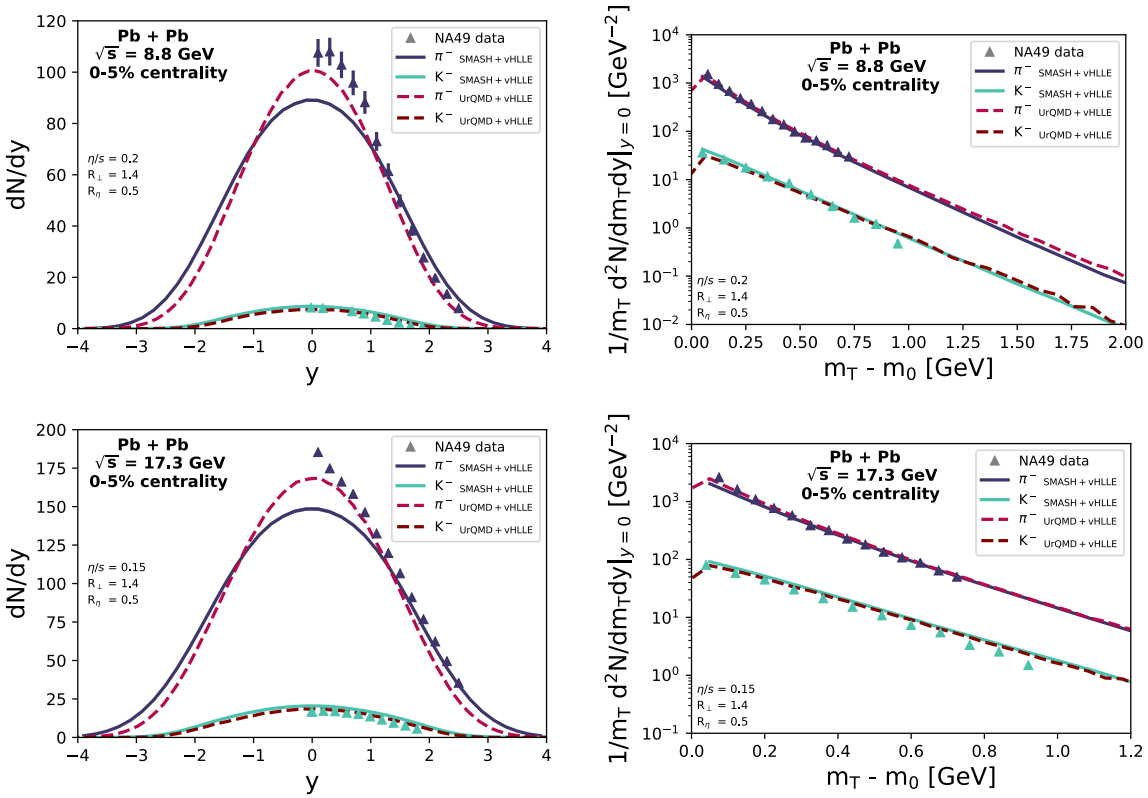

Figure 2.12.: Comparison of the dN/dy spectra (left) and m_T spectra (right) in central Pb+Pb collisions at $\sqrt{s_{NN}}$ = 8.8 GeV (upper) and 17.3 GeV (lower) between the `SMASH-vHLLE-hybrid` (solid lines) and the `UrQMD+vHLLE` hybrid (dashed) for π^- and K^-. Results for the `UrQMD+vHLLE` hybrid are taken from [59]. Identical smearing parameters and viscosities are applied. The experimental NA49 data is taken from [223–226].

three particle species. This finding is considered another validation of the presented model, in particular regarding the hydrodynamical evolution. Moreover, it is reassuring to see that both fluid dynamics codes, which have been thoroughly tested, lead to identical results when relying on identical initial conditions.

2.3.4. Comparison to a UrQMD+vHLLE Hybrid Approach

The final validation of the `SMASH-vHLLE-hybrid` consists of comparing its outcome to results obtained in a `UrQMD+vHLLE` hybrid approach which was successfully applied to study heavy-ion collisions between $\sqrt{s_{NN}}$ = 7.7 GeV and $\sqrt{s_{NN}}$ = 200.0 GeV [59]. The `UrQMD+vHLLE` hybrid approach is constructed similarly to the `SMASH-vHLLE-hybrid`. It relies on a 3D initial state extracted at constant proper time from `UrQMD`, the hydrodynamical evolution is performed with `vHLLE`, and `UrQMD` again realizes the hadronic rescatterings. Effectively, the only difference between the `UrQMD+vHLLE` hybrid approach and the `SMASH-vHLLE-hybrid` is the transport model employed for the hadronic stages. Although `UrQMD` and `SMASH` are conceptually similar, there are small differences regarding the degrees of freedom, cross sections, or in the application of Pythia to perform the string excitations. In particular the latter is important to properly model the baryon stopping dynamics at intermediate and high collision energies

[172].
In Fig. 2.12, the rapidity distributions (left column) and transverse mass spectra (right column) of π^- and K^- are presented. Results for Pb+Pb collisions at $\sqrt{s_{NN}} = 8.8$ GeV can be found in the upper row, those at $\sqrt{s_{NN}} = 17.3$ GeV in the lower row. Results from the `SMASH-vHLLE-hybrid` are represented by solid lines, those from the `UrQMD+vHLLE` hybrid by dashed lines (taken from [59]). For consistency, identical smearing parameters and viscosities are applied to model the hydrodynamical evolution in both cases. Note, that these differ from the ones listed in Table 2.2 below, where the default smearing parameters of the `SMASH-vHLLE-hybrid` are collected. The applied values within this validation study are indicated directly on the figures. It is found that the dN/dy distribution of pions from the `SMASH-vHLLE-hybrid` is wider than the one from the `UrQMD+vHLLE` hybrid, but peaks at lower mid-rapidity yields. This is observed for both collision energies. Furthermore, the shapes of the kaon dN/dy distributions are similar, but the `UrQMD+vHLLE` hybrid produces smaller kaon yields than the `SMASH-vHLLE-hybrid`. The m_T spectra of both approaches are in good agreement, only at low transverse masses small differences are observed which are in line with those made in the dN/dy spectra.
In summary, it is reassuring that both hybrid approaches provide similar results in terms of dN/dy and m_T spectra. This serves as another validation of the novel hybrid approach introduced in this work and provides some hints towards differences between the `SMASH` and `UrQMD` transport approaches.

2.4. Hadron Production with the SMASH-vHLLE-hybrid

In this section, the `SMASH-vHLLE-hybrid` introduced above is applied to model relativistic heavy-ion collisions ranging from $\sqrt{s_{NN}} = 4.3$ GeV to $\sqrt{s_{NN}} = 200.0$ GeV. Particular emphasis is put on collisions at low and intermediate collision energies, that is at $\sqrt{s_{NN}} = 4.3$, 7.7, and 17.3 GeV, which are expected to provide access to specifically this region of the QCD phase diagram where a first order phase transition and critical end point are expected (c.f. Sec. 1.2). This region of the QCD phase diagram is experimentally studied within the NA61/SHINE experiment at CERN [25], the BESII program at BNL [24] as well as at future FAIR [27], NICA [28] and J-PARC-HI [227] facilities. It shall be noted, that the `SMASH-vHLLE-hybrid` is not the first hybrid approach employed to model heavy-ion collisions at these intermediate collisions energies. Previous works relying on different initial conditions, hydrodynamic evolutions and hadronic transport approaches include for instance [55, 57, 59, 63]. However, these have either not been applied below $\sqrt{s_{NN}} = 7.7$ GeV or have issues properly reproducing the experimentally observed baryon stopping dynamics at low collision energies. Yet, it is crucial to correctly capture the baryon stopping dynamics in order to accurately model the evolution at low and intermediate collision energies. Furthermore, studies regarding fluctuations of conserved charges can only be conducted properly once the baryon dynamics are reasonably well reproduced. It shall further be noted, that recent progress in terms of modelling heavy-ion collisions at low collisions energies was made in [114, 153, 154], where frameworks towards a more dynamical initialization of the hydrodynamic stage were introduced. This is of greater importance the lower the collision energy and hence the longer-lived the initial state.
The results presented in this section are published in [6].

$\sqrt{s_{NN}}$ [GeV]	4.3	6.4	7.7	8.8	17.3	27.0	39.0	62.4	130.0	200.0
η/s	0.2	0.2	0.2	0.2	0.15	0.12	0.08	0.08	0.08	0.08
$R_\perp$	1.4	1.4	1.4	1.4	1.4	1.0	1.0	1.0	1.0	1.0
R_η	1.3	1.2	1.2	1.0	0.7	0.4	0.3	0.6	0.8	1.0

Table 2.2.: Shear viscosities (η/s), transverse Gaussian smearing parameters ($R_\perp$), and longitudinal Gaussian smearing parameters (R_η) applied in this work for the hydrodynamical evolution at different collision energies. Note, that Pb+Pb collisions are simulated at $\sqrt{s_{NN}}$ = 6.4, 8.8, 17.3 GeV, Au+Au collisions at $\sqrt{s_{NN}}$ = 4.3, 7.7, 27.0, 39.0, 62.4, 130.0, 200.0 GeV.

Centrality Class	0-5 %	5-10 %	10-20 %	20-30 %	30-40 %	40-50 %
b [fm] (Au+Au)	0 - 3.3	3.3 - 4.6	4.6 - 6.5	6.5 - 7.9	7.9 - 8.5	8.5 - 10.3
b [fm] (Pb+Pb)	0 - 3.1	3.1 - 4.5	4.5 - 6.6	6.6 - 8.2	8.2 - 9.5	9.5 - 10.6

Table 2.3.: Impact parameter ranges b applied in this work within the `SMASH-vHLLE-hybrid` to model Au+Au collisions and Pb+Pb collisions at different centrality classes from 0-5% to 40-50% most central collisions.

2.4.1. Configuration Details: Viscosities, Smearing Parameters, and Impact Parameters

As described in Sec. 2.2.2, there is some ambiguity in choosing the magnitude of the transversal and longitudinal smearing parameters employed at the initialization of the hydrodynamical evolution. These parameters are not well-constrained; they are rather deduced by manually tuning them to improve the agreement with experimentally measured hadron spectra. Concretely, the dN/dy and m_T spectra of pions, protons and kaons are consulted to find the most suitable combination of $R_\perp$ and R_η at each collision energy. For the shear viscosities, we rely on the values obtained within [59]. Bulk viscous corrections are neglected for the studies presented in this section. The shear viscosities η/s, transverse Gaussian smearing parameters $R_\perp$, and longitudinal Gaussian smearing parameters R_η applied within the `SMASH-vHLLE-hybrid` at a range of collision energies between $\sqrt{s_{NN}}$ = 4.3 GeV to $\sqrt{s_{NN}}$ = 200.0 GeV are presented in Table 2.2. Note, that Pb+Pb collisions are simulated for $\sqrt{s_{NN}}$ = 6.4, 8.8, and 17.3 GeV, while Au+Au collisions are simulated at all other energies. This is to be in agreement with the experiments performed at the different collider facilities.
Furthermore, the collisions simulated with the `SMASH-vHLLE-hybrid` are performed at a range of different impact parameters to also study the centrality dependence of the final state observables. For each centrality class, the initial conditions are extracted from `SMASH` relying on a specific range for the impact parameter. The impact parameters employed for these studies are determined with the Glauber model [65, 66, 145] and are listed in Table 2.3.

The `SMASH-vHLLE-hybrid` is employed as follows: `SMASH` is executed 100 times for a given collision system to provide the initial conditions for 100 event-by-event hydrodynamics simulations. 1000 events for the hadronic rescattering stage are further sampled from each hydrodynamical freezeout hypersurface and evolved in the afterburner stage. The code versions `SMASH-vHLLE-hybrid:a1f823a`, `SMASH-2.0.2`, `vHLLE:bce38e0`, `vhlle_params:99ef7b4`, and `SMASH-hadron-sampler-1.0` are used throughout this work.

2.4.2. Particle Spectra: Rapidity and Transverse Mass Spectra

The SMASH-vHLLE-hybrid is applied to model Au+Au and Pb+Pb collisions at low and intermediate collision energies, that is Au+Au collisions at $\sqrt{s_{NN}} = 4.3$ GeV ($E_{lab} = 8$ AGeV) and at $\sqrt{s_{NN}} = 7.7$ GeV ($E_{lab} = 30$ AGeV), and Pb+Pb collisions at $\sqrt{s_{NN}} = 17.3$ GeV ($E_{lab} = 158$ AGeV). The viscosities and smearing parameters applied for the hydrodynamical evolution are those listed in Table 2.2. An impact parameter range of $b \in [0, 3.3]$ fm in the case of Au+Au collisions and of $b \in [0, 3.1]$ fm in the case of Pb+Pb collisions is used as a proxy for 0-5% most central collisions. In Fig. 2.13 the dN/dy spectra (left column) and m_T spectra (right column) of π^-, p, and K^- in Au+Au/Pb+Pb collisions are presented at these collision energies. Results for $\sqrt{s_{NN}} = 4.3$ GeV can be found in the upper row, those for $\sqrt{s_{NN}} = 7.7$ GeV in the centre row, and those for $\sqrt{s_{NN}} = 17.3$ GeV in the lower row. The obtained particle spectra are compared to results obtained with a pure transport evolution via SMASH to assess the implications of an intermediate hydrodynamical stage. These are denoted by dashed lines while solid lines mark the results obtained with the SMASH-vHLLE-hybrid. Where available, the obtained spectra are further confronted with experimental data from the E866 [228, 229], STAR [230], and NA49 [223–226] collaborations.
With regards to the dN/dy spectra it is observed that, across all collision energies, the application of a hybrid model instead of a pure transport evolution decreases the pion yield and enhances the kaon production. The agreement with experimental measurements for π^- and K^- is improved. This observation is in line with those made in previous works, e.g. [59, 63, 114]. It is further found that the longitudinal dynamics of protons are qualitatively captured properly across all three collision energies, that is the rising impact of baryon transparency for higher collision energies [231]. The SMASH-vHLLE-hybrid is successful at describing the single-peak structure observed at $\sqrt{s_{NN}} = 4.3$ GeV as well as the double-peak structure at $\sqrt{s_{NN}} = 7.7$ GeV and $\sqrt{s_{NN}} = 17.3$ GeV. It is thus capable of reproducing the experimentally observed magnitude of baryon stopping at intermediate collision energies. The agreement with experimental data for proton dN/dy spectra is improved significantly once the SMASH-vHLLE-hybrid is employed instead of a pure transport evolution. Yet, the agreement is not perfect. Note, that within the SMASH-vHLLE-hybrid, finite baryon diffusion [153, 154] is not yet accounted for in the hydrodynamical stage. It will have an impact on the proton rapidity distribution which might alleviate the discrepancy. This effort is left for future work. Nonetheless, the qualitative (and almost quantitative) agreement of the proton rapidity distribution with experimental measurements over a large range of beam energies is considered an important pre-requisite for further studies of phase transition signals with the SMASH-vHLLE-hybrid.
Regarding the dN/dm_T spectra in Fig. 2.13 (right column), across all collision energies probed, a significant hardening of the π^-, p, and K^- spectra is observed when employing the SMASH-vHLLE-hybrid instead of a pure transport evolution with SMASH. This is again in line with observations made in other studies with hybrid approaches [59, 63]. The hardening of the dN/dm_T spectra in the hybrid setup noticeably improves the agreement with experimental measurements compared to a pure transport evolution for all collision energies in Fig. 2.13, in particular regarding the slopes of the dN/dm_T distributions.

Summarizing the findings from Fig. 2.13, the SMASH-vHLLE-hybrid is successful at describing the dN/dy and dN/dm_T spectra of π^-, p, and K^- in Au+Au/Pb+Pb collisions performed at $\sqrt{s_{NN}} = 4.3$, 7.7 and 17.3 GeV. A decent agreement with experimental measurements at these collision energies is obtained. Furthermore, the baryon stopping power is well reproduced at the above-listed energies, thus demonstrating that the longitudinal baryon dynamics are

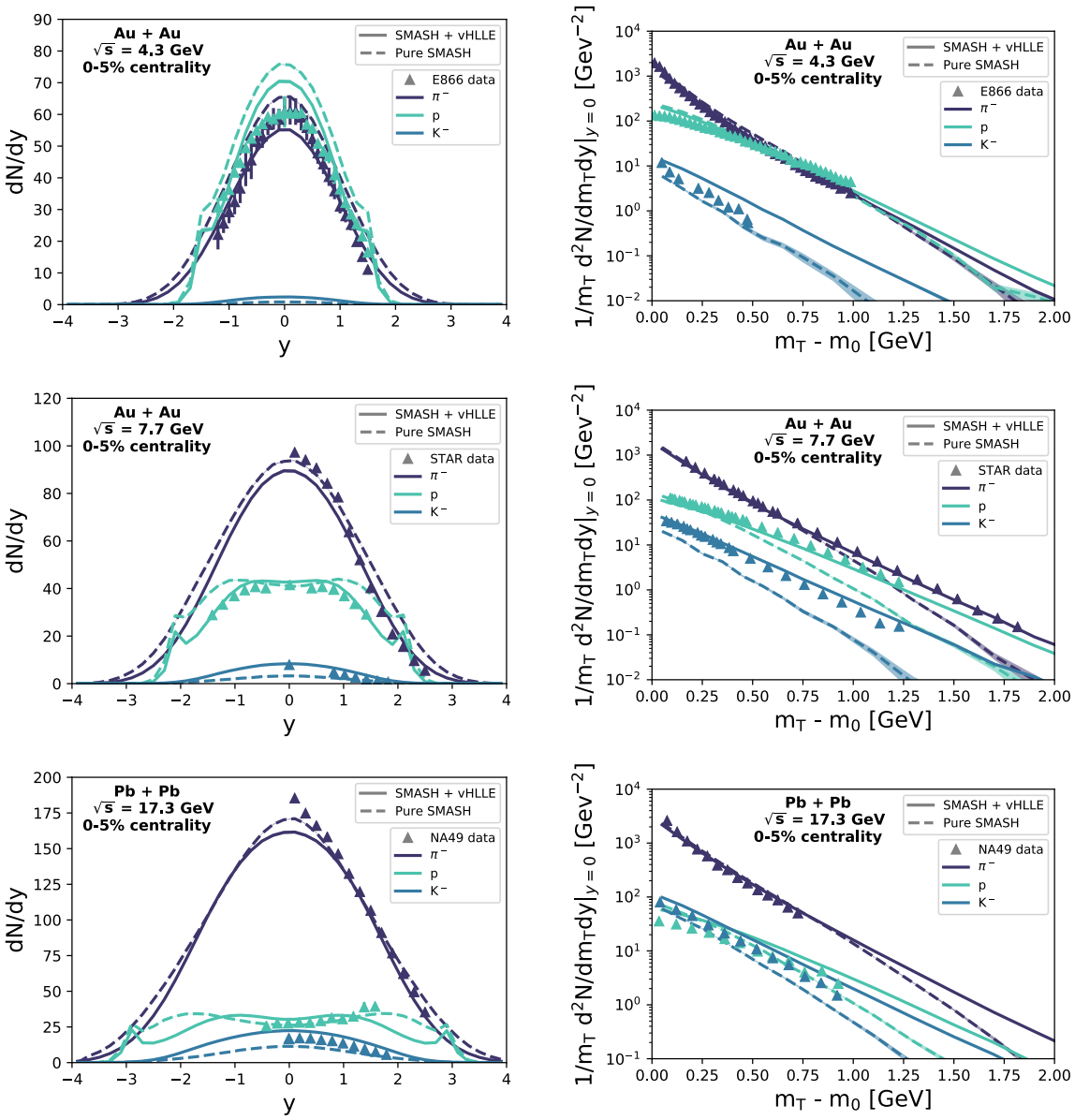

Figure 2.13.: dN/dy spectra (left) and m_T spectra (right) of π^-, p, and K^- for central Au+Au/Pb+Pb collisions at $\sqrt{s_{NN}}$ = 4.3 GeV (upper), $\sqrt{s_{NN}}$ = 7.7 GeV (center), and $\sqrt{s_{NN}}$ = 17.3 GeV (lower). The results obtained within the `SMASH-vHLLE-hybrid` (solid lines) are compared to those obtained when running only `SMASH` (dashed lines). The E866 data is taken from [228, 229], the STAR data from [230], and the NA49 data from [223–226]. Results for additional collision energies can be found in C.

captured properly.
It shall be noted, that similar observations are also made for Au+Au/Pb+Pb collisions at a range of other collision energies. For completeness, the corresponding figures can be found in App. C.

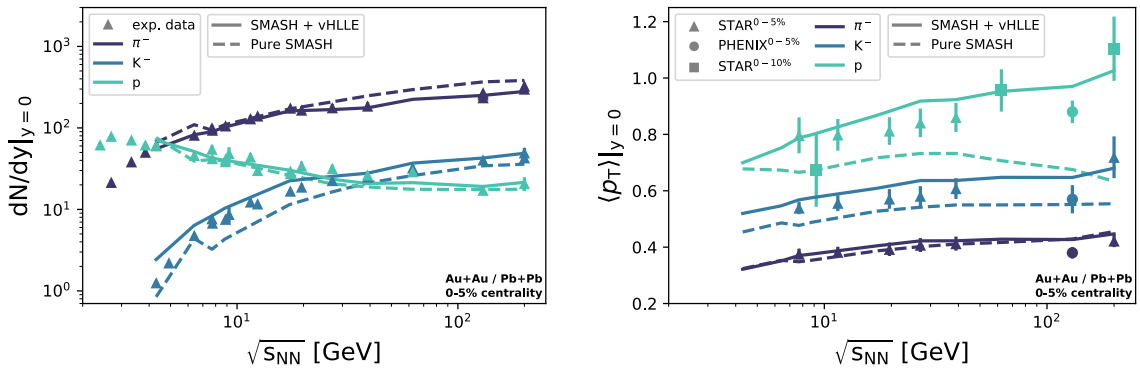

Figure 2.14.: Mid-rapidity yield (left) and mean p_T (right) excitation functions as extracted from the SMASH-vHLLE-hybrid (solid lines) in comparison to a pure SMASH evolution (dashed lines) and to experimental data collected from [223, 226, 228, 230, 232–235].

2.4.3. Excitation Functions

Excitation functions are a useful means to study the energy-dependence of an observable. In this section, excitation functions for the mid-rapidity yield $dN/dy|_{y=0}$ and the mean transverse momentum $\langle p_T \rangle$ of π^-, p, and K^- is investigated for Au+Au/Pb+Pb collisions between $\sqrt{s_{NN}}$ = 4.3 GeV and $\sqrt{s_{NN}}$ = 200.0 GeV. The reproduction of the yield and of the mean transverse momentum is almost equivalent to reproducing these species' full transverse mass spectra. The results obtained with the SMASH-vHLLE-hybrid are again compared to those from a pure transport evolution via SMASH and confronted with experimental data, where available. Also, the viscosities and smearing parameters employed are again those listed in Tab. 2.2 and the impact parameter ranges for the different centralities probed can be found in Tab. 2.3.

In Fig. 2.14, the mid-rapidity yield excitation function is presented on the left and the mean transverse momentum excitation function on the right. They are presented as a function of collision energy $\sqrt{s_{NN}}$. Solid lines denote results from the SMASH-vHLLE-hybrid, with an intermediate hydrodynamical stage, dashed lines results from SMASH relying on a pure transport evolution. The markers indicate experimental data measured by the E895 [228, 232], E866 [235], NA49 [223, 226, 234], and STAR [230, 233] collaborations.

The $dN/dy|_{y=0}$ excitation functions determined within the SMASH-vHLLE-hybrid are in good agreement with experimental measurements. It is nearly perfect for the measured π^- and p yields, but the K^- yields are systematically overestimated. This could be improved by employing more dynamical initial conditions, as recently realized in [114]. It is further found that the excitation functions from the SMASH-vHLLE-hybrid show a smooth behaviour for rising collision energies, while a kink is observed between $\sqrt{s_{NN}}$ = 6 GeV and $\sqrt{s_{NN}}$ = 8 GeV in the pure SMASH case. This kink is unphysical and stems from the non-trivial transition from resonance dynamics to string dynamics within SMASH. It can thus be deduced that the SMASH-vHLLE-hybrid is better suited to smoothly and consistently describe the dynamics at intermediate collision energies.

Regarding the $\langle p_T \rangle|_{y=0}$ excitation functions displayed in the right panel of Fig. 2.14 the agreement with experimental data is also improved once a hybrid model is applied instead of a pure transport evolution. Most importantly, the $\langle p_T \rangle$ of protons rises with rising collision energies, which is in line with experimental observations, while in the pure SMASH case it decreases

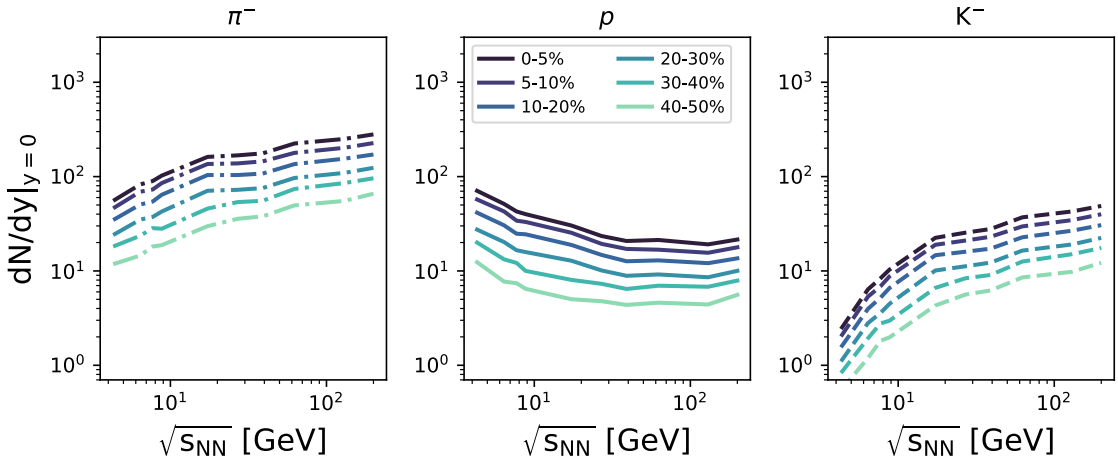

Figure 2.15.: Mid-rapidity yield excitation functions of π^- (left), p (center), and K^- (right) for different centrality classes as obtained in Au+Au/Pb+Pb collisions with the `SMASH-vHLLE-hybrid`. Darker colours correspond to more central collisions, lighter colours to more peripheral collisions.

for collisions above $\sqrt{s_{NN}} \approx 30$ GeV. The application of a hybrid model is thus essential to properly capture the transversal baryon dynamics, especially towards higher collision energies.

Centrality Dependence

In addition, it is possible to study the dependence of these excitation functions on the centrality of the collisions. This study is conducted for results obtained within the `SMASH-vHLLE-hybrid` for six different centrality classes ranging from 0-5% to 40-50% most central collisions (c.f. Tab. 2.3 for corresponding impact parameters).

In Fig. 2.15 the mid-rapidity yield excitation functions as obtained in Au+Au/Pb+Pb collisions between $\sqrt{s_{NN}} = 4.3$ GeV and $\sqrt{s_{NN}} = 200.0$ GeV with the `SMASH-vHLLE-hybrid` are presented for different centrality classes. The π^- excitation functions are found on the left, those for p in the center, and those for K^- on the right. More central collisions are represented by darker colours, more peripheral collisions by lighter colours. It is observed that the general shapes of the excitations functions for π^-, p, and K^- are independent of the centrality of the collision. Their magnitudes show a significant but systematic centrality dependence though. The more peripheral the collision, the lower the resulting yield. This is not surprising as the overlap region and hence the effective volume of the hot and dense fireball is smaller in less central collisions.
The centrality dependence of the pion, proton and kaon $\langle p_T \rangle$ is further presented in Fig. 2.16. Again, more central collisions are represented by darker colours, more peripheral collisions by lighter colours. Results for π^- are displayed by dashed-dotted lines, p by solid lines, and K^- by dashed lines. It is observed that the $\langle p_T \rangle$ excitation functions of all three particle species generally depend little on the centrality of the collision, yet more peripheral collisions result in smaller mean transverse momenta of pions, protons and kaons. This is again related to the smaller effective volume created in peripheral as compared to central collisions. The centrality dependence increases with decreasing collision energies and is most pronounced in

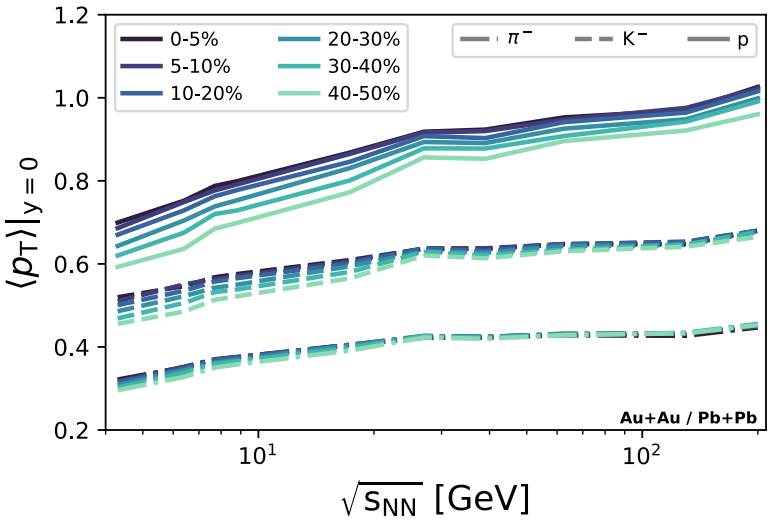

Figure 2.16.: Mean transverse momentum excitation functions of π^- (dashed-dotted), p (solid), and K^- (dashed) for different centrality classes as obtained in Au+Au/Pb+Pb collisions with the `SMASH-vHLLE-hybrid`. Darker colours correspond to more central collisions, lighter colours to more peripheral collisions.

the case of protons and least pronounced in the case of pions.

2.4.4. Collective Flow

The anisotropic flow created in Au+Au/Pb+Pb collisions at different collision energies and centralities is analyzed. For this, the integrated elliptic flow v_2 and the integrated triangular flow v_3 of charged particles are determined within the `SMASH-vHLLE-hybrid` for collision energies between $\sqrt{s_{NN}} = 4.3$ GeV and $\sqrt{s_{NN}} = 200.0$ GeV and for centralities ranging from 0-5% to 40-50%. The corresponding impact parameter ranges are those listed in Tab. 2.3. The event plane method, which is explained in App. A.4.1, is employed to obtain v_2 and v_3. The outcome is compared to experimental data from the STAR collaboration [236]. Note, that the STAR results are determined from two-particle correlations, the comparison is therefore not perfectly equivalent. Yet, it has been shown that both methods yield similar results [237]. The integrated charged particle v_2 (left) and v_3 (right) as a function of collision energy are presented in Fig. 2.17, where solid lines denote the outcome of the `SMASH-vHLLE-hybrid` and the markers the results measured by the STAR collaboration. Again, more central collisions are represented by darker colours, more peripheral collisions by lighter colours.
It is observed that for central collisions, the v_2 extracted from the `SMASH-vHLLE-hybrid` is in decent agreement with measurements from STAR across all collision energies, while for more peripheral collisions the agreement is good at high collision energies, but the measured v_2 is significantly underestimated towards lower collision energies. Furthermore, it becomes apparent that the v_2 determined from the `SMASH-vHLLE-hybrid` in 20-30%, 30-40% and 40-50% most central collisions is characterized by a clear kink around $\sqrt{s_{NN}} \approx 40.0$ GeV and decreases much more than in more central collisions when moving towards lower collision energies. This observation is related to a too short lifetime of the hot and dense fireball in

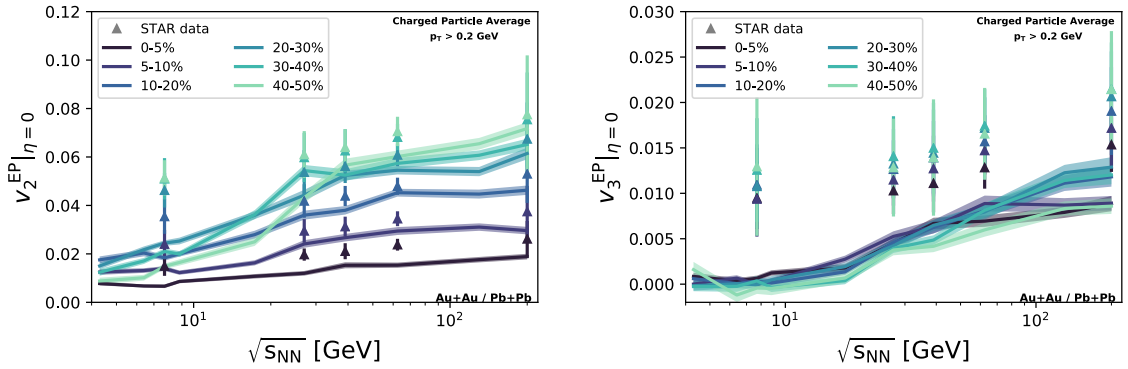

Figure 2.17.: Integrated v_2 (left) and integrated v_3 (right) excitation functions of charged particles at mid-rapidity as a function of collision energy, obtained with the `SMASH-vHLLE-hybrid` in Au+Au/Pb+Pb collisions. More central collisions are marked by darker colours, more peripheral collisions by lighter colours. The STAR data is taken from [236].

the hydrodynamical stage. This lifetime of the hydrodynamical stage τ_{hydro} is presented as a function of collision energy for different centralities in Fig. 2.18. Again, darker colours denote more central collisions, lighter colours more peripheral collisions. It is determined via

$$\tau_{\text{hydro}} = \langle\, \tau_{\text{end}} \,\rangle_{\text{events}} \;-\; \tau_0 \tag{2.46}$$

with τ_0 being the proper time at initialization of hydrodynamics and τ_{end} the proper time at which the last cell falls below the critical energy density. $\langle\ \rangle_{\text{events}}$ denotes the average over all events. It is observed that for increasing centralities, the lifetime of the fireball decreases continuously. This is expected from the geometrically smaller overlap region in less central collisions resulting in smaller volumes and thus shorter-lived fireballs. Furthermore, it becomes evident that the hydrodynamical lifetime is nearly independent of the collision energy above $\sqrt{s_{NN}} \approx 50$ GeV. Below $\sqrt{s_{NN}} \approx 50$ GeV however, the lifetime is reduced substantially with decreasing collision energies. This implies, that especially in peripheral collisions at low and intermediate collision energies, the hydrodynamical evolution lasts only a few fm/c, which is seemingly too short for collective dynamics to develop. The resulting v_2 is thus significantly underestimated. This underestimation might be alleviated by implementing more dynamical initial conditions better suited to capture the underlying dynamics at low collision energies, similar to recent efforts made in [114].
In the case of the integrated charged particle triangular flow v_3 on the other hand (c.f. right panel of Fig. 2.17), the experimentally obtained v_3 is underestimated across the entire energy range and for all centralities by the `SMASH-vHLLE-hybrid`. This observation might be related to the Gaussian smearing kernel employed at initialization of hydrodynamics to generate smooth density profiles (c.f. Sec. 2.2.2). Initial state fluctuations, which are responsible for the generation of v_3, might thus be smeared too much and the resulting v_3 is underestimated. Additionally, as detailed above, the too short hydrodynamical evolution could also be responsible for an underestimation of the integrated v_3.

It can generally be stated that collective flow observables are very sensitive to the presence of an intermediate fluid dynamic evolution and also to the employed transport coefficients. It

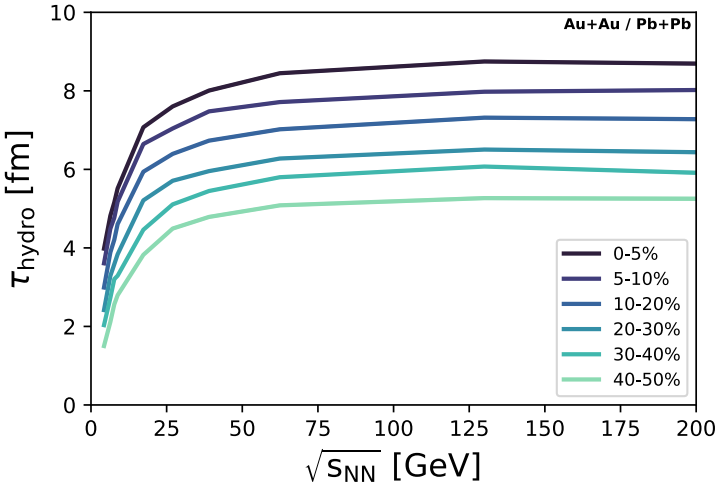

Figure 2.18.: Lifetime of the hydrodynamically evolved fireball in Au+Au/Pb+Pb collisions within the `SMASH-vHLLE-hybrid` as a function of collision energy and for different centralities. More central collisions are marked by darker colours, more peripheral collisions by lighter colours.

is important to further systematically study how these coefficients behave with more realistic temperature and net baryon density dependent transport coefficients. Their implementation in `vHLLE` and the corresponding analysis is however left for future work.

2.4.5. Summary

In this section, the `SMASH-vHLLE-hybrid` has been employed to study hadron production in Au+Au and Pb+Pb collisions between $\sqrt{s_{NN}} = 4.3$ GeV and $\sqrt{s_{NN}} = 200.0$ GeV. First, dN/dy and dN/dm_T spectra of π^-, p, and K^- are presented for collisions at low and intermediate collision energies. It is found that the agreement with experimental measurements improved significantly once employing the `SMASH-vHLLE-hybrid` instead of a pure transport evolution relying on `SMASH`. In particular, it is demonstrated that the `SMASH-vHLLE-hybrid` can properly reproduce the longitudinal baryon stopping dynamics observed experimentally. Second, excitation functions for the mid-rapidity yield and the mean transverse momentum of π^-, p, and K^- have been extracted from the `SMASH-vHLLE-hybrid` between $\sqrt{s_{NN}} = 4.3$ GeV and $\sqrt{s_{NN}} = 200.0$ GeV. Again, the agreement with experimental data is improved as compared to employing a pure `SMASH` evolution, especially in view of baryon dynamics. It is further found that both observables show only small dependencies on the collision centralities when probing centralities between 0-5% and 40-50%. Third, the integrated elliptic flow v_2 and triangular flow v_3 of charged particles as a function of collision energy are confronted with STAR data for different centralities. A good agreement is obtained for v_2 in central collisions as well as at high collision energies. Otherwise, v_2 and v_3 are underestimated, which is explained with a too short lifetime of the hydrodynamical fireball as well as with the smearing kernel employed at the initialization of hydrodynamics.
The `SMASH-vHLLE-hybrid` relies on initial conditions obtained on a hypersurface of constant proper time. However, this assumption is questionable at low collision energies, where the dynamics tend to be comparably slow. An extension of the `SMASH-vHLLE-hybrid` by more dynamical initial conditions, similar to efforts made in [114], thus constitute the next step,

to improve the applicability at FAIR/NICA collision energies.

The SMASH-vHLLE-hybrid established in this section is as a state-of-the-art hybrid model to theoretically describe relativistic heavy-ion collisions at a wide range of collision energies. It constitutes a baseline for future studies, to e.g. systematically invesitate the impact of different viscosities, equations of state, or the (anti-)proton annihilation and regeneration study conducted below.

2.5. Annihilation and Regeneration of (Anti-)Protons in the SMASH-vHLLE-hybrid

Thermal models are generally successful at describing the final state hadron abundances measured across a wide range of collision energies. One of the few exceptions to this end are protons and anti-protons whose yields are overestimated by thermal predictions. This might be related to the lack of late-stage hadronic rescatterings in thermal models (c.f. Sec. 1.2.2). In particular the inclusion of proton anti-proton ($p\bar{p}$) annihilations in the late stages have been shown to improve the agreement with experimentally measured proton and anti-proton abundances [121, 122, 124–126]. In these considerations, the impact of the corresponding regeneration process is neglected, that is the back reaction, which is estimated to be non-negligible [238, 239].
In this section, the SMASH-vHLLE-hybrid is employed to study the annihilation and regeneration of protons and anti-protons in the late stages of heavy-ion collisions between $\sqrt{s_{NN}} = 17.3$ GeV and $\sqrt{s_{NN}} = 5.02$ TeV. The impact of the regeneration reaction in the non-equilibrium afterburner is assessed and quantified for different centralities. It shall be noted, that this study was majorly conducted by my collaborators [240, 241], whilst my contribution consists of providing the SMASH-vHLLE-hybrid including its modifications to be employed with averaged initial conditions instead of the default event-by-event setup. The results presented in the following are published in [3].

2.5.1. Mechanism of (Anti-)Proton Annihilation and Regeneration

$p\bar{p}$ annihilations and regenerations in the rescattering stage of the SMASH-vHLLE-hybrid are realized with the SMASH transport approach, for it is employed to model the non-equilibrium afterburner evolution. Therein, the annihilation of $p\bar{p}$ pairs is implemented as a $5 \leftrightarrow 2$ process via

$$p + \bar{p} \rightarrow 5\ \pi\ . \tag{2.47}$$

The regeneration process is implemented either as a direct

$$5\ \pi \rightarrow p + \bar{p} \tag{2.48}$$

process, via multi-particle interactions, or as a chain of binary interactions through

$$5\ \pi \rightarrow 2\ \rho + \pi \rightarrow h_1 + \rho \rightarrow p + \bar{p}\ . \tag{2.49}$$

The direct process corresponds to the theoretically more rigorous treatment, but is computationally much more expensive. It relies on the stochastic collision criterion to realize the five pion interaction, for which the collision probability is provided in Eq. (2.5). The chain

of binary interactions serves as a proxy for the direct treatment relying on a geometric collision criterion. These collision criteria are in greater detail described in Sec. 2.1.3. It is further verified in [3] that both treatments fulfill the principle of detailed balance, which is of fundamental importance to consistently describe a reaction along with its reverse process [189]. Note though, that the regeneration process through a chain of two-body interactions (Eq. 2.49) is slower than the direct treatment, owing to the finite lifetimes of the intermediate resonances. It has yet to be assessed, how large the impact of these different treatments is on the final state observables. It shall further be noted, that the $p\bar{p}$ inelastic cross section is assumed to be saturated by multi-pion interactions of the kind $p+\bar{p} \rightarrow m\ \pi$, with $m = 2, 3, ...$ [242–244]. As an effective approach, only the $p + \bar{p} \rightarrow 5\ \pi$ process is implemented in SMASH though, as a proxy for all multi-pion interactions. This is motivated from the average number of pions produced being $m = 5$ [242] in the energy range relevant for the $p\bar{p}$ annihilations subject of this work.

2.5.2. Quantifying the Annihilation and Regeneration in Heavy-Ion Collisions

In the following, the SMASH-vHLLE-hybrid is employed to simulate Au+Au collisions at $\sqrt{s_{NN}} = 39.0$ GeV and $\sqrt{s_{NN}} = 200.0$ GeV, as well as Pb+Pb collisions at $\sqrt{s_{NN}} = 17.3$ GeV, $\sqrt{s_{NN}} = 2.76$ TeV, and $\sqrt{s_{NN}} = 5.02$ TeV. As opposed to the results presented in Sec. 2.4 the SMASH-vHLLE-hybrid is not employed in an event-by-event hydrodynamics setup. The hydrodynamical evolution is rather initialized once from an averaged initial state, obtained from 100 SMASH events (for 0-5%, 20-30% and 40-50% centrality classes). For the presented study a precise description of experimental data is not aimed at, but rather at a quantification of the annihilation and regeneration reactions occurring in the late rescattering stage. This justifies the application of a simplified and computationally less expensive setup relying on a single averaged initial state for the hydrodynamical evolution. A shear viscosity of $\eta/s = 0.1$ and a bulk viscosity of $\zeta/s = 0.05$ are employed, as they are known to reproduce bulk properties at high collision energies well [56, 181]. For the afterburner evolution, 2000 events are sampled from the freezeout hypersurface created at $e_{crit} = 0.5$ GeV/fm^3.

The impact of (anti-)proton annihilation and regeneration reactions on the proton and anti-proton yields as a function of time can be deduced from Fig. 2.19. Here, $t = 0$ corresponds to the initial time of the afterburner evolution. Darker colours denote protons, lighter colours anti-protons. The total 4π multiplicity is presented in the upper panels, while the mid-rapidity yield can be found in the lower panels. The individual figures are to be understood as follows: The dotted lines represent the final particle yields when directly decaying all hadronic resonances on the freezeout hypersurface without further propagation in the afterburner. This is conceptually similar, yet not identical, to the instantaneous chemical freezeout in thermal models [116, 117]. The dashed lines are the particle yields obtained when relying on a non-equilibrium afterburner, accounting for the annihilation reaction but not the regeneration. For the resulting particle yields, including also the back reaction, one has to differentiate between the stochastic and resonance treatments described above. Results obtained with the resonance treatment (through a chain of binary interactions) are represented by solid lines, those obtained with the stochastic treatment (direct 5→2 process) by open markers. The filled, black markers are the experimentally measured multiplicities.
It is observed that, as expected from previous works, accounting for annihilation reactions reduces the (anti-)proton yields [121, 122], and results in an improved agreement with experimental measurements. The subsequent consideration of the regeneration reaction enhances the yield again, by 20-50%, depending on the rapidity selection employed. The effect of the

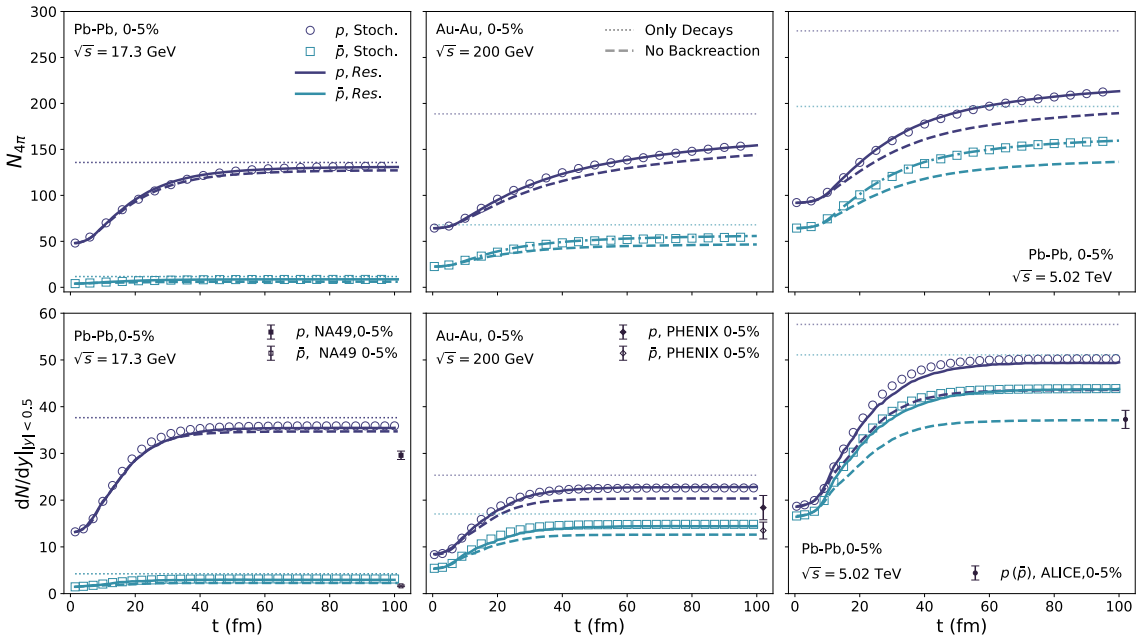

Figure 2.19.: Time evolution of the total proton (darker blue) and anti-proton (lighter blue) yields (upper panels) and their mid-rapidity yield (lower panels) for different collision systems and energies: Pb+Pb collisions at $\sqrt{s_{NN}}$ = 17.3 GeV (left panel), Au+Au collisions at $\sqrt{s_{NN}}$ = 200.0 GeV (centre panel) and Pb+Pb collisions at $\sqrt{s_{NN}}$ = 5.02 TeV (right panel). Results for the stochastic approach are represented by markers, those for the resonance treatment by solid lines. The experimental data (black markers) is taken from [245, 246].

$p\bar{p}$ regeneration is hence encapsulated in the difference between the dashed lines (only annihilation) and solid lines (annihilation and regeneration). Their ratio is referred to as the *regeneration factor*. Furthermore, one finds that the resulting (anti-)proton yields are independent of the framework employed to realize the annihilation process. In fact, the results are perfectly equivalent. Note, that this finding is in contrast to previous studies for d catalysis reactions at lower beam energies, where multi-step and multi-particle treatments revealed differences [175]. Moreover, the fact that there are no differences observed in the context of the presented study could be explained with a pion rich and longer-lived medium that minimizes the effects of a slower reaction due to finite lifetimes. As both treatments yield identical results, in what follows only those for the resonance treatment are presented.

It is possible to investigate the total numbers of annihilation and regeneration reactions occuring in the hadronic rescattering stage. These numbers can be found in Fig. 2.20, where the upper panel displays the total number if collisions, N_{coll}, observed in Au+Au/Pb+Pb collisions as a function of collision energy for different centralities. Pb+Pb collisions are performed at $\sqrt{s_{NN}}$ = 17.3 GeV, 2.76 TeV, and 5.02 TeV while Au+Au collisions are performed at $\sqrt{s_{NN}}$ = 39.0 GeV and 200.0 GeV. Results for 0-5% most central collisions are displayed on the left, those for 20-30% most central collisions in the centre and those for 40-50% most central collisions on the right. The total numbers of $p\bar{p}$ annihilations are represented by circles, those of $p\bar{p}$ regenerations by diamonds and, for reference, the total $B\bar{B}$ annihilations by squares. Note though, that except for $N\bar{N}$ annihilations the latter are not realized via resonance dynamics but via string fragmentation relying on `Pythia` (c.f. Sec. 2.1.4). Result-

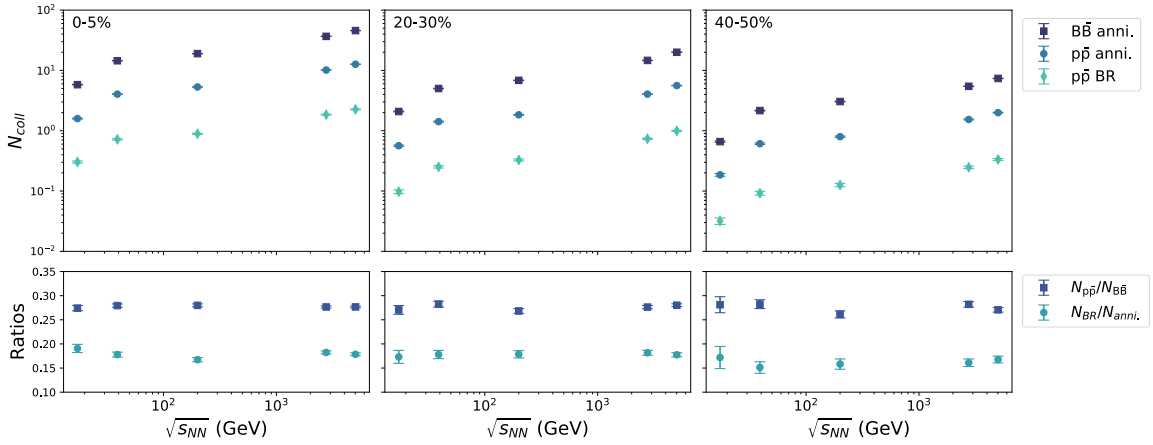

Figure 2.20.: Total reaction numbers for Au+Au collisions at $\sqrt{s_{NN}}$ = 39.0 GeV and $\sqrt{s_{NN}}$ = 200.0 GeV and Pb+Pb collisions at $\sqrt{s_{NN}}$ = 17.3 GeV, $\sqrt{s_{NN}}$ = 2.76 TeV, and $\sqrt{s_{NN}}$ = 5.02 TeV at different centralities: 0-5% (left), 20-30% (center), 40-50% (right). $p\bar{p}$ annihilations are represented by circles, their regeneration by diamonds and $B\bar{B}$ annihilations by squares. In the lower panel the ratio of $p\bar{p}$ regenerations to back reactions is presented with diamonds, the ratio of $p\bar{p}$ annihilations to $B\bar{B}$ annihilations by squares. Results are presented for the full rapidity range.

ingly, the back reaction is unaccounted for and detailed balance is broken. In the lower panel, ratios are presented for the number of $p\bar{p}$ regeneration reactions to $p\bar{p}$ annihilations with diamonds as well as for $p\bar{p}$ annihilations to $B\bar{B}$ annihilations with squares. The former gives an estimate about how many $p\bar{p}$ pairs lost to annihilation are restored with the back reaction process. The latter contains the contribution of $p\bar{p}$ annihilations to all $B\bar{B}$ annihilations and can, in combination with the regeneration factor, be employed to provide an estimate about the amount of $B\bar{B}$ pairs restored in regeneration reactions.
It is found that, regarding the full rapidity range in Fig. 2.20, 15-20% of all $p\bar{p}$ pairs lost in annihilation processes are restored in the back reaction, independently of the energy or centrality of the collision. Translated to the final (anti-)proton yield (c.f. Fig. 2.19), this implies that 20-30% of the total yield is re-generated by the back reaction when considering the entire rapidity range, and up to 50% at mid-rapidity. These findings are compatible with results from [239], where a regeneration of 20% was reported for the 4π multiplicity. Therefore, the impact of the back reaction of $p\bar{p}$ annihilations in the hadronic rescattering stage is not negligible and needs to be accounted for when providing an estimate about the final state (anti-)proton yields. In addition, it becomes evident in Fig. 2.20 that $p\bar{p}$ annihilations make up 25-30% of all $B\bar{B}$ annihilations, also across all collision energies and centralities. The stability of these numbers provides a possibility to extrapolate the findings for the amount of $p\bar{p}$ regenerations to the more general $B\bar{B}$ regenerations.

2.5.3. Summary

In this section, the `SMASH-vHLLE-hybrid` is employed to simulate Au+Au/Pb+Pb collisions between $\sqrt{s_{NN}}$ = 17.3 GeV and $\sqrt{s_{NN}}$ = 5.02 TeV, relying on an averaged `SMASH` initial state for a single hydrodynamical event. The importance of the annihilation and regeneration of

$p\bar{p}$ pairs in the late hadronic rescattering stage has been assessed by means of the detailed balance fulfilling $p + \bar{p} \leftrightarrow 5\ \pi$ reaction. It is found that, independently of the energy or centrality of the collision, 15-20% of all $p\bar{p}$ pairs lost to annihilation are re-stored with the back reaction. This implies that of the total (anti-)proton yield, 20-30% is re-generated in the full rapidity range and around 50% at mid-rapidity considering the late rescattering stage. The $p\bar{p}$ restoring back reaction contributes significantly to the final (anti-)proton yields and needs hence be accounted for. A chemical freezeout attributed to a single temperature and baryon chemical potential is not capable of properly estimating the final (anti-)proton yields for lack of non-equilibrium effects in the rescattering stage. It is yet to be investigated how large the impact of the back reaction is on observables other than the yield, for instance on anisotropic flow. Furthermore, it is important to extend the regeneration framework by baryon anti-baryon annihilations and regenerations as well as other $2 \rightarrow n$ processes.
Nonetheless, the observed importance of the regeneration reaction for the final proton yield needs to be accounted for when extracting e.g. QCD transport coefficients [56, 181] that rely on the proton spectra. Also it might have an impact on the switching criterion in hydrodynamics+transport approaches as the final proton spectra are particularly sensitive to the switching temperature or energy density [247]. However, a thorough investigation of these implications is beyond the scope of this work.

2.6. Synopsis

In this chapter, the `SMASH-vHLLE-hybrid` has been introduced as a novel hybrid approach capable of describing heavy-ion collisions between $\sqrt{s_{NN}} = 4.3$ GeV and $\sqrt{s_{NN}} = 5.02$ TeV, which is publicly available [209]. It consists of the transport approach `SMASH` for the initial and final state and relies on the 3+1D viscous hydrodynamics approach `vHLLE` for the intermediate fluid dynamical evolution. The properties of the different submodules and the realization of the interfaces have been explained. The `SMASH-vHLLE-hybrid` has been successfully validated regarding consistency at the interfaces and global on-average conservation laws. In particular, the importance of an accurate hadron gas equation of state for the particlization process is emphasized in view of quantum number conservation. As such, the equation of state of the `SMASH` hadron resonance gas has been determined down to an energy density of $e = 0.01$ GeV/fm^3 and made available on Github [206]. In addition, results of the `SMASH-vHLLE-hybrid` are compared to those obtained in hybrid approaches consisting of `SMASH` + `CLVisc` and `vHLLE` + `UrQMD`. For the former, an excellent agreement is obtained, while in the case of the latter differences in the final particle spectra are found. These stem from differences in the underlying transport theoretical evolutions provided by `UrQMD` and `SMASH`.

Furthermore, dN/dy and dN/dm_T spectra of pions, kaons and protons have been obtained with the `SMASH-vHLLE-hybrid` for Au+Au/Pb+Pb collisions between $\sqrt{s_{NN}} = 4.3$ GeV and $\sqrt{s_{NN}} = 200.0$ GeV. These are compared to results from a pure transport evolution and confronted with experimental data. It is found that the agreement with experimental measurements improved significantly once relying on a hybrid approach characterized by an intermediate fluid dynamical stage. This holds in particular for the baryon stopping dynamics at intermediate collision energies. The transition from a single-peak structure at low collision energies to a double-peak structure towards higher energies is well reproduced. Similar observations are made for $dN/dy|_{y=0}$ and $\langle p_T \rangle$ excitation functions where the qualitative agreement with experimental data improved once relying on a hybrid approach instead of

a pure transport evolution. In addition, the integrated elliptic and triangular flow, v_2 and v_3, of charged particles has been determined with the `SMASH-vHLLE-hybrid` for a range of collision energies and centralities. A good agreement with experimental data is found for high collision energies as well as central collisions, but v_2 and v_3 is else underestimated. This is related to a too short lifetime of the fluid-dynamical fireball in peripheral collisions and at low collision energies and to the smearing kernel employed at initialization of the hydrodynamical stage.

The `SMASH-vHLLE-hybrid` has further been employed to study the impact of $p\bar{p}$ annihilations and regenerations in the late rescattering stage of Au+Au/Pb+Pb collisions between $\sqrt{s_{NN}} = 17.3$ GeV and $\sqrt{s_{NN}} = 5.02$ TeV. The importance of accounting for the back reaction is demonstrated regarding the $p + \bar{p} \leftrightarrow 5\ \pi$ reaction for which the reverse process is implemented either as a direct multi-particle interaction or as a chain of binary interactions. The specific realization is however found to not have an impact on the resulting (anti-)proton yields, owing to the high abundance of pions in the medium and its comparably long lifetime. The back reaction is found to have a significant impact on the final (anti-)proton yields and needs hence be accounted for when modelling the late rescattering stage. It is observed that in the full rapidity range, 20-30% of the yield lost to annihilations is re-generated by the back reaction, at mid-rapidity even 50%. The impact of the regeneration reaction on other observables has yet to be assessed though.

To summarize, the `SMASH-vHLLE-hybrid` has been successfully developed, combining the `SMASH` transport approach with the `vHLLE` hydrodynamics model. It has been validated and subsequently applied to heavy-ion collisions at a broad range of collision energies and centralities where particle yields, spectra and flow are studied. In the future, it can be utilized with different equations of state to evolve the hot and dense fireball - with or without a critical end point or first order phase transition - to study their impact on particle spectra, flow, or other observables. Also, the `SMASH-vHLLE-hybrid` has only been employed with constant transport coefficients. The extension by energy or baryon density-dependent transport coefficients constitutes the next step to also analyze their impact on final state observables.
In addition, it is important to extend the `SMASH-vHLLE-hybrid` by more dynamical initial conditions, similar to efforts made in [114], in order to provide a better description of heavy-ion collisions at in particular FAIR/NICA energies, where the collision dynamics are slower and the assumption of thermalization on a hypersurface of constant proper time is questionable.

3

Direct Photons from the Hadronic Rescattering Stage

Photons are penetrating probes in relativistic heavy-ion collisions that carry direct and unperturbed information from all stages of the collision to the detector. Their properties in high-energy collisions are however not yet fully understood. No model is capable of simultaneously describing their measured yield and elliptic flow; an observation denoted the *direct photon puzzle* [142]. Recent progress to alleviate the tension between theory and experimental photon data includes an improved description of early-stage pre-equilibrium photons [143–152] which are particularly important at higher transverse momenta. At lower transverse momenta, the leading contributions are photons produced in hadronic interactions. Up to now, they have in most cases been accounted for on a macroscopic basis, by folding a hydrodynamical evolution with thermal photon emission rates [134, 140, 141, 248–250]. Alternatively, they have been described on an entirely microscopic basis [251], as well as in a hybrid approach [252]. The latter does however rely on previous results for the underlying photon cross sections (see [253]) and neglects bremsstrahlung contributions. A different hybrid approach is employed in this work. It provides a consistent treatment of hadronic photon production above and below the switching temperature and accounts for photons from $2 \to 2$ scattering processes as well as meson bremsstrahlung and thus allows for a more realistic description.

In this chapter, the properties of photons from hadronic interactions in relativistic heavy-ion collisions is studied within a hybrid approach. For this, the production of photons in $2 \to 2$ scatterings as well as Bremsstrahlung processes is implemented in the hadronic transport approach `SMASH` (c.f. Sec. 2.1). This requires knowledge of the cross sections underlying the photon producing interactions, which are derived from effective field theories. It shall be mentioned that the cross sections for photon production in $2 \to 2$ scatterings were determined in [254], but their extension to broad ρ mesons is subject of the presented thesis. The bremsstrahlung cross sections were recently derived and provided by a collaborator [240]. The implementation and validation of both photon production frameworks in `SMASH` on the other hand are part of this PhD project.
In the following, the field theories underlying the cross sections for photon production in $2 \to 2$ scatterings and bremsstrahlung processes are introduced. The cross sections are presented, and their implementation in `SMASH` is briefly described and validated. In continuation, `SMASH` is employed as an afterburner in a `MUSIC+SMASH` hybrid to study the impact of non-equilibrium dynamics in the late rescattering stage of heavy-ion collisions at RHIC/LHC energies. A significant enhancement of photon v_2 at low p_T in the late rescattering stage is observed in a non-equilibrium setup as compared to a local-equilibrium description. This demonstrates the necessity of proper non-equilibrium dynamics for the late and dilute hadronic stage.
The results presented in this chapter are published in [1, 2, 5].

3.1. Photon Production Cross Sections

As described in Sec. 1.1.1, QCD is a non-abelian SU(3) theory that is spontaneously broken with respect to chiral symmetry. According to Goldstone's theorem, every spontaneously broken continuous symmetry is accompanied by the generation of massless Goldstone bosons [255, 256]. There are 8 Goldstone bosons related to the spontaneous breaking of the SU(3) chiral symmetry. Those Goldstone bosons can serve as degrees of freedom in effective chiral field theories.
Effective field theories are a means to describe non-analytically solvable theories by focusing on only the relevant degrees of freedom in a certain energy range. Their applicability is thus restricted to this very same energy scale [257]. For the description of QCD at low energies, the relevant energy scale is $\Lambda \approx 1$ GeV, which corresponds to the hadronic mass scale originating from spontaneous symmetry breaking [12]. The appropriate degrees of freedom are therefore hadrons, characterized by a mass of $m \ll \Lambda$. The effective Lagrangian is obtained by expanding the fundamental Lagrangian in terms of momenta and neglecting all contributions higher than p^2, which is considered accurate up to corrections of the order of $\frac{p^2}{\Lambda^2}$ [258]. The different energy scales are hence decoupled, which allows studying the low-energy regime of QCD [259].

One of the most prominent effective field theories in QCD is *chiral effective field theory*, relying on perturbation theory [260–262]. It describes the low-energy region of QCD, where quarks and gluons are confined. In chiral perturbation theory, the lightest mesons – pions, kaons, and the eta meson – are the commonly used appropriate degrees of freedom. They are the Goldstone bosons of the spontaneously broken chiral symmetry [263], and their scattering properties are assumed to solely depend on the pion decay amplitude $f_\pi \approx 93$ MeV [258]. Chiral perturbation theory with mesonic degrees of freedom constitutes the theoretical framework to determine the cross sections for photon production in the $2 \to 2$ scattering and Bremsstrahlung processes, which are the subject of in this chapter. Details regarding the underlying frameworks are provided in the following.

3.1.1. Photons from $2 \to 2$ Scatterings

The field-theoretical framework employed to determine the photon cross sections in $\pi - \rho$ scatterings is described in great detail in [264, 265]. Hence, only a brief introduction is provided in the following and the interested reader is referred to the original publications for further details. The underlying field theory can be classified as a chiral effective field theory with mesonic degrees of freedom. It relies on a massive Yang-Mills approach [8], capable of accounting for pseudoscalar, vector and axial vector mesons as well as the photon. The corresponding Lagrangian, containing kinetic and interaction terms, reads

$$
\begin{aligned}
\mathcal{L} =& \frac{1}{8} F_\pi^2 \, \mathrm{Tr}\left(D_\mu U D^\mu U^\dagger\right) + \frac{1}{8} F_\pi^2 \, \mathrm{Tr}\left(M\left(U + U^\dagger - 2\right)\right) - \\
& \frac{1}{2} \, \mathrm{Tr}\left(F^L_{\mu\nu} F^{L\mu\nu} + F^R_{\mu\nu} F^{R\mu\nu}\right) + m_0^2 \, \mathrm{Tr}\left(A^L_\mu A^{L\mu} + A^R_\mu A^{R\mu}\right) + \\
& \gamma \, \mathrm{Tr}\left(F^L_{\mu\nu} U F^{R\mu\nu} U^\dagger\right) - i\xi \, \mathrm{Tr}\left(D_\mu U D_\nu U^\dagger F^{L\mu\nu} + D_\mu U^\dagger D_\nu U F^{R\mu\nu}\right) - \\
& \frac{2 e m_V^2}{\tilde{g}} B_\mu \, \mathrm{Tr}\left(Q \tilde{V}^\mu\right) - \frac{1}{4} (\partial_\mu B^\nu - \partial_\nu B^\mu)^2 + \\
& \frac{2 e^2 m_0^2}{g_0^2} B_\mu B^\mu \mathrm{Tr}\left(Q^2\right) + g_{VV\phi} \, \varepsilon_{\mu\nu\alpha\beta} \, \mathrm{Tr}\left[\partial^\mu V^\nu \partial^\alpha V^\beta \phi\right],
\end{aligned}
\tag{3.1}
$$

where

$$
\begin{aligned}
& U = \exp\left(\frac{2i}{F_\pi} \phi\right) \qquad \text{with} \qquad \phi = \begin{pmatrix} \frac{\pi^0}{\sqrt{2}} + \frac{\eta_8}{\sqrt{6}} & \pi^+ & K^+ \\ \pi^- & \frac{\eta_8}{\sqrt{6}} - \frac{\pi^0}{\sqrt{2}} & K^0 \\ K^- & \bar{K}^0 & -\frac{2}{\sqrt{6}} \eta_8 \end{pmatrix} \\
& A^L_\mu = \frac{1}{2} (V_\mu + A_\mu) \qquad A^R_\mu = \frac{1}{2} (V_\mu - A_\mu) \\
& D_\mu = \partial_\mu - i g_0 A^L_\mu + i g_0 A^R_\mu \\
& F^{L,R}_{\mu\nu} = \partial_\mu A^{L,R}_\nu - \partial_\nu A^{L,R}_\mu - i g_0 [A^{L,R}_\mu, A^{L,R}_\nu] \\
& M = \frac{2}{3}\left(m_K^2 + \frac{1}{2} m_\pi^2\right) - \frac{2}{\sqrt{3}}\left(m_K^2 - m_\pi^2\right) \lambda_8.
\end{aligned}
\tag{3.2}
$$

Here, ϕ, V_μ and A_μ are the pseudoscalar, vector and axial vector meson fields, respectively. F_π is the pion decay constant and λ_i are the Gell-Mann matrices [13]. The coupling constants, widths and remaining parameters are chosen such that they correspond to set (II) in the categorization made in [264]. These are:

$$
\begin{aligned}
& C = 0.059 && \delta = -0.64251 && \eta_1 = 2.22388 \text{ GeV}^{-1} \\
& \tilde{g} = 6.4483 && Z = 0.8429 \text{ GeV}^{-1} && \eta_2 = 2.39014 \text{ GeV}^{-1} \\
& \xi = 0.0585 && \Gamma_{a_1} = 0.4 \text{ GeV} && C_4 = -0.140942 \text{ GeV}^{-2} \\
& \gamma = -0.2913 && m_0 = 0.875 \text{ GeV} && g_{\pi\rho\omega} = \begin{cases} 11.93 \text{ GeV}^{-1} \text{ w/o FF} \\ 22.6 \text{ GeV}^{-1} \text{ w FF} \end{cases}
\end{aligned}
\tag{3.3}
$$

Note, that the ρ meson is treated as a stable particle within this framework, neglecting its finite width. The cross sections are derived under its stability assumption, but they are extended to account for finite-width ρ mesons in Sec. 3.2.2. Furthermore, the coupling at the π-ρ-ω vertex $g_{\pi\rho\omega}$ depends on whether or not form factors are applied. Within this framework, a

hadronic dipole form factor of the shape

$$\hat{F}(\bar{t}) = \left(\frac{2\,\Lambda^2}{2\Lambda^2 - \bar{t}(E_\gamma)} \right)^2 \tag{3.4}$$

is employed, where $\Lambda = 1$ GeV. This form factor enters the computations of the cross sections through muliplication via

$$\sigma \to \hat{F}(\bar{t})^4 \; \sigma \; . \tag{3.5}$$

The value of the form factor depends only on the value for $\bar{t}$ which, following [265], can be parametrized as a function of the photon energy E_γ as

$$\begin{aligned} \bar{t}_\pi = \; & 34.5096 \text{ GeV}^{-0.737} \; E^{0.737} - 67.557 \text{ GeV}^{-0.7584} \; E^{0.7584} + \\ & 32.858 \text{ GeV}^{-0.7806} \; E^{0.7806} \end{aligned} \tag{3.6}$$

$$\begin{aligned} \bar{t}_\omega = & -61.595 \text{ GeV}^{-0.9979} \; E^{0.9979} \; + \; 28.592 \text{ GeV}^{-1.1579} \; E^{1.1579} + \\ & 37.738 \text{ GeV}^{-0.9317} \; E^{0.9317} - 5.282 \text{ GeV}^{-1.3686} \; E^{1.3686}, \end{aligned} \tag{3.7}$$

where the parametrizations $\bar{t}_\pi$ and $\bar{t}_\omega$ are applied to photon processes mediated by (π, ρ, a_1) mesons or the ω meson, respectively. In SMASH , there are eight different processes implemented to model photon production in $2 \to 2$ scatterings. Following [264, 265], these can be categorized into processes mediated by either (π, ρ, a_1) mesons or the ω meson:

$$\pi^\pm + \pi^\mp \to (\pi, \rho, a_1) \to \rho^0 + \gamma \tag{3.8a}$$
$$\pi^\pm + \pi^0 \to (\pi, \rho, a_1) \to \rho^\pm + \gamma \tag{3.8b}$$

$$\pi^\pm + \rho^0 \to (\pi, \rho, a_1) \to \pi^\pm + \gamma \tag{3.8c}$$
$$\pi^0 + \rho^\pm \to (\pi, \rho, a_1) \to \pi^\pm + \gamma \tag{3.8d}$$
$$\pi^\pm + \rho^\mp \to (\pi, \rho, a_1) \to \pi^0 + \gamma \tag{3.8e}$$

$$\pi^0 + \rho^0 \to \omega \to \pi^0 + \gamma \tag{3.8f}$$
$$\pi^\pm + \rho^\mp \to \omega \to \pi^0 + \gamma \tag{3.8g}$$
$$\pi^0 + \rho^\pm \to \omega \to \pi^\pm + \gamma \tag{3.8h}$$

Here, the first block corresponds to $\pi + \pi \to \rho + \gamma$ processes, which are mediated exclusively by (π, ρ, a_1) mesons, the second block to $\pi \; + \rho \to \pi + \gamma$ processes mediated by (π, ρ, a_1) mesons, and the third block to $\pi \; + \rho \to \pi + \gamma$ processes mediated by the ω meson. Note, that the only difference between the second and third block is the mediating meson(s), both

are characterized by a π and a ρ meson in the initial state and by a pion and a photon in the final state. Processes (3.8d) and (3.8h) as well as (3.8e) and (3.8g) are even indistinguishable regarding the initial and final state particles. Following [264, 265] they are treated separately for the derivation and validation of the cross sections, but their combined contribution is implemented in SMASH, as described in Sec. 3.2.

Cross Sections

The differential and total photon production cross sections are required as input for SMASH to implement the aforementioned processes. The analytical expressions for the differential cross section $\frac{d\sigma}{dt}$ are determined from

$$\frac{d\sigma}{dt} = \frac{1}{64\ \pi\ s\ p_{c.m.}^2}\ |\mathcal{M}|^2, \tag{3.9}$$

where s is the squared center-of-mass energy of the binary scattering process, $p_{c.m.}$ its center-of-mass momentum and $|\mathcal{M}|^2$ the squared matrix element. It is obtained from deriving the Feynman rules from the Lagrangian presented in Eq. (3.1) and with these evaluating the corresponding Feynman diagrams contributing to each process. This is in greater detail described in [254]. The Feynman diagrams and corresponding matrix elements of processes (3.8a) to (3.8h) are listed in App. F. Finally, the total cross sections follow from Eq. (3.9), by integration over the Mandelstam variable t (c.f. App. D).
The analytical expressions of the differential and total cross sections characterizing the photon producing processes (3.8a) - (3.8h) have been derived within the field-theoretical framework described above. These expressions are however too lengthy to be presented here. They are provided in C++ format on Github, where they are embedded in the PHOXTROT project [266].

In Fig. 3.1, the differential cross sections $\frac{d\sigma}{dt}(t, \sqrt{s})$ and the total cross sections $\sigma(\sqrt{s})$ for the $2 \to 2$ scattering processes (3.8a) to (3.8h) are presented. The left column contains the differential cross sections, the right column the total cross sections. In the upper row, $\pi+\pi \to (\pi, \rho, a_1) \to \rho+\gamma$ processes are displayed, in the centre row $\pi+\rho \to (\pi, \rho, a_1) \to \pi+\gamma$ processes, and in the lower row $\pi + \rho \to \omega \to \pi + \gamma$ processes. Note, that as the differential cross sections depend on t and on $\sqrt{s}$, the presented figures are provided at $\sqrt{s} = 1$ GeV. It is found that the differential, as well as the total cross sections of the different processes, show different dependencies on t and $\sqrt{s}$. Clear peaks characterize the differential cross sections for $\pi + \pi \to \rho + \gamma$ processes while the $\pi\ + \rho \to \pi + \gamma$ processes are comparably flat. It is further observed that the differential cross sections for $\pi\ + \rho \to \pi + \gamma$ processes mediated by (π, ρ, a_1) mesons vanish at $t = t_{max}$, while those mediated by the ω meson (except for the $\pi^0 + \rho \to \pi + \gamma$ process) do not. These different properties of $\frac{d\sigma}{dt}(t, \sqrt{s})$ are translated into different angular distributions of the photons produced in SMASH in the different $2 \to 2$ scattering processes (c.f. Sec. 3.2). Regarding the total cross sections, it is observed that the (π, ρ, a_1) mediated processes, $\pi + \pi \to \rho + \gamma$ and $\pi\ + \rho \to \pi + \gamma$, diverge at the thresholds which are $\sqrt{s} = m_\rho$ and $\sqrt{s} = m_\pi + m_\rho$, respectively. The ω mediated processes on the other hand nearly vanish at the thresholds but monotonically increase with rising collision energies. These cross sections are subsequently implemented into SMASH to model hadronic photon production in $2 \to 2$ scatterings. Details about the implementation are provided in Sec. 3.2.

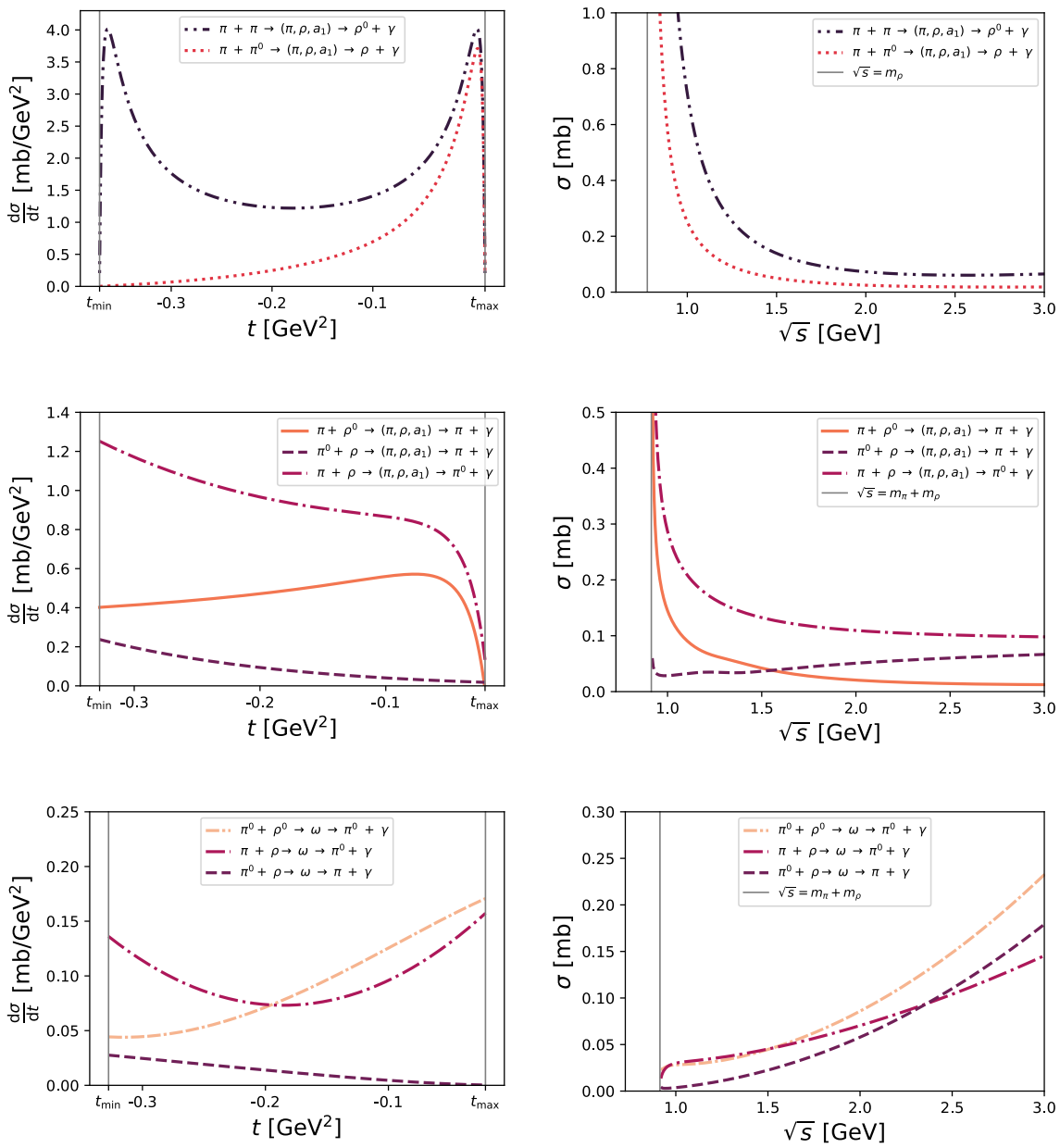

Figure 3.1.: Differential (left) and total (right) cross sections for photon production processes (3.8a) to (3.8h) as a function of Mandelstam t and $\sqrt{s}$, respectively. The upper row contains $\pi + \pi \to (\pi, \rho, a_1) \to \rho + \gamma$ processes, the centre row $\pi + \rho \to (\pi, \rho, a_1) \to \pi + \gamma$ processes, and the lower row $\pi + \rho \to \omega \to \pi + \gamma$ processes. The differential cross sections $\frac{d\sigma}{dt}$ are plotted at $\sqrt{s} = 1.0$ GeV.

3.1.2. Photons from Pion Bremsstrahlung

In addition to $2 \to 2$ scatterings, photons can also be produced from pion bremsstrahlung in SMASH. These are processes of the kind $\pi + \pi \to \pi + \pi + \gamma$ involving π mesons in different electric charge states. In the following, only a brief description of the underlying theory is provided. For further details, the interested reader is referred to appendix A of [5] and the

references therein.
The cross sections are derived within the One Boson Exchange model (OBE) [267, 268], which is an effective field theory successfully describing elastic pion scatterings. The incoming and outgoing pions are assumed to be stable particles, while unstable resonances mediate their interactions. In this work, these include σ, ρ, and $f_2(1270)$ mesons which are scalar, vector, and tensor resonances, respectively. Their interaction Lagrangian reads

$$\mathcal{L}_{\text{int}} = g_\sigma \, \sigma \, \partial_\mu \pi_a \, \partial^\mu \pi_a + g_\rho \, \epsilon_{abc} \, \rho_a^\mu \, \pi_b \, \partial_\mu \pi_c + g_f \, f_{\mu\nu} \, \partial^\mu \pi_a \, \partial^\nu \pi_a \, , \tag{3.10}$$

where π_a and ρ_a with component indices $a = 1, 2, 3$ denote the π and ρ iso-triplets and $f_{\mu\nu}$ the $f_2(1270)$ tensor resonance, ϵ_{abc} is the Levi-Civita tensor and g_σ, g_ρ, and g_f denote the coupling constants to the σ, ρ, and $f_2(1270)$ resonances, respectively. They are determined from fitting the elastic $\pi+\pi$ cross section to experimental data, relying on the resonance pole masses and widths from the `SMASH` degrees of freedom. The resulting coupling constants are

$$g_\sigma = 5.377 \text{GeV}^{-1}, \qquad g_\rho = 6.015, \qquad g_f = 4.33 \text{GeV}^{-1} \, . \tag{3.11}$$

Additionally, the finite size of the resonances is accounted for by employing a form factor in the u and t channels which effectively suppresses high momentum transfers p. This form factor reads

$$h_\alpha(p^2) = \frac{m_\alpha^2 - m_\pi^2}{m_\alpha^2 - p^2} \, , \tag{3.12}$$

with $\alpha = \{\sigma, \rho, f\}$.
The electromagnetic interaction, responsible for photon emission, is accounted for by additionally incorporating a local U(1) symmetry [269]. Hence, the interaction Lagrangian from Eq. (3.10) is extended by the following electromagnetic contributions

$$\mathcal{L}_{\text{EM}} = \mathcal{L}_{\pi\pi\gamma} + \mathcal{L}_{\rho\rho\gamma} + \mathcal{L}_{\pi\pi\sigma\gamma} + \mathcal{L}_{\pi\pi\rho\gamma} + \mathcal{L}_{\pi\pi f\gamma} \tag{3.13}$$

which are listed explicitly in the appendix of [269].

There are seven different photon production channels in $\pi + \pi$ bremsstrahlung processes, accounting for the different electric charge states of the incoming and outgoing pions:

$$\pi^+ + \pi^- \to (\sigma, \rho^0, f) \to \pi^+ + \pi^- + \gamma \tag{3.14a}$$
$$\pi^\pm + \pi^\mp \to (\sigma, \rho^0, f) \to \pi^\pm + \pi^\mp + \gamma \tag{3.14b}$$
$$\pi^\pm + \pi^0 \to \rho^\pm \to \pi^\pm + \pi^0 + \gamma \tag{3.14c}$$
$$\pi^+ + \pi^- \to (\sigma, \rho^0, f) \to \pi^0 + \pi^0 + \gamma \tag{3.14d}$$
$$\pi^0 + \pi^0 \to (\sigma, \rho^0, f) \to \pi^+ + \pi^- + \gamma \tag{3.14e}$$

For these, gauge symmetry is conserved via the Ward-Takahashi identities. The only exception is process (3.14c), where the inclusion of the form factor from Eq. (3.12) effectively breaks

gauge invariance in the $\mathcal{L}_{\rho\rho\gamma}$ term of the Lagrangian. This is corrected for by introducing another from factor determined from $k_\mu \mathcal{M}^\mu = 0$ and thus enforcing the Ward-Takahashi identity.

Cross Sections

The cross sections required for the implementation in SMASH include the differential cross sections with respect to the photon momentum k and the scattering angle ϑ, $\frac{d\sigma_\gamma}{dk}$ and $\frac{d\sigma_\gamma}{d\vartheta}$, as well as the total cross section σ_γ. As described above for the case of $2 \to 2$ scatterings, these cross sections can be determined from the corresponding matrix elements, which in turn are derived from the underlying Feynman diagrams with the Feynman rules encapsulated in the Lagrangian from Eqs. (3.10) and (3.13). The cross sections further follow from

$$\begin{aligned} d\sigma_\gamma = & \frac{1}{2\sqrt{s\,(s-4\,m_\pi^2)}}\,|\mathcal{M}|^2\,\frac{d^3p_1}{2\,(2\pi)^3\,E_1}\,\frac{d^3p_2}{2\,(2\pi)^3\,E_2}\,\frac{d^3k}{2\,(2\pi)^3\,k} \\ & \times\,(2\pi)^4\,\delta^4(p_a+p_b-p_1-p_2-k) \end{aligned} \tag{3.15}$$

$$\begin{aligned} = & \frac{1}{2\sqrt{s\,(s-4\,m_\pi^2)}}\,|\mathcal{M}|^2\,\frac{d^3p_1}{2\,(2\pi)^3\,E_1}\,\frac{d^3p_2}{2\,(2\pi)^3\,E_2}\,\frac{k\,\sin(\vartheta)\,dk\,d\vartheta}{2\,(2\pi)^2} \\ & \times\,(2\pi)^4\,\delta^4(p_a+p_b-p_1-p_2-k), \end{aligned} \tag{3.16}$$

where s is the squared center-of-mass energy of the collision, $|\mathcal{M}|^2$ is the squared matrix element, p_a and p_b denote the incoming pion momenta, p_1 and p_2 the outgoing pion momenta, and k the photon momentum. E_1 and E_2 are the energies of the outgoing pions and m_π the pion mass. ϑ is the scattering angle with respect to the momentum axis in the rest frame of the incoming pion pair.
To yield $\frac{d\sigma_\gamma}{dk}$ and $\frac{d\sigma_\gamma}{d\vartheta}$, Eq. (3.16) is integrated over ϑ and k, respectively, and the total cross section by integration over both. As this expression diverges for $k \to 0$, the k-integration is carried out down to $k = 0.001$ GeV. The final expressions for $\frac{d\sigma_\gamma}{dk}$, $\frac{d\sigma_\gamma}{d\vartheta}$, and σ_γ were determined numerically. They are provided in tabularized format as well as wrapped by a 2D interpolation in C++ format on Github. As the $2 \to 2$ scattering process cross sections, these are also embedded in the PHOXTROT project [266].

In the upper row of Fig. 3.2, the differential cross sections $\frac{d\sigma_\gamma}{dk}$ and $\frac{d\sigma_\gamma}{d\vartheta}$ are presented, split by production processes listed in (3.14a) to (3.14e). On the left, $\frac{d\sigma_\gamma}{dk}$ is presented as a function of the photon momentum k, $\frac{d\sigma_\gamma}{d\vartheta}$ as a function of the scattering angle ϑ on the right. It is observed that the $\frac{d\sigma_\gamma}{dk}$ cross sections diverge at $k \to 0$ and decrease for rising photon momenta. The cross sections for the $\pi^\pm + \pi^\mp \to \pi^\pm + \pi^\mp + \gamma$ and the $\pi^\pm + \pi^0 \to \pi^\pm + \pi^0 + \gamma$ process are further characterized by a bump at $k \approx 0.2$ GeV, which is caused by the exchange of the ρ resonance. The $\frac{d\sigma_\gamma}{d\vartheta}$ cross sections, on the other hand, are symmetric and characterized by peaks at forward and backward angles. This means that photons are dominantly produced approximately in the direction of the momentum axis in the rest frame of the incoming pion pair and in approximately the opposite direction.
In the lower panel of Fig. 3.2, the fully-integrated total cross sections σ_γ for the same processes are presented, including their combined total. It is characterized by two clear peaks

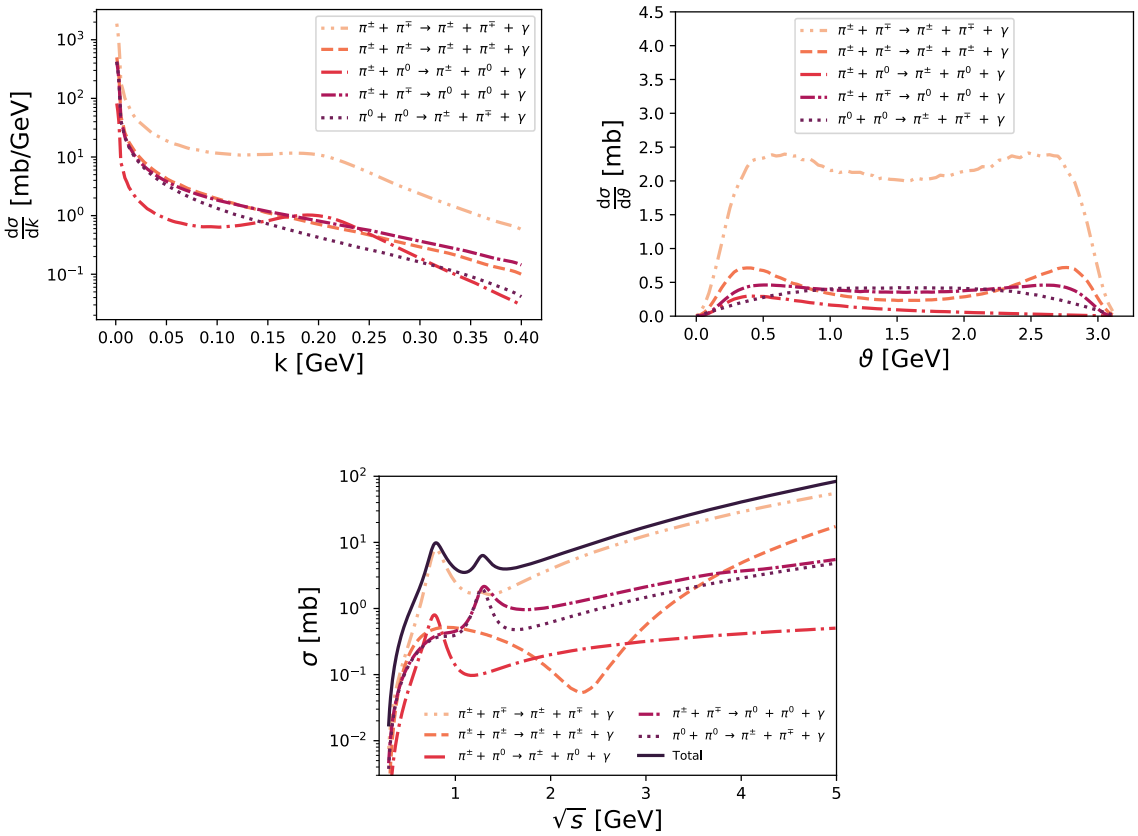

Figure 3.2.: Differential cross sections $\frac{d\sigma_\gamma}{dk}$ (upper left) and $\frac{d\sigma_\gamma}{d\vartheta}$ (upper right), as well as total cross sections σ_γ (lower) for photons produced in $\pi + \pi \to \pi + \pi + \gamma$ bremsstrahlung processes, split by processes listed in (3.14a) to (3.14e). The differential cross sections are plotted at a center-of-mass energy of $\sqrt{s} = 1.0$ GeV.

at the pole masses of the ρ and $f_2(1270)$ resonances. Furthermore, the cross sections of all processes vanish for $\sqrt{s} \to 0$ and increase for rising $\sqrt{s}$.
These cross sections are subsequently implemented into SMASH to model hadronic photon production from pion bremsstrahlung.

3.2. Photon Production in SMASH

The production of photons in hadronic interactions is implemented in SMASH for $2 \to 2$ scatterings as well as pion bremsstrahlung processes relying on the field-theoretical frameworks detailed above. A perturbative treatment is applied, which is motivated by the weakness of the electromagnetic interaction as compared to the strong interaction. The produced photons are assumed to escape the strongly-interacting medium without further interactions as their mean free path is much larger than the system size. The perturbative treatment employed in SMASH is inspired by previous efforts made in [270, 271].

Photon production in SMASH is implemented as follows: The hadronic evolution is executed normally, and in addition, a photon process is always performed if the initial particles of

a hadronic interaction are identical to the initial state of either of the $2 \to 2$ scattering or bremsstrahlung processes listed in (3.8a) to (3.8h) and (3.14a) to (3.14e). Subsequently the photon process is performed, and the final state particles sampled. These are directly printed to a separate photon output and not further propagated in the evolution. Instead, the underlying hadronic interaction is performed as if no photon producing scattering had occurred. However, since the cross sections for photon processes are orders of magnitude smaller than those for hadronic interactions, such a procedure would naturally result in a significant overestimation of photon production. This can be corrected for by introducing a weighting factor accounting for the reduced probability of a photon interaction to occur instead of a hadronic interaction. This weighting factor is defined as

$$W_\gamma = \frac{\sigma_\gamma}{\sigma_{\mathsf{had}}} \ , \tag{3.17}$$

where σ_γ denotes the cross section of the photon process and σ_{had} the cross section of the underlying hadronic interaction. The specific weight that characterizes the produced photon needs to be considered for any subsequent analysis. This weight can also be interpreted such that instead of a full photon, only a fraction of a photon, namely W_γ of a photon, is produced.

The application of a perturbative treatment furthermore allows to introduce the concept of fractional photons. Fractional photons are a mean to properly account for the angular distributions of the final state photons by properly reproducing their phase space distribution. This is in particular important to study harmonic flow coefficients of photons in the context of heavy-ion collisions. It is achieved by, instead of sampling only one photon with weight W_γ, N_{frac} fractional photons are sampled with different kinematic properties such that the entire phase space is covered. If fractional photons are employed, the weighting factor defined in Eq. (3.17) needs to be reformulated to

$$W_\gamma^{2\to2} = \frac{\frac{d\sigma_\gamma}{dt}\ \Delta t}{N_{\mathrm{frac}}\ \sigma_{\mathrm{had}}} \tag{3.18}$$

in the case of $2 \to 2$ scatterings, and

$$W_\gamma^{\mathsf{brems}} = \frac{\sqrt{\frac{d\sigma_\gamma}{dk}\Delta k\ \frac{d\sigma_\gamma}{d\theta}\Delta\theta}}{N_{\mathsf{frac}}\ \sigma_{\mathsf{had}}} \tag{3.19}$$

in the case of bremsstrahlung photons. Here, Δt, Δk, and $\Delta\vartheta$ are the available ranges for Mandelstam t, the photon energy k and the scattering angle ϑ, respectively. The differential cross sections with respect to t, k, and ϑ are $\frac{d\sigma_\gamma}{dt}$, $\frac{d\sigma_\gamma}{dk}$, and $\frac{d\sigma_\gamma}{d\theta}$. It is through the weighting factor that the angular distributions enter the properties of the sampled photon. The differential cross sections are evaluated for each of the N_{frac} fractional photons with their previously sampled kinematic properties. For $2 \to 2$ scatterings, those kinematic properties are fully determined once a value for Mandelstam t is sampled, randomly from

$$t \in [t_{min}, t_{max}], \tag{3.20}$$

with

$$t_{min} = m_a^2 + m_1^2 - \frac{(s + m_a^2 - m_b^2)(s + m_1^2)}{2s} - \frac{(s - m_1^2)\sqrt{(s^2 + m_a^2 - m_b^2)^2 - 4sm_a^2}}{4s}, \tag{3.21}$$

$$t_{max} = m_a^2 + m_1^2 - \frac{(s + m_1^2)(s + m_a^2 - m_b^2)}{2s} + \frac{(s - m_1^2)\sqrt{(s^2 + m_a^2 - m_b^2)^2 - 4sm_a^2}}{4s}, \tag{3.22}$$

where m_a and m_b are the masses of the incoming particles, m_1 the mass of the outgoing hadron, and s the squared center-of-mass energy of the scattering process.
In the case of bremsstrahlung photons, a 3-body phase space needs to be sampled for the final state, requiring k and ϑ to be sampled from

$$k \in [0.001 \text{ GeV}, \frac{s - 4\ m_\pi^2}{2\ \sqrt{s}}] \qquad \text{and} \qquad \theta_k \in [0, \pi], \tag{3.23}$$

where m_π is the pion mass.

3.2.1. Validation

An important process accompanying any implementation of a new feature is the subsequent validation. In the following, the above described photon production frameworks in SMASH are validated in terms of the thermal photon rate in an equilibrated medium. The thermal photon rate accounts for the number of photons that are produced per unit time and volume from the underlying medium. It follows directly from kinetic theory [253] and is defined as

$$k\frac{dR}{d^3k} = N \int \delta^4(p_a + p_b - p_1 - k)\ |\mathcal{M}|^2\ f(E_a)\ f(E_b)\ f(E_1)\ \frac{d^3p_a\ d^3p_b\ d^3p_1}{16\ (2\pi)^8} \tag{3.24}$$

in the case of $2 \to 2$ scatterings. Again, p_a, p_b, E_a and E_b denote the momenta and energies of the incoming hadrons, p_1 and E_1 those of the outgoing hadron. k is the photon momentum, N the degeneracy factor, $f(E_i)$ the distribution function of particle i, and $|\mathcal{M}|^2$ the squared matrix element of the process taken into consideration. The theoretical expectations for the photon rate can be directly determined once the underlying matrix elements are known. They are provided by [272] and employed to validate photon production in $2 \to 2$ scatterings in SMASH.
It is straight-forward to extend Eq. (3.24) to account for bremsstrahlung processes. The corresponding rates have already been determined in [273] and are parametrized in [274]. We thus refrain from repeating this procedure, but directly confront the bremsstrahlung photon rates from SMASH with the parametrizations provided therein.

The photon rates for the SMASH hadron resonance gas are extracted in an infinite matter simulation relying on the SMASH box modus (c.f. 2.1.6). This box is initialized at a temperature

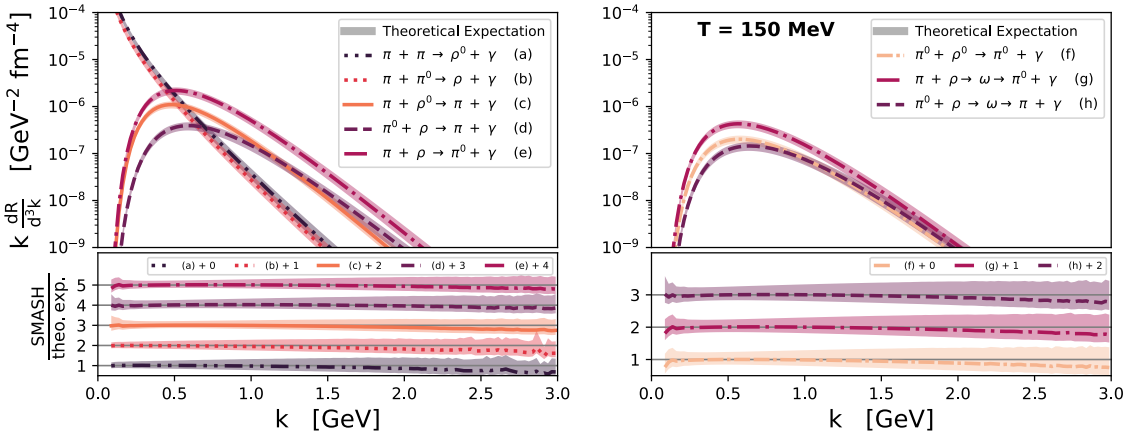

Figure 3.3.: Comparison of the thermal photon rates for (π, ρ, a_1)-mediated processes, (3.8a) to (3.8e) (left) and for ω-mediated processes, (3.8f) to (3.8h) (right), as determined with SMASH (thin lines) to theoretical expectations [272] (bands) in an infinite matter simulation at a temperature of $T = 150$ MeV. Form factors are neglected for this comparison. Also, to to be consistent with the underlying effective field theory at tree level, $\Gamma_\rho = 0$ GeV is employed.

of $T = 150$ MeV with π and ρ mesons[1] according to their thermal multiplicity expectation values. It is evolved for $t = 100$ fm and the hadronic as well as photon producing interactions are performed. The thermal photon rate can be determined from the properties of the produced photons via

$$k \frac{dR}{d^3k} = k \frac{dN}{4\pi\, k^2\, dk\, \Delta t\, V} = \frac{1}{4\pi\, k\, \Delta t\, V} \frac{dN}{dk}\,, \tag{3.25}$$

where Δt is the runtime of the simulation, V the volume of the system and k the energy of the photon. The box employed for this work has a volume of $V = 1000$ fm^3.

$2 \to 2$ Scatterings

$2 \to 2$ Scatterings In Fig. 3.3, the thermal photon rate as a function of the photon energy is presented for the $2 \to 2$ scattering processes implemented in SMASH, neglecting form factor corrections. To be in accordance with the underlying field theory at tree level, the ρ meson is treated as a stable particle with $\Gamma_\rho = 0$ GeV. An extension to account for its resonance nature is made in Sec. 3.2.2. (π, ρ, a_1)-mediated processes (3.8a) to (3.8e) are displayed on the left in Fig. 3.3, ω-mediated processes (3.8f) to (3.8h) on the right. In the upper panels, lines denote the photon rate extracted from SMASH, bands the theoretical expectation from [272]. In the lower panels, the ratio of the SMASH rate to its theoretical expectation is presented, shifted by constant integers. Therein, lines denote the ratio, bands the statistical uncertainty extracted from the SMASH simulation. Within uncertainties, an excellent agreement is obtained between

[1] Note, that while the properties of a_1 and ω mesons enter the cross sections for $2 \to 2$ scatterings and those of the σ and $f_2(1270)$ mesons the cross sections for bremsstrahlung processes, they are not required as degrees of freedom for the infinite matter simulation. Owing to the perturbative treatment, their properties are merely parameters for the production cross sections, but those resonances are never actually formed.

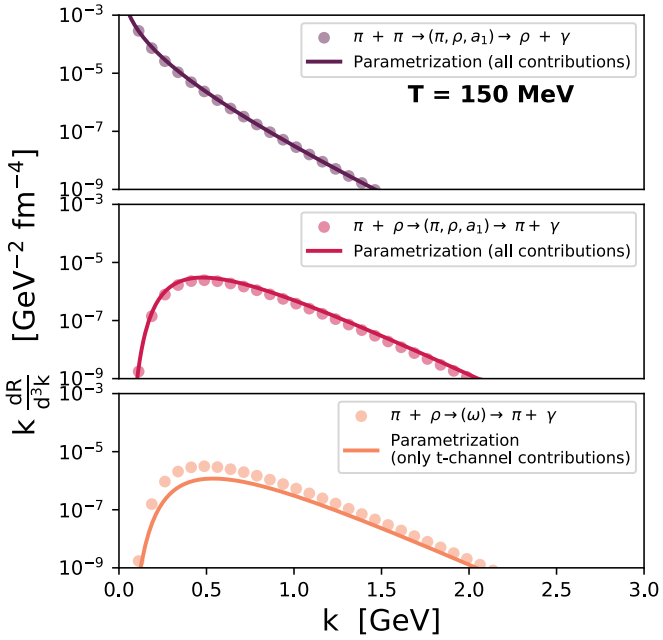

Figure 3.4.: Comparison of the combined photon rates for $\pi + \pi \to \rho + \gamma$ processes mediated by (π, ρ, a_1) mesons (upper panel), for $\pi + \rho \to \pi + \gamma$ processes mediated by (π, ρ, a_1) mesons (centre panel), and for $\pi + \rho \to \pi + \gamma$ processes mediated by the ω meson (lower panel) as extracted from SMASH (markers) to the parametrizations provided in [264] (lines). Note, that for the ω mediated $\pi + \rho \to \pi + \gamma$ processes the parametrizations account only for t-channel contributions while in SMASH both the t and the s channel are implemented. Form factors are included in SMASH as well as in the parametrizations. For consistency, $\Gamma_\rho = 0$ GeV is again applied.

the photon rates extracted from SMASH and their theoretically expected counterparts, thus validating the presented cross sections for photon production in $2 \to 2$ scatterings as well as their implementation in SMASH.

Furthermore, the thermal photon rates for $2 \to 2$ scattering processes (3.8a) to (3.8h) have been parametrized in [264], including form factor corrections. These rates are implemented in MUSIC, a 3 + 1D hydrodynamic code for heavy-ion collisions [108, 134, 275, 276], to describe photon production in the hadronic phase. They are employed in Sec. 3.3 to assess the implications of non-equilibrium dynamics for photon production in the late stages in heavy-ion collisions.
In Fig. 3.4, these parametrizations are compared to the corresponding photon rates from SMASH. The upper panel displays the photon rate for $\pi + \pi \to \rho + \gamma$ processes mediated by (π, ρ, a_1) mesons, the centre panel the photon rate for $\pi + \rho \to \pi + \gamma$ processes mediated by (π, ρ, a_1) mesons, and the lower panel $\pi + \rho \to \pi + \gamma$ processes mediated by the ω meson. Results obtained from SMASH are represented by markers, the parametrizations from [264] by solid lines. It is observed that while the (π, ρ, a_1) mediated processes for $\pi + \pi \to \rho + \gamma$ as well as $\pi + \rho \to \pi + \gamma$ scatterings are in perfect agreement with the parametrizations, the SMASH rates and parametrizations differ significantly for the ω mediated $\pi + \rho \to \pi + \gamma$ scatterings. This disagreement stems from different contributions underlying the SMASH

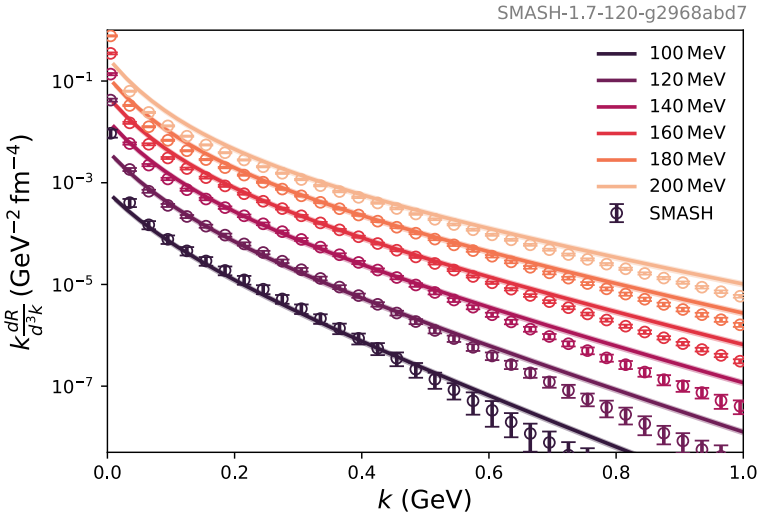

Figure 3.5.: Comparison of the total thermal bremsstrahlung rate, that is the combined contribution from processs (3.14a) - (3.14e), as determined with SMASH (markers) to the parametrization provided in [274] (lines) in an infinite matter simulation at temperatures between $T = 100$ MeV and $T = 200$ MeV. Lower temperatures are displayed by lighter colours, higher temperatures by darker colours.

implementation and the parametrizations. While the above described cross sections for ω mediated processes account for all contributing Feynman diagrams, that is s- and t-channels, the parametrization only contains t-channel contributions. The s-channels on the other hand are absorbed in the in-medium ρ spectral function [264]. SMASH relies on vacuum properties though, such that the s-channels need to be explicitly included in the corresponding cross sections. An excess of the SMASH rate as compared to the parametrization is thus expected. Nevertheless, the excellent agreement in the case of the (π, ρ, a_1) mediated processes serves as another validation of the SMASH framework for photon production in $2 \to 2$ scatterings.

Bremsstrahlung

Similar to $2 \to 2$ scatterings, the bremsstrahlung rates from SMASH are also confronted with their respective parametrizations in order to validate the bremsstrahlung framework. In Fig. 3.5, the thermal photon rate as a function of the photon energy is presented for photons produced in bremsstrahlung processes in SMASH. The total contribution, that is the combined photon rate from processes (3.14a) - (3.14e), is displayed for different temperatures ranging from $T = 100$ MeV to $T = 200$ MeV. Lighter colours denote lower temperatures, darker colours higher temperatures. The bremsstrahlung rate extracted from SMASH is represented by markers, the parametrization from [274] by solid lines. A nearly-perfect agreement is obtained for photon energies below $k \approx 0.5$ GeV. For higher photon energies the bremsstrahlung rates from SMASH exceed those provided by the parametrization. This mismatch at higher photon energies is related to inconsistencies between the kinetic parameters of the One Boson Exchange model used to determine the rates in [273], underlying the parametrizations, and those employed to determine the cross sections for SMASH. The kinetic parameters of the latter, that is the masses and widths of the mesonic resonances, are chosen such that they

match the SMASH degrees of freedom. Small differences in the resulting photon rates, that become more pronounced the higher the photon energy, are therefore expected. Nonetheless, the good agreement in the low and intermediate energy regime serves as a good validation of the bremsstrahlung cross sections provided by [240] and their implementation in SMASH.

3.2.2. Extension to Broad ρ Mesons

Up to now, the cross sections implemented in SMASH for $2 \to 2$ scatterings[2] rely on the assumption that ρ mesons are stable particles instead of broad resonances, to be in accordance with the underlying effective field theory at tree level. It is however known from experiment [18] that ρ mesons are characterized by a width of $\Gamma_\rho \approx 0.149$ GeV. Accurate theoretical models thus call for a consideration of this non-vanishing width when computing the corresponding cross sections. While such considerations are challenging within the underlying field theory, lifting it from tree level to first order, it is comparibly easily feasible within SMASH, by modifying the properties of the ρ meson degree of freedom. The same infinite matter simulation as in Sec. 3.2.1 can therefore be conducted with ρ mesons characterized by $\Gamma_\rho = 0.149$ GeV instead of $\Gamma_\rho = 0$ GeV and the corresonding photon rate determined. Consequently, their mass distribution then follows a vacuum Breit-Wigner distribution (c.f. Eq. 2.2), as detailed in Sec. 2.1.2.
There is however one caveat to simply employing this photon framework to broad ρ mesons: The photon production processes (3.8a), (3.8d), and (3.8e) are each characterized by one contributing Feynman diagram in which the scattering processes does not only contain a ρ meson in the initial or final state, but is also mediated by a ρ meson. Hence, there are two ρ mesons involved in the scattering, one in the initial or final state, and the other in the intermediate state. As those ρ mesons could in principle have different masses, problems in the conservation of the electromagnetic current J^μ are entailed such that

$$\partial_\mu J^\mu \neq 0. \tag{3.26}$$

This violation of current conservation stems from some contributions in the matrix elements of processes (3.8a), (3.8d) and (3.8e) being proportional to

$$\Delta \equiv \frac{m_\rho^2 - u}{M_\rho^2 - u}, \tag{3.27}$$

where m_ρ denotes the mass of the incoming or outgoing ρ meson and M_ρ the mass of the intermediate one. Current conservation is only assured for $\Delta = 1$. In the case of $\Gamma_\rho = 0$ GeV, it applies that

$$m_\rho = M_\rho \qquad \Leftrightarrow \qquad \Delta = 1 \tag{3.28}$$

whereas in the case of broad ρ mesons,

$$m_\rho \neq M_\rho \qquad \Leftrightarrow \qquad \Delta \neq 1. \tag{3.29}$$

generally holds. Eq. (3.29) is particularly problematic in view of current conservation, as $\Delta \neq 1$ implies the electromagnetic current is not conserved in processes (3.8a), (3.8d) and

[2] For photons produced in bremsstrahlung processes, the resonance nature of the ρ meson is already accounted for in the cross section computation (c.f. Sec. 3.1.2). As a result, there is no need to explicitly extend the framework to cope with non-stable ρ mesons.

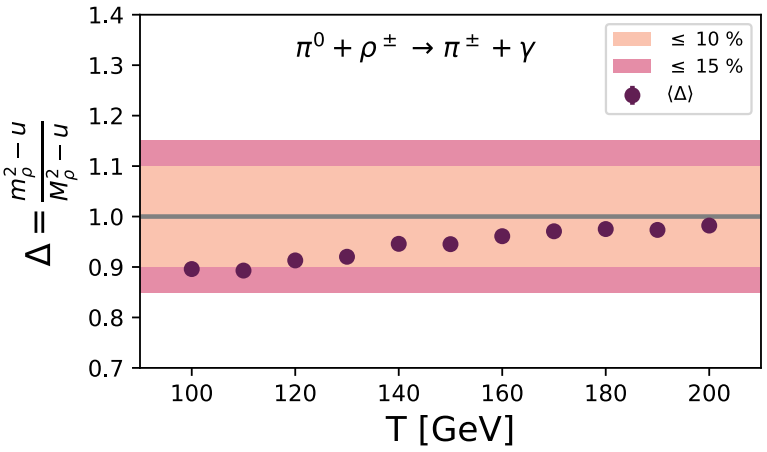

Figure 3.6.: Average value of the current conservation breaking term, Δ, as a function of the temperature T for process (3.8d). $M_\rho = 0.776$ GeV is employed for the intermediate ρ meson while m_ρ and u are extracted from the SMASH evolution.

(3.8e). To circumvent this problem, the cross sections used in the photon producing scattering processes are computed with $m_\rho = M_\rho$, such that $\Delta = 1$ is enforced, and current conservation is assured. However, this treatment is not exactly accurate, since the incoming/outgoing and the intermediate ρ meson can in principle have different masses. At the same time, their masses are on average expected to be the pole mass, which suggests the average difference between m_ρ and M_ρ is small and Δ can be approximated with unity. This justifies the assumption of $m_\rho = M_\rho$ which is employed in SMASH to extend photon production in $2 \rightarrow 2$ scatterings to broad ρ mesons whilst at the same time giving rise to a systematic error. To assess the magnitude of the introduced uncertainty, two further analyses are undertaken: (i) the average value of Δ is investigated and (ii) a contact term is derived to explicitly restore current conservation.

In Fig. 3.6 the average value of Δ is presented as exemplarily extracted from SMASH for process (3.8d) for different initialization temperatures of a thermally equilibrated box. Owing to the perturbative photon treatment in SMASH, the intermediate ρ meson is never formed; hence its mass is not accessible. To nonetheless estimate the effect of a broad initial ρ meson on Δ, M_ρ is approximated with the ρ pole mass, such that $M_\rho = 0.776$ GeV. The mass of the incoming ρ meson follows from the underlying dynamics. The markers denote the mean values of Δ, the orange band a deviation of 10% from unity, the pink band a deviation of 15%. It becomes apparent that the average value of Δ differs by at most 11% from the current conserving expectation of $\Delta = 1$ in the temperature range from $T = 100$ - 200 MeV. Furthermore, Δ approaches unity for rising temperatures, thus lessening the issue of a non-conserved electromagnetic current.

In addition, it is possible to define a contact term in order to explicitly restore current conservation. This endevour is undertaken exemplarily for process (3.8d) where current conservation is violated in the case of $m_\rho \neq M_\rho$ as the condition

$$k_\mu \mathcal{M}^\mu = 0 \tag{3.30}$$

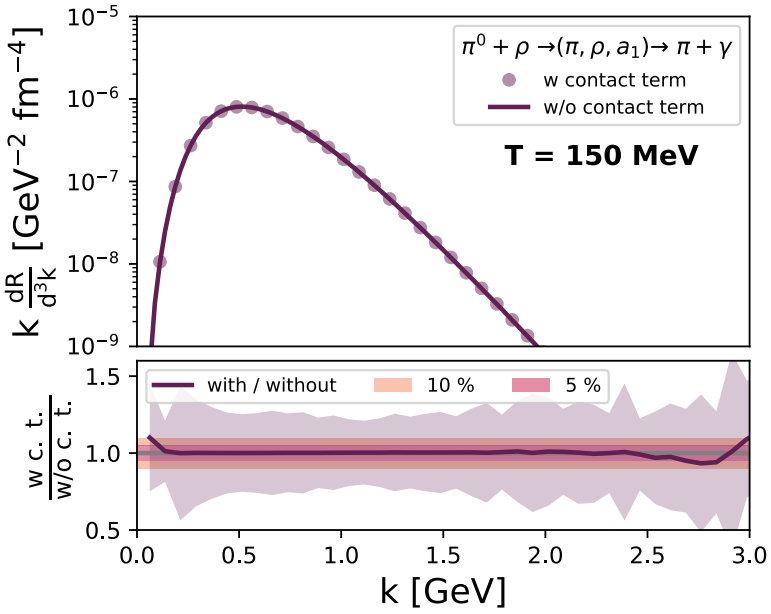

Figure 3.7.: Thermal photon rate for process $\pi^0+\rho^\pm \rightarrow \pi^\pm+\gamma$ (3.8d) as determined with (solid line) and without (markers) considering an additional contact term to restore current conservation in the case of broad ρ mesons at $T = 150$ MeV. In the lower panel, the ratio of of both rates is displayed.

is not fulfilled anymore. In Eq. (3.30), k_μ denotes the photon momentum and $\mathcal{M}^\mu$ the matrix element before contraction with the photon polarization vector. To restore current conservation, a contact term $\mathcal{M}_c^\mu$ is incoherently added to the matrix element such that

$$k_\mu \left(\mathcal{M}^\mu + \mathcal{M}_c^\mu\right) = 0. \tag{3.31}$$

It shall be noted, though, that there is no unambiguous definition for $\mathcal{M}_c^\mu$ following condition (3.30). It is possible to construct a contact term of the shape

$$\mathcal{M}_c'^{\,\mu} = (\mathcal{M}_c^\mu + A\ k^\mu), \tag{3.32}$$

with A being an arbitrary function of the kinematic variables. Since $k_\mu k^\mu$ always vanishes, condition (3.30) is trivially fulfilled for arbitrary A. The simplest case is considered in this assessment, implying a minimal modification where $A = 0$.
With the modified matrix element $\mathcal{M} + \mathcal{M}_c$ it is possible to re-compute the cross section for process (3.8d), incoherently accounting for the new contribution. This cross section can further be implemented in `SMASH` and the corresponding thermal photon rate of process (3.8d) determined. This is presented in Fig. 3.7, where the thermal photon rate corrected by a contact term is displayed with the solid line, the rate obtained without it by markers. Both are extracted from an infinite matter simulation in `SMASH` at $T = 150$ MeV employing $\Gamma_\rho = 0.149$ GeV. The lower panel shows the ratio of both rates, accompanied by a statistical error band. It is found that both rates are nearly identical and the implications from considering the contact term negligible. In fact, the ratio of both rates is, within errors, consistent with unity. This finding is further generalized to the photon processes (3.8a) and (3.8e), which also suffer from contributing Feynman diagrams involving initial/final as well as intermediate

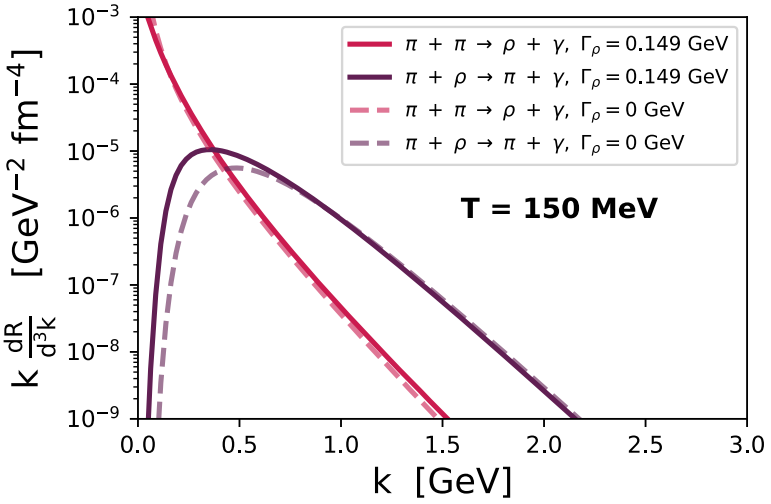

Figure 3.8.: Final, thermal photon rates for combined $\pi + \pi \to \rho + \gamma$ processes (pink) and combined $\pi + \rho \to \pi + \gamma$ processes (purple) from a SMASH infinite matter simulation at $T = 150$ MeV. Results obtained with stable ρ mesons are marked by dashed lines, those obtained with broad ρ mesons with solid lines. Form factors are considered.

state ρ mesons. Since the resulting photon rate remains unaffected, it is not necessary to explicitly determine the corresponding contact terms and account for them in the cross sections.

Relying on the above findings, the transition from a stable to a broad ρ meson for photon production in $2 \to 2$ scatterings in SMASH is realized as follows: The cross sections derived in Sec. 3.1.1 for processes (3.8a), (3.8d), and (3.8e) are employed as determined above without additional corrections from a contact term. This is justified since the total photon rate remains unaffected when considering the contact term (c.f. Fig. 3.7). Furthermore, the mass of the intermediate ρ meson, which is never formed due to the perturbative treatment, is approximated with the mass of the incoming/outgoing ρ meson. The systematic error introduced therewith is quantified to be $\leq 11\%$ but is in most cases significantly smaller (c.f. Fig. 3.6).

In continuation, it is possible to determine the final photon rates from $2 \to 2$ processes, accounting for the finite width of the ρ meson and properly employing the form factors as described in Eqs. (3.4) and (3.5). The resulting cross sections for $\pi + \pi \to \rho + \gamma$ processes are thus

$$\sigma_{\pi + \pi \to \rho + \gamma} = \hat{F}(\bar{t}_\pi)^4 \; \sigma'_{\pi + \pi \to \rho + \gamma}, \tag{3.33}$$

and those for $\pi + \rho \to \pi + \gamma$ processes

$$\sigma_{\pi + \rho \to \pi + \gamma} = \hat{F}(\bar{t}_\pi)^4 \; \sigma'_{\pi + \rho \to (\pi,\rho,a_1) \to \pi + \gamma} + \hat{F}(\bar{t}_\omega)^4 \; \sigma'_{\pi + \rho \to \omega \to \pi + \gamma}\,, \tag{3.34}$$

where primed cross sections denote those determined via Eq. (3.9) and subsequent integration,

while unprimed quantities are their form-factor corrected counterpart. Note, that (π, ρ, a_1) mediated processes and ω mediated processes are combined incoherently, but considering their respective form factors.
The resulting photon rates as extracted from an infinite matter simulation with SMASH at a temperature of $T = 150$ MeV are presented in Fig. 3.8. Dashed lines denote results obtained with stable ρ mesons, solid lines those obtained considering the finite ρ width of $\Gamma_\rho = 0.149$ GeV. Most notably, a significant enhancement of the photon rate in the region of low photon energies, $k \leq 0.7$ GeV, is observed for $\pi + \rho \to \pi + \gamma$ processes. At the same time, the photon rate is slightly reduced for higher photon energies. For $\pi + \pi \to \rho + \gamma$ processes on the other hand, an opposite trend is observed, although significantly less pronounced.

The photon rates presented for the case of broad ρ mesons in Fig. 3.8, including form factor corrections, constitute the final result for the realization of photon production in $2 \to 2$ scatterings in SMASH. The corresponding bremsstrahlung photon rates are presented in Fig. 3.5. These two production channels constitute the leading contributions for photon production in hadronic interactions. They are subsequently employed in a MUSIC+SMASH hybrid to assess the importance of non-equilibrium dynamics for photon production in the hadronic rescattering stage of relativistic heavy-ion collisions at RHIC and LHC energies. This is detailed below.

3.3. Out-of-Equilibrium Photon Production in the Hadronic Afterburner

In this section, the importance of non-equilibrium dynamics for photon production in the late stages of relativistic heavy-ion collisions is assessed. More concretely, a hybrid model consisting of the hydrodynamics code MUSIC and the hadronic transport model SMASH is employed to simulate heavy-ion collisions at RHIC and LHC energies in view of photon production. The results presented in the following are published in [4].

While hadronic observables measured at RHIC and at the LHC are well described with hydrodynamics+transport hybrid models, photon data remain a challenge. As described in Sec. 1.2.3, no theoretical model can simultaneously describe the measured yield and elliptic flow of direct photons at mid-rapidity, which is referred to as the *direct photon puzzle* [142]. The magnitude of the momentum anisotropy of direct photons measured by PHENIX [127, 129] and ALICE [131] is of similar magnitude as that of pions. This is understood to stem from the anisotropic flow velocity of the medium that is small at initialization but large at later times, when the pions are produced. The large momentum anisotropy of direct photons therefore demands an understanding of the electromagnetic emissivity in the later, hadronic stages of the collision.
Up to now, the production of photons in the late stages of heavy-ion collisions has in most cases been accounted for within macroscopic frameworks. Relativistic hydrodynamics is employed and the temperature profile of the evolution folded with thermal photon emission rates [134, 140, 141, 248–250]. In addition, previous efforts include photon production in a microscopic approach [251], as well as in a hybrid approach [252]. In contrast to the MUSIC+SMASH hybrid employed in this work, the latter relies on previous results for cross sections describing photon production in $2 \to 2$ scatterings (see [253]), and is lacking contributions from bremsstrahlung processes.
In the following, a consistent calculation of photon production is presented, where the thermal

photon emission rates employed for the macroscopic evolution rely on the same field-theoretical framework as the cross sections employed for the microscopic evolution. This allows for assessing the differences between local equilibrium and non-equilibrium photon emission from the late hadronic stage.

3.3.1. The MUSIC+SMASH Hybrid

The `MUSIC+SMASH` hybrid is a hybrid model suitable to describe relativistic heavy-ion collisions at RHIC/LHC energies. In this section, it is employed to study the production of photons at these collision energies. It relies on the viscous hydrodynamics model `MUSIC` for the description of the hot and dense fireball while `SMASH` is applied to model the late hadronic rescattering stage.

Initial Conditions

The $\mathrm{T_RENT_O}$ model provides the initial conditions for the hydrodynamical evolution within the `MUSIC+SMASH` hybrid employed in this work. $\mathrm{T_RENT_O}$ (Reduced Thickness Event-by-event Nuclear Topology) [67] is an effective, non-dynamical initial conditions model that provides Monte Carlo entropy profiles. It relies on the assumption that entropy is produced once the participant thickness functions of two nuclei eikonally overlap. If this condition is met, the colliding nuclei are represented by a fluctuating, reduced thickness function which is proportional to the initial transverse entropy distribution. The conversion of the reduced nuclear thickness function into an entropy distribution is realized with a scalar field whose parameters are tuned to match experimental measurements.

In this work, $\mathrm{T_RENT_O}$ is applied to provide initial conditions for Au+Au collisions at $\sqrt{s_{NN}} = 200.0$ GeV and Pb+Pb collisions at $\sqrt{s_{NN}} = 2.76$ TeV. An impact parameter of $b = 5$ fm is used, as a proxy for mid-central collisions, that is the 10-20% centrality bin.

Hydrodynamical Evolution

The 3+1D hydrodynamics model `MUSIC` [108, 134, 275, 276] is applied to evolve the hot and dense fireball according to 2^{nd} order relativistic viscous hydrodynamics. It relies on the Kurganov-Tadmor algorithm [107] to solve the hydrodynamic equations (c.f. Eq. (1.8) and Eq. (1.9)). `MUSIC` has already been applied successfully to study anisotropic flow in event-by-event hydrodynamics simulations [275, 277], photon production [134], as well as small systems [278] and transport coefficients [211]. Furthermore, it is embedded in the JETSCAPE project [279], which is a modular integrated software framework to study heavy-ion collisions at high collision energies.

Although `MUSIC` is capable of simulating the evolution of the hot and dense medium in 3+1 dimensions, we fall back to a 2+1D evolution in the context of this work. This is justified from the fact that the observables of interest refer to the mid-rapidity region, where 3+1D and 2+1D are expected to yield identical results. Furthermore, the study conducted in Sec. 3.3 is of qualitative nature. Hence, only a single hydroynamical event is simulated, omitting event-by-event fluctuations as well as viscosities. A focus on ideal hydrodynamics allows for a realistic first test scenario without the uncertainties from non-thermal corrections to the hadronic momentum distribution associated with viscous hydrodynamics (see, e.g., [181, 280, 281] and references therein for a recent discussion). The evolution is initialized from an energy

density profile generated with T_RENT_O at $\tau = 0.4$ fm. At initialization, the transverse flow is set to zero, but transverse flow is created dynamically during the evolution. The equation of state employed matches lattice QCD calculations [19] at higher temperatures and a hadron resonance gas with the SMASH degrees of freedom at lower temperatures [282, 283]. The hydrodynamical evolution is performed down to a temperature of $T = 150$ MeV, where the fluid elements are re-transformed into particles.

Photon Production Thermal photon emission is calculated by folding thermal photon emission rates with the spacetime profile of temperature and flow velocity characterizing the hydrodynamical evolution.
The production of photons in the hydrodynamic stage relies on two contributions: partonic photon production and hadronic photon production. At higher temperatures the relevant degrees of freedom are quarks and gluons; which means electromagnetic emission originates from partonic interactions. The corresponding photon emission rates are those for a weakly-coupled quark-gluon plasma at leading order in the coupling constant g_s [284]. The coupling is fixed with $g_s = 2$. Towards lower temperatures at RHIC/LHC energies the medium undergoes a cross-over to hadronic degrees of freedom. The exact photon emission rates for temperatures at the QCD cross-over is however still under investigation [285–287]. To nonetheless approximate the transition from partonic to hadronic rates in this temperature regime, a transition temperature of $T = 180$ MeV (as e.g. in [134]) is chosen. The photon rates describing photon emission in the hadronic stage include mesonic $2 \to 2$ scatterings of pions, ρ mesons and kaons [264] as well as meson bremsstrahlung [273, 274]. Note, that a subset of the $2 \to 2$ rates employed within MUSIC are those used in Fig. 3.4 to validate the implementation of $2 \to 2$ scatterings in SMASH. This also applied to the bremsstrahlung validation in Fig. 3.5.

MUSIC is capable of simulating photon production from a wide range of production processes, partially beyond what is implemented in SMASH. It is however important that for the benchmark study presented in Sec. 3.3 the hadronic thermal photon rate folded with the hydrodynamic profiles includes only emission channels that are also implemented in SMASH. This benchmark study aims at assessing the importance of non-equilibrium dynamics in the hadronic rescattering stage by confronting photon production via thermal rates and hydrodynamics with its counterpart from hadronic transport. To allow for a methodical comparison, both models should thus rely on the same underlying processes. Hence, the photon production processes considered in the following are:

$$2 \leftrightarrow 2 \text{ scatterings: } \pi + \rho \to \pi + \gamma$$

$$\text{Bremsstrahlung: } \pi + \pi \to \pi + \pi + \gamma$$

The attentive reader might miss the $\pi + \pi \to \rho + \gamma$ scattering process contributing to photon production in $2 \to 2$ scatterings. This process is implemented in the MUSIC photon production framework and also in SMASH. However, it is already implicitly accounted for by the bremsstrahlung processes. To prevent double counting, $2 \to 2$ scatterings are restricted to only $\pi + \rho \to \pi + \gamma$ interactions for the scope of this work. It shall further be noted, that the above listed production channels constitute only a subset of the full hadronic photon production processes. Yet, they provide the leading contributions for photon emission in a hadronic

medium, owing to the large coupling and high abundances of pions and ρ mesons [265, 288]. Hadronic photon production within MUSIC below the transition temperature $T = 180$ MeV thus relies on the thermal photon rates for $2 \to 2$ scatterings and bremsstrahlung processes provided in [264, 273, 274].

Particlization

Particlization of the fluid elements is achieved with a Cooper-Frye sampler provided by [289]. This sampler relies on a freezeout hypersurface of constant temperature, in this case $T = 150$ MeV. The particles are sampled according to the SMASH hadron resonance gas degrees of freedom, where resonances are sampled at their respective pole masses [290, 291].
Similar to the SMASH-hadron-sampler described in Sec. 2.2.3, the sampling procedure within the MUSIC+SMASH hybrid is realized such that first, the mean particle multiplicites are evaluated for each particle species from the properties of the freezeout hypersurface in a grand-canonical ensemble. For each event, the particle multiplicites are sampled from a Poisson distribution around the species' mean multiplicity. Subsequently, the produced particles are assigned momentum according to the Cooper-Frye formular (c.f. Eq. 1.10) via rejection sampling. However, since neither the sampler itself, nor its specific sampling procedure is subject of the presented PhD work, it is not further elaborated on. The interested reader is referred to [290] for an in-depth introduction.

Afterburner Evolution

The resulting particle lists produced by the sampler subsequently serve as initial conditions for the hadronic afterburner evolution via SMASH. This is achieved with the SMASH list modus, as described in Sec. 2.1.6.
The medium is evolved, and the remaining hadronic interactions performed until it is too dilute. Photon emission in $2 \to 2$ scatterings as well as from pion bremsstrahlung is enabled, following the implementation detailed in Sec. 3.2.

3.3.2. Model Configuration

The aim of the study presented in this section is to assess the implications of non-equilibrium dynamics in the late stages of heavy-ion collisions for photon production. This is achieved by comparing two different approaches:

A: $\mathrm{T_RENT_O}$ + Hydrodynamics ($T > 150$ MeV) + Hadronic transport

B: $\mathrm{T_RENT_O}$ + Hydrodynamics ($T > 150$ MeV) +
Hydrodynamics (150 MeV$> T >$120 MeV)

where "setup A" corresponds to the transport (non-equilibrium) description of the late hadronic stage and "setup B" to the approximation of this stage using ideal hydrodynamics. The identical $\mathrm{T_RENT_O}$ event providing the initial conditions is used for both setups. They rely on the MUSIC+SMASH hybrid detailed above, although within "setup B" the non-equilibrium afterburner is replaced by performing the hydrodynamical evolution down to lower temperatures. Note, that for hydrodynamics below ($T > 150$ MeV), the choice of the

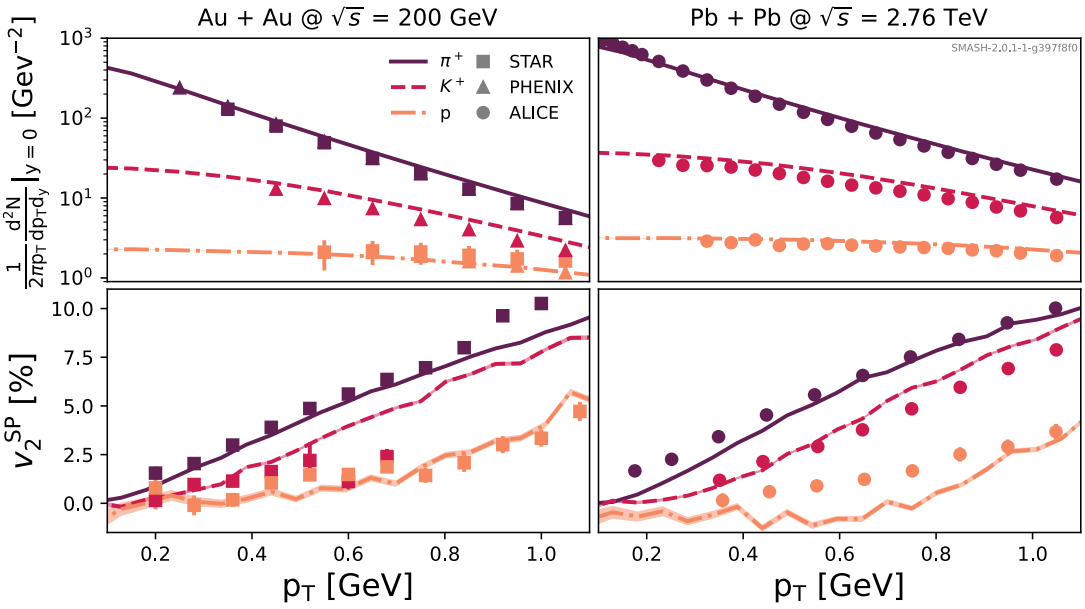

Figure 3.9.: Pion, kaon and proton spectra from the `MUSIC+SMASH` hybrid in comparison to STAR [292, 293], PHENIX [294], and ALICE [295, 296] data in 10-20% most central collisions. The upper panel shows the p_T spectrum, and the lower panel the v_2. RHIC results are displayed on the left, LHC results on the right. The impact parameter used for the T_RENT_O event is b = 5 fm, to match approximately the data's 10-20% centrality bin.

space time region, at which thermal electromagnetic radiation is produced is not well constrained. Hence, there is some ambiguity in choosing this region from contours of uniform temperature. Photon emission from hydrodynamics below ($T > 150$ MeV) is always provided by a range in the context of this work. The lower limit of this range corresponds to photon emission between $T = 150$ MeV (the particlization temperature) and $T = 140$ MeV; the upper limit is for photons radiated between $T = 150$ MeV and $T = 120$ MeV. Note, that these small changes in temperature correspond to a significant increase in spacetime volume of photon emission, considering the rate of cooling of the plasma at late times.
It shall further be noted, that to obtain the afterburner results in "setup A", SMASH version `SMASH-2.0.1-1-g397f8f0` is applied and the results are averaged over 40,000 events. Ten "fractional photons" are used to properly sample the photon angular distributions.

3.3.3. Validation

Before the `MUSIC+SMASH` hybrid is applied to study photon production in Au+Au collisions at $\sqrt{s_{NN}} = 200.0$ GeV and in Pb+Pb collisions at $\sqrt{s_{NN}} = 2.76$ TeV, it is validated with respect to hadron production and the consistency of the employed photon rates. The former is realized in Fig. 3.9, where the left column corresponds to collisions in the RHIC setup, the right column to collisions in the LHC setup. In the upper row, the p_T spectra of pions (solid lines), kaons (dashed lines), and protons (dash-dotted lines) are presented; in the lower row their pT-differential v_2 as determined with the scalar product method (c.f. App. A.4.1). A decent agreement with experimental data from the STAR, PHENIX and ALICE collaboration is obtained. Given the fact that ideal hydrodynamics is used, initialized from one single

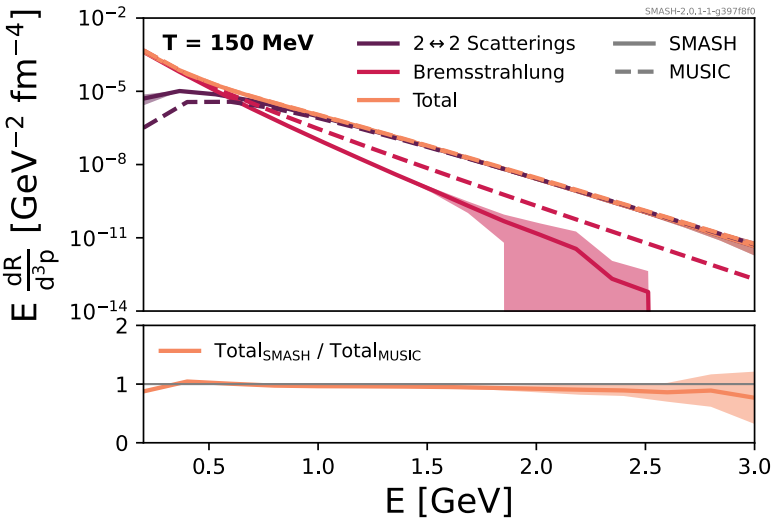

Figure 3.10.: Comparison of the thermal photon rates at T = 150 MeV as used in MUSIC (dashed lines) to the photon rate extracted from SMASH (solid lines) in an infinite matter setup, according to their process origins. The lower panel shows the ratio of the total thermal photon rates from SMASH to those used in MUSIC .

T_RENT_O event, this is considered a sufficiently good validation of the presented model for the purpose of the qualitative study that is to be conducted.
In addition, the thermal photon rates that are to be folded with the temperature profile for the macroscopic evolution [264, 273, 274] and the photon rates extracted from the microscopic model in an equilibrium setup are compared in Fig. 3.10 at a temperature of T = 150 MeV. Solid lines denote the results extracted from SMASH, dashed lines the rate employed on top of the hydrodynamical evolution from MUSIC. In the upper panel, the contributions from $2 \to 2$ scatterings and bremsstrahlung as well as their combined total are displayed seperately. The ratio of the total photon rate extracted from SMASH to the total rate used within MUSIC is displayed in the lower panel. The agreement is good, although not perfect. The observed differences are expected for the following reasons: Regarding the photon rate for $2 \to 2$ scatterings, SMASH relies on the extension to broad ρ mesons as detailed in Sec. 3.2.2. The rates employed with MUSIC on the other hand are the parametrizations from [264], wherein the ρ meson is assumed to be stable. Nonetheless, we have decided to make use of this SMASH feature for the sake of a more realistic description rather than a perfectly equivalent comparison. The differences observed in Fig. 3.10 for $2 \to 2$ scatterings are, as expected, in line with observations made in Fig. 3.8. Regarding the bremsstrahlung rate, the deviations found in Fig. 3.5 towards higher photon energies are also observed in Fig. 3.10. They are related to small inconsistencies in the choice of resonance properties and couplings for the photon rates and cross sections, as in greater detail described in Sec. 3.2.1.
Overall, the total photon rates of the two approaches are in good agreement though, as becomes apparent in the lower panel of Fig. 3.10, containing their ratio. This is because in the low energy regime, where the differences in the ρ treatment are most striking, the thermal photon rate is dominated by bremsstrahlung photons. In the higher energy regime, where the mismatch of the bremsstrahlung parameters becomes more relevant, the bremsstrahlung contribution is subleading and photons from $2 \to 2$ scatterings dominate the thermal photon rate.

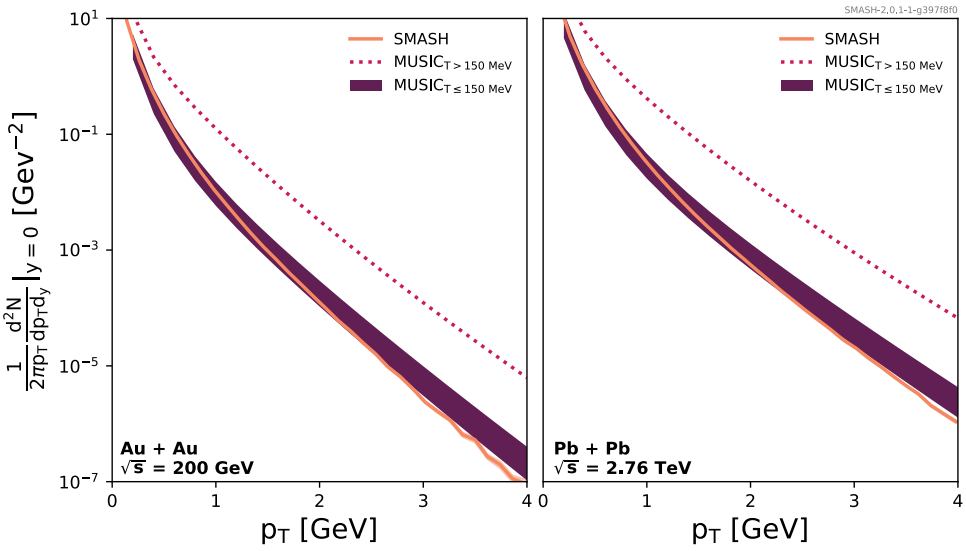

Figure 3.11.: Transverse momentum spectra of photons from the late hadronic rescattering stage in Au+Au collisions at $\sqrt{s_{NN}}$ = 200 GeV (left) and Pb+Pb collisions at $\sqrt{s_{NN}}$ = 2.76 TeV (right). Results of a non-equilibrium treatment in the afterburner are displayed by lines, while bands correspond to the results of hydrodynamics ($T < 150$ MeV) and thermal rates. For the latter, the lower and upper limits are provided by radiating photons down to $T = 140$ MeV and down to $T = 120$ MeV, respectively. The dotted line denotes the contribution of photons originating from hydrodynamics above $T = 150$ MeV.

3.3.4. Results

The hybrid approach detailed in the previous section is applied to calculate photon production in heavy-ion collisions at RHIC and at the LHC: Au+Au collisions at $\sqrt{s_{NN}}$ = 200.0 GeV, and Pb+Pb collisions at $\sqrt{s_{NN}}$ = 2.76 TeV, respectively. In both cases an impact parameter of b = 5 fm is applied as a proxy for a mid-central collision (c.f. Fig. 3.9).

First, the p_T spectra of photons produced in the hadronic rescattering stage are compared between the non-equilibrium treatment ("setup A") and the local equilibrium evolution folded with thermal rates ("setup B") in Fig. 3.11. Results for RHIC are displayed on the left, those for LHC on the right. Solid lines denote the p_T spectra obtained from `SMASH`, bands those from hydrodynamics and thermal rates below $T = 150$ MeV. The reader is reminded that this band accounts for the uncertainty in choosing the temperature range considered for the electromagnetic emission at low temperatures (c.f. Sec. 3.3.2). For reference, the dotted line accounting for contributions above $T = 150$ MeV is presented as well. It is observed that for $p_T \lesssim 2$ GeV, the photon spectrum obtained in the late stage of the non-equilibrium ("setup A") lies entirely within the band determined in the late stage of the local equilibrium ("setup B"). In general, this is the most relevant range of p_T for photons produced at lower energy densities: higher p_T photons are dominated by photons produced at higher temperature, or by prompt photons. Overall, the spectra of photons from the non-equilibrium approach are softer. This is visible across the entire p_T range, although it is more evident for $p_T \gtrsim 2$ GeV, where the non-equilibrium results fall outside the band

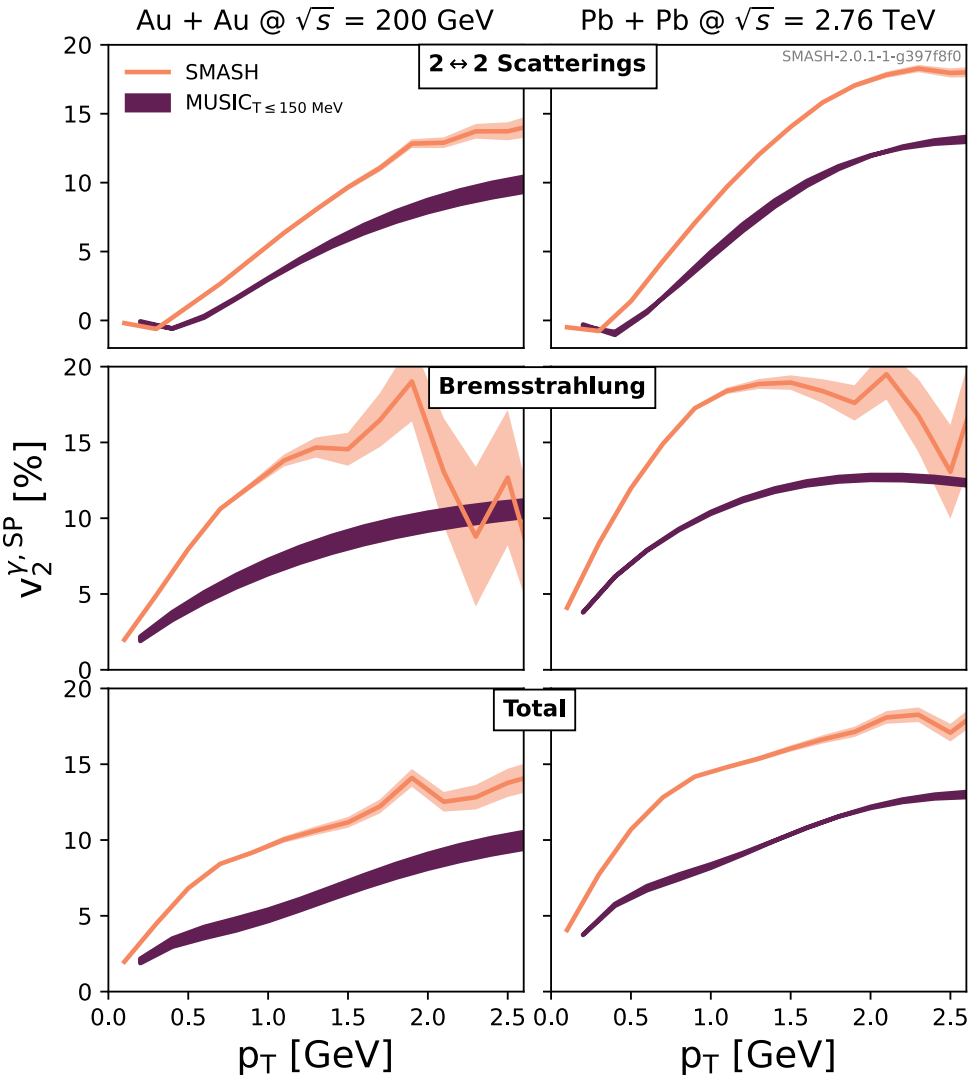

Figure 3.12.: Elliptic flow of photons from the late hadronic rescattering stage in Au+Au collisions at $\sqrt{s_{NN}} = 200$ GeV (left) and Pb+Pb collisions at $\sqrt{s_{NN}} = 2.76$ TeV (right) according to their production processes. Results of a non-equilibrium treatment in the afterburner are displayed by lines, while bands correspond to the results of the low-temperature hydrodynamic description. For the latter, the lower and upper limits are provided by radiating photons from $T = 150$ MeV down to $T = 140$ MeV and down to $T = 120$ MeV, respectively. Bands accompanying the SMASH curves denote the statistical uncertainty therein.

calculated with hydrodynamics and thermal rates. As discussed above, there are differences between the thermal photon emission rates calculated with SMASH and those used in combination with hydrodynamics. However, this difference is very small in the combined bremsstrahlung and $\pi + \rho \to \pi + \gamma$ rates; too small to explain the softening of the spectra observed in Fig. 3.11. The observed softening is thus attributed to non-equilibrium effects.

Second, the p_T-differential v_2 of photons produced in the hadronic rescattering stage is com-

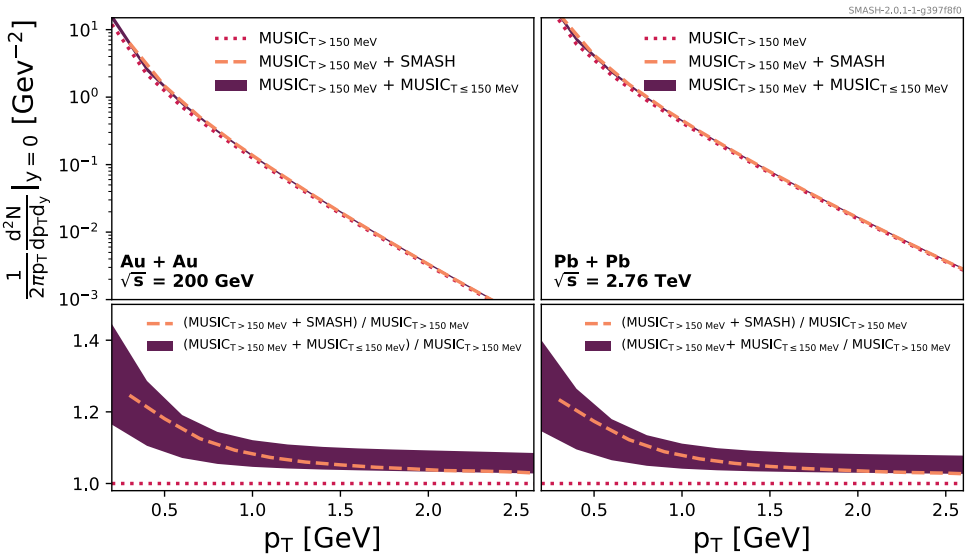

Figure 3.13.: Combined p_T spectra of photons produced at $T > 150$ MeV and in the hadronic afterburner stage in Au+Au collisions at $\sqrt{s_{NN}} = 200$ GeV (left) and Pb+Pb collisions at $\sqrt{s_{NN}} = 2.76$ TeV (right). Results applying a non-equilibrium afterburner are denoted with dashed lines, the low-temperature hydrodynamic description with bands and the high-temperature hydrodynamic description with dotted lines. The lower panel shows the ratio, normalized to the high-temperature hydrodynamic description. Note, that the lower and upper limits of the low-temperature hydrodynamic description are obtained by radiating photons from $T = 150$ MeV down to $T = 140$ MeV and down to $T = 120$ MeV, respectively.

pared between the non-equilibrium treatment obtained within "setup A" and the local equilibrium + thermal rates treatment within "setup B". This is is presented in Fig. 3.12. Again, darker bands denote the results obtained from the local-equilibrium space-time evolution from MUSIC folded with thermal rates, lighter lines the results from the out-of-equilibrium treatment by means of SMASH. The bands accompanying the SMASH curves indicate the statistical uncertainty. Results for Au+Au collisions at $\sqrt{s_{NN}} = 200$ GeV can be found on the left, those for Pb+Pb collisions at $\sqrt{s_{NN}} = 2.76$ TeV on the right. The upper panel shows the v_2 carried by photons produced in $2 \to 2$ scatterings, the centre panel the v_2 of photons from bremsstrahlung processes and the lower panel their combined total, properly weighted by their p_T spectra. The v_2 is calculated with the scalar product method. This is explained in detail in [134, 139] regarding the macroscopic description with MUSIC and in [297] as well as in App. A.4.1 regarding the microscopic description with SMASH.

For $2 \to 2$ scatterings at low transverse momenta, both SMASH and the local-equilibrium hydrodynamic approach yield a small v_2. This stems from the weak energy dependence of the $2 \to 2$ photon rate at low energy, where softer rates result in smaller v_2 than harder rates. At higher p_T, the v_2 characterizing the photons evolved with SMASH notably exceeds that obtained with ideal hydrodynamics.

In the case of bremsstrahlung photons, the v_2 obtained with SMASH is significantly larger than its hydrodynamical counterpart; up to $\approx 70\%$ at RHIC and up to 65% at LHC. Although the thermal rate from SMASH is softer than the thermal rates used with MUSIC (c.f. Fig. 3.10),

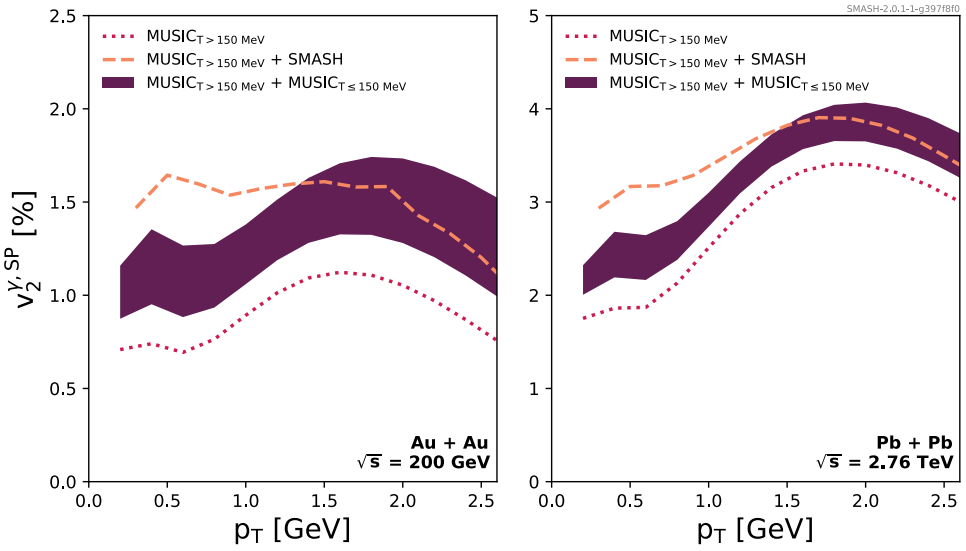

Figure 3.14.: Combined v_2 of photons from the QGP and the hadronic afterburner stage in Au+Au collisions at $\sqrt{s_{NN}} = 200$ GeV (left) and Pb+Pb collisions at $\sqrt{s_{NN}} = 2.76$ TeV (right). Results applying a non-equilibrium afterburner are denoted with dashed lines, the low-temperature hydrodynamic description with bands, and the thermal photons from $T > 150$ MeV with dotted lines. Note, that the lower and upper limits of bands are obtained by radiating photons from $T = 150$ MeV down to $T = 140$ MeV and down to $T = 120$ MeV, respectively.

this $\sim 10\%$ effect does not explain the much larger v_2 obtained in the SMASH afterburner application.

The combined photon v_2 from bremsstrahlung and $2 \to 2$ scatterings is also found to be significantly higher from SMASH than from hydrodynamics, consistent with the larger v_2 observed for the individual channels. This clear enhancement of photon v_2 is attributed to non-equilibrium effects in SMASH. Across the presented p_T range, the enhancement can be quantified to a factor of 1-2 at RHIC as well as at the LHC, relative to the v_2 obtained from hydrodynamics.

The photon p_T spectra and v_2 presented above are extracted solely from the late hadronic rescattering stage. It is further important to combine these contributions with those obtained above $T = 150$ MeV, to assess how significant the found differences remain, once the vast amount of photons produced at earlier times is accounted for. The full in-medium picture is obtained by combining hadronic photons from both approaches with the thermal radiation from partonic and hadronic interactions emitted with $T > 150$ MeV. For the p_T spectra, this is realized in Fig. 3.13, for v_2 in Fig. 3.14. As before, results for RHIC are presented on the left, results for LHC on the right. The pink dotted lines show the contribution with $T > 150$ MeV as obtained by hydrodynamics with thermal rates. The full photon spectra from the non-equilibrium afterburner ("setup A") are denoted with orange dashed lines; those estimated with hydrodynamics and thermal rates at late times ("setup B") with purple bands. For the sake of readability, a ratio plot is included in the lower panel of Fig. 3.14, where the local equilibrium as well as the non-equilibrium contributions combined with the $T > 150$ MeV contribution are normalized to the p_T spectrum of photons produced at $T > 150$ MeV.

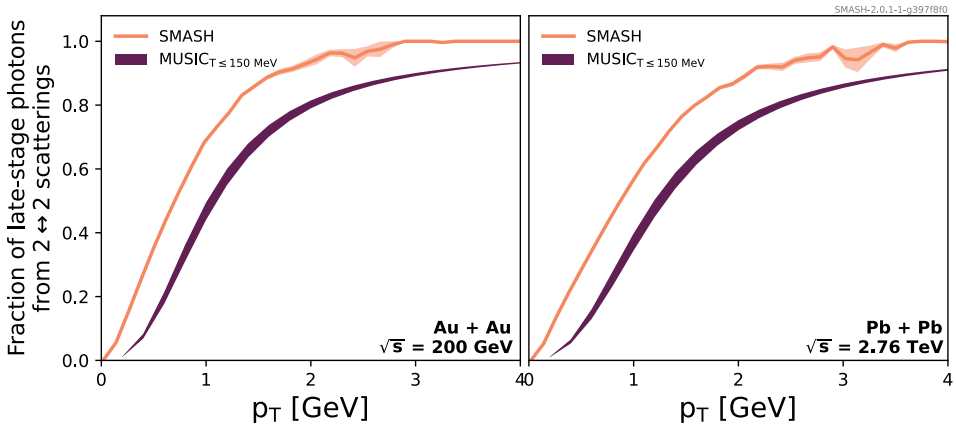

Figure 3.15.: Fraction of late-stage photons originating from $2 \to 2$ processes, compared to the sum of $2 \to 2$ and bremsstrahlung, as a function of p_T . Left panel is for Au+Au collisions at $\sqrt{s_{NN}} = 200$ GeV and right panel for Pb+Pb collisions at $\sqrt{s_{NN}} = 2.76$ TeV. Results of a non-equilibrium treatment in the afterburner are displayed by the lighter lines, while the darker bands correspond to the results of hydrodynamics ($T < 150$ MeV) and thermal rates. For the latter, the lower and upper limits of the bands are provided by radiating photons from $T = 150$ MeV down to $T = 140$ MeV and down to $T = 120$ MeV, respectively. Bands accompanying the SMASH curves denote the statistical uncertainty therein.

Regarding the full p_T spectra, it is found that the results obtained within "setup A", relying on non-equilibrium dynamics for the afterburner, lie entirely within the bands provided by the local equilibrium evolution folded with thermal rates ("setup B"). Yet, the effect of softer photon spectra in the out-of-equilibrium case is also visible for the combined contribution: At lower p_T the `SMASH` curve lies at the upper end of the band provided by hydrodynamics, whereas it approaches its lower end towards higher p_T. Nonetheless, non-equilibrium dynamics in the rescattering stage are found to have only minor implications for photon p_T spectra at RHIC and LHC energies.

For the full photon v_2 on the other hand, some of the differences observed in Fig. 3.12 between the non-equilibrium and local-equilibrium treatment of the late rescattering stage are still visible in the full photon v_2, even after accounting for the contribution of photons produced at $T > 150$ MeV. In Fig. 3.14 this becomes apparent from the orange dotted line representing the non-equilibrium treatment clearly falling out of the band provided by hydrodynamics and thermal rates. At RHIC and at the LHC, the v_2 of photons produced within the "MUSIC + SMASH" setup is significantly larger than that estimated with "MUSIC + MUSIC" for $p_T \lesssim 1.4$ GeV. At higher p_T, the the non-equilibrium result obtained within "setup A" lies within the band provided by the local equilibrium "setup B". This disagreement of the two approaches at low p_T but approximate agreement at high p_T can be explained as follows: At high p_T , the vast majority of photons stem from hydrodynamics at $T > 150$ MeV, exceeding contributions from $T \leq 150$ MeV by multiple orders of magnitude (c.f. Fig. 3.11). Resultingly, the combined v_2 is mostly dominated by contributions from hydrodynamics at $T > 150$ MeV, thus drowning the signal coming from the later stages of the evolution. Moving towards lower p_T, the relative contribution of photons produced in the afterburner stage is, although not dominant, significantly higher (c.f. Fig. 3.11). Consequently, the v_2 carried by these photons is much less diluted than at high p_T and the impact of photons produced in the

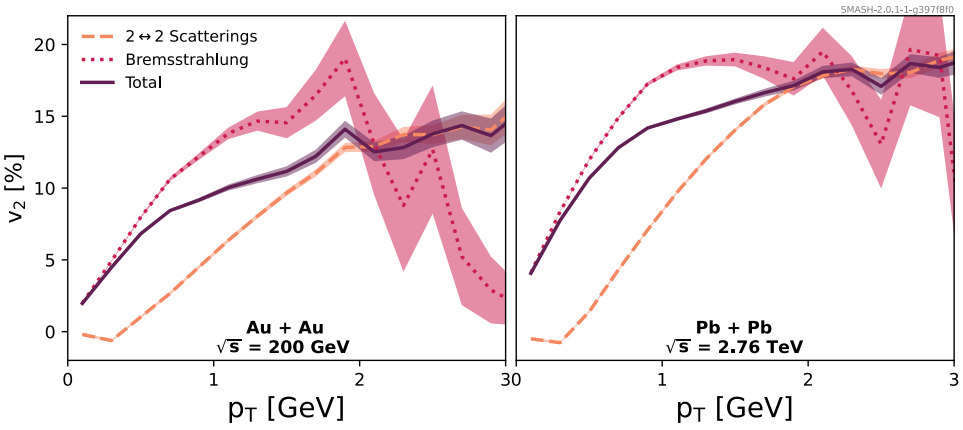

Figure 3.16.: Elliptic flow of photons from the late hadronic stage in Au+Au collisions at $\sqrt{s_{NN}}$ = 200 GeV (left) and Pb+Pb collisions at $\sqrt{s_{NN}}$ = 2.76 TeV (right) as obtained from the non-equilibrium SMASH afterburner. Dashed lines correspond to photons from $2 \to 2$ scatterings, dotted lines to photons from bremsstrahlung, and solid lines to the combined v_2 of photons from $2 \to 2$ and bremsstrahlung processes. Bands denote the statistical uncertainty.

late stages is enhanced. Furthermore, since the v_2 of photons produced in the late stage of the non-equilibrium "setup A" largely exceeds that of photons produced with hydrodynamics and thermal rates at $T > 150$ MeV, this excess is sufficient to notably increase the resulting v_2. Quantitatively, the v_2 determined within the non-equilibrium "setup A" is enhanced by up to 30% at RHIC and by up to 20% at the LHC as compared to the local-equilibrium "setup B". These numbers rely on the assumption that photons are emitted continuously down to a temperature of $T = 120$ MeV in the "MUSIC + MUSIC" setup.
Hence, proper non-equilibrium dynamics in the late rescattering stages of heavy-ion collisions are of fundamental importance for the photon v_2 at low p_T. The application of an equilibrium treatment via hydrodynamics and thermal rates is not sufficient to properly capture the underlying dynamics that lead to an enhancement of v_2 out of equilibrium.

Composition of the Late Stage Photons

In the following, particular emphasis is put on the photons produced in the late rescattering stage to assess the relative contributions of photons originating from $2 \to 2$ scatterings and from bremsstrahlung processes.
For this, the fraction of photons produced in $2 \to 2$ scatterings in the late stages as a function of p_T is presented in Fig. 3.15. Results for RHIC are again displayed on the left, those for LHC on the right. The orange lines, accompanied by statistical uncertainties, correspond to the non-equilibrium treatment via SMASH and the purple band to the local-equilibrium evolution from MUSIC folded with thermal photon rates below $T = 150$ MeV. At both collision energies it is observed that at low p_T the dominant contribution comes from bremsstrahlung processes while at higher p_T $2 \to 2$ scatterings dominate, which is expected from the shapes of the thermal rates in Fig. 3.10. It is also consistent with the relatively low scattering energies of pions in the afterburner: bremsstrahlung photons with $p_T > 2.5$ GeV are rarely produced in the transport evolution. Furthermore, the transition point between bremsstrahlung and $2 \to 2$ scatterings systematically occurs at a smaller p_T for SMASH than

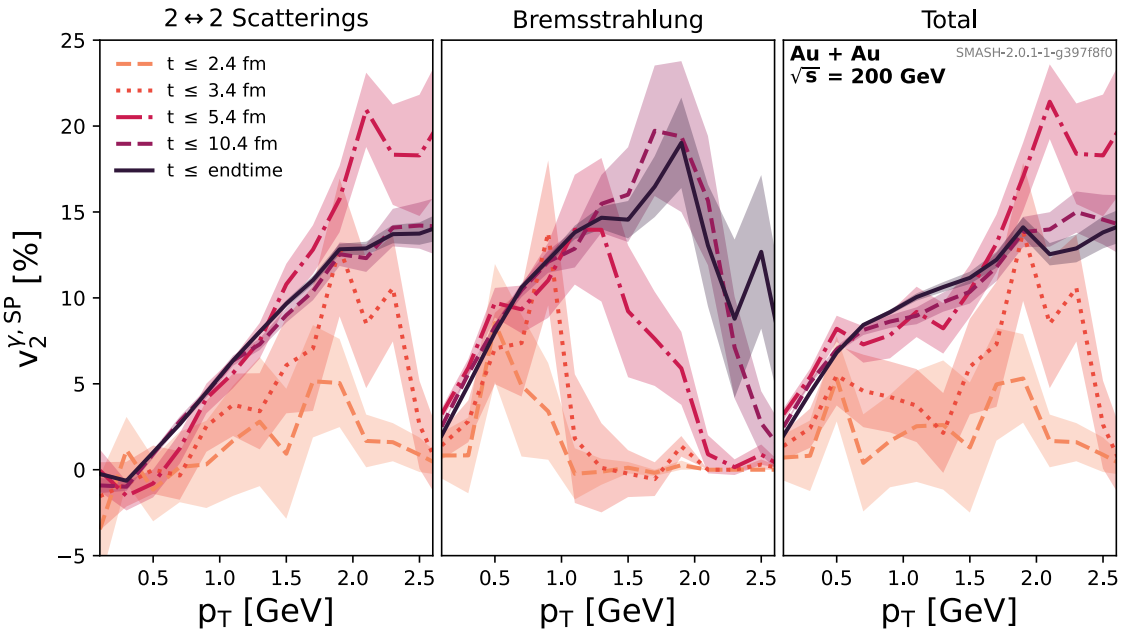

Figure 3.17.: Time evolution of photon v_2 as computed in the hadronic afterburner ("setup A"). The left panel contains the v_2 of photons originating from $2 \to 2$ scatterings, the centre panel the v_2 of photons from bremsstrahlung processes, and the right panel their weighted average. The different lines correspond to different times, up to which photons are considered to determine v_2. Bands denote the statistical uncertainty.

for the hydrodynamics, which is again related to the differences in the rates shown in Fig. 3.10.

This transition of photons produced predominantly in bremsstrahlung processes to photons originating mostly from $2 \to 2$ scatterings is also reflected in the shape and composition of the final v_2, as demonstrated in Fig. 3.16. For the sake of readability, only results obtained with SMASH are presented therein, as the qualitative message is identical. Besides, the very same results are, although arranged differently, already depicted in Fig. 3.12. In Fig. 3.16, the v_2 of photons from $2 \to 2$ scatterings is presented with dashed lines, the v_2 of bremsstrahlung photons with dotted lines, and the solid lines denotes their combined total. Regarding the composition of the total v_2 it becomes evident that at low p_T it is largely dominated by bremsstrahlung photons, while for rising p_T the influence of photons originating from $2 \to 2$ scatterings increases until it is entirely dominated by the latter.
It can thus be concluded that the bremsstrahlung photons from the hadronic stage are mainly responsible for the higher elliptic flow at low transverse momenta observed in the out-of-equilibrium scenario.

Time Evolution of the v_2 Coefficients

In the following, the v_2 from the non-equilibrium afterburner (SMASH) is further analyzed with respect to its time evolution. Its p_T-differential as well as its p_T-integrated version are considered. As collisions at RHIC and LHC energies yield qualitatively similar results, what is presented in the following is restricted to the RHIC setup: Au+Au collisions at

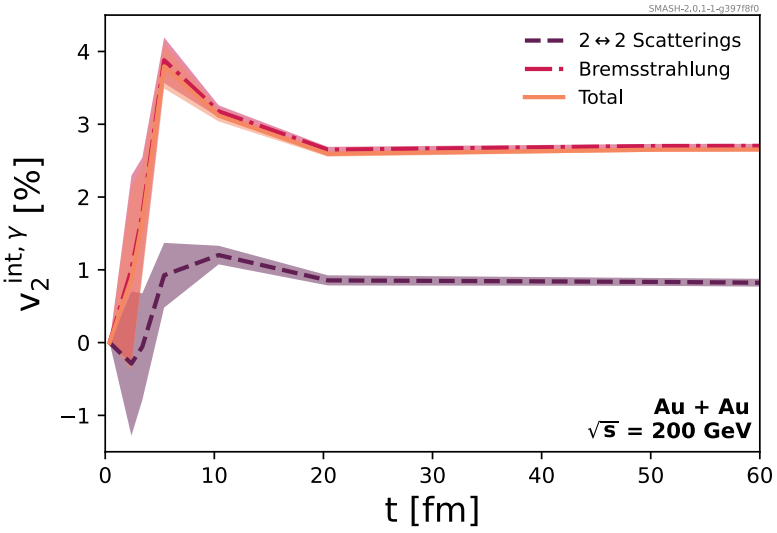

Figure 3.18.: Integrated v_2 of photons as a function of time, split by their process origins and obtained with the SMASH afterburner. Photons from $2 \to 2$ scatterings are displayed with the dashed line, photons from bremsstrahlung processes with the dashed-dotted line and their combination with the solid line. Bands denote the statistical uncertainty.

$\sqrt{s_{NN}} = 200.0$ GeV.
Fig. 3.17 contains the time evolution of the photon v_2 from SMASH according to their production process. $2 \to 2$ scatterings are presented in the left panel, bremsstrahlung processes in the centre and the total contribution on the right. The differently coloured lines correspond to different times until which photons are considered to determine v_2. Earlier times are represented by lighter colours, later times by darker colours. It is observed that for both hadronic scattering channels, that is $2 \to 2$ scatterings and bremsstrahlung, these anisotropies rise fast in time and later decrease slightly. This behaviour is of course also visible in the total v_2 displayed in the rightmost panel.
These findings become more apparent when considering the time evolution of v_2 in its p_T-integrated version, which can be found in Fig. 3.18. The integrated v_2 is presented as a function of time, split by production process. The dashed line denotes the integrated v_2 of photons from $2 \to 2$ scatterings, the dashed-dotted line the v_2 of photons from bremsstrahlung processes, and the solid line their combined total. The rapid increase of photon momentum anisotropies at early times, followed by the small decrease towards later times, as observed in Fig. 3.17, is clearly visible, including a peak around $t \approx 5$ fm.
Furthermore, it becomes apparent how vastly the total integrated v_2 is dominated by photons produced in bremsstrahlung processes and thus by photons produced at low p_T (c.f. Fig. 3.15). Considering the entire p_T range, it can be stated that $\approx 95\%$ of all photons stem from bremsstrahlung processes while only $\approx 5\%$ are produced in $2 \to 2$ scatterings.

The increase of photon v_2 in Fig. 3.17 and in Fig. 3.18 is related to the dynamical production of thermal pions (and other resonances) from the hypersurface. Since this hypersurface is not created at constant time, but at constant temperature, the sampled particles enter the SMASH evolution at different times. This implies that, as time evolves, more and more parent pions come into existence and interact with each other, as well as with ρ mesons. The photons

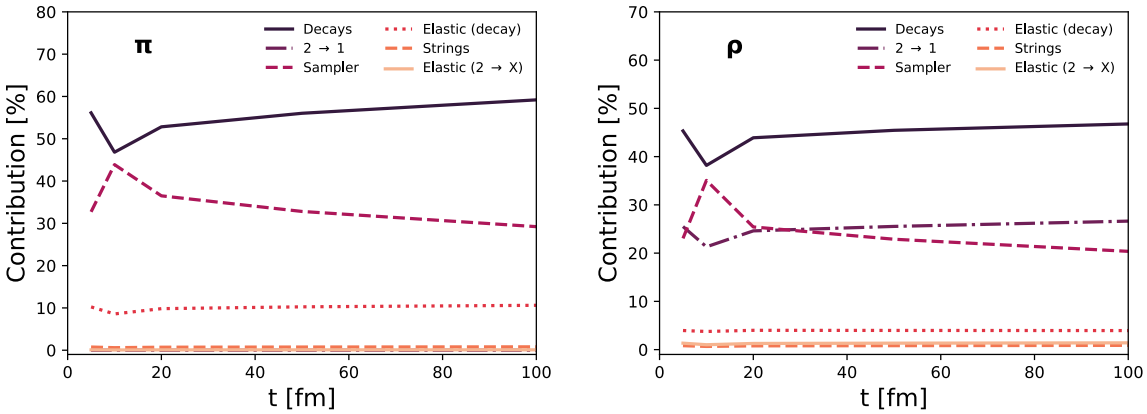

Figure 3.19.: Relative contributions of production processes of pions (left) and ρ meson (right) from whose scatterings a photon is subsequently produced in the late rescattering stage modeled by SMASH. The different production processes are represented by different line styles.

produced in these interactions are characterized by the anisotropies carried by the transition hypersurface, and then directly converted by the sampler. These anisotropies originate directly from the hydrodynamical evolution at transition time and, owing to the hadronic transport being less effective at isotropization than hydrodynamics, the signal sees less suppression at later times.

The decrease on the other hand is majorly attributed to a dynamical feed-down, which is a well known phenomenon (see [123]). The particles created in the particlization process are sampled from the full set of degrees of freedom of the SMASH hadron resonance gas, including high-mass resonances. These resonances are, because of their heavy nature, less sensitive to flow. As the medium evolves, they decay and produce daughter pions and ρ mesons characterized by less v_2 than those directly sampled from the freezeout hypersurface. The decrease of photon anisotropies in time is then a result of the depletion of such high-mass resonances.

Both effects, the dynamical productions of pions and ρ mesons directly from the hypersurface and the dynamical feed-down of high-mass resonances are also evident in Fig. 3.19. Therein, the pions and ρ mesons whose scatterings result in photon production are analyzed regarding their origin. Origin in this case refers to the specific process in which the parent particles were produced. They can either stem directly from the sampler, i.e. the freezeout hypersurface (pink dashed), or be dynamically produced in the evolution. The latter includes pions and ρ mesons that stem from decays of higher resonances (purple solid), from $2 \rightarrow 1$ resonance formations (purple dashed-dotted), from string processes (orange dashed), or elastic scatterings of pions and ρ mesons that either originate from resonance decays (orange dotted) or are produced in inelastic scatterings (orange solid). These relative contributions are presented as a function of time, accounting for all pions and ρ mesons that are produced up to time t. The pion origins are presented on the left, those of ρ mesons on the right. It is clearly found that the sampler contributions rise rapidly at early times for both particle species, corresponding to the dynamical addition of pions and ρ mesons from the hypersurface to the evolution. After $\approx$ 10 fm, their integrated contribution is successively reduced. For decays on the other hand, their contribution is at a minimum after $\approx$ 10 fm and then successively rises, which accounts for the dynamical feed down of high-mass hadronic resonances. This is in line with the interpretations made for Fig. 3.17 and Fig. 3.18.

3.4. Synopsis

In this chapter, particular focus has been laid on the production of photons from hadronic interactions and on the implications of non-equilibrium dynamics for late-stage photon production in relativistic heavy-ion collisions.

First, the differential and total cross sections for photon production in $2 \to 2$ scattering processes $\pi + \rho \to \pi + \gamma$ and $\pi + \pi \to \rho + \gamma$ as well as in bremsstrahlung processes $\pi + \pi \to \pi + \pi + \gamma$ have been derived from effective field theory. The resulting cross sections are collected in the `PHOXTROT` project, which is published on Github [266].
These cross sections have been subsequently implemented in the hadronic transport approach `SMASH` relying on a perturbative treatment. The implementation is validated successfully in an infinite matter simulation. The resulting thermal photon rates agree well with their theoretical expectations as well as with parametrizations of these rates. Furthermore, the photon production framework for $2 \to 2$ scatterings in `SMASH` has been extended to also account for the finite width of the ρ meson.

In continuation, the photon production framework in `SMASH` is employed within a `MUSIC+SMASH` hybrid to study Au+Au collisions at $\sqrt{s_{NN}} = 200$ GeV and Pb+Pb collisions at $\sqrt{s_{NN}} = 2.76$ TeV. The impact of non-equilibrium dynamics in the afterburner is assessed by comparing its outcome to results obtained by approximating the late stages with ideal hydrodynamics and thermal rates. Identical photon production channels, relying on the same field-theoretical frameworks, are considered in the non-equilibrium and the local equilibrium setup to provide a methodical comparison framework. It is found that, at both collision energies, the non-equilibrium treatment results in softer late-stage photon p_T spectra as well as significantly enhanced momentum anisotropies in terms of v_2 as compared to a local-equilibrium treatment. After combination of these late-stage contributions with those estimated from hydrodynamics above $T = 150$ MeV, the differences observed in the p_T spectra are modest. For v_2 on the other hand, a significant enhancement of photon anisotropies is observed both at RHIC and at the LHC for $p_T \lesssim 1.4$ GeV, once relying on non-equilibrium dynamics for the rescattering stage. At higher p_T the resulting v_2 is largely dominated by photons produced above the transition temperature, thus drowning the signal from photons produced in the late hadronic interactions.
Although obtained in a simplified setup omitting event-by-event fluctuations and viscosities, the presented results demonstrate the importance of realistic non-equilibrium dynamics in the late stages of relativistic heavy-ion collisions in view of electromagnetic probes. They are particularly important to properly capture the dynamics at low p_T. In order to assess the implications of late stage hadronic non-equilibrium dynamics on the direct photon puzzle and confront the results with experimental measurements, it is important to repeat the presented study accounting for event-by-event fluctuations as well as viscous corrections in addition to the inclusion of the "primordial" photons computed by means of pQCD [134]. This allows to properly capture deviations from local equilibrium in the hydrodynamics phase above and below the switching temperature. On the other hand, additional challenges are introduced, especially from the uncertainty in mapping viscous hydrodynamics to a non-thermal hadronic momentum distribution. Furthermore, in the presented work, only contributions from π-ρ scatterings and π-π bremsstrahlung are considered. To fully describe hadronic photon production in its entirety, it is important to extend this framework by additional meson-baryon and baryon-baryon interactions and to thus go beyond the leading contributions.

4
Conclusions

The main subject of this thesis is the study of hadron and photon production in relativistic heavy-ion collisions by means of hydrodynamics+transport approaches. Two different kinds of such hybrid approaches are employed in this work, the `SMASH-vHLLE-hybrid` and a `MUSIC+SMASH` hybrid. While the former is capable of simulating heavy-ion collisions covering a wide range of collision energies down to $\sqrt{s_{NN}} = 4.3$ GeV, reproducing the correct baryon stopping powers, the latter provides a framework to consistently model photon production in the hadronic stage of high-energy heavy-ion collisions.

The `SMASH-vHLLE-hybrid` is a novel state-of-the-art hybrid approach whose development constitutes a major contribution to this thesis. It couples the hadronic transport `SMASH` to the 3+1D viscous hydrodynamics approach `vHLLE`. Therein, `SMASH` is employed to provide the fluctuating 3D initial conditions and to model the late hadronic rescattering stage, and `vHLLE` for the fluid dynamical evolution of the hot and dense fireball. The initial conditions are provided on a hypersurface of constant proper time, and the macroscopic evolution of the fireball is carried out down to an energy density of $e_{crit} = 0.5$ GeV/fm^3, where particlization occurs. Consistency at the interfaces is verified in view of global, on-average quantum number conservation and the `SMASH-vHLLE-hybrid` is validated by comparison to `SMASH+CLVisc` as well as `UrQMD+vHLLE` hybrid approaches. The establishment of the `SMASH-vHLLE-hybrid` to theoretically describe heavy-ion collisions at intermediate and high collision energies forms a basis for a range of extensions and future research projects. It is further made available to the heavy-ion community by virtue of being published on Github.
The `SMASH-vHLLE-hybrid` is applied to simulate Au+Au/Pb+Pb collisions between $\sqrt{s_{NN}} = 4.3$ GeV and $\sqrt{s_{NN}} = 200.0$ GeV. A good agreement with the experimentally measured rapidity and transverse mass spectra is obtained. In particular the baryon stopping dynamics are well reproduced at low, intermediate, and high collision energies. Excitation functions for the mid-rapidity yield and mean transverse momentum of pions, protons and kaons are demonstrated to agree well with their experimentally measured counterpart. These results further validate the approach and provide a solid baseline for potential future studies. The importance of annihilations and regenerations of protons and anti-protons is additionally investigated in Au+Au/Pb+Pb collisions between $\sqrt{s_{NN}} = 17.3$ GeV and $\sqrt{s_{NN}} = 5.02$ TeV with the `SMASH-vHLLE-hybrid`. It is found that, regarding the $p + \bar{p} \leftrightarrow 5\ \pi$ reaction, 20-50% (depending on the rapidity range) of the (anti-)proton yield lost to annihilations in the hadronic rescattering stage is restored owing to the back reaction. The back reaction thus constitutes a non-negligible contribution to the final (anti-)proton yield and should not be neglected when modelling the late rescattering stage of heavy-ion collisions.

The `MUSIC+SMASH` hybrid is a hybrid approach ideally suited to model the production of photons in relativistic heavy-ion collisions. Therein, the macroscopic production of photons in the hadronic stage in `MUSIC` relies on the identical effective field theories as

the photon cross sections implemented in SMASH for the microscopic production. The MUSIC+SMASH hybrid thus provides the first consistent framework to the end of hadronic photon production. It accounts for $2 \rightarrow 2$ scattering processes of the kind $\pi + \rho \rightarrow \pi + \gamma$ and pion bremsstrahlung processes $\pi + \pi \rightarrow \pi + \pi + \gamma$. The MUSIC+SMASH hybrid is employed in an ideal 2D setup to systematically assess the importance of non-equliibrium dynamics in the hadronic rescattering stage on mid-rapidity transverse momentum spectra and elliptic flow of photons at RHIC/LHC energies. This is achieved by comparing the outcome of the MUSIC+SMASH hybrid, involving an out-of-equilibrium late rescattering stage, to macroscopically approximating late stage photon production by means of MUSIC, employed down to temperatures well below the switching temperature. It is found that non-equilibrium dynamics have only minor implications for photon transverse momentum spectra, but significantly enhance the photon elliptic flow. At RHIC energies, an enhancement of up to 70%, and at LHC of up to 65% is observed in the non-equilibrium afterburner as compared to its hydrodynamical counterpart. In combination with the large amount of photons produced above the particlization temperature, these differences are modest regarding the transverse momentum spectra, but a significant enhancement of the elliptic flow is observed at low transverse momenta. Below $p_T \approx 1.4$ GeV, the combined v_2 is enhanced by up to 30% at RHIC, and up to 20% at the LHC within the non-equilibrium setup as compared to its approximation via hydrodynamics. Non-equilibrium dynamics in the hadronic rescattering stage are hence important, especially in view of momentum anisotropies at low transverse momenta. These findings thus contribute to the understanding of low-p_T photons produced in heavy-ion collisions at RHIC/LHC energies and the MUSIC+SMASH hybrid employed for this study provides a baseline for additional studies regarding photon production in the future.

Outlook

One major achievement of this PhD work is the creation of the SMASH-vHLLE-hybrid approach. It can serve as a starting point for a range of possible extensions and future research projects. Among these is, for example, the extension by more dynamical initial conditions to provide a more accurate description of heavy-ion collisions at FAIR/NICA collision energies, which aim at the region of the QCD phase diagram where the first order phase transition and the critical end point are expected. In addition, it is important to extend the currently constant viscosities employed for the hydrodynamical evolution in the SMASH-vHLLE-hybrid by a density or temperature dependence to model the fluid more accurately. This further allows to systematically investigate the impact of higher or lower viscosities on final state observables. Furthermore, the SMASH-vHLLE-hybrid can be applied with different equations of state for the fluid dynamical evolution - with and without first order phase transition. It is important to employ these and assess the implications for final state observables, with particular focus on those sensitive to a phase transition.
Another important finding in this PhD work is the importance of non-equilibrium dynamics in the hadronic rescattering stage of high-energy heavy-ion collisions for photon production. Up to now, only a simplified study has been conducted, relying on averaged initial conditions and ideal hydrodynamics. It is important to repeat this study in a more realistic scenario, including event-by-event fluctuations as well as viscosities. Furthermore, it is necessary to combine the contributions of photons produced in the fluid dynamical stage and the hadronic rescattering stage with those produced in the early stages; to ultimately compare to data. The inclusion of additional photon production channels also allows to describe photon production in heavy-ion collisions more accurately. In particular, towards lower collision

energies, it is important to also account for photons from baryon interactions, which are currently not accouted for in the framework presented herein.

To summarize, the approaches and frameworks presented in this thesis provide a good baseline for further extensions and studies in order to improve the understanding of hadron and photon production in relativistic heavy-ion collisions across a wide range of collision energies. More broadly, such future studies of hadrons and photons may contribute to enhance the understandig of the properties of the fundamental building blocks of matter, of which everything that surrounds us is made of.

Bibliography

[1] Anna Schäfer, Juan M. Torres-Rincon, Jonas Rothermel, Niklas Ehlert, Charles Gale, and Hannah Elfner. "Benchmarking a nonequilibrium approach to photon emission in relativistic heavy-ion collisions". In: *Phys. Rev. D* 99.11 (2019), p. 114021.

[2] Anna Schäfer, Juan M. Torres-Rincon, Charles Gale, and Hannah Elfner. "A Non-Equilibrium Approach to Photon Emission from the Late Stages of Relativistic Heavy-Ion Collisions". In: *Nucl. Phys. A* 1005 (2021). Ed. by Feng Liu, Enke Wang, Xin-Nian Wang, Nu Xu, and Ben-Wei Zhang, p. 121772.

[3] Oscar Garcia-Montero, Jan Staudenmaier, Anna Schäfer, Juan M. Torres-Rincon, and Hannah Elfner. "The role of proton-antiproton regeneration in the late stages of heavy-ion collisions". In: (July 2021).

[4] Anna Schäfer, Iurii Karpenko, and Hannah Elfner. "Conservation laws in a novel hybrid approach". In: Sept. 2021.

[5] Anna Schäfer, Oscar Garcia-Montero, Jean-François Paquet, Hannah Elfner, and Charles Gale. "Out-of-Equilibrium Photon Production in the Late Stages of Relativistic Heavy-Ion Collisions". In: (Nov. 2021).

[6] Anna Schäfer, Iurii Karpenko, Xiang-Yu Wu, Jan Hammelmann, and Hannah Elfner. "Particle production in a hybrid approach for a beam energy scan of Au+Au/Pb+Pb collisions between $\sqrt{s_{\mathrm{NN}}} = 4.3$ GeV and $\sqrt{s_{\mathrm{NN}}} = 200.0$ GeV". In: (Dec. 2021).

[7] H. Fritzsch, Murray Gell-Mann, and H. Leutwyler. "Advantages of the Color Octet Gluon Picture". In: *Phys. Lett. B* 47 (1973), pp. 365–368.

[8] Chen-Ning Yang and Robert L. Mills. "Conservation of Isotopic Spin and Isotopic Gauge Invariance". In: *Phys. Rev.* 96 (1954). Ed. by Jong-Ping Hsu and D. Fine, pp. 191–195.

[9] David J. Gross and Frank Wilczek. "Ultraviolet Behavior of Nonabelian Gauge Theories". In: *Phys. Rev. Lett.* 30 (1973). Ed. by J. C. Taylor, pp. 1343–1346.

[10] H. David Politzer. "Reliable Perturbative Results for Strong Interactions?" In: *Phys. Rev. Lett.* 30 (1973). Ed. by J. C. Taylor, pp. 1346–1349.

[11] Siegfried Bethke. "α_s at Zinnowitz 2004". In: *Nucl. Phys. B Proc. Suppl.* 135 (2004). Ed. by J. Blumlein, S. O. Moch, and T. Riemann, pp. 345–352.

[12] Volker Koch. "Aspects of chiral symmetry". In: *Int. J. Mod. Phys. E* 6 (1997), pp. 203–250.

[13] Murray Gell-Mann. "Symmetries of baryons and mesons". In: *Phys. Rev.* 125 (1962), pp. 1067–1084.

[14] R. Rapp, J. Wambach, and H. van Hees. "The Chiral Restoration Transition of QCD and Low Mass Dileptons". In: *Landolt-Bornstein* 23 (2010). Ed. by R. Stock, p. 134.

[15] Yoichiro Nambu and G. Jona-Lasinio. "DYNAMICAL MODEL OF ELEMENTARY PARTICLES BASED ON AN ANALOGY WITH SUPERCONDUCTIVITY. II". In: *Phys. Rev.* 124 (1961). Ed. by T. Eguchi, pp. 246–254.

[16] Paul A. M. Dirac. "Quantum theory of emission and absorption of radiation". In: *Proc. Roy. Soc. Lond. A* 114 (1927), p. 243.

[17] R. P. Feynman. “A Relativistic cutoff for classical electrodynamics”. In: *Phys. Rev.* 74 (1948). Ed. by L. M. Brown, pp. 939–946.

[18] P. A. Zyla et al. “Review of Particle Physics”. In: *PTEP* 2020.8 (2020), p. 083C01.

[19] A. Bazavov et al. “Equation of state in (2+1)-flavor QCD”. In: *Phys. Rev. D* 90 (2014), p. 094503.

[20] Szabocls Borsanyi, Zoltan Fodor, Christian Hoelbling, Sandor D. Katz, Stefan Krieg, and Kalman K. Szabo. “Full result for the QCD equation of state with 2+1 flavors”. In: *Phys. Lett. B* 730 (2014), pp. 99–104.

[21] Kenji Fukushima and Chihiro Sasaki. “The phase diagram of nuclear and quark matter at high baryon density”. In: *Prog. Part. Nucl. Phys.* 72 (2013), pp. 99–154.

[22] Misha A. Stephanov, K. Rajagopal, and Edward V. Shuryak. “Signatures of the tricritical point in QCD”. In: *Phys. Rev. Lett.* 81 (1998), pp. 4816–4819.

[23] Volker Friese. “Prospects for the study of baryon-rich matter at new facilities”. In: *PoS* CORFU2018 (2019). Ed. by Konstantinos Anagnostopoulos et al., p. 186.

[24] Lokesh Kumar. “Review of Recent Results from the RHIC Beam Energy Scan”. In: *Mod. Phys. Lett. A* 28 (2013), p. 1330033.

[25] Ludwik Turko. “Looking for the Phase Transition—Recent NA61/SHINE Results”. In: *Universe* 4.3 (2018). Ed. by David Blaschke, Alexander Ayriyan, Alexandra Friesen, and Hovik Grigorian, p. 52.

[26] Marek Gazdzicki. “Onset of Deconfinement and Critical Point: NA49 and NA61/SHINE at the CERN SPS”. In: *Eur. Phys. J. ST* 155 (2008), pp. 37–44.

[27] Frank Wilczek. “Prelude to Compressed Baryonic Matter”. In: *Lect. Notes Phys.* 814 (2011), pp. 1–10.

[28] V. Kekelidze, A. Kovalenko, R. Lednicky, V. Matveev, I. Meshkov, A. Sorin, and G. Trubnikov. “Prospects for the dense baryonic matter research at NICA”. In: *Nucl. Phys. A* 956 (2016). Ed. by Y. Akiba, S. Esumi, K. Fukushima, H. Hamagaki, T. Hatsuda, T. Hirano, and K. Shigaki, pp. 846–849.

[29] Tetyana Galatyuk. “HADES overview”. In: *Nucl. Phys. A* 931 (2014). Ed. by Peter Braun-Munzinger, Bengt Friman, and Johanna Stachel, pp. 41–51.

[30] T. Ablyazimov et al. “Challenges in QCD matter physics –The scientific programme of the Compressed Baryonic Matter experiment at FAIR”. In: *Eur. Phys. J. A* 53.3 (2017), p. 60.

[31] D. P. Morrison et al. “The PHENIX experiment at RHIC”. In: *Nucl. Phys. A* 638 (1998). Ed. by T. Hatsuda, Y. Miake, K. Yagi, and S. Nagamiya, pp. 565–570.

[32] Jay N. Marx. “The STAR experiment at RHIC”. In: *10th Winter Workshop on Nuclear Dynamics*. Jan. 1994.

[33] K. Aamodt et al. “The ALICE experiment at the CERN LHC”. In: *JINST* 3 (2008), S08002.

[34] G. Aad et al. “The ATLAS Experiment at the CERN Large Hadron Collider”. In: *JINST* 3 (2008), S08003.

[35] S. Chatrchyan et al. “The CMS Experiment at the CERN LHC”. In: *JINST* 3 (2008), S08004.

[36] Jun Xu. "Transport approaches for the description of intermediate-energy heavy-ion collisions". In: *Prog. Part. Nucl. Phys.* 106 (2019), pp. 312–359.

[37] J. Weil et al. "Particle production and equilibrium properties within a new hadron transport approach for heavy-ion collisions". In: *Phys. Rev. C* 94.5 (2016), p. 054905.

[38] O. Buss, T. Gaitanos, K. Gallmeister, H. van Hees, M. Kaskulov, O. Lalakulich, A. B. Larionov, T. Leitner, J. Weil, and U. Mosel. "Transport-theoretical Description of Nuclear Reactions". In: *Phys. Rept.* 512 (2012), pp. 1–124.

[39] W. Ehehalt and W. Cassing. "Relativistic transport approach for nucleus nucleus collisions from SIS to SPS energies". In: *Nucl. Phys. A* 602 (1996), pp. 449–486.

[40] Pawel Danielewicz. "Determination of the mean field momentum dependence using elliptic flow". In: *Nucl. Phys. A* 673 (2000), pp. 375–410.

[41] P. Danielewicz and G. F. Bertsch. "Production of deuterons and pions in a transport model of energetic heavy ion reactions". In: *Nucl. Phys. A* 533 (1991), pp. 712–748.

[42] Y. Nara, N. Otuka, A. Ohnishi, K. Niita, and S. Chiba. "Study of relativistic nuclear collisions at AGS energies from p + Be to Au + Au with hadronic cascade model". In: *Phys. Rev. C* 61 (2000), p. 024901.

[43] C. Hartnack, Z. X. Li, L. Neise, G. Peilert, A. Rosenhauer, H. Sorge, Horst Stoecker, W. Greiner, and J. Aichelin. "Quantum Molecular Dynamics: A Microscopic Model From Unilac to CERN Energies". In: *Nucl. Phys. A* 495 (1989). Ed. by W. Cassing and U. Mosel, pp. 303C–320C.

[44] Akira Ono, Hisashi Horiuchi, Toshiki Maruyama, and Akira Ohnishi. "Antisymmetrized version of molecular dynamics with two nucleon collisions and its application to heavy ion reactions". In: *Prog. Theor. Phys.* 87 (1992), pp. 1185–1206.

[45] H. Sorge, Horst Stoecker, and W. Greiner. "RELATIVISTIC QUANTUM MOLECULAR DYNAMICS APPROACH TO NUCLEAR COLLISIONS AT ULTRARELATIVISTIC ENERGIES". In: *Nucl. Phys. A* 498 (1989). Ed. by G. A. Baym, P. Braun-Munzinger, and S. Nagamiya, pp. 567C–576C.

[46] S. A. Bass et al. "Microscopic models for ultrarelativistic heavy ion collisions". In: *Prog. Part. Nucl. Phys.* 41 (1998), pp. 255–369.

[47] Akira Ono et al. "Comparison of heavy-ion transport simulations: Collision integral with pions and Δ resonances in a box". In: *Phys. Rev. C* 100.4 (2019), p. 044617.

[48] W. Cassing and E. L. Bratkovskaya. "Parton transport and hadronization from the dynamical quasiparticle point of view". In: *Phys. Rev. C* 78 (2008), p. 034919.

[49] Zi-Wei Lin, Che Ming Ko, Bao-An Li, Bin Zhang, and Subrata Pal. "A Multi-phase transport model for relativistic heavy ion collisions". In: *Phys. Rev. C* 72 (2005), p. 064901.

[50] Zhe Xu and Carsten Greiner. "Thermalization of gluons in ultrarelativistic heavy ion collisions by including three-body interactions in a parton cascade". In: *Phys. Rev. C* 71 (2005), p. 064901.

[51] Bin Zhang. "ZPC 1.0.1: A Parton cascade for ultrarelativistic heavy ion collisions". In: *Comput. Phys. Commun.* 109 (1998), pp. 193–206.

[52] Chun Shen. "Dynamic modeling for heavy-ion collisions". In: *19th International Conference on Strangeness in Quark Matter*. Aug. 2021.

[53] Bjoern Schenke, Chun Shen, and Prithwish Tribedy. "Running the gamut of high energy nuclear collisions". In: *Phys. Rev. C* 102.4 (2020), p. 044905.

[54] Hannah Petersen. "Anisotropic flow in transport + hydrodynamics hybrid approaches". In: *J. Phys. G* 41.12 (2014), p. 124005.

[55] Xiang-Yu Wu, Guang-You Qin, Long-Gang Pang, and Xin-Nian Wang. "(3+1)-D viscous hydrodynamics CLVisc at finite net baryon density: identified particle spectra, anisotropic flows and flow fluctuations across BES energies". In: (July 2021).

[56] D. Everett et al. "Multisystem Bayesian constraints on the transport coefficients of QCD matter". In: *Phys. Rev. C* 103.5 (2021), p. 054904.

[57] Chun Shen, Gabriel Denicol, Charles Gale, Sangyong Jeon, Akihiko Monnai, and Bjoern Schenke. "A hybrid approach to relativistic heavy-ion collisions at the RHIC BES energies". In: *Nucl. Phys. A* 967 (2017). Ed. by Ulrich Heinz, Olga Evdokimov, and Peter Jacobs, pp. 796–799.

[58] Jonah E. Bernhard, J. Scott Moreland, Steffen A. Bass, Jia Liu, and Ulrich Heinz. "Applying Bayesian parameter estimation to relativistic heavy-ion collisions: simultaneous characterization of the initial state and quark-gluon plasma medium". In: *Phys. Rev. C* 94.2 (2016), p. 024907.

[59] Iu. A. Karpenko, P. Huovinen, H. Petersen, and M. Bleicher. "Estimation of the shear viscosity at finite net-baryon density from $A + A$ collision data at $\sqrt{s_{NN}} = 7.7 - 200$ GeV". In: *Phys. Rev. C* 91.6 (2015), p. 064901.

[60] Chun Shen, Zhi Qiu, Huichao Song, Jonah Bernhard, Steffen Bass, and Ulrich Heinz. "The iEBE-VISHNU code package for relativistic heavy-ion collisions". In: *Comput. Phys. Commun.* 199 (2016), pp. 61–85.

[61] Tetsufumi Hirano, Pasi Huovinen, Koichi Murase, and Yasushi Nara. "Integrated Dynamical Approach to Relativistic Heavy Ion Collisions". In: *Prog. Part. Nucl. Phys.* 70 (2013), pp. 108–158.

[62] Piotr Bozek and Wojciech Broniowski. "Charge conservation and the shape of the ridge of two-particle correlations in relativistic heavy-ion collisions". In: *Phys. Rev. Lett.* 109 (2012), p. 062301.

[63] Hannah Petersen, Jan Steinheimer, Gerhard Burau, Marcus Bleicher, and Horst Stöcker. "A Fully Integrated Transport Approach to Heavy Ion Reactions with an Intermediate Hydrodynamic Stage". In: *Phys. Rev. C* 78 (2008), p. 044901.

[64] Chiho Nonaka and Steffen A. Bass. "Space-time evolution of bulk QCD matter". In: *Phys. Rev. C* 75 (2007), p. 014902.

[65] R. J. Glauber. "Cross-sections in deuterium at high-energies". In: *Phys. Rev.* 100 (1955), pp. 242–248.

[66] Michael L. Miller, Klaus Reygers, Stephen J. Sanders, and Peter Steinberg. "Glauber modeling in high energy nuclear collisions". In: *Ann. Rev. Nucl. Part. Sci.* 57 (2007), pp. 205–243.

[67] J. Scott Moreland, Jonah E. Bernhard, and Steffen A. Bass. "Alternative ansatz to wounded nucleon and binary collision scaling in high-energy nuclear collisions". In: *Phys. Rev. C* 92.1 (2015), p. 011901.

[68] Bjoern Schenke, Prithwish Tribedy, and Raju Venugopalan. "Event-by-event gluon multiplicity, energy density, and eccentricities in ultrarelativistic heavy-ion collisions". In: *Phys. Rev. C* 86 (2012), p. 034908.

[69] Bjoern Schenke, Prithwish Tribedy, and Raju Venugopalan. "Fluctuating Glasma initial conditions and flow in heavy ion collisions". In: *Phys. Rev. Lett.* 108 (2012), p. 252301.

[70] L. Rezzolla and O. Zanotti. *Relativistic Hydrodynamics*. OUP Oxford, 2013. ISBN: 9780191509919.

[71] Philippe de Forcrand. "Simulating QCD at finite density". In: *PoS* LAT2009 (2009). Ed. by Chuan Liu and Yu Zhu, p. 010.

[72] C. R. Allton, S. Ejiri, S. J. Hands, O. Kaczmarek, F. Karsch, E. Laermann, C. Schmidt, and L. Scorzato. "The QCD thermal phase transition in the presence of a small chemical potential". In: *Phys. Rev. D* 66 (2002), p. 074507.

[73] Sz. Borsanyi, G. Endrodi, Z. Fodor, S. D. Katz, S. Krieg, C. Ratti, and K. K. Szabo. "QCD equation of state at nonzero chemical potential: continuum results with physical quark masses at order $\mathfrak{mu}^2$". In: *JHEP* 08 (2012), p. 053.

[74] R. Bellwied, S. Borsanyi, Z. Fodor, S. D. Katz, A. Pasztor, C. Ratti, and K. K. Szabo. "Fluctuations and correlations in high temperature QCD". In: *Phys. Rev. D* 92.11 (2015), p. 114505.

[75] Z. Fodor and S. D. Katz. "A New method to study lattice QCD at finite temperature and chemical potential". In: *Phys. Lett. B* 534 (2002), pp. 87–92.

[76] Matteo Giordano, Kornel Kapas, Sandor D. Katz, Daniel Nogradi, and Attila Pasztor. "Radius of convergence in lattice QCD at finite μ_B with rooted staggered fermions". In: *Phys. Rev. D* 101.7 (2020), p. 074511.

[77] Volodymyr Vovchenko, Attila Pasztor, Zoltan Fodor, Sandor D. Katz, and Horst Stoecker. "Repulsive baryonic interactions and lattice QCD observables at imaginary chemical potential". In: *Phys. Lett. B* 775 (2017), pp. 71–78.

[78] J. N. Guenther, R. Bellwied, S. Borsanyi, Z. Fodor, S. D. Katz, A. Pasztor, C. Ratti, and K. K. Szabó. "The QCD equation of state at finite density from analytical continuation". In: *Nucl. Phys. A* 967 (2017). Ed. by Ulrich Heinz, Olga Evdokimov, and Peter Jacobs, pp. 720–723.

[79] Matteo Giordano, Kornel Kapas, Sandor D. Katz, Daniel Nogradi, and Attila Pasztor. "New approach to lattice QCD at finite density; results for the critical end point on coarse lattices". In: *JHEP* 05 (2020), p. 088.

[80] J. Steinheimer, S. Schramm, and H. Stocker. "An Effective chiral Hadron-Quark Equation of State". In: *J. Phys. G* 38 (2011), p. 035001.

[81] Juan M. Torres-Rincon and Joerg Aichelin. "Equation of state of a quark-meson mixture in the improved Polyakov–Nambu–Jona-Lasinio model at finite chemical potential". In: *Phys. Rev. C* 96.4 (2017), p. 045205.

[82] A. Peshier, Burkhard Kampfer, and G. Soff. "The Equation of state of deconfined matter at finite chemical potential in a quasiparticle description". In: *Phys. Rev. C* 61 (2000), p. 045203.

[83] J. M. Karthein, D. Mroczek, A. R. Nava Acuna, J. Noronha-Hostler, P. Parotto, D. R. P. Price, and C. Ratti. "Strangeness-neutral equation of state for QCD with a critical point". In: *Eur. Phys. J. Plus* 136.6 (2021), p. 621.

[84] Agnieszka Sorensen and Volker Koch. "Phase transitions and critical behavior in hadronic transport with a relativistic density functional equation of state". In: *Phys. Rev. C* 104.3 (2021), p. 034904.

[85] Volodymyr Vovchenko, Mark I. Gorenstein, and Horst Stoecker. "Monte Carlo approach to the excluded-volume hadron resonance gas in grand canonical and canonical ensembles". In: *Phys. Rev. C* 98.6 (2018), p. 064909.

[86] M. Albright, J. Kapusta, and C. Young. "Matching Excluded Volume Hadron Resonance Gas Models and Perturbative QCD to Lattice Calculations". In: *Phys. Rev. C* 90.2 (2014), p. 024915.

[87] L. M. Satarov, M. N. Dmitriev, and I. N. Mishustin. "Equation of state of hadron resonance gas and the phase diagram of strongly interacting matter". In: *Phys. Atom. Nucl.* 72 (2009), pp. 1390–1415.

[88] Dirk H. Rischke, Mark I. Gorenstein, Horst Stoecker, and Walter Greiner. "Excluded volume effect for the nuclear matter equation of state". In: *Z. Phys. C* 51 (1991), pp. 485–490.

[89] Jacquelyn Noronha-Hostler, Jorge Noronha, and Carsten Greiner. "Hadron Mass Spectrum and the Shear Viscosity to Entropy Density Ratio of Hot Hadronic Matter". In: *Phys. Rev. C* 86 (2012), p. 024913.

[90] Abhijit Majumder and Berndt Muller. "Hadron Mass Spectrum from Lattice QCD". In: *Phys. Rev. Lett.* 105 (2010), p. 252002.

[91] J. Noronha-Hostler, M. Beitel, C. Greiner, and I. Shovkovy. "Dynamics of Chemical Equilibrium of Hadronic Matter Close to T(c)". In: *Phys. Rev. C* 81 (2010), p. 054909.

[92] V. Vovchenko, D. V. Anchishkin, and M. I. Gorenstein. "Hadron Resonance Gas Equation of State from Lattice QCD". In: *Phys. Rev. C* 91.2 (2015), p. 024905.

[93] Keun-Young Kim, Sang-Jin Sin, and Ismail Zahed. "The Chiral Model of Sakai-Sugimoto at Finite Baryon Density". In: *JHEP* 01 (2008), p. 002.

[94] Eva Lope-Oter and Felipe J. Llanes-Estrada. "Unbiased interpolated neutron-star EoS at finite T for modified gravity studies". In: (July 2021).

[95] Anton Motornenko, Jan Steinheimer, Volodymyr Vovchenko, Stefan Schramm, and Horst Stoecker. "Equation of state for hot QCD and compact stars from a mean field approach". In: *Phys. Rev. C* 101.3 (2020), p. 034904.

[96] Amiram Harten, Peter Lax, and Bram van Leer. "On Upstream Differencing and Godunov-Type Schemes for Hyperbolic Conservation Laws". In: *SIAM Rev* 25 (Jan. 1983), pp. 35–61.

[97] Bernd Einfeldt. "On Godunov-Type Methods for Gas Dynamics". In: *Siam Journal on Numerical Analysis - SIAM J NUMER ANAL* 25 (Apr. 1988), pp. 294–318.

[98] V. Schneider, U. Katscher, D. H. Rischke, B. Waldhauser, J. A. Maruhn, and C. D. Munz. "New algorithms for ultrarelativistic numerical hydrodynamics". In: *J. Comput. Phys.* 105 (1993), pp. 92–107.

[99] Iu. Karpenko, P. Huovinen, and M. Bleicher. "A 3+1 dimensional viscous hydrodynamic code for relativistic heavy ion collisions". In: *Comput. Phys. Commun.* 185 (2014), pp. 3016–3027.

[100] Kazuhisa Okamoto, Yukinao Akamatsu, and Chiho Nonaka. "A new relativistic hydrodynamics code for high-energy heavy-ion collisions". In: *Eur. Phys. J. C* 76.10 (2016), p. 579.

[101] Jay P Boris and David L Book. "Flux-corrected transport. I. SHASTA, a fluid transport algorithm that works". In: *Journal of Computational Physics* 11.1 (1973), pp. 38–69. ISSN: 0021-9991.

[102] D.L. Book, J.P. Boris, and K. Hain. "Flux-corrected transport II: Generalizations of the method". In: *Journal of Computational Physics* 18.3 (1975), pp. 248–283. ISSN: 0021-9991.

[103] J.P Boris and D.L Book. "Flux-corrected transport. III. Minimal-error FCT algorithms". In: *Journal of Computational Physics* 20.4 (1976), pp. 397–431. ISSN: 0021-9991.

[104] D. Kuzmin, R. Löhner, and S. Turek. *Flux–Corrected Transport*. Scientific Computation. 3-540-23730-5. Springer, 2005.

[105] Etele Molnar, Hannu Holopainen, Pasi Huovinen, and Harri Niemi. "Influence of temperature-dependent shear viscosity on elliptic flow at backward and forward rapidities in ultrarelativistic heavy-ion collisions". In: *Phys. Rev. C* 90.4 (2014), p. 044904.

[106] Long-Gang Pang, Hannah Petersen, and Xin-Nian Wang. "Pseudorapidity distribution and decorrelation of anisotropic flow within the open-computing-language implementation CLVisc hydrodynamics". In: *Phys. Rev. C* 97.6 (2018), p. 064918.

[107] Alexander Kurganov and Eitan Tadmor. "New High-Resolution Central Schemes for Nonlinear Conservation Laws and Convection–Diffusion Equations". In: *Journal of Computational Physics* 160.1 (2000), pp. 241–282. ISSN: 0021-9991.

[108] Bjoern Schenke, Sangyong Jeon, and Charles Gale. "(3+1)D hydrodynamic simulation of relativistic heavy-ion collisions". In: *Phys. Rev. C* 82 (2010), p. 014903.

[109] Fred Cooper and Graham Frye. "Comment on the Single Particle Distribution in the Hydrodynamic and Statistical Thermodynamic Models of Multiparticle Production". In: *Phys. Rev. D* 10 (1974), p. 186.

[110] Pasi Huovinen and Hannah Petersen. "Particlization in hybrid models". In: *Eur. Phys. J. A* 48 (2012), p. 171.

[111] Mikolaj Chojnacki, Adam Kisiel, Wojciech Florkowski, and Wojciech Broniowski. "THERMINATOR 2: THERMal heavy IoN generATOR 2". In: *Comput. Phys. Commun.* 183 (2012), pp. 746–773.

[112] C. Schwarz, D. Oliinychenko, L. G. Pang, S. Ryu, and H. Petersen. "Different realizations of Cooper–Frye sampling with conservation laws". In: *J. Phys. G* 45.1 (2018), p. 015001.

[113] Dmytro Oliinychenko and Volker Koch. "Microcanonical Particlization with Local Conservation Laws". In: *Phys. Rev. Lett.* 123.18 (2019), p. 182302.

[114] Yukinao Akamatsu, Masayuki Asakawa, Tetsufumi Hirano, Masakiyo Kitazawa, Kenji Morita, Koichi Murase, Yasushi Nara, Chiho Nonaka, and Akira Ohnishi. "Dynamically integrated transport approach for heavy-ion collisions at high baryon density". In: *Phys. Rev. C* 98.2 (2018), p. 024909.

[115] Dmytro Oliinychenko and Hannah Petersen. "Forced canonical thermalization in a hadronic transport approach at high density". In: *J. Phys. G* 44.3 (2017), p. 034001.

[116] A. Andronic, P. Braun-Munzinger, and J. Stachel. "Thermal hadron production in relativistic nuclear collisions: The Hadron mass spectrum, the horn, and the QCD phase transition". In: *Phys. Lett. B* 673 (2009). [Erratum: Phys.Lett.B 678, 516 (2009)], pp. 142–145.

[117] A. Andronic, P. Braun-Munzinger, K. Redlich, and J. Stachel. "The statistical model in Pb-Pb collisions at the LHC". In: *Nucl. Phys. A* 904-905 (2013). Ed. by Thomas Ullrich, Bolek Wyslouch, and John W. Harris, pp. 535c–538c.

[118] J. Stachel, A. Andronic, P. Braun-Munzinger, and K. Redlich. "Confronting LHC data with the statistical hadronization model". In: *J. Phys. Conf. Ser.* 509 (2014). Ed. by David Evans, Simon Hands, Roman Lietava, Rosa Romita, and Orlando Villalobos Baillie, p. 012019.

[119] Anton Andronic, Peter Braun-Munzinger, Krzysztof Redlich, and Johanna Stachel. "Decoding the phase structure of QCD via particle production at high energy". In: *Nature* 561.7723 (2018), pp. 321–330.

[120] Anton Andronic, Peter Braun-Munzinger, Bengt Friman, Pok Man Lo, Krzysztof Redlich, and Johanna Stachel. "The thermal proton yield anomaly in Pb-Pb collisions at the LHC and its resolution". In: *Phys. Lett. B* 792 (2019), pp. 304–309.

[121] Francesco Becattini, Marcus Bleicher, Thorsten Kollegger, Michael Mitrovski, Tim Schuster, and Reinhard Stock. "Hadronization and Hadronic Freeze-Out in Relativistic Nuclear Collisions". In: *Phys. Rev. C* 85 (2012), p. 044921.

[122] Jan Steinheimer, Jörg Aichelin, and Marcus Bleicher. "Nonthermal p/π Ratio at LHC as a Consequence of Hadronic Final State Interactions". In: *Phys. Rev. Lett.* 110.4 (2013), p. 042501.

[123] J. Steinheimer, J. Aichelin, M. Bleicher, and H. Stöcker. "Influence of the hadronic phase on observables in ultrarelativistic heavy ion collisions". In: *Phys. Rev. C* 95.6 (2017), p. 064902.

[124] K. Werner, Iu. Karpenko, T. Pierog, M. Bleicher, and K. Mikhailov. "Event-by-Event Simulation of the Three-Dimensional Hydrodynamic Evolution from Flux Tube Initial Conditions in Ultrarelativistic Heavy Ion Collisions". In: *Phys. Rev. C* 82 (2010), p. 044904.

[125] F. Becattini, Eduardo Grossi, Marcus Bleicher, Jan Steinheimer, and Reinhard Stock. "Centrality dependence of hadronization and chemical freeze-out conditions in heavy ion collisions at $\sqrt{s_{NN}} = 2.76$ TeV". In: *Phys. Rev. C* 90.5 (2014), p. 054907.

[126] Iu. A. Karpenko, Yu. M. Sinyukov, and K. Werner. "Uniform description of bulk observables in the hydrokinetic model of $A + A$ collisions at the BNL Relativistic Heavy Ion Collider and the CERN Large Hadron Collider". In: *Phys. Rev. C* 87.2 (2013), p. 024914.

[127] A. Adare et al. "Observation of direct-photon collective flow in $\sqrt{s_{NN}} = 200$ GeV Au+Au collisions". In: *Phys. Rev. Lett.* 109 (2012), p. 122302.

[128] A. Adare et al. "Centrality dependence of low-momentum direct-photon production in Au+Au collisions at $\sqrt{s_{NN}} = 200$ GeV". In: *Phys. Rev. C* 91.6 (2015), p. 064904.

[129] A. Adare et al. "Azimuthally anisotropic emission of low-momentum direct photons in Au+Au collisions at $\sqrt{s_{NN}} = 200$ GeV". In: *Phys. Rev. C* 94.6 (2016), p. 064901.

[130] Jaroslav Adam et al. "Direct photon production in Pb-Pb collisions at $\sqrt{s_{NN}} = 2.76$ TeV". In: *Phys. Lett. B* 754 (2016), pp. 235–248.

[131] Shreyasi Acharya et al. "Direct photon elliptic flow in Pb-Pb collisions at $\sqrt{s_{NN}} = 2.76$ TeV". In: *Phys. Lett. B* 789 (2019), pp. 308–322.

[132] Jaroslav Adam et al. "Direct photon production in Pb-Pb collisions at $\sqrt{s_{NN}} = 2.76$ TeV". In: *Phys. Lett. B* 754 (2016), pp. 235–248.

[133] Shreyasi Acharya et al. "Direct photon elliptic flow in Pb-Pb collisions at $\sqrt{s_{NN}} = 2.76$ TeV". In: *Phys. Lett. B* 789 (2019), pp. 308–322.

[134] Jean-François Paquet, Chun Shen, Gabriel S. Denicol, Matthew Luzum, Björn Schenke, Sangyong Jeon, and Charles Gale. "Production of photons in relativistic heavy-ion collisions". In: *Phys. Rev. C* 93.4 (2016), p. 044906.

[135] O. Linnyk, V. Konchakovski, T. Steinert, W. Cassing, and E. L. Bratkovskaya. "Hadronic and partonic sources of direct photons in relativistic heavy-ion collisions". In: *Phys. Rev. C* 92.5 (2015), p. 054914.

[136] Hendrik van Hees, Min He, and Ralf Rapp. "Pseudo-critical enhancement of thermal photons in relativistic heavy-ion collisions?" In: *Nucl. Phys. A* 933 (2015), pp. 256–271.

[137] Rupa Chatterjee, Hannu Holopainen, Thorsten Renk, and Kari J. Eskola. "Collision centrality and τ_0 dependence of the emission of thermal photons from fluctuating initial state in ideal hydrodynamic calculation". In: *Phys. Rev. C* 85 (2012), p. 064910.

[138] Ilkka Helenius, Kari J. Eskola, and Hannu Paukkunen. "Centrality dependence of inclusive prompt photon production in d+Au, Au+Au, p+Pb, and Pb+Pb collisions". In: *JHEP* 05 (2013), p. 030.

[139] Young-Min Kim, Chang-Hwan Lee, Derek Teaney, and Ismail Zahed. "Direct photon elliptic flow at energies available at the BNL Relativistic Heavy Ion Collider and the CERN Large Hadron Collider". In: *Phys. Rev. C* 96.1 (2017), p. 015201.

[140] Chun Shen, Ulrich W Heinz, Jean-Francois Paquet, and Charles Gale. "Thermal photons as a quark-gluon plasma thermometer reexamined". In: *Phys. Rev. C* 89.4 (2014), p. 044910.

[141] Rupa Chatterjee, Hannu Holopainen, Thorsten Renk, and Kari J. Eskola. "Enhancement of thermal photon production in event-by-event hydrodynamics". In: *Phys. Rev. C* 83 (2011), p. 054908.

[142] Gabor David. "Direct real photons in relativistic heavy ion collisions". In: *Rept. Prog. Phys.* 83.4 (2020), p. 046301.

[143] Oscar Garcia-Montero, Nicole Löher, Aleksas Mazeliauskas, Jürgen Berges, and Klaus Reygers. "Probing the evolution of heavy-ion collisions using direct photon interferometry". In: *Phys. Rev. C* 102.2 (2020), p. 024915.

[144] Jessica Churchill, Li Yan, Sangyong Jeon, and Charles Gale. "Emission of electromagnetic radiation from the early stages of relativistic heavy-ion collisions". In: *Phys. Rev. C* 103.2 (2021), p. 024904.

[145] Oscar Garcia-Montero. "Non-equilibrium photons from the bottom-up thermalization scenario". In: (Sept. 2019).

[146] L. Oliva, M. Ruggieri, S. Plumari, F. Scardina, G. X. Peng, and V. Greco. "Photons from the Early Stages of Relativistic Heavy Ion Collisions". In: *Phys. Rev. C* 96.1 (2017), p. 014914.

[147] Akihiko Monnai. "Prompt, pre-equilibrium, and thermal photons in relativistic nuclear collisions". In: *J. Phys. G* 47.7 (2020), p. 075105.

[148] Sigtryggur Hauksson, Sangyong Jeon, and Charles Gale. "Photon emission from quark-gluon plasma out of equilibrium". In: *Phys. Rev. C* 97.1 (2018), p. 014901.

[149] Moritz Greif, Florian Senzel, Heiner Kremer, Kai Zhou, Carsten Greiner, and Zhe Xu. "Nonequilibrium photon production in partonic transport simulations". In: *Phys. Rev. C* 95.5 (2017), p. 054903.

[150] Charles Gale, Jean-François Paquet, Bjoern Schenke, and Chun Shen. "Event-plane decorrelation of photons produced in the early stage of heavy-ion collisions". In: *PoS* HardProbes2020 (2021), p. 039.

[151] Charles Gale, Jean-François Paquet, Björn Schenke, and Chun Shen. "Probing Early-Time Dynamics and Quark-Gluon Plasma Transport Properties with Photons and Hadrons". In: *Nucl. Phys. A* 1005 (2021). Ed. by Feng Liu, Enke Wang, Xin-Nian Wang, Nu Xu, and Ben-Wei Zhang, p. 121863.

[152] Lusaka Bhattacharya, Radoslaw Ryblewski, and Michael Strickland. "Photon production from a nonequilibrium quark-gluon plasma". In: *Phys. Rev. D* 93.6 (2016), p. 065005.

[153] Lipei Du, Ulrich Heinz, and Gojko Vujanovic. "Hybrid model with dynamical sources for heavy-ion collisions at BES energies". In: *Nucl. Phys. A* 982 (2019). Ed. by Federico Antinori, Andrea Dainese, Paolo Giubellino, Vincenzo Greco, Maria Paola Lombardo, and Enrico Scomparin, pp. 407–410.

[154] Chun Shen and Björn Schenke. "Dynamical initial state model for relativistic heavy-ion collisions". In: *Phys. Rev. C* 97.2 (2018), p. 024907.

[155] *https://smash-transport.github.io*.

[156] Dmytro Oliinychenko, Vinzent Steinberg, Janus Weil, Jan Staudenmaier, Matthias Kretz, Anna Schäfer, Hannah Elfner (Petersen), Sangwook Ryu, Jonas Rothermel, Justin Mohs, Feng Li, Agnieszka Sorensen, Damjan Mitrovic, LongGang Pang, Jan Hammelmann, Andy Goldschmidt, Markus Mayer, Oscar Garcia-Montero, Natey Kübler, and Nikita. *smash-transport/smash: SMASH-2.0*. Version SMASH-2.0. Dec. 2020.

[157] *http://theory.gsi.de/~smash/doc/current*.

[158] *http://theory.gsi.de/~smash/userguide/current*.

[159] *https://github.com/smash-transport/smash-analysis*.

[160] *http://theory.gsi.de/~smash/smash-analysis/current*.

[161] J. B. Rose, J. M. Torres-Rincon, A. Schäfer, D. R. Oliinychenko, and H. Petersen. "Shear viscosity of a hadron gas and influence of resonance lifetimes on relaxation time". In: *Phys. Rev. C* 97.5 (2018), p. 055204.

[162] Jan Hammelmann, Juan M. Torres-Rincon, Jean-Bernard Rose, Moritz Greif, and Hannah Elfner. "Electrical conductivity and relaxation via colored noise in a hadronic gas". In: *Phys. Rev. D* 99.7 (2019), p. 076015.

[163] Jean-Bernard Rose, Moritz Greif, Jan Hammelmann, Jan A. Fotakis, Gabriel S. Denicol, Hannah Elfner, and Carsten Greiner. "Cross-conductivity: novel transport coefficients to constrain the hadronic degrees of freedom of nuclear matter". In: *Phys. Rev. D* 101.11 (2020), p. 114028.

[164] J. B. Rose, J. M. Torres-Rincon, and H. Elfner. "Inclusive and effective bulk viscosities in the hadron gas". In: *J. Phys. G* 48.1 (2020), p. 015005.

[165] Philipp Dorau, Jean-Bernard Rose, Daniel Pablos, and Hannah Elfner. "Jet Quenching in the Hadron Gas: An Exploratory Study". In: *Phys. Rev. C* 101.3 (2020), p. 035208.

[166] J. Tindall, J. M. Torres-Rincon, J. B. Rose, and H. Petersen. "Equilibration and freeze-out of an expanding gas in a transport approach in a Friedmann–Robertson–Walker metric". In: *Phys. Lett. B* 770 (2017), pp. 532–538.

[167] Jan Staudenmaier, Natey Kübler, and Hannah Elfner. "Particle production in AgAg collisions at $\mathsf{E_{Kin}} = \mathsf{1.58A}$ GeV within a hadronic transport approach". In: *Phys. Rev. C* 103.4 (2021), p. 044904.

[168] Dmytro Oliinychenko and Chun Shen. "Resonance production in PbPb collisions at 5.02 TeV via hydrodynamics and hadronic afterburner". In: (May 2021).

[169] Justin Mohs, Martha Ege, Hannah Elfner, and Markus Mayer. "Collective flow at SIS energies within a hadronic transport approach: Influence of light nuclei formation and equation of state". In: (Dec. 2020).

[170] V. Steinberg, J. Staudenmaier, D. Oliinychenko, F. Li, Ö. Erkiner, and H. Elfner. "Strangeness production via resonances in heavy-ion collisions at energies available at the GSI Schwerionensynchrotron". In: *Phys. Rev. C* 99.6 (2019), p. 064908.

[171] Vinzent Steinberg, Jan Steinheimer, Hannah Elfner, and Marcus Bleicher. "Constraining resonance properties through kaon production in pion–nucleus collisions at low energies". In: *J. Phys. G* 48.2 (2021), p. 025109.

[172] Justin Mohs, Sangwook Ryu, and Hannah Elfner. "Particle Production via Strings and Baryon Stopping within a Hadronic Transport Approach". In: *J. Phys. G* 47.6 (2020), p. 065101.

[173] Dmytro Oliinychenko, Long-Gang Pang, Hannah Elfner, and Volker Koch. "Microscopic study of deuteron production in PbPb collisions at $\sqrt{\mathsf{s}} = \mathsf{2.76TeV}$ via hydrodynamics and a hadronic afterburner". In: *Phys. Rev. C* 99.4 (2019), p. 044907.

[174] Dmytro Oliinychenko, Chun Shen, and Volker Koch. "Deuteron production in AuAu collisions at $\sqrt{\mathsf{s_{NN}}}$ =7–200 GeV via pion catalysis". In: *Phys. Rev. C* 103.3 (2021), p. 034913.

[175] Jan Staudenmaier, Dmytro Oliinychenko, Juan M. Torres-Rincon, and Hannah Elfner. "Deuteron production in relativistic heavy ion collisions via stochastic multiparticle reactions". In: *Phys. Rev. C* 104.3 (2021), p. 034908.

[176] Jan Staudenmaier, Janus Weil, Vinzent Steinberg, Stephan Endres, and Hannah Petersen. "Dilepton production and resonance properties within a new hadronic transport approach in the context of the GSI-HADES experimental data". In: *Phys. Rev. C* 98.5 (2018), p. 054908.

[177] Ying-Xun Zhang et al. "Comparison of heavy-ion transport simulations: Collision integral in a box". In: *Phys. Rev. C* 97.3 (2018), p. 034625.

[178] G. Jhang et al. "Symmetry energy investigation with pion production from Sn+Sn systems". In: *Phys. Lett. B* 813 (2021), p. 136016.

[179] Maria Colonna et al. "Comparison of heavy-ion transport simulations: Mean-field dynamics in a box". In: *Phys. Rev. C* 104.2 (2021), p. 024603.

[180] Jan Hammelmann, Alba Soto-Ontoso, Massimiliano Alvioli, Hannah Elfner, and Mark Strikman. "Influence of the neutron-skin effect on nuclear isobar collisions at energies available at the BNL Relativistic Heavy Ion Collider". In: *Phys. Rev. C* 101.6 (2020), p. 061901.

[181] D. Everett et al. "Phenomenological constraints on the transport properties of QCD matter with data-driven model averaging". In: *Phys. Rev. Lett.* 126.24 (2021), p. 242301.

[182] Stefan Teis. "Transporttheoretische Beschreibung von relativistischen Schwerionenkollisionen bei SIS-Energien". PhD thesis. Giessen U., 1996.

[183] M. Tanabashi et al. "Review of Particle Physics". In: *Phys. Rev. D* 98.3 (2018), p. 030001.

[184] D. M. Manley and E. M. Saleski. "Multichannel resonance parametrization of pi N scattering amplitudes". In: *Phys. Rev. D* 45 (1992), pp. 4002–4033.

[185] J. Cugnon. "Monte Carlo calculation of high-energy heavy-ion interactions". In: *Phys. Rev. C* 22 (1980), pp. 1885–1896.

[186] T. Kodama, S. B. Duarte, K. C. Chung, R. Donangelo, and R. A. M. S. Nazareth. "Causality and relativistic effects in intranuclear cascade calculations". In: *Phys. Rev. C* 29 (1984), pp. 2146–2152.

[187] Damjan Mitrovic. "Lorentz invariance of collision criteria in relativistic heavy-ion collisions". MA thesis. Johann Wolfgang Goethe-University, Frankfurt am Main, Germany, 2020.

[188] Tetsufumi Hirano and Yasushi Nara. "Dynamical modeling of high energy heavy ion collisions". In: *PTEP* 2012 (2012), 01A203.

[189] Jan Staudenmaier. "Multi-particle interactions in hadronic transport approaches". PhD thesis. Johann Wolfgang Goethe-University, Frankfurt am Main, Germany, 2021.

[190] Janus Weil. "Vector Mesons in Medium in a Transport Approach". PhD thesis. Giessen U., 2013.

[191] Dmytro Oliinychenko, Long-Gang Pang, Hannah Elfner, and Volker Koch. "Centrality dependence of deuteron production in Pb+Pb collisions at 2.76 TeV via hydrodynamics and hadronic afterburner". In: *MDPI Proc.* 10.1 (2019). Ed. by Javier Albacete, Jana Bielcikova, Alessandro Grelli, Jiangyong Jia, Jorge Noronha, Hannah Elfner (nee Petersen), Lijuan Ruan, Sevil Salur, Bjoern Schenke, and Anthony Timmins, p. 6.

[192] Dmytro Oliinychenko. "Interfaces between relativistic hydrodynamics and transport for the dynamical description of heavy ion collisions". PhD thesis. Frankfurt U., July 2017.

[193] Jean-Bernard Rose. "Transport coefficients in the hadronic medium". PhD thesis. Goethe U., Frankfurt (main), 2020.

[194] V. Dmitriev, O. Sushkov, and C. Gaarde. "Δ Formation in the ^{1}H (^{3}He, ^{3}H) Δ^{++} Reaction at Intermediate-energies". In: *Nucl. Phys. A* 459 (1986), pp. 503–524.

[195] G. Graef, J. Steinheimer, Feng Li, and Marcus Bleicher. "Deep sub-threshold Ξ and Λ production in nuclear collisions with the UrQMD transport model". In: *Phys. Rev. C* 90 (2014), p. 064909.

[196] Martin Effenberger. "Eigenschaften von Hadronen in Kernmaterie in einem vereinheitlichten Transportmodell". PhD thesis. Giessen U., 1999.

[197] Torbjorn Sjostrand, Stephen Mrenna, and Peter Z. Skands. "A Brief Introduction to PYTHIA 8.1". In: *Comput. Phys. Commun.* 178 (2008), pp. 852–867.

[198] Torbjörn Sjöstrand and Marius Utheim. "Hadron Interactions for Arbitrary Energies and Species, with Applications to Cosmic rays". In: (Aug. 2021).

[199] J. Cugnon, J. Vandermeulen, and D. L'Hote. "Simple parametrization of cross-sections for nuclear transport studies up to the GeV range". In: *Nucl. Instrum. Meth. B* 111 (1996), pp. 215–220.

[200] G. Agakishiev et al. "Baryon resonance production and dielectron decays in proton-proton collisions at 3.5 GeV". In: *Eur. Phys. J. A* 50 (2014), p. 82.

[201] Maciej Rybczynski, Grzegorz Stefanek, Wojciech Broniowski, and Piotr Bozek. "GLISSANDO 2 : GLauber Initial-State Simulation AND mOre. . . , ver. 2". In: *Comput. Phys. Commun.* 185 (2014), pp. 1759–1772.

[202] Ulrich W. Heinz and Kang Seog Lee. "Dileptons from rho mesons as a fast clock for heavy ion collisions". In: *Nucl. Phys. A* 544 (1992). Ed. by T. C. Awes, F. E. Obenshain, F. Plasil, M. R. Strayer, and C. Y. Wong, pp. 503–508.

[203] Guo-Qiang Li and C. M. Ko. "Can dileptons reveal the in-medium properties of vector mesons?" In: *Nucl. Phys. A* 582 (1995), pp. 731–748.

[204] G.B. Arfken, H.J. Weber, and F.E. Harris. *Mathematical Methods for Physicists: A Comprehensive Guide*. Elsevier Science, 2013. ISBN: 9780123846549.

[205] GSL Project Contributors. *GSL - GNU Scientific Library - GNU Project - Free Software Foundation (FSF)*. http://www.gnu.org/software/gsl/. 2010.

[206] *https://github.com/smash-transport/smash-HRG-EoS*.

[207] *https://github.com/yukarpenko/hadronSampler*.

[208] *https://cmake.org*.

[209] *https://github.com/smash-transport/smash-vhlle-hybrid*.

[210] G. S. Denicol, S. Jeon, and C. Gale. "Transport Coefficients of Bulk Viscous Pressure in the 14-moment approximation". In: *Phys. Rev. C* 90.2 (2014), p. 024912.

[211] S. Ryu, J. F. Paquet, C. Shen, G. S. Denicol, B. Schenke, S. Jeon, and C. Gale. "Importance of the Bulk Viscosity of QCD in Ultrarelativistic Heavy-Ion Collisions". In: *Phys. Rev. Lett.* 115.13 (2015), p. 132301.

[212] *https://github.com/yukarpenko/vhlle*.

[213] W. Israel and J. M. Stewart. "Transient relativistic thermodynamics and kinetic theory". In: *Annals Phys.* 118 (1979), pp. 341–372.

[214] I. Karpenko and F. Becattini. "Study of Λ polarization in relativistic nuclear collisions at $\sqrt{s_{\rm NN}} = 7.7$ –200 GeV". In: *Eur. Phys. J. C* 77.4 (2017), p. 213.

[215] *https://github.com/smash-transport/smash-hadron-sampler*.

[216] J. Cleymans, H. Oeschler, K. Redlich, and S. Wheaton. "Status of chemical freeze-out". In: *J. Phys. G* 32 (2006), S165–S170.

[217] J. Cleymans and K. Redlich. "Unified description of freezeout parameters in relativistic heavy ion collisions". In: *Phys. Rev. Lett.* 81 (1998), pp. 5284–5286.

[218] Steffen A. Bass, Hannah Petersen, Cory Quammen, Hal Canary, Christopher G. Healey, and Russell M. Taylor II. "Probing the QCD Critical Point with Relativistic Heavy-Ion Collisions". In: *Central Eur. J. Phys.* 10 (2012), pp. 1278–1281.

[219] Iurii Karpenko. Private Communication. 2019-2021.

[220] Dmytro Oliinychenko, Shuzhe Shi, and Volker Koch. "Effects of local event-by-event conservation laws in ultrarelativistic heavy-ion collisions at particlization". In: *Phys. Rev. C* 102.3 (2020), p. 034904.

[221] Volodymyr Vovchenko. "Correcting event-by-event fluctuations in heavy-ion collisions for exact global conservation laws with the generalized subensemble acceptance method". In: (June 2021).

[222] *https://gitlab.com/snowhitiger/PyVisc*.

[223] S. V. Afanasiev et al. "Energy dependence of pion and kaon production in central Pb + Pb collisions". In: *Phys. Rev. C* 66 (2002), p. 054902.

[224] C. Alt et al. "Energy and centrality dependence of antiproton and proton production in relativistic Pb + Pb collisions at the CERN SPS". In: (Dec. 2005).

[225] C. Alt et al. "Pion and kaon production in central Pb + Pb collisions at 20-A and 30-A-GeV: Evidence for the onset of deconfinement". In: *Phys. Rev. C* 77 (2008), p. 024903.

[226] T. Anticic et al. "Centrality dependence of proton and antiproton spectra in Pb+Pb collisions at 40A GeV and 158A GeV measured at the CERN SPS". In: *Phys. Rev. C* 83 (2011), p. 014901.

[227] H. Sako et al. "Towards the heavy-ion program at J-PARC". In: *Nucl. Phys. A* 931 (2014). Ed. by Peter Braun-Munzinger, Bengt Friman, and Johanna Stachel, pp. 1158–1162.

[228] J. L. Klay et al. "Charged pion production in 2 to 8 agev central au+au collisions". In: *Phys. Rev. C* 68 (2003), p. 054905.

[229] L Ahle et al. "An Excitation function of K- and K+ production in Au + Au reactions at the AGS". In: *Phys. Lett. B* 490 (2000), pp. 53–60.

[230] L. Adamczyk et al. "Bulk Properties of the Medium Produced in Relativistic Heavy-Ion Collisions from the Beam Energy Scan Program". In: *Phys. Rev. C* 96.4 (2017), p. 044904.

[231] C. Blume. "Centrality and energy dependence of proton, light fragment and hyperon production". In: *J. Phys. G* 34 (2007). Ed. by Yu-Gang Ma, Zhi-Yuan Zhu, En-Ke Wang, Xu Cai, Huan-Zhong Huang, and Xin-Nian Wang, S951–954.

[232] J. L. Klay et al. "Longitudinal flow from 2-A-GeV to 8-A-GeV Au+Au collisions at the Brookhaven AGS". In: *Phys. Rev. Lett.* 88 (2002), p. 102301.

[233] B. I. Abelev et al. "Identified particle production, azimuthal anisotropy, and interferometry measurements in Au+Au collisions at s(NN)**(1/2) = 9.2- GeV". In: *Phys. Rev. C* 81 (2010), p. 024911.

[234] C. Alt et al. "Energy and centrality dependence of anti-p and p production and the anti-Lambda/anti-p ratio in Pb+Pb collisions between 20/A-GeV and 158/A-Gev". In: *Phys. Rev. C* 73 (2006), p. 044910.

[235] L Ahle et al. "An Excitation function of K- and K+ production in Au + Au reactions at the AGS". In: *Phys. Lett. B* 490 (2000), pp. 53–60.

[236] L. Adamczyk et al. "Harmonic decomposition of three-particle azimuthal correlations at energies available at the BNL Relativistic Heavy Ion Collider". In: *Phys. Rev. C* 98.3 (2018), p. 034918.

[237] L. Adamczyk et al. "Inclusive charged hadron elliptic flow in Au + Au collisions at $\sqrt{s_{NN}}$ = 7.7 - 39 GeV". In: *Phys. Rev. C* 86 (2012), p. 054908.

[238] Ralf Rapp and Edward V. Shuryak. "Resolving the anti-baryon production puzzle in high-energy heavy ion collisions". In: *Phys. Rev. Lett.* 86 (2001), pp. 2980–2983.

[239] Yinghua Pan and Scott Pratt. *Baryon Annihilation and Regeneration in Heavy Ion Collisions*. 2014.

[240] Oscar Garcia-Montero. Private Communication. 2019-2021.

[241] Jan Staudenmaier. Private Communication. 2019-2021.

[242] Carl B. Dover, T. Gutsche, M. Maruyama, and Amand Faessler. "The Physics of nucleon - anti-nucleon annihilation". In: *Prog. Part. Nucl. Phys.* 29 (1992), pp. 87–174.

[243] P. Koch, Berndt Muller, and Johann Rafelski. "Strangeness in Relativistic Heavy Ion Collisions". In: *Phys. Rept.* 142 (1986), pp. 167–262.

[244] W. Cassing. "Anti-baryon production in hot and dense nuclear matter". In: *Nucl. Phys. A* 700 (2002), pp. 618–646.

[245] Shreyasi Acharya et al. "Production of charged pions, kaons, and (anti-)protons in Pb-Pb and inelastic pp collisions at $\sqrt{s_{NN}}$ = 5.02 TeV". In: *Phys. Rev. C* 101.4 (2020), p. 044907.

[246] S. S. Adler et al. "Identified charged particle spectra and yields in Au+Au collisions at S(NN)**1/2 = 200-GeV". In: *Phys. Rev. C* 69 (2004), p. 034909.

[247] Sangwook Ryu, Jean-François Paquet, Chun Shen, Gabriel Denicol, Björn Schenke, Sangyong Jeon, and Charles Gale. "Effects of bulk viscosity and hadronic rescattering in heavy ion collisions at energies available at the BNL Relativistic Heavy Ion Collider and at the CERN Large Hadron Collider". In: *Phys. Rev. C* 97.3 (2018), p. 034910.

[248] Hendrik van Hees, Charles Gale, and Ralf Rapp. "Thermal Photons and Collective Flow at the Relativistic Heavy-Ion Collider". In: *Phys. Rev. C* 84 (2011), p. 054906.

[249] Rupa Chatterjee and Pingal Dasgupta. "Ratio of photon anisotropic flow in relativistic heavy ion collisions". In: (June 2021).

[250] P. Huovinen, M. Belkacem, P. J. Ellis, and Joseph I. Kapusta. "Dileptons and photons from coarse grained microscopic dynamics and hydrodynamics compared to experimental data". In: *Phys. Rev. C* 66 (2002), p. 014903.

[251] O. Linnyk, E. L. Bratkovskaya, and W. Cassing. "Effective QCD and transport description of dilepton and photon production in heavy-ion collisions and elementary processes". In: *Prog. Part. Nucl. Phys.* 87 (2016), pp. 50–115.

[252] Bjorn Bauchle and Marcus Bleicher. "Direct photon calculations in heavy-ion collisions at $\sqrt{s_{NN}}$ = 62.4 - 200 AGeV in a (3+1) dimensional hybrid approach". In: *Phys. Rev. C* 82 (2010), p. 064901.

[253] Joseph I. Kapusta, P. Lichard, and D. Seibert. "High-energy photons from quark - gluon plasma versus hot hadronic gas". In: *Nucl. Phys. A* 544 (1992). Ed. by T. C. Awes, F. E. Obenshain, F. Plasil, M. R. Strayer, and C. Y. Wong, pp. 485C–492C.

[254] Anna Schäfer. "Photon Production in Hadronic Processes According to an Effective Chiral Field Theory". MA thesis. Johann Wolfgang Goethe-University, Frankfurt am Main, Germany, 2017.

[255] J. Goldstone. "Field Theories with Superconductor Solutions". In: *Nuovo Cim.* 19 (1961), pp. 154–164.

[256] Jeffrey Goldstone, Abdus Salam, and Steven Weinberg. "Broken Symmetries". In: *Phys. Rev.* 127 (1962), pp. 965–970.

[257] Steven Weinberg. "Phenomenological Lagrangians". In: *Physica A* 96.1-2 (1979). Ed. by S. Deser, pp. 327–340.

[258] H. Georgi. "Effective field theory". In: *Ann. Rev. Nucl. Part. Sci.* 43 (1993), pp. 209–252.

[259] Thomas Appelquist and J. Carazzone. "Infrared Singularities and Massive Fields". In: *Phys. Rev. D* 11 (1975), p. 2856.

[260] Steven Weinberg. "Nonlinear realizations of chiral symmetry". In: *Phys. Rev.* 166 (1968), pp. 1568–1577.

[261] J. Gasser and H. Leutwyler. "Chiral Perturbation Theory to One Loop". In: *Annals Phys.* 158 (1984), p. 142.

[262] H. Leutwyler. "On the foundations of chiral perturbation theory". In: *Annals Phys.* 235 (1994), pp. 165–203.

[263] Ulf-G. Meissner. "Chiral QCD: baryon dynamics". In: (July 2000). Ed. by M. Shifman and Boris Ioffe, pp. 417–505.

[264] Simon Turbide, Ralf Rapp, and Charles Gale. "Hadronic production of thermal photons". In: *Phys. Rev. C* 69 (2004), p. 014903.

[265] Simon Turbide. "Electromagnetic radiation from matter under extreme conditions". PhD thesis. Department of Physics, McGill University Montreal, 2006.

[266] *https://github.com/smash-transport/photrot*.

[267] Shuzo Ogawa, Minoru Yonezawa, Shoji Sawada, Tamotsu Ueda, and Wataro Watari. "One boson exchange model". In: *Prog. Theor. Phys. Suppl.* 39 (1967), pp. 140–189.

[268] C. H. Li and C. M. Ko. "Cascade production from anti-kaon induced reactions on lambda and sigma". In: *Nucl. Phys. A* 712 (2002), pp. 110–130.

[269] H. C. Eggers, R. Tabti, Charles Gale, and K. Haglin. "Dilepton bremsstrahlung from pion pion scattering in a relativistic OBE model". In: *Phys. Rev. D* 53 (1996), pp. 4822–4837.

[270] Bjoern Baeuchle and Marcus Bleicher. "Direct photon emission from hadronic sources: Hydrodynamics versus Transport theory". In: *Eur. Phys. J. C* 62 (2009). Ed. by Steffen Bass, Helen Caines, Manuel Calderon de la Barca Sanchez, Alessandro De Falco, Christian Kuhn, James Nagle, Marzia Nardi, Carlos Salgado, and Julia Velkovska, pp. 75–80.

[271] Björn Bäuchle. "Direct Photons in Heavy-Ion Collisions". PhD thesis. Johann Wolfgang Goethe-University, Frankfurt am Main, Germany, 2010.

[272] Juan M. Torres-Rincon. Private Communication. 2016-2017.

[273] W. Liu and R. Rapp. "Low-energy thermal photons from meson-meson bremsstrahlung". In: *Nucl. Phys. A* 796 (2007), pp. 101–121.

[274] Matthew Heffernan, Paul Hohler, and Ralf Rapp. "Universal Parametrization of Thermal Photon Rates in Hadronic Matter". In: *Phys. Rev. C* 91.2 (2015), p. 027902.

[275] Bjorn Schenke, Sangyong Jeon, and Charles Gale. "Elliptic and triangular flow in event-by-event (3+1)D viscous hydrodynamics". In: *Phys. Rev. Lett.* 106 (2011), p. 042301.

[276] *http://www.physics.mcgill.ca/music/*.

[277] Charles Gale, Sangyong Jeon, Björn Schenke, Prithwish Tribedy, and Raju Venugopalan. "Event-by-event anisotropic flow in heavy-ion collisions from combined Yang-Mills and viscous fluid dynamics". In: *Phys. Rev. Lett.* 110.1 (2013), p. 012302.

[278] Chun Shen, Jean-François Paquet, Gabriel S. Denicol, Sangyong Jeon, and Charles Gale. "Collectivity and electromagnetic radiation in small systems". In: *Phys. Rev. C* 95.1 (2017), p. 014906.

[279] J. H. Putschke et al. "The JETSCAPE framework". In: (Mar. 2019).

[280] Mike McNelis, Derek Everett, and Ulrich Heinz. "Particlization in fluid dynamical simulations of heavy-ion collisions: The i S3D module". In: *Comput. Phys. Commun.* 258 (2021), p. 107604.

[281] Denes Molnar. "Self-consistent conversion of a one-component bulk viscous fluid to particles". In: (Dec. 2020).

[282] Jonah E. Bernhard. "Bayesian parameter estimation for relativistic heavy-ion collisions". PhD thesis. Duke U., Apr. 2018.

[283] `https://github.com/j-f-paquet/eos_maker`.

[284] Peter Brockway Arnold, Guy D. Moore, and Laurence G. Yaffe. "Photon emission from quark gluon plasma: Complete leading order results". In: *JHEP* 12 (2001), p. 009.

[285] Marco Cè, Tim Harris, Harvey B. Meyer, Aman Steinberg, and Arianna Toniato. "Rate of photon production in the quark-gluon plasma from lattice QCD". In: *Phys. Rev. D* 102.9 (2020), p. 091501.

[286] G. Jackson and M. Laine. "Testing thermal photon and dilepton rates". In: *JHEP* 11 (2019), p. 144.

[287] Charles Gale, Yoshimasa Hidaka, Sangyong Jeon, Shu Lin, Jean-François Paquet, Robert D. Pisarski, Daisuke Satow, Vladimir V. Skokov, and Gojko Vujanovic. "Production and Elliptic Flow of Dileptons and Photons in a Matrix Model of the Quark-Gluon Plasma". In: *Phys. Rev. Lett.* 114 (2015), p. 072301.

[288] Charles Gale and Kevin L. Haglin. "Electromagnetic radiation from relativistic nuclear collisions". In: (June 2003). Ed. by Rudolph C. Hwa and Xin-Nian Wang, pp. 364–429.

[289] Sangwook Ryu. Private Communication. 2019-2020.

[290] Sangwook Ryu, Sangyong Jeon, Charles Gale, Bjoern Schenke, and Clint Young. "MUSIC with the UrQMD Afterburner". In: *Nucl. Phys. A* 904-905 (2013). Ed. by Thomas Ullrich, Bolek Wyslouch, and John W. Harris, pp. 389c–392c.

[291] Sangwook Ryu. "Integrated description of heavy ion collisions at RHIC and the LHC". PhD thesis. McGill U., 2016.

[292] B. I. Abelev et al. "Identified baryon and meson distributions at large transverse momenta from Au+Au collisions at s(NN)**(1/2) = 200-GeV". In: *Phys. Rev. Lett.* 97 (2006), p. 152301.

[293] J. Adams et al. "Azimuthal anisotropy in Au+Au collisions at s(NN)**(1/2) = 200-GeV". In: *Phys. Rev. C* 72 (2005), p. 014904.

[294] S. S. Adler et al. "Identified charged particle spectra and yields in Au+Au collisions at S(NN)**1/2 = 200-GeV". In: *Phys. Rev. C* 69 (2004), p. 034909.

[295] Betty Abelev et al. "Centrality dependence of π, K, p production in Pb-Pb collisions at $\sqrt{s_{NN}}$ = 2.76 TeV". In: *Phys. Rev. C* 88 (2013), p. 044910.

[296] Betty Bezverkhny Abelev et al. "Elliptic flow of identified hadrons in Pb-Pb collisions at $\sqrt{s_{NN}}$ = 2.76 TeV". In: *JHEP* 06 (2015), p. 190.

[297] Markus Mayer. "Anisotropic flow and the nuclear equation of state in heavy-ion collisions at the GSI-SIS energies". MA thesis. Johann Wolfgang Goethe-University, Frankfurt am Main, Germany, 2017.

[298] C. Patrignani et al. "Review of Particle Physics". In: *Chin. Phys. C* 40.10 (2016), p. 100001.

[299] Natey Kübler. "Vorhersagen der Teilchenproduktion in Ag+Ag Kollisionen bei Ekin=1.67A GeV im Rahmen eines hadronischen Transportmodells". BA thesis. 2019.

[300] Jaroslav Adam et al. "Higher harmonic flow coefficients of identified hadrons in Pb-Pb collisions at $\sqrt{s_{NN}}$ = 2.76 TeV". In: *JHEP* 09 (2016), p. 164.

[301] Georges Aad et al. "Measurement of the azimuthal anisotropy for charged particle production in $\sqrt{s_{NN}}$ = 2.76 TeV lead-lead collisions with the ATLAS detector". In: *Phys. Rev. C* 86 (2012), p. 014907.

[302] Hannu Holopainen, Harri Niemi, and Kari J. Eskola. "Event-by-event hydrodynamics and elliptic flow from fluctuating initial state". In: *Phys. Rev. C* 83 (2011), p. 034901.

[303] Ante Bilandzic, Raimond Snellings, and Sergei Voloshin. "Flow analysis with cumulants: Direct calculations". In: *Phys. Rev. C* 83 (2011), p. 044913.

[304] Ante Bilandzic. "Anisotropic flow measurements in ALICE at the large hadron collider". PhD thesis. Utrecht U., 2012.

[305] Arthur M. Poskanzer and S. A. Voloshin. "Methods for analyzing anisotropic flow in relativistic nuclear collisions". In: *Phys. Rev. C* 58 (1998), pp. 1671–1678.

[306] M. D. McKay, R. J. Beckman, and W. J. Conover. "A Comparison of Three Methods for Selecting Values of Input Variables in the Analysis of Output from a Computer Code". In: *Technometrics* **2** 21 (1979).

[307] M. Botje. "NA49 energy scan results for central lead-lead collisions at the CERN SPS". In: *39th Rencontres de Moriond on QCD and High-Energy Hadronic Interactions*. July 2004, pp. 329–332.

[308] K. Adcox et al. "Single identified hadron spectra from s(NN)**(1/2) = 130-GeV Au+Au collisions". In: *Phys. Rev. C* 69 (2004), p. 024904.

[309] I. G. Bearden et al. "Nuclear stopping in Au + Au collisions at s(NN)**(1/2) = 200-GeV". In: *Phys. Rev. Lett.* 93 (2004), p. 102301.

[310] I. G. Bearden et al. “Charged meson rapidity distributions in central Au+Au collisions at s(NN)**(1/2) = 200-GeV”. In: *Phys. Rev. Lett.* 94 (2005), p. 162301.

[311] J. Adams et al. “Identified particle distributions in pp and Au+Au collisions at s(NN)**(1/2) = 200 GeV”. In: *Phys. Rev. Lett.* 92 (2004), p. 112301.

[312] I. Arsene et al. “Centrality dependent particle production at y=0 and y ˜ 1 in Au + Au collisions at s(NN)**(1/2) = 200-GeV”. In: *Phys. Rev. C* 72 (2005), p. 014908.

[313] S. Mandelstam. “Determination of the pion - nucleon scattering amplitude from dispersion relations and unitarity. General theory”. In: *Phys. Rev.* 112 (1958), pp. 1344–1360.

Appendices

A

Observables in Heavy-Ion Collisions

In the following, different observables in heavy-ion collisions are collected and briefly introduced. This list is however by no means exhaustive, it is rather restricted to observables that are discussed within the scope of this thesis.

A.1. Rapidity Spectra: $\mathrm{d}N/\mathrm{d}y$

The momentum rapidity y is often used as a measure for the relativistic velocity along the longitudinal axis. The rapidity of a particle [298] is defined as

$$y = \frac{1}{2} \ln\left(\frac{E + p_z}{E - p_z}\right), \tag{A.1}$$

with E being the energy of the particle and p_z its momentum along the longitudinal axis. A common observable is the $\mathrm{d}N/\mathrm{d}y$ spectrum, a histogram in rapidity. It encapsulates information about the longitudinal dynamics of the collision. For collisions of identical nuclei, the $\mathrm{d}N/\mathrm{d}y$ spectrum is symmetric around 0. It can further be applied to demonstrate the effect of baryon stopping. Baryon stopping manifests itself in the rapidity spectra of baryons where a transition from a single-peak to a double-peak structure can be observed for rising collision energies. See e.g. the rapidity spectra presented in Sec. 2.4.

A.2. Transverse Momentum and Transverse Mass Spectra: $\mathrm{d}N/\mathrm{d}p_T$ and $\mathrm{d}N/\mathrm{d}m_T$

The transverse momentum and mass of a particle [298] are defined as

$$p_T = \sqrt{p_x^2 + p_y^2} \qquad \text{and} \qquad m_T = \sqrt{m^2 + p_T^2}\,, \tag{A.2}$$

respectively. p_T is the transverse momentum, p_x and p_y the momenta in x and y direction, m_T the transverse mass and m the rest mass of the particle. Histograms in p_T and m_T, that is $\mathrm{d}N/\mathrm{d}p_T$ and $\mathrm{d}N/\mathrm{d}m_T$ spectra, are a common observable to capture the transversal dynamics of the collision. $\mathrm{d}N/\mathrm{d}p_T$ and $\mathrm{d}N/\mathrm{d}m_T$ spectra are usually displayed on a logarithmic y axis, where both exhibit an approximately linear shape. The corresponding slope is then directly related to the softness or hardness of the underlying interactions. Steeper spectra imply softer interactions and thus less energetic collisions. In addition, the slope of $\mathrm{d}N/\mathrm{d}m_T$ spectra can be related to the effective temperature of the medium at kinetic freezeout. As kinetic freezeout, the very moment in the evolution is denoted, after which no further momentum-changing interactions (elastic or inelastic scatterings) occur since the medium is too dilute. The effective temperature can be extracted from the inverse slope parameter obtained from fitting the $\mathrm{d}N/\mathrm{d}m_T$ spectra according to a Boltzmann distribution [299].

A.3. Excitation Functions

Excitation functions provide a means to demonstrate the evolution of an observable upon variation of the collision energy. As such, the x-axis of any excitation function is usually the collision energy in terms of $\sqrt{s_{NN}}$, E_{lab} or p_{lab}. The y-axis on the other hand can in principle be any observable. Within this thesis, excitation functions are presented for the following observables:

- **mid-rapidity yield** The particle yield in the mid-rapidity slice.
- **4π multiplicity** The full particle multiplicity in the entire phase space.
- $\langle \mathbf{p_T} \rangle$ The mean transverse momentum.
- **integrated $\mathbf{v_2}$** The integrated elliptic flow coefficient.
- **integrated $\mathbf{v_3}$** The integrated triangular flow coefficient.

A.4. Harmonic Flow Coefficients: v_n

The azimuthal distribution of particles in the transversal direction gives access to another set of observables, the harmonic flow coefficients. The overlap region in non-central collisions is not isotropic, but characterized by spatial anisotropies. These spatial anisotropies are translated into momentum anisotropies throughout the evolution of the medium, which in turn affect the azimuthal distribution of the final state particles. The latter can be expressed in terms of a Fourier series of the azimuthal angle ϕ [297]:

$$\frac{dN}{d\phi} = \frac{1}{2\pi}\left[1 + \sum_{n=1}^{\infty} 2\, v_n \cos\left[n\,(\phi - \Psi_{RP})\right]\right] \tag{A.3}$$

In the above, N is the particle yield, Ψ_{RP} is the azimuthal angle of the reaction plane and v_n are the harmonic flow coefficients that characterize the collective behaviour of the medium. As such, the first harmonic flow coefficient (v_1) provides an estimate of the directed flow of the medium, the second (v_2) of the ellipticity of the medium and the third (v_3) of the triangularity of the medium. Higher harmonic flow coefficients, e.g. v_4, v_5 or v_6, are also well defined from Eq. (A.3) and have been measured experimentally [300, 301], but are not subject of this work. It shall be noted that even in central collisions, where the initial overlap region is approximately isotropic, momentum anisotropies, although not as pronounced in peripheral collisions, can be observed. These stem from fluctuations in the initial state resulting in small spatial anisotropies that are also translated into momentum anisotropies throughout the evolution.

A.4.1. Determination of v_n

There are different possibilities to determine the anisotropic flow coefficients v_n from a collection of particles. Among these are for example the *reaction plane method* (RP), the *event plane method* (EP), the *scalar product method* (SP) or the determination from *multi-particle correlations* [297, 302–304]. In the context of this thesis, v_2 and v_3 are determined relying on the event plane method as well as on the scalar product method. These two are hence

explained in greater detail in the following.
For the determination of v_n according to both of these methods, the complex event flow vector Q_n is required. It is defined as

$$Q_n = \sum_{j=1}^{N} w_j \, \exp(i \, n \, \phi_j), \tag{A.4}$$

where the sum runs over all particles in the system, w_j is the particles' weight and the angle ϕ is related to the particles' momentum via:

$$\phi = \arctan\left(\frac{p_x}{p_y}\right) \tag{A.5}$$

In the context of this work, the transverse momentum is employed as weight, such that

$$\begin{aligned} w_j &= p_{T,j}^2 \qquad \text{for} \qquad v_2 \\ w_j &= p_{T,j}^3 \qquad \text{for} \qquad v_3 \end{aligned} \tag{A.6}$$

Other choices are also possible though [305]. From the event flow vector is is further possible to calculate the event plane angle Ψ_n via

$$\Psi_n = \frac{1}{n} \arctan\left(\frac{Im(Q_n)}{Re(Q_n)}\right). \tag{A.7}$$

This angle characterizes the spatial orientation of the event plane.

For both the event plane method and the scalar product, the flow of each particle in a certain bin (e.g. in p_T, η, y, ...) is calculated first and the resulting values for v_n averaged over all particles in the bin and over all events. In the case of the integrated v_n, no classification into bins is required, the average is hence performed over all particles in the system as well as all events. The determintion of v_n of a particle with both methods is explained in the following.

Event Plane Method

Within the event plane method, the flow of a particle is determined from

$$v_n = \frac{\langle \cos\left(n \left[\phi - \Psi_n\right]\right) \rangle}{R} \tag{A.8}$$

where R is the resolution factor, accounting for the deviation of the estimated event plane angle Ψ_n from its true orientation. It can be determined by dividing the underlying event into two subevents A and B. In the context of this work, these are associated to positive and negative space-time rapidity η. The resolution factor is then defined as

$$R = \sqrt{\left\langle \cos\left(n \left[\Psi_A - \Psi_B\right]\right) \right\rangle_{events}} \tag{A.9}$$

with Ψ_A and Ψ_B being the event plane angles of the two subevents.

Scalar Product Method

The scalar product method also relies on the flow vector Q_n, as defined in Eq. (A.4), but also on the complex unit vector u_n characterizing each particle. It is defined as

$$u_n = \frac{w_j \, \exp(i \, n \, \phi_j)}{|w_j \, \exp(i \, n \, \phi_j)|} \tag{A.10}$$

relying on the weight w_j as defined in Eq. (A.6). The flow of a particle is, as the name suggests, determined by means of the scalar product of Q_n and u_n

$$v_n = \frac{u_n \, Q_n^*}{R} \tag{A.11}$$

where Q_n^* denotes the complex conjugate of Q_n and R is the resolution factor as defined in Eq. (A.9).

B

Parametrizing the SMASH Hadron Resonance Gas Equation of State

As briefly mentioned in Sec. 2.1.8, different attempts were made to find a parametrization of the SMASH equation of state for it to be applied more easily in hydrodynamics+transport approaches. Unfortunately, these efforts remain unsuccessful, yet the different attempts are briefly documemted in the following.
The purpose of the equation of state is to perform the mapping $(e, n_B, n_Q) \rightarrow (T, p, \mu_B, \mu_Q, \mu_S)$. The coupled equations (c.f. Eqs. 2.22) are currently being solved once for different combinations of e, n_B and n_Q and stored in a table. The resulting thermodynamic quantities need thus be looked up for a given set of (e, n_B, n_Q) and interpolated between the grid points, if necessary. This procedure is time-consuming and introduces uncertainties owing to finite grid effects in the interpolation. An alternative solution consists of directly solving the coupled thermodynamic equations directly within the hydrodynamical simulation for each cell individually, relying on its exact, specific densities. This procedure is time-wise however even less effective and requires large computational resources. A parametrization from which one could directly calculate the thermodynamic quantities and that relies on a limited number of parameters only would thus be the most efficient solution.

The attempts to find a parametrization $f(e, n_B, n_Q)$ of the SMASH hadron resonance gas equation of state relied on polynomial-inspired ansatzes. These include:

1. $f(e, n_B, n_Q) = \sum_{i,j,k=0}^{N_{Dim}} a_{ijk} e^i n_B^j n_Q^k$
2. $f(e, n_B, n_Q) = \frac{\sum_{i,j,k=0}^{N_{Dim}} a_{ijk} e^i n_B^j n_Q^k}{\sum_{i,j,k=0}^{N_{Dim}} b_{ijk} e^i n_B^j n_Q^k} + c_0$
3. $f(e, n_B, n_Q) = \sum_{i,j,k=0}^{N_{Dim}} a_{ijk} \log(b_{ijk}\, e^i)\, n_B^j\, n_Q^k$
4. $f(e, n_B, n_Q) = \sum_{i,j,k=0}^{N_{Dim}} a_{ijk}\, (b_{ijk}\, e^i)^{-c_{ijk}}\, n_B^j\, n_Q^k$

Here, a_{ijk}, b_{ijk}, or c_{ijk} denote the sets of parameters that are to be determined and that fully characterize the parametrization. The major problem with these is however the rapidly growing number of parameters N_{Param} for larger N_{Dim}. To give an example, in the second case $N_{Dim} = 3$ implies $N_{Param} = 55$. Large values for N_{Dim} are however necessary in order to obtain an accurate parametrization, since the equation of state is a non-trivial function.
In addition, a good initial approximation for a_{ijk}, b_{ijk}, and c_{ijk} is essential in order for the solver to succeed. To find such a good initial approximation, a Latin Hypercube Sampling (LHS) procedure [306], where the parameter space is covered in a more efficient way to provide better initial guesses, was explored in addition to a uniform sampling in

parameter space. Neither resulted in satisfying initial guesses and thus parametrizations of the underlying equation of state though.
Furthermore, the possibility of utilizing Chebyshev nodes as grid points to minimize strong oscillations at the edges of the equation of state have been explored, but these did not alleviate the issues either.

To summarize, different possibilities to find a suitable parametrization for the `SMASH` hadron resonance gas equation of state have been explored. Neither of these resulted in a satisfactory solution though. The `SMASH` equation of state is hence published in tabularized format under [206], which still requires interpolations in between the grid points.

C

Additional Hadron Spectra from the SMASH-vHLLE-hybrid

In this chapter, dN/dy and dN/dm_T spectra for π^-, p, and K^- at a range of additional collision energies for central Au+Au/Pb+Pb collisions are presented. The viscosities and smearing parameter employed for the hydrodynamical evolution can be found in Tab. 2.2. Results from the `SMASH-vHLLE-hybrid` are represented by solid lines, those from a pure transport evolution with dashed lines.

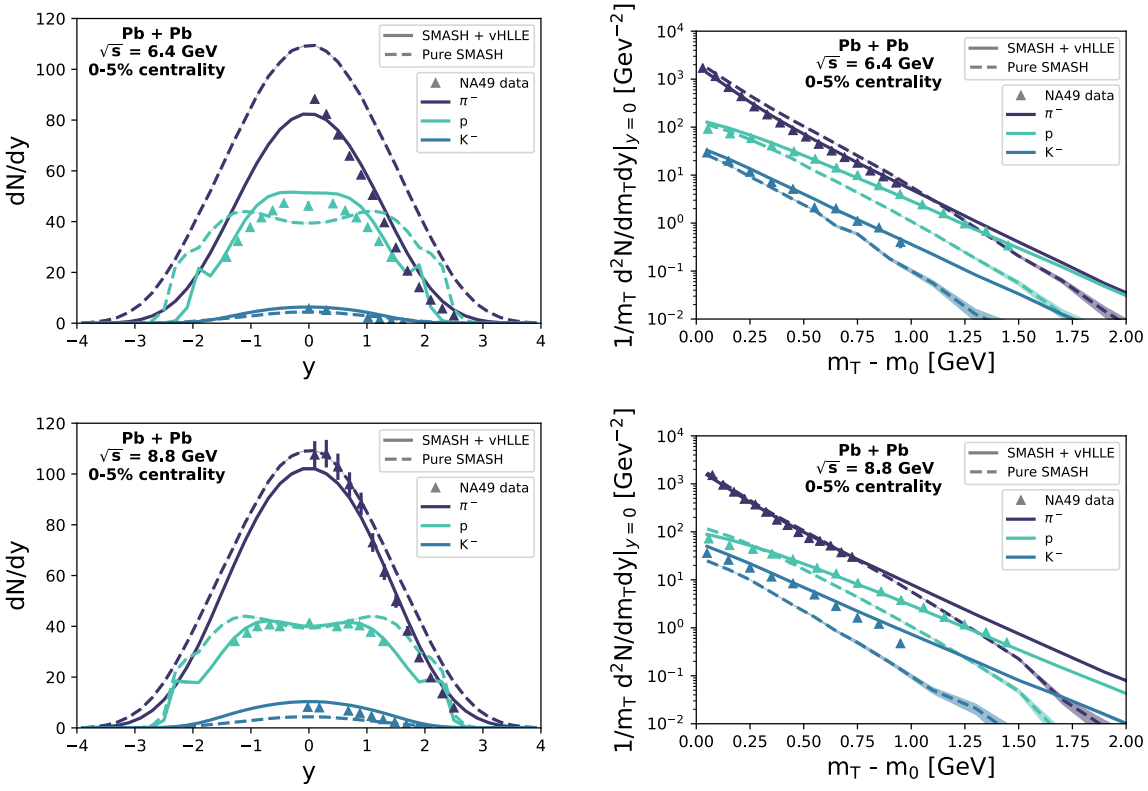

Figure C.1.: dN/dy spectra (left) and m_T spectra (right) of π^-, p, and K^- for central Pb+Pb collisions at $\sqrt{s_{NN}} = 6.4$ GeV (upper) and $\sqrt{s_{NN}} = 8.8$ GeV (lower). The results obtained within the `SMASH-vHLLE-hybrid` (solid lines) are compared to those obtained when running only `SMASH` (dashed lines). The data is from [223–225, 307].

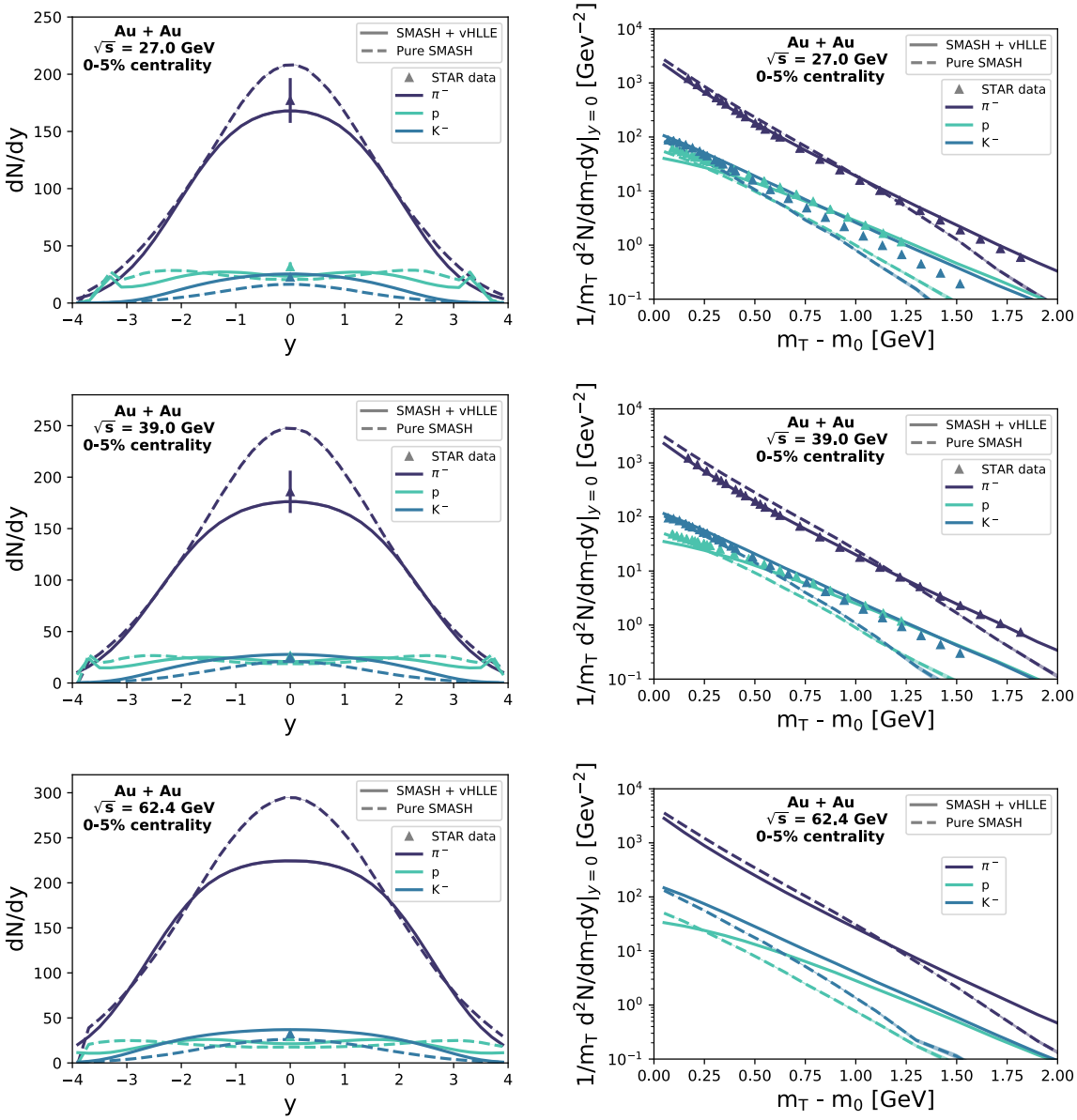

Figure C.2.: dN/dy spectra (left) and m_T spectra (right) of π^-, p, and K^- for central Au+Au collisions at $\sqrt{s_{NN}} = 27.0$ GeV (upper), $\sqrt{s_{NN}} = 39.0$ GeV (center), and $\sqrt{s_{NN}} = 62.4$ GeV (lower). The results obtained within the `SMASH-vHLLE-hybrid` (solid lines) are compared to those obtained when running only `SMASH` (dashed lines). The data is from [230].

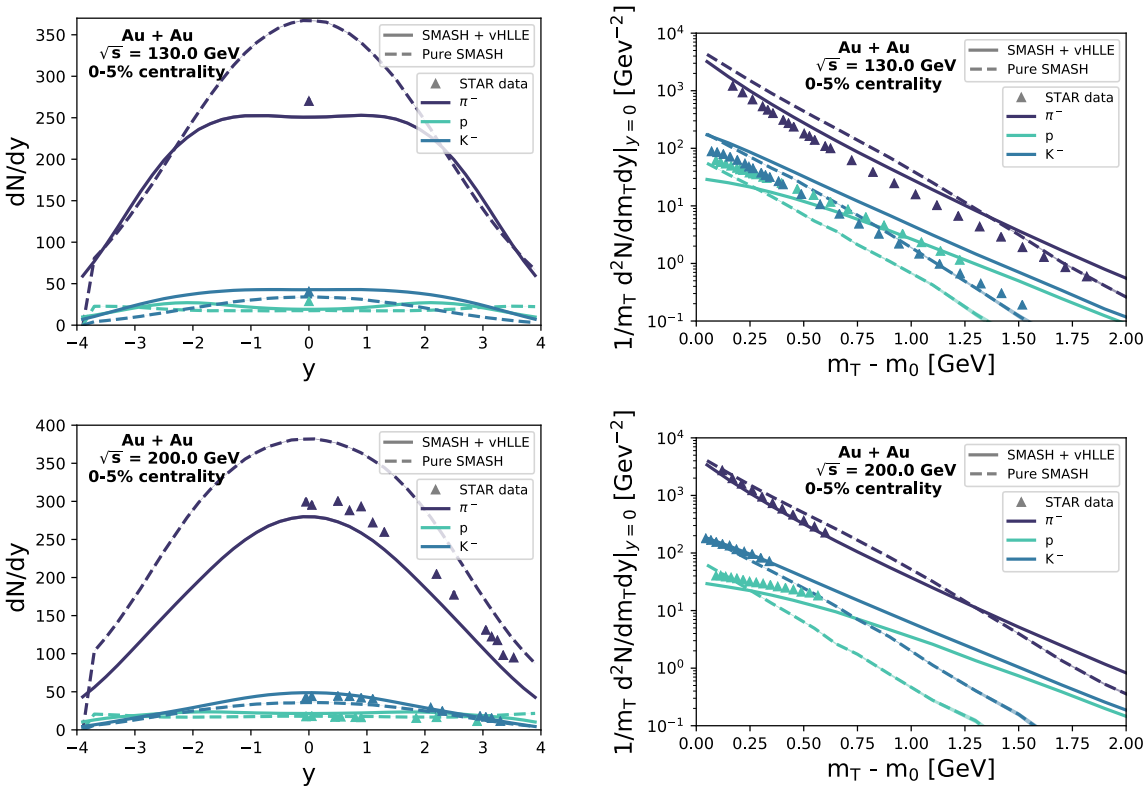

Figure C.3.: dN/dy spectra (left) and m_T spectra (right) of π^-, p, and K^- for central Au+Au collisions at $\sqrt{s_{NN}}$ = 130.0 GeV (upper) and $\sqrt{s_{NN}}$ = 200.0 GeV (lower). The results obtained within the `SMASH-vHLLE-hybrid` (solid lines) are compared to those obtained when running only `SMASH` (dashed lines). The data is from [230, 294, 308–312].

D

Mandelstam Variables and Relativistic Kinematics

Mandelstam variables [313] are the main variables describing $2 \to 2$ scattering processes as they contain information about the energies, momenta and scattering angles of the colliding particles. There are three different channels through which 4-momentum can be exchanged in a $A + B \to C + D$ scattering process: s, t and u-channel. Correspondingly, there are 3 Mandelstam variables, defined as

$$s = (p_A^\mu + p_B^\mu)^2 = (p_C^\mu + p_D^\mu)^2 \tag{D.1}$$

$$t = (p_A^\mu - p_C^\mu)^2 = (p_B^\mu - p_D^\mu)^2 \tag{D.2}$$

$$u = (p_A^\mu - p_D^\mu)^2 = (p_B^\mu - p_C^\mu)^2 \tag{D.3}$$

where p_i^μ is the 4-momentum of the i-th particle. Those three quantities are sufficient to completely describe the kinematics of a $2 \to 2$ scattering process. It is a big advantage, that the Mandelstam variables are Lorentz invariant, e.g. their values are independent of the reference frame. They can thus be used for the transition from one reference frame to another.

As can easily be shown, s, t and u are not independent, but rather related via

$$s + t + u = m_A^2 + m_B^2 + m_C^2 + m_D^2 \tag{D.4}$$

which results from the kinematic property $p^\mu p_\mu = m^2$. Moreover, Eqs. (D.1)-(D.3) relate the contracted 4-momenta of two particles to their masses and one mandelstam variable. To give an example, Eq. (D.2) can be used to find the relation:

$$t = (p_A^\mu - p_C^\mu)\ (p_{A\mu} - p_{C\mu}) \tag{D.5}$$

$$= m_A^2 + m_C^2 - 2\ p_A \cdot p_C \tag{D.6}$$

$$\Leftrightarrow \qquad p_A \cdot p_C = \frac{1}{2}(m_A^2 + m_C^2 - t) \tag{D.7}$$

The contracted momenta, $p_A \cdot p_C$ can therefore be expressed in terms of t, m_A and m_C.

Following this example, 6 relations can be derived, containing any possible combination of contracting 4-momenta. Those relations have been used extensively to simplify the extracted scattering amplitudes squared $\overline{|\mathcal{M}|^2}$ in Section 3.1.1.

E
Gell-Mann Matrices

The Gell-Mann matrices are a set of 8 traceless, hermitian 3x3 matrices that form a basis of the SU(3) symmetry group. They are defined as

$$\lambda_1 = \begin{pmatrix} 0 & 1 & 0 \\ 1 & 0 & 0 \\ 0 & 0 & 0 \end{pmatrix} \quad \lambda_2 = \begin{pmatrix} 0 & -i & 0 \\ i & 0 & 0 \\ 0 & 0 & 0 \end{pmatrix} \quad \lambda_3 = \begin{pmatrix} 1 & 0 & 0 \\ 0 & -1 & 0 \\ 0 & 0 & 0 \end{pmatrix} \quad \lambda_4 = \begin{pmatrix} 0 & 0 & 1 \\ 0 & 0 & 0 \\ 1 & 0 & 0 \end{pmatrix}$$
$$\lambda_5 = \begin{pmatrix} 0 & 0 & -i \\ 0 & 0 & 0 \\ i & 0 & 0 \end{pmatrix} \quad \lambda_6 = \begin{pmatrix} 0 & 0 & 0 \\ 0 & 0 & 1 \\ 0 & 1 & 0 \end{pmatrix} \quad \lambda_7 = \begin{pmatrix} 0 & 0 & 0 \\ 0 & 0 & -i \\ 0 & i & 0 \end{pmatrix} \quad \lambda_8 = \frac{1}{\sqrt{3}} \begin{pmatrix} 1 & 0 & 0 \\ 0 & 1 & 0 \\ 0 & 0 & 2 \end{pmatrix} \tag{E.1}$$

and are linearly independent. Furthermore, they fulfil the orthogonality relation

$$\mathrm{Tr}(\lambda_i \, \lambda_j) = 2\delta_{ij} \tag{E.2}$$

with δ_{ij} being the Kronecker delta, and satisfy the commutation relations

$$\left[\frac{\lambda_i}{2}, \frac{\lambda_j}{2}\right] = f_{ijk} \, \frac{\lambda_k}{2}. \tag{E.3}$$

Here, f_{ijk} are the completely antisymmetric structure constants defined as

$$f_{123} = 1 \tag{E.4}$$
$$f_{147} = f_{165} = f_{246} = f_{257} = f_{345} = f_{376} = \frac{1}{2} \tag{E.5}$$
$$f_{458} = f_{678} = \frac{\sqrt{3}}{2} \tag{E.6}$$

As the Gell-Mann matrices are a representation of the SU(3) symmetry group, they serve as a basis for the chiral effective field theory described in Section **??**.

F

Photon Production Channels

In this section, the contributing Feynman diagrams and corresponding matrix elements for the photon production processes (3.8c)-(3.8b) are listed. They are taken from [265]. The values for the parameters appearing in the matrix elements can be found in Appendix **??**.

F.1. $\pi + \rho \to \pi + \gamma$

$\pi^\pm + \rho^0 \to (\pi, \rho, a_1) \to \pi^\pm + \gamma$

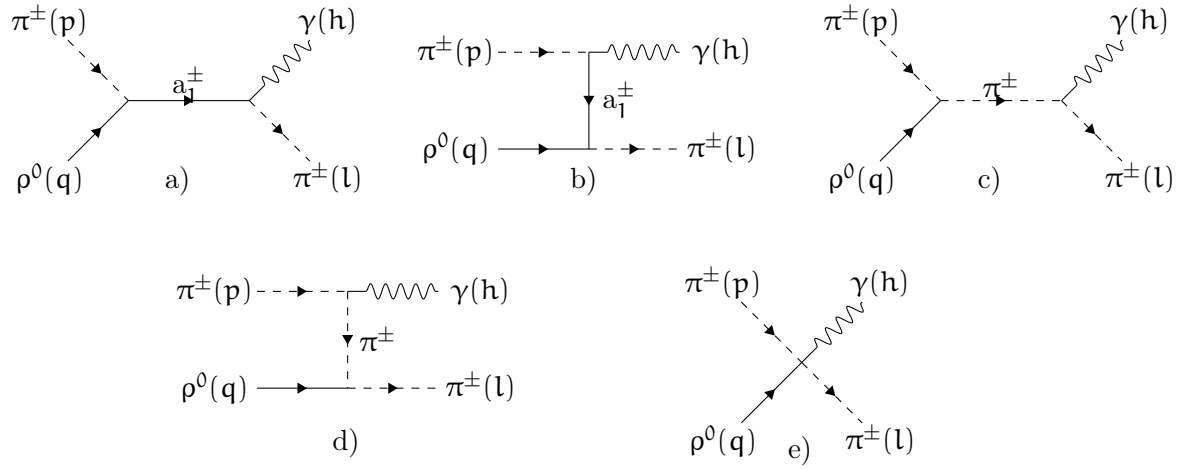

$$\mathcal{M}_a = \frac{-C\hat{g}^2}{2(s - m_{a1}^2 + i m_{a1}\Gamma_{a1})} \Big[(\eta_1 - \eta_2)^2 \ (-g^{\mu\nu}\ p\cdot q\ l\cdot h + p\cdot q\ h^\mu l^\nu - p^\mu l^\nu\ q\cdot h + p^\mu q^\nu\ l\cdot h) + \eta_2(\eta_1 - \eta_2) m_\rho^2\ (l\cdot h\ g^{\mu\nu} - h^\mu l^\nu)\Big]\ \epsilon_\mu(q)\epsilon_\nu^*(h)$$

$$\mathcal{M}_b = \frac{-C\hat{g}^2}{2(t - m_{a1}^2)} \Big[(\eta_1 - \eta_2)^2 \ (-g^{\mu\nu}\ p\cdot h\ l\cdot q + p\cdot h\ l^\mu q^\nu + h^\mu p^\nu\ q\cdot l - l^\mu p^\nu\ q\cdot h) + \eta_2(\eta_1 - \eta_2) m_\rho^2\ (-p\cdot h g^{\mu\nu} + h^\mu p^\nu\Big]\ \epsilon_\mu(q)\epsilon_\nu^*(h)$$

$$\mathcal{M}_c = -2C\hat{g}^2\ (1 - \frac{\delta}{2})\ \frac{l^\nu p^\mu}{(s - m_\pi^2)}\ \epsilon_\mu(q)\epsilon_\nu^*(h)$$

$$\mathcal{M}_d = -2C\hat{g}^2\ (1 - \frac{\delta}{2})\ \frac{p^\nu l^\mu}{(t - m_\pi^2)}\ \epsilon_\mu(q)\epsilon_\nu^*(h)$$

$$\mathcal{M}_e = C\left[g^{\mu\nu}\hat{g}^2\ (1 - \frac{\delta}{2}) + \left(\frac{\hat{g}^2\delta}{m_\rho^2} - 4C_4\hat{g}^2\right)\ (g^{\mu\nu}\ ^{q\cdot h} - h^\mu q^\nu)\right]\ \epsilon_\mu(q)\epsilon_\nu^*(h)$$

$\pi^0 + \rho^\pm \to (\pi, \rho, \alpha_1) \to \pi^\pm + \gamma$

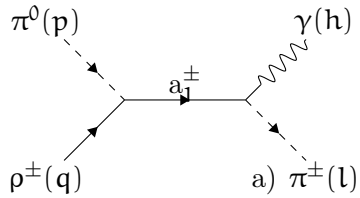

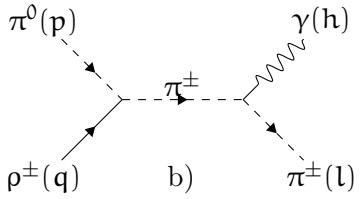

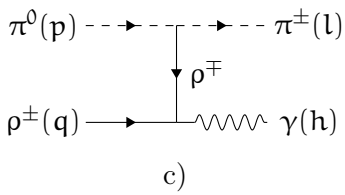

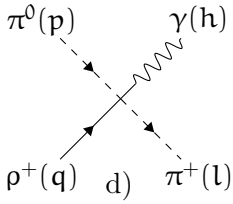

$$\mathcal{M}_a = \frac{C\hat{g}^2}{2(s - m_{a1}^2 + im_{a1}\Gamma_{a1})} \Big[(\eta_1 - \eta_2)^2 \ (-g^{\mu\nu}\ p\cdot q\ l\cdot h + p\cdot q\ h^\mu l^\nu - p^\mu l^\nu\ q\cdot h + p^\mu q^\nu\ l\cdot h) + \eta_2(\eta_1 - \eta_2)m_\rho^2\ (l\cdot h\ g^{\mu\nu} - h^\mu l^\nu)\Big]\ \ \epsilon_\mu(q)\epsilon_\nu^*(h)$$

$$\mathcal{M}_b = -\ 2C\hat{g}^2\ (1 - \frac{\delta}{2})\ \frac{l^\nu p^\mu}{(s - m_\pi^2)}\ \epsilon_\mu(q)\epsilon_\nu^*(h)$$

$$\mathcal{M}_c = -\ C\ \frac{\hat{g}^2}{2(u - m_\rho^2)}\ \left(1 - \frac{\delta}{2} - \frac{\delta(u - m_\rho^2)}{2m_\rho^2}\right)\ [(l+p)\cdot(q+h)\ g^{\mu\nu}\ - 2h^\mu(l+p)^\nu - 2q^\nu(l+p)^\mu]\ \ \epsilon_\mu(q)\epsilon_\nu^*(h)$$

$$\mathcal{M}_d = C\ \Big[-g^{\mu\nu}\ \frac{\hat{g}^2}{2}\ (1 - \frac{\delta}{2}) + \frac{\hat{g}^2\delta}{2m_\rho^2}\ (-2h\cdot l g^{\mu\nu} + 2h^\mu l^\nu + q^\nu(p+l)^\mu) + 2C_4\hat{g}^2\ (g^{\mu\nu}q\cdot h - h^\mu q^\nu)\Big]\ \ \epsilon_\mu(q)\epsilon_\nu^*(h)$$

$\pi^{\pm} + \rho^{\pm} \to (\pi, \rho, a_1) \to \pi^0 + \gamma$

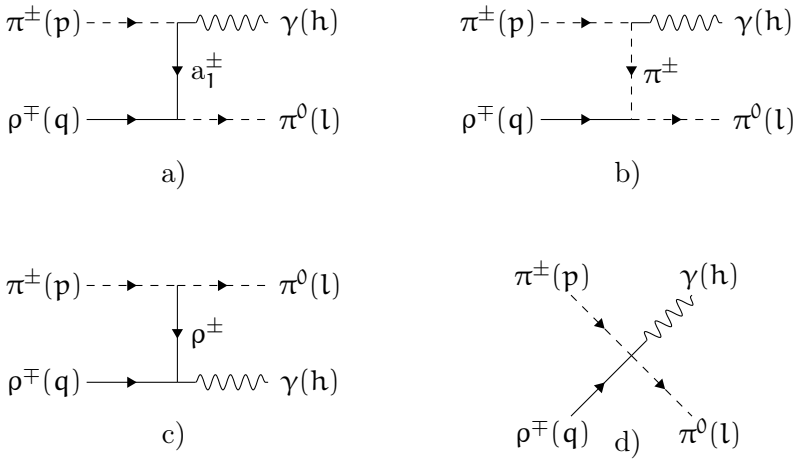

$$\mathcal{M}_a = \frac{C\hat{g}^2}{2(t-m_{a1}^2)} \Big[(\eta_1-\eta_2)^2 \ (-g^{\mu\nu}\ p\cdot h\ l\cdot q + p\cdot h\ l^\mu q^\nu + h^\mu p^\nu\ q\cdot l - l^\mu p^\nu\ q\cdot h) + \eta_2(\eta_1-\eta_2)m_\rho^2\ (-p\cdot h\ g^{\mu\nu} + h^\mu p^\nu)\Big]\ \epsilon_\mu(q)\epsilon_\nu^*(h)$$

$$\mathcal{M}_b = 2C\hat{g}^2\ (1-\frac{\delta}{2})\ \frac{p^\nu l^\mu}{(t-m_\pi^2)}\ \epsilon_\mu(q)\epsilon_\nu^*(h)$$

$$\mathcal{M}_c = C\ \frac{\hat{g}^2}{2(u-m_\rho^2)}\ \left(1-\frac{\delta}{2}-\frac{\delta(u-m_\rho^2)}{2m_\rho^2}\right)\ [(l+p)\cdot(q+h)\ g^{\mu\nu}\ -2h^\mu(l+p)^\nu - 2q^\nu(l+p)^\mu]\ \epsilon_\mu(q)\epsilon_\nu^*(h)$$

$$\mathcal{M}_d = C\ \Big[-g^{\mu\nu}\ \frac{\hat{g}^2}{2}\ (1-\frac{\delta}{2}) + \frac{\hat{g}^2\delta}{2m_\rho^2}\,(2h\cdot p g^{\mu\nu} - 2h^\mu p^\nu - q^\nu(p+l)^\mu) + 2C_4\hat{g}^2\,(g^{\mu\nu}q\cdot h - h^\mu q^\nu)\Big]\ \epsilon_\mu(q)\epsilon_\nu^*(h)$$

$\pi^0 + \rho^0 \to \omega \to \pi^0 + \gamma$

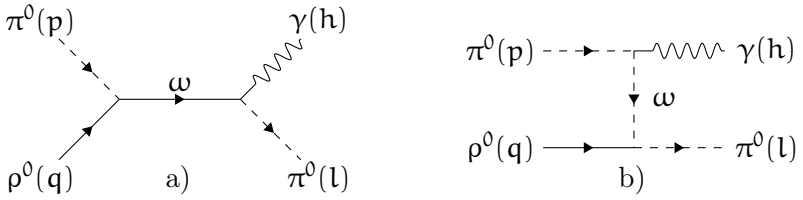

$$\mathcal{M}_a = \frac{-C g^2_{\pi\rho\omega}}{(s - m^2_\omega)} \, (p+q)_\alpha \, (p+q)_y \, h_\mu q_x \left(-g_{\beta\gamma} + \frac{(p+q)_\beta \, (p+q)_\gamma}{m^2_\omega} \right) \, \varepsilon^{\mu\nu\alpha\beta} \varepsilon^{x\sigma y\gamma} \, \epsilon_\sigma(q) \epsilon^*_\nu(h)$$

$$\mathcal{M}_b = \frac{-C g^2_{\pi\rho\omega}}{(t - m^2_\omega)} \, (p-h)_\alpha \, (p-h)_y \, h_\mu q_x \left(-g_{\beta\gamma} + \frac{(p-h)_\beta \, (p-h)_\gamma}{m^2_\omega} \right) \, \varepsilon^{\mu\nu\alpha\beta} \varepsilon^{x\sigma y\gamma} \, \epsilon_\sigma(q) \epsilon^*_\nu(h)$$

$\pi^\pm + \rho^\pm \to \omega \to \pi^0 + \gamma$

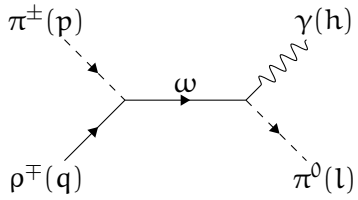

$$\mathcal{M} = \frac{-C g^2_{\pi\rho\omega}}{(s - m^2_\omega)} \, (p+q)_\alpha \, (p+q)_y \, h_\mu q_x \left(-g_{\beta\gamma} + \frac{(p+q)_\beta \, (p+q)_\gamma}{m^2_\omega} \right) \, \varepsilon^{\mu\nu\alpha\beta} \varepsilon^{x\sigma y\gamma} \, \epsilon_\sigma(q) \epsilon^*_\nu(h)$$

$\pi^0 + \rho^\pm \to \omega \to \pi^\pm + \gamma$

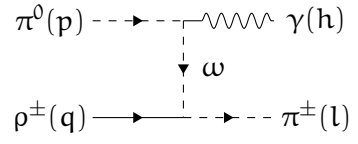

$$\mathcal{M} = \frac{-C g^2_{\pi\rho\omega}}{(t - m^2_\omega)} \, (p-h)_\alpha \, (p-h)_y \, h_\mu q_x \left(-g_{\beta\gamma} + \frac{(p-h)_\beta \, (p-h)_\gamma}{m^2_\omega} \right) \, \varepsilon^{\mu\nu\alpha\beta} \varepsilon^{x\sigma y\gamma} \, \epsilon_\sigma(q) \epsilon^*_\nu(h)$$

F.2. $\pi + \pi \to \rho + \gamma$

$\pi^{\pm} + \pi^{\pm} \to (\pi, \rho, a_1) \to \rho^0 + \gamma$

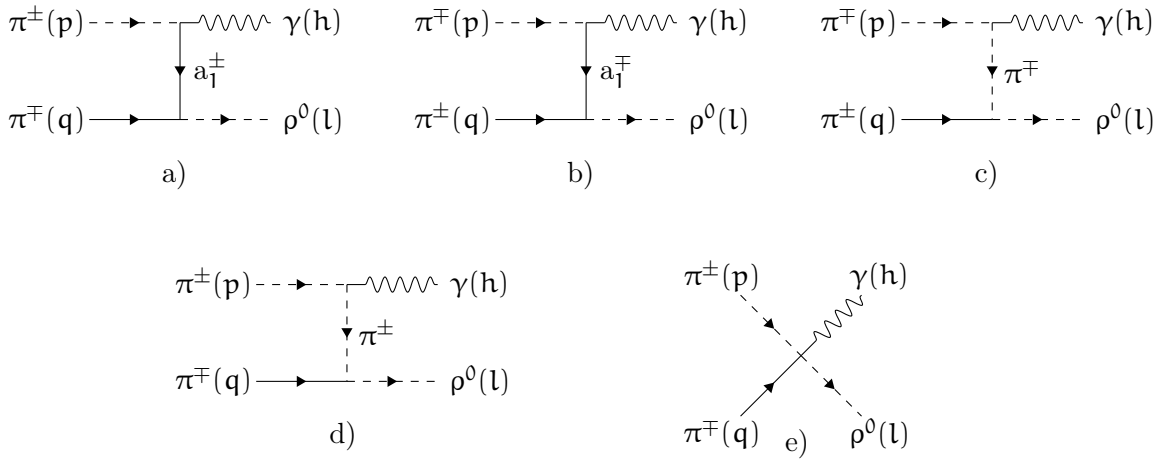

$$\mathcal{M}_a = \frac{-C\hat{g}^2}{2(s - m_{a1}^2 + im_{a1}\Gamma_{a1})} \Big[(\eta_1 - \eta_2)^2 \ (-g^{\mu\nu}\ p\cdot l\ q\cdot h + p\cdot l\ h^{\mu}q^{\nu} - p^{\mu}q^{\nu}\ l\cdot h + p^{\mu}l^{\nu}\ q\cdot h)$$
$$+\eta_2(\eta_1 - \eta_2)m_{\rho}^2\ (-q\cdot h\ g^{\mu\nu} + h^{\mu}q^{\nu})\Big]\ \epsilon_{\mu}(-l)\epsilon_{\nu}^*(h)$$

$$\mathcal{M}_b = \frac{-C\hat{g}^2}{2(t - m_{a1}^2)} \Big[(\eta_1 - \eta_2)^2 \ (-g^{\mu\nu}\ p\cdot h\ q\cdot l + p\cdot h\ q^{\mu}l^{\nu} + h^{\mu}p^{\nu}\ l\cdot q - q^{\mu}p^{\nu}\ l\cdot h) +$$
$$\eta_2(\eta_1 - \eta_2)m_{\rho}^2\ (-p\cdot h g^{\mu\nu} + h^{\mu}p^{\nu}\Big]\ \epsilon_{\mu}(-l)\epsilon_{\nu}^*(h)$$

$$\mathcal{M}_c = -2C\hat{g}^2\ (1 - \frac{\delta}{2})\ \frac{-q^{\nu}p^{\mu}}{(s - m_{\pi}^2)}\ \epsilon_{\mu}(-l)\epsilon_{\nu}^*(h)$$

$$\mathcal{M}_d = 2C\hat{g}^2\ (1 - \frac{\delta}{2})\ \frac{p^{\nu}q^{\mu}}{(t - m_{\pi}^2)}\ \epsilon_{\mu}(-l)\epsilon_{\nu}^*(h)$$

$$\mathcal{M}_e = C\left[g^{\mu\nu}\hat{g}^2\ (1 - \frac{\delta}{2}) + \left(\frac{\hat{g}^2\delta}{m_{\rho}^2} - 4C_4\hat{g}^2\right)\ (-g^{\mu\nu\ l\cdot h} + h^{\mu}l^{\nu})\right]\ \epsilon_{\mu}(-l)\epsilon_{\nu}^*(h)$$

$\pi^{\pm} + \pi^0 \to (\pi, \rho, a_1) \to \rho^{\pm} + \gamma$

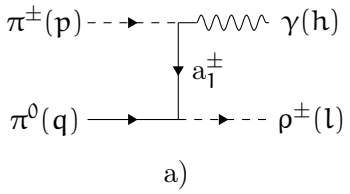

a)

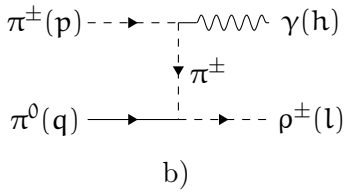

b)

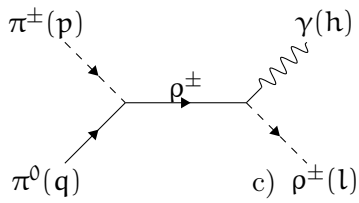

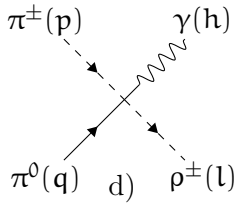

$$\mathcal{M}_a = \frac{C\hat{g}^2}{2(t - m_{a1}^2)} \Big[(\eta_1 - \eta_2)^2 \ (-g^{\mu\nu}\ p\cdot h\ q\cdot l + p\cdot h\ q^{\mu}l^{\nu} + h^{\mu}p^{\nu}\ l\cdot q - q^{\mu}p^{\nu}\ l\cdot h) + \eta_2(\eta_1 - \eta_2)m_{\rho}^2\ (-p\cdot h\ g^{\mu\nu} + h^{\mu}p^{\nu})\Big]\ \epsilon_{\mu}(-l)\epsilon_{\nu}^*(h)$$

$$\mathcal{M}_b = -2C\hat{g}^2\ (1 - \frac{\delta}{2})\ \frac{p^{\nu}q^{\mu}}{(t - m_{\pi}^2)}\ \epsilon_{\mu}(-l)\epsilon_{\nu}^*(h)$$

$$\mathcal{M}_c = C\ \frac{\hat{g}^2}{2(u - m_{\rho}^2)}\ \left(1 - \frac{\delta}{2} - \frac{\delta(u - m_{\rho}^2)}{2m_{\rho}^2}\right)\ [(p - q)\cdot(h - l)\ g^{\mu\nu}\ - 2h^{\mu}(p - q)^{\nu} - 2q^{\nu}(p - q)^{\mu}]\ \epsilon_{\mu}(-l)\epsilon_{\nu}^*(h)$$

$$\mathcal{M}_d = C\ \Big[-g^{\mu\nu}\ \frac{\hat{g}^2}{2}\ (1 - \frac{\delta}{2}) + \frac{\hat{g}^2\delta}{2m_{\rho}^2}\,(2h\cdot p g^{\mu\nu} - 2h^{\mu}p^{\nu} - l^{\nu}(p - q)^{\mu}) + 2C_4\hat{g}^2\,(-g^{\mu\nu}l\cdot h + h^{\mu}l^{\nu})\Big]\ \epsilon_{\mu}(q)\epsilon_{\nu}^*(h)$$